



HAL
open science

Numerical and experimental studies for the optimization and protection of NI-MI HTS coils

Clément Genot

► **To cite this version:**

Clément Genot. Numerical and experimental studies for the optimization and protection of NI-MI HTS coils. Micro and nanotechnologies/Microelectronics. Université Grenoble Alpes [2020-..], 2022. English. NNT : 2022GRALT072 . tel-03946319

HAL Id: tel-03946319

<https://theses.hal.science/tel-03946319v1>

Submitted on 19 Jan 2023

HAL is a multi-disciplinary open access archive for the deposit and dissemination of scientific research documents, whether they are published or not. The documents may come from teaching and research institutions in France or abroad, or from public or private research centers.

L'archive ouverte pluridisciplinaire **HAL**, est destinée au dépôt et à la diffusion de documents scientifiques de niveau recherche, publiés ou non, émanant des établissements d'enseignement et de recherche français ou étrangers, des laboratoires publics ou privés.

THÈSE

Pour obtenir le grade de

DOCTEUR DE L'UNIVERSITÉ GRENOBLE ALPES

École doctorale : EEATS - Electronique, Electrotechnique, Automatique, Traitement du Signal (EEATS)

Spécialité : GENIE ELECTRIQUE

Unité de recherche : Laboratoire de Génie Electrique

Etudes numériques et expérimentales pour l'optimisation et la protection des bobinages HTc NI-MI

Numerical and experimental studies for the optimization and protection of NI-MI HTS coils

Présentée par :

Clément GENOT

Direction de thèse :

Pascal TIXADOR

Directeur de thèse

Philippe FAZILLEAU

Ingénieur-chercheur, CEA

Co-encadrant de thèse

Thibault LECREVISSE

Ingénieur-chercheur, CEA

Co-encadrant de thèse

Rapporteurs :

Marco BRESCHI

PROFESSEUR ASSOCIE, Alma Mater Studiorum-Univ di Bologna

Frédéric SIROIS

PROFESSEUR, Ecole Polytechnique de Montréal

Thèse soutenue publiquement le **5 octobre 2022**, devant le jury composé de :

Pascal TIXADOR

PROFESSEUR DES UNIVERSITES, UNIVERSITE GRENOBLE ALPES

Directeur de thèse

Marco BRESCHI

PROFESSEUR ASSOCIE, Alma Mater Studiorum-Univ di Bologna

Rapporteur

Frédéric SIROIS

PROFESSEUR, Ecole Polytechnique de Montréal

Rapporteur

Luca BOTTURA

DOCTEUR EN SCIENCES, CERN

Examineur

Alexandre TORRE

INGENIEUR DOCTEUR, CEA CENTRE DE CADARACHE

Examineur

Eric BEAUGNON

PROFESSEUR DES UNIVERSITES, UNIVERSITE GRENOBLE ALPES

Président

Invités :



« On souffre au quotidien pour vivre des moments comme ça, des émotions comme ça, donc ça fait plaisir de se laisser aller un peu quand ça gagne. »

Antoine Dupont

Remerciements

Je tiens tout d'abord à remercier mon tuteur, Thibault Lécresse, pour toutes les connaissances qu'il m'a transmises, pour l'ensemble de ses judicieux conseils et pour le temps consacré à suivre mes travaux durant ces trois années.

Je remercie également mon directeur de thèse, Pascal Tixador, pour l'ensemble des suivis réguliers durant cette thèse qui m'ont permis de mener à bien l'ensemble de ces travaux. Mais aussi pour son expérience et tous ces conseils qui m'ont permis de réaliser cette thèse.

Je remercie aussi mon autre tuteur, Philippe Fazilleau de m'avoir suivi durant ces trois années et accompagné dans l'utilisation du modèle PEEC.

Je remercie les membres de mon jury, mes rapporteurs Marco Breschi et Frédéric Sirois pour leur lecture attentive de mon mémoire et pour leurs remarques pertinentes, ainsi que Luca Bottura, Alexandre Torre et Eric Beaugnon, examinateurs de ma thèse.

Je tiens aussi à remercier Claire Antoine pour toutes les connaissances qu'elle m'a transmises sur la préparation et l'analyse de mes échantillons. Cela m'a permis de réaliser une étude approfondie sur la résistance de contact. Je tiens aussi à remercier David Longuevergne pour son aide lors de l'utilisation du MEB, et Thomas Proslie pour la réalisation des dépôts ALD.

Merci à toi Guillaume, pour ton aide concernant les différents calculs réalisés, mais aussi pour toutes ces discussions fortes intéressantes et les parties de jeu de rôle !

A mes deux collègues de thèse, Mahmoud et Simon, avec qui j'ai bien rigolé et réalisé de nombreuses parties d'échecs.

A toi Iryna, d'avoir été à mes côtés durant ce long travail. Ta présence m'a apporté énormément de soutien, cela m'a énormément aidé.

A mes parents Maurice et Valérie, ma sœur Aude (Nia ha ha !!!) et mes amis, pour leur soutien et les bons moments passés avec eux.

A mon petit doudou chat qui est arrivé en même temps que cette thèse, qui était là tous les soirs pour m'accueillir chez moi (même si tu attendais en partie le repas du soir, « miaou miaou » je sais...).

A Hugo Raymond, pour m'avoir fait faire un tour à moto (mais aussi pour son aide lors de la conception du dispositif expérimental).

A l'ensemble de mes collègues au LEAS, et mon chef de laboratoire Lionel Quettier, pour tous les petits conseils bien utiles et les bons moments lors de la pause du midi. Mais aussi aux stagiaires du laboratoire, notamment pour les nombreuses parties de billard !

Au XV de France d'avoir remporté le grand chelem en 2022 !

A Michel De Sousa, Christophe Mayri et aux techniciens pour leur aide pour mettre en place ma station expérimentale. Mais aussi aux deux stagiaires, Viktor et Emmanuel, que j'ai encadré durant cette thèse qui m'ont aidé à réaliser des mesures expérimentales supplémentaires dans le cadre de mes travaux.

Et enfin à Xavier Chaud et Jung-bin Song du LNCMI à Grenoble pour leur aide dans la réalisation de mesures expérimentales, fortement utiles pour mes travaux de thèse.

Contents

Contents.....	4
Abstract.....	7
Résumé.....	9
I NI and MI protection: state of the art.....	12
I. 1 General introduction to superconductivity.....	13
I. 1. 1 The phenomenon of superconductivity	13
I. 1. 2 Low-Temperature Superconductors (LTS)	14
I. 2 High-Temperature Superconductor (HTS)	15
I. 2. 1 First-generation HTS superconductors.....	16
I. 2. 2 Second-generation HTS superconductors	17
I. 2. 3 High-field electromagnets using HTS superconductors.....	19
I. 3 Protection of superconducting coils.....	21
I. 3. 1 The different methods of protection against the quench phenomenon.....	21
I. 3. 2 The quench propagation velocity for HTS	22
I. 3. 3 No-Insulation pancake: a method of protection for REBCO coils.....	23
I. 4 Objectives of this work	28
II Behavior of superconducting coils during transient regimes, influence of the contact resistivity.....	31
II. 1 Partial Element Equivalent Circuit (PEEC) model.....	32
II. 1. 1 Electrical equation	32
II. 1. 2 Thermal equation	35
II. 1. 3 Mutual inductance	37
II. 1. 4 Components of magnetic induction	41
II. 1. 5 Parameterization of the critical surface of REBCO conductors.....	43
II. 1. 6 Functioning and limitations of the PEEC model.....	44
II. 1. 7 An opening for a reduction of the computation time of the PEEC model.....	45
II. 2 Simulation of a No- or Metal-Insulation simple pancake.....	47
II. 2. 1 Influence of the contact resistivity during a quench.....	47
II. 2. 2 Simple pancake in ramp-up operation, influence of the contact resistivity....	55
II. 2. 3 Rapid discharge, influence of the contact resistivity	60

II. 2. 4	Partial-Insulation simple pancake.....	61
II. 2. 5	Conclusion	64
II. 3	Simulation of a multi-pancake coil	64
II. 3. 1	Quench propagation by magnetic coupling	64
II. 3. 2	Energy balance	75
II. 3. 3	Conclusion multi-pancake coil	77
II. 4	Simulation of a simple racetrack coil.....	77
II. 5	Conclusion	78
III	Understanding and control of the contact resistivity between HTS tapes	81
III. 1	Contact resistivity in NI and MI coils from the literature.....	82
III. 2	Experimental measurements of contact resistivity between superconducting tapes with or without metallic co-wound tape.....	83
III. 2. 1	Presentation of the experimental setup.....	83
III. 2. 2	Contact resistivity measurements between superconducting tapes	87
III. 2. 3	Conclusion experimental measurements of contact resistivity between superconducting tapes	104
III. 3	Experimental measurements of contact resistivity between superconducting tapes with an Atomic Layer Deposition	105
III. 3. 1	Introduction	105
III. 3. 2	Contact resistivity with 100 nm Atomic Layer Deposition	108
III. 3. 3	Parameters that could have explained the small increase in contact resistivity with Atomic Layer Deposition	109
III. 3. 4	Phenomena responsible of the small increase in contact resistivity with Atomic Layer Deposition	113
III. 3. 5	Modification of the contact resistivity behavior as a function of the load with Atomic Layer Deposition	119
III. 3. 6	Contact resistivity with 1 μm Atomic Layer Deposition.....	120
III. 3. 7	Conclusion of the Atomic Layer Deposition	121
IV	Coil protection	123
IV. 1	Introduction.....	124
IV. 2	Protection with NI/MI and voltage limitation.....	124
IV. 2. 1	Simulation of a simple pancake with voltage limitation	124
IV. 2. 2	Experimental results: two Theva-SuperPower double pancakes coil.....	136
IV. 2. 3	Simulation: two Theva-SuperPower double pancakes coil	141
IV. 3	Magnetic shielding.....	149
IV. 3. 1	Magnetic shielding: modification of the PEEC model.....	149
IV. 3. 2	Simulations with magnetic shielding.....	150

IV. 4	Conclusion	155
V	General conclusion	157
VI	Appendix	160
VI. 1	Partial Element Equivalent Circuit (PEEC) model, Chapter II.....	160
VI. 1. 1	Electrical equation	160
VI. 1. 2	Thermal equation	164
VI. 1. 3	Mutual inductance in racetrack.....	167
VI. 2	Contact resistivity measurements between superconducting tapes, Chapter III..	171
VI. 3	Micro soldering, Chapter III	173
VII	Bibliography	176

Abstract

REBCO No- or Metal-Insulation (NI and MI) windings open the way for very high field magnets, but their transient operation must be understood and optimized. The protection of electromagnets made of insulated windings using high-temperature superconductors (HTS) remains difficult to implement because of the low speed of quench propagation. For this reason, the traditional insulation can be removed and replaced with metallic tape. Having a No- or Metal-Insulation coil provides protection and improves the thermal stability of the magnet. The aim of this work is to understand the phenomenon of redistribution of radial and azimuthal currents during transient regimes in No- or Metal-Insulation HTS coils, which provides a self-protecting feature but also can lead to mechanical problems during transient regimes. The turn-to-turn contact resistivity has been measured for several configurations and under different conditions.

For this purpose, a PEEC (Partial Element Equivalent Circuit) code simulating the case of a simple pancake subjected to a quench was used. This model allows to monitor the values of the radial and azimuthal currents (for each sector of each turn) within the pancake as a function of time. The code was modified to simulate the behavior of a coil consisting of several pancakes during a quench, or during other transient regimes (ramp-up operation, rapid discharge). A model for NI-MI simple racetrack has also been implemented in the code.

The behavior of an NI-MI coil during transient regimes is mainly based on the value of the electrical contact resistivity between each turn. This parameter has to be evaluated to have accurate models.

Experimental measurements were carried out to measure the contact resistivity R_{ct} between non-insulated 6 mm wide HTS superconducting tapes as a function of the mechanical pressure applied to a stack (up to 70 MPa) and cooled down at liquid nitrogen temperature (77 K). A large number of samples were tested for different manufacturers, mainly without insulation (NI) or with metal insulation (MI). Changing the nature of the insulation between the turns changes the value of the contact resistivity and thus the behavior of a coil during a transient regime. While mechanical stress affects contact resistivity, it has also been shown that the number of mechanical cycles affects it to a greater or lesser extent depending on the technology used. In a second part, ALD (Atomic Layer Deposition) of ZnO/Al₂O₃ of a few hundred nanometers applied on superconducting or metallic tapes were tested in order to modify the contact resistivity R_{ct} . The aim is to deposit an insulating material on a tape in order to tune the contact resistivity between two tapes. We will see that this method is not optimal for this type of application.

Finally, the PEEC model was completed to study the behavior of a simple or multi-pancake during a quench with voltage limitation of the power supply. The principle is to use the high increase in the resistivity of an MI pancake during a quench and to adjust the maximum voltage of the current source to obtain a rapid decline of the supply current passively once the voltage is reached. This is an effective way of protecting a coil. Simulations and experimental measurements were carried out on a magnet made of four pancakes to demonstrate the use of MI technology to improve the protection against quenches.

In summary, this work led to an electromagnetic advanced tool to design and optimize HTS NI-MI coil with experimental extensive data about contact resistivity under different conditions. Experiments have confirmed the simulations.

Résumé

Les aimants REBCO sans, ou avec isolation métallique, ouvrent la voie aux aimants à très haut champ, mais leur fonctionnement transitoire doit être étudié et optimisé. La protection des électro-aimants utilisant des supraconducteurs à haute température critique (HTc) reste aujourd'hui difficile à mettre en œuvre du fait de la faible vitesse de propagation du quench. Pour cela, l'isolation traditionnelle a été enlevée, puis remplacée par une isolation métallique. Avoir une bobine non isolée, ou avec une isolation métallique, assure la protection et améliore la stabilité thermique de l'aimant. L'objectif des recherches est de comprendre le phénomène de redistribution des courants radiaux et azimutaux durant le régime transitoire dans les bobines HTc non isolées, ce qui peut engendrer des problèmes mécaniques lors d'un quench dans un aimant.

Pour cela, un programme PEEC (Partial Element Equivalent Circuit) simulant le cas d'une simple galette soumise à un quench a été repris. Ce modèle permet d'observer localement les valeurs des courants radiaux et azimutaux (pour chaque secteur de chaque spire) au sein de la galette en fonction du temps. Ce programme a ensuite été modifié pour simuler le comportement d'une bobine constituée de plusieurs galettes soumises à un quench, ou durant d'autres régimes transitoires (chargement, décharge rapide). Le modèle d'une simple racetrack NI-MI (No-Insulation et Metal-Insulation) a également été implémenté dans le code. Le comportement d'une bobine NI-MI durant un régime transitoire repose principalement sur la valeur de la résistance électrique de contact entre chaque spire. Une étude expérimentale poussée de ce paramètre a été menée.

Des mesures expérimentales ont été réalisées dans le but de mesurer la résistance de contact R_{ct} entre des rubans supraconducteurs HTc de 6 mm de large non isolés en fonction de la contrainte appliquée sur un empilement de rubans (jusqu'à 70 MPa) et refroidi à l'azote liquide (77 K). De nombreux échantillons ont été testés pour différents constructeurs, principalement sans isolation (NI) ou avec isolation métallique (MI). Venir modifier la nature de l'isolation entre les spires modifie la valeur de la résistance de contact et donc le comportement d'une bobine lors d'un régime transitoire. Si la contrainte mécanique influe sur la résistance de contact, il a aussi été montré que le nombre de cycles mécaniques vient modifier celle-ci de manière plus ou moins marquée selon la technologie utilisée. Dans une seconde partie, les dépôts ALD (Atomic Layer Deposition) en ZnO/Al₂O₃ de quelques centaines de nanomètres, sur des rubans métalliques de co-bobinage ou directement sur les rubans supraconducteurs, ont été testés afin de modifier la résistance de contact R_{ct} . L'idée ici est de faire un dépôt de matière isolante sur un ruban afin d'augmenter de manière significative la résistance de contact et par la suite, de la contrôler.

Enfin, le modèle PEEC a été complété afin d'étudier le comportement d'une bobine lors d'un quench avec une limitation en tension de la source d'alimentation en courant. Le principe est d'utiliser la forte augmentation de la résistance d'une galette MI lors d'un quench, et d'ajuster la tension maximale de la source de courant pour obtenir une chute rapide du courant d'alimentation de manière passive. Cela permet de protéger efficacement une bobine. Des simulations ainsi que des mesures expérimentales ont été menées sur une bobine constituée

de quatre galettes MI afin de montrer l'intérêt de la technologie MI pour améliorer la protection contre les quenches.

Chapter I

NI and MI protection: state of the art

This chapter is a general introduction of electromagnets protection made of High-Temperature Superconductors (HTS) REBCO tapes, which were the material studied in this work. Firstly, a general introduction to superconductivity is given. In the second part, HTS materials are presented with a focus on REBCO tapes, including the reasons for their use and the specific characteristics that make it difficult to provide effective protection against quench. In the last part, different methods to protect electromagnets against quench made of HTS REBCO tapes are presented, focusing in a second section on HTS REBCO coils without the electrical insulation between the superconducting tapes and its variants.

I. 1 General introduction to superconductivity

I. 1. 1 The phenomenon of superconductivity

I. 1. 1. 1 The discovery of superconductors over time

Superconductivity is a remarkable phenomenon presented by certain metals, alloys or ceramics, whose electrical resistivity becomes practically zero below a certain temperature, called the critical temperature. Gilles Holst discovered this phenomenon in 1911 under the direction of Heike Kammerling Onnes in the Netherlands, on a mercury filament cooled with liquid helium (to a temperature of 4.2 K). Inversely, at a temperature above the critical temperature, the superconducting material behaves like ordinary resistive materials, it is the normal state. Although this phenomenon was discovered in the early 20th century, the first real applications with superconducting materials start in the 1960s.

Over time, new superconducting materials were discovered, with increasingly efficient properties. In 1986, superconducting oxides were discovered paving the way for critical temperature above 80 K. These are known as High-Temperature Superconductors (HTS). In 2001, new superconducting materials were discovered, such as magnesium diboride (MgB_2). The main superconducting materials, their year of discovery and critical temperature, are presented in Figure I-1.

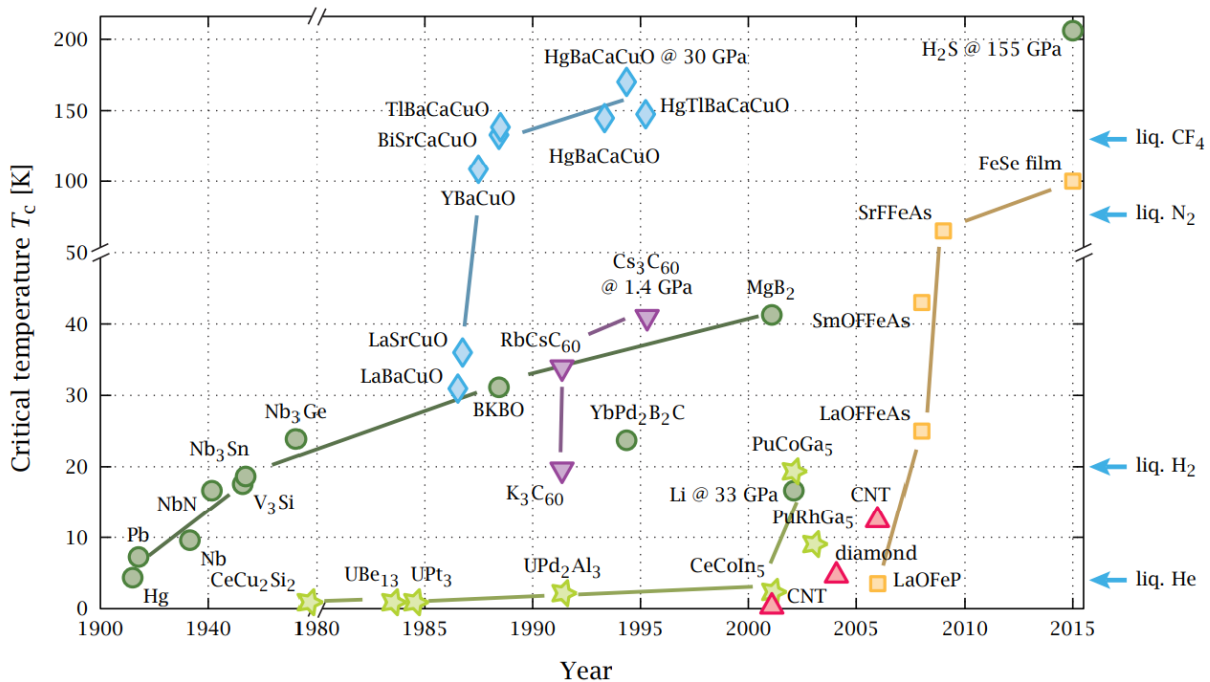


Figure I-1: Critical temperature of different superconducting materials according to their year of discovery [1]. LTS superconductors (green circles), the cuprates (blue diamonds), and the iron-based superconductors (yellow squares).

I. 1. 1. 2 The limits of the superconducting state: the critical surface

There are two types of superconductivity, type I and type II.

Type I superconductors materials have only one single and small critical induction B_c , usually under 0.1 T. Below this critical field B_c , the material is superconducting. Their use is therefore limited, and not even usable for large installations.

Type II superconductors are characterized by two critical inductions B_{c1} and B_{c2} . Under B_{c1} , those materials show the same behavior than type I. Above B_{c1} , they are in a mixed state with superconducting zones called vortexes and normal zones. Superconductivity only vanishes above B_{c2} except on the surface. B_{c2} may be higher (10 T and more) than type I B_c [2], [3] so the great interest for the type II.

The critical current density J_c is the third value determining whether a superconducting material is in its superconducting or dissipative state. However, the transition from the superconducting to the dissipative state is not instantaneous. Therefore, the critical current density is fixed by convention to be in agreement with an arbitrary electric field criterion E_0 . In the case of HTS, the common value of E_0 is 10^{-4} V/m.

Thus, three interdependent values define the superconducting or dissipative state of the material: the critical temperature T_c , the critical magnetic induction B_c and the critical current density J_c . These three parameters form the critical surface of the superconductor. In Figure I-2 on the right, the critical surfaces have been plotted using fits for NbTi (work of L. Bottura [4]), for Nb₃Sn (work of B. Bordini [5]) and for a Fujikura REBCO HTS tape whose fit has been proposed by J. Fleiter [6].

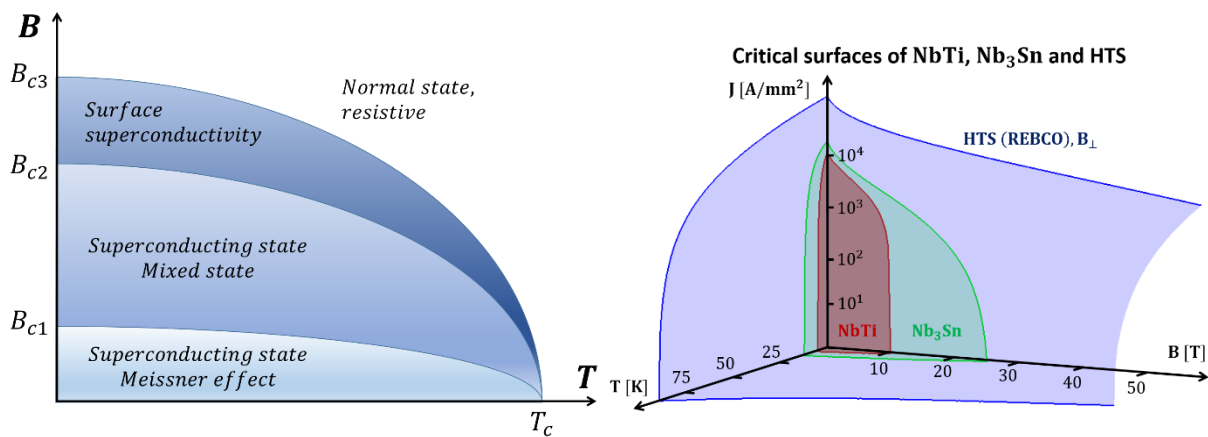


Figure I-2: On the left, phase diagram of a LTS type II superconductor. On the right, critical surfaces of NbTi [4], Nb₃Sn [5] and HTS Fujikura tape [6] with a field perpendicular to the tape surface.

The difference between NbTi and Nb₃Sn is observable, notably in the higher critical magnetic induction for Nb₃Sn compared to NbTi. This difference is even more pronounced between Nb₃Sn and Fujikura REBCO HTS tape. The critical magnetic induction of REBCO is greater than 100 T at 4.2 K, making the material highly attractive for applications generating high magnetic inductions. In the case of HTS, the critical area also depends on the angle between the tape surface and the magnetic induction. In the case of Figure I-2 on the right, the critical area is plotted in the worst case for the HTS tape: with a field perpendicular to the tape surface. For Low-Temperature Superconductors (LTS, mainly NbTi and Nb₃Sn), the critical temperature is the most restrictive but they remain the most used material due to their development stage and low/moderate cost. The temperature margin for the LTS between the superconducting state and the dissipative state is smaller compared to the HTS.

I. 1. 2 Low-Temperature Superconductors (LTS)

Thanks to superconductors, it is possible to carry high current densities and thus generate strong magnetic fields without dissipating energy. Currently, LTS are the most widely used in the field of superconductivity. More than 90% of applications use Niobium-Titanium (NbTi) or Niobium-Tin (Nb₃Sn). This is particularly true for NbTi, which is the only superconducting material that is truly industrial.

I. 1. 2. 1 Niobium-Titanium (NbTi)

Niobium titanium (NbTi) is currently the most widely used superconducting material. This material has the advantage of being cost-effective and not very sensitive to mechanical stress. It is possible to generate magnetic induction up to 12 T by cooling the material to 1.8 K (superfluid helium), or up to 8 T with cooling to 4.2 K. The cost of 1 m long conductor with a critical current of 1 kA for NbTi is about 1 \$ at 4.2 K (1 \$/kA/m) [7]. It is the most industrially superconductor material that is actually used in industry today. In particular, it is possible to produce cables of several kilometers in length, which has made it possible to carry out major projects such as the Large Hadron Collider (LHC) at CERN [8].

NbTi is also used for Magnetic Resonance Imaging (MRI) and Nuclear Magnetic Resonance (NMR). The most powerful MRI scanner in the world today is Iseult. It can generate a magnetic induction of 11.7 T in an opening of 90 cm [9].

However, with this type of superconducting material, it is not possible to generate magnetic fields higher than 12 T. Above this magnetic induction, the superconducting state of the material is lost. Other superconducting materials must be used, such as Niobium-Tin.

I. 1. 2. 2 Niobium-Tin (Nb₃Sn)

In order to generate stronger magnetic fields, other superconducting materials are used. This is particularly the case with Nb₃Sn. It has a higher critical temperature than NbTi (18 K versus 9.5 K at 0 T; 10.4 K versus 4.2 K at 11 T), as well as a higher critical induction than NbTi (25.5 T versus 14 T at 1.8 K; 23.2 T versus 11 T at 4.2 K). Having a higher critical temperature ensures a better thermal stability of the magnet.

Generating magnetic inductions greater than 12 T is therefore possible with the Niobium-Tin. However, these disadvantages of Nb₃Sn are cost, complexity of implementation and its poor mechanical tolerances. Indeed, its critical properties are highly dependent to mechanical stresses. In addition, in order to be in its superconducting state, the conductor containing the niobium and tin must be heat treated (with temperatures up to 700°C) to form Nb₃Sn. After heat treatment, the material is brittle. Therefore, the winding is usually done before the heat treatment to avoid damage to the superconducting cable.

Finally, although performances of Nb₃Sn is more attractive than NbTi, its price is higher. We are talking here about 8 \$/kA/m at 4.2 K [7]. Cross-sectional images of NbTi and Nb₃Sn cables examples are available in [Figure I-3](#).

However, the practical magnetic induction of Nb₃Sn is limited to about 25 T at 1.8 K. The use of High-Temperature Superconductors is necessary to generate very strong magnetic fields.

I. 2 High-Temperature Superconductor (HTS)

The discovery in 1986 of the mixed oxide of barium, copper and lanthanum LaBaCuO, the first High-Temperature Superconductor (HTS) discovered, marked an important advance in superconductivity, as it was 12 K higher than the highest critical temperature at the time. Subsequently, other superconductors with even higher T_c were discovered quite rapidly. This is the case of YBa₂Cu₃O_{7- δ} (YBCO), with a critical temperature T_c of 92 K and a critical induction $B_{c2} = 140$ T at $T = 0$ K. This sudden increase in critical temperature ([Figure I-1](#)) allows a simplest cooling like the use of liquid nitrogen (65-77 K). This makes it possible to significantly reduce the costs associated with cryogenic cooling.

The major difference between LTS and HTS superconductors is, of course, the value of the critical temperature T_c . LTS have a critical temperature below 30 K, while HTS have a critical temperature above 30 K. In addition, they show a higher magnetic induction B_{c2} and critical current density J_c for the same operating temperature. It is illustrated in Figure I-2 on the right, where the critical surface area of the Fujikura tape (HTS) is significantly larger than that of Nb_3Sn and $NbTi$. This behavior can also be observed through the critical current comparison of different superconductors performed by P. J. Lee [10] and shown in Figure I-3. Today, there are mainly two generations of HTS superconductors: the first and the second generation.

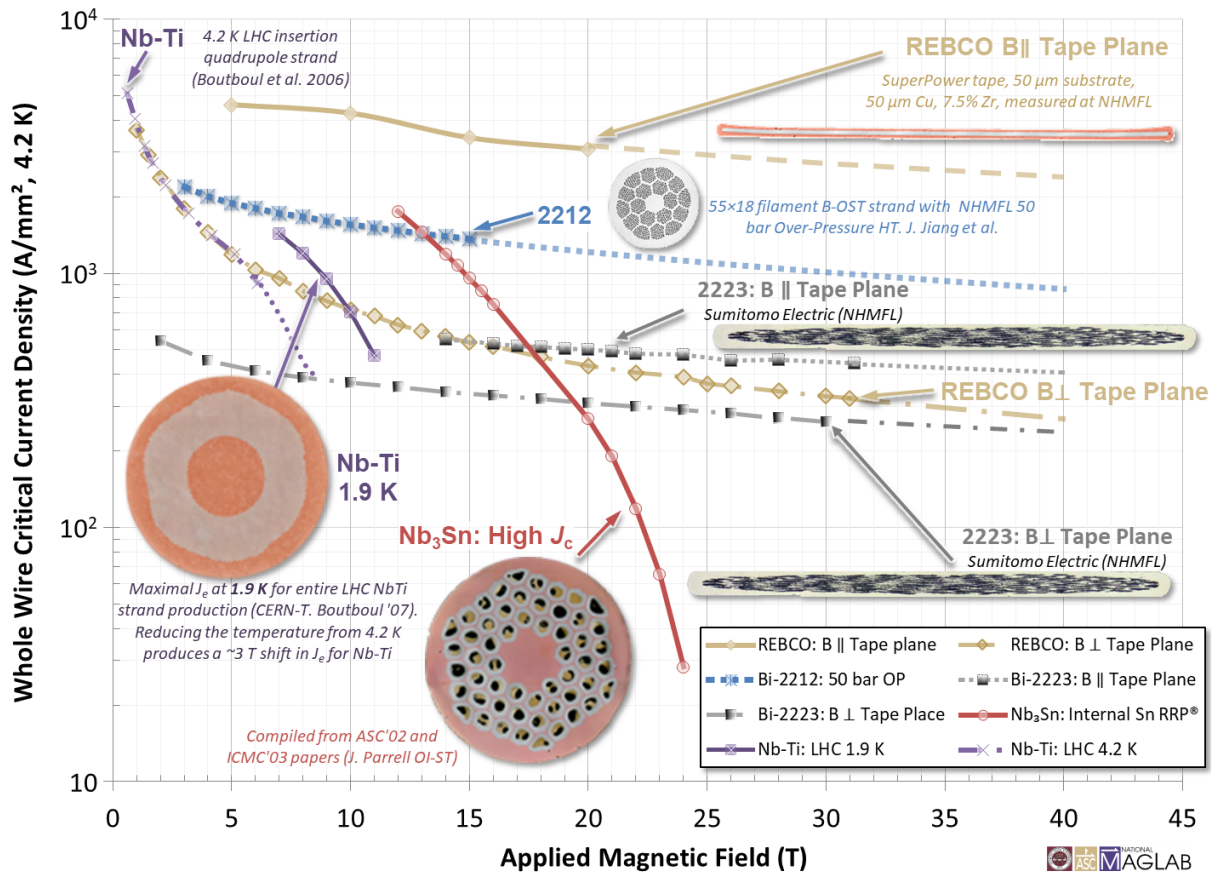


Figure I-3: Engineering critical current density vs. applied field for superconductors available in long lengths [10].

I. 2. 1 First-generation HTS superconductors

Bi-2212 (tape or round wire, with a critical temperature T_c of 86 K) and Bi-2223 (flat tape, with a critical temperature T_c of 110 K) are first-generation HTS (1G). Cross-sectional images are available in Figure I-3. They have different formulae depending on the stoichiometry, with Bismuth, Strontium, Calcium, Copper and Oxide as elements. They are named "BSCCO", grouping $Bi_2Sr_2CaCu_2O_{8-x}$ for Bi-2212 and $Bi_2Sr_2Ca_2Cu_3O_{10-x}$ for Bi-2223 [11], [12]. Their design is based on classical metallurgical methods (extrusion, rolling, annealing). Although the properties of BSCCO are more attractive than LTS superconductors, the cost is still quite high: 100 \$/kA/m [7]. The prospects for cost reduction remain low because of the high proportion of silver, which continues to rise in price.

I. 2. 2 Second-generation HTS superconductors

The Second-generation HTS (2G) show attractive properties compared to NbTi and Nb₃Sn because they allow high current densities to be carried under high magnetic induction, which is necessary in the design of high field magnets. Thus, the main advantage of 2G HTS is to have a high current density under a high magnetic field. Indeed, above 25 T, HTS are more interesting than LTS (Figure I-3). However, their use is limited today due to the price and protection against quench which is not controlled. The quench and the protection are discussed in section II. 2.

All this second-generation (2G) HTS superconductors are grouped under the term REBCO (for Rare Earth Barium Copper Oxide, with the formulation REBa₂Cu₃O_{7-δ}). The term RE often stands for Yttrium (Y), but also other elements such as Gadolinium (Gd), Neodymium (Nd), Samarium (Sm). These are deposited and coated conductors. The advantage of the second-generation is to reduce production costs. REBCO materials are currently expensive (100 \$/kA/m) but they include less expensive/rare materials compared to BSCCO 2223. The price is mainly due to the process and its yield, and not to the materials. Therefore, it is possible to imagine a reduction in price with the increase in the lengths produced, which is not the case with BSCCO. Moreover, the \$/kA/m ratio will continue to fall over the next few years, in particular due to better efficiency and quality of the superconducting layers of the tape, but also due to a new generation of more efficient artificial pinning [13]. The manufacturing principle is different compared to first-generation superconductors and LTS. For 2G HTS, they are not manufactured using conventional metallurgical techniques, but by deposition of thin layers of a few micrometers.

I. 2. 2. 1 Composition of second-generation HTS tapes

As with most superconductors, superconducting material is a fraction of the cable or the tape. Indeed, in the case of 2G HTS, the composition of the tapes becomes complex. A 2G HTS tape consists of several layers deposited on industrial flexible substrates. The thickness of the different layers varies depending on the manufacturer. The width of the tapes generally varies between 2 and 12 mm. They are composed of a substrate layer that works as a mechanical support (usually Hastelloy® or Nickel alloy), with a thickness of 30 to 140 μm, used for its attractive properties to withstand high mechanical stresses of several hundred MPa in tension. This characteristic can be observed in particular through FUJIKURA's manufacturer data [14]. The greater the thickness of the substrate, the greater the tensile force that can be applied before a critical current drop is observed. However, increasing the thickness of the substrate reduces the engineering current density and the minimum bending diameter.

There are two techniques for producing these tapes. The first is the RABiTS technique (Rolling Assisted Bi-axially Textured Substrates, first proposed by A. Goyal [15]). The YBCO layer is deposited through buffer layers onto the textured nickel substrate to avoid the reaction of YBCO with the nickel.

The second is the IBAD technique (Ion Beam Assisted Deposition [16]). In this second technique, the substrate is often a layer of Hastelloy® on which a layer of Ytria-Stabilized Zirconia (YSZ) is deposited and biaxially textured by ion bombardment, with thicknesses of less than 1 μm. These buffer layers are used to induce a bi-axial texture for the superconducting REBCO layers (with a thickness varying from 0.1 to 5 μm) in order to align the superconducting grains to obtain a better critical current. A silver layer of 2 to 4 μm is present for protection against external attack and to facilitate current injection. This layer can also act as a stabilizer. Finally, a copper layer coating all the previous layers, with a thickness of between 0 and 60 μm per side, serving as a stabilizer. The IBAD technique offers better results, but the manufacturing

process is expensive and time consuming due to the ion bombardment. In the case of Theva, the total thickness of the buffer layers is more than 3 μm because it uses the ISD (Inclined Substrate Deposition) method with MgO layers above Hastelloy[®] to texture the REBCO layer [17].

An example of a second-generation HTS tape is shown in Figure I-4. On the right, a microscopic section of a Theva tape used for the work in Chapter III. From the bottom to the top, a part of the substrate, the buffer layers, the superconducting layer, the silver layer and the copper layer are clearly visible.

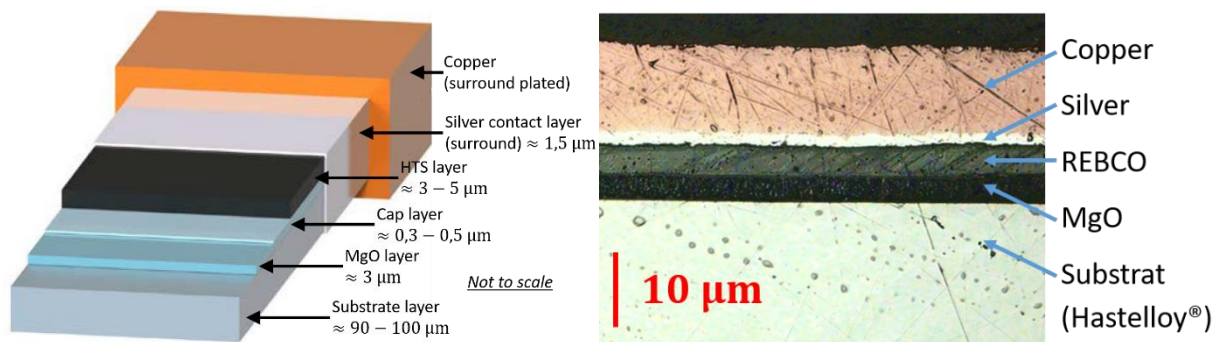


Figure I-4: Architecture of the Theva tape, thicknesses of the layers [18]. Microscopic section of a Theva tape.

However, the coated structure of the tape makes it particularly sensitive to delamination, and it is relatively brittle. This is a detachment of the layers from each other, especially between the superconducting layer and the substrate or copper layer. The delamination strength of YBCO coated conductors under transverse tensile stress has been studied by D. C. van der Laan [19], showing a relatively low delamination resistivity of less than 15 MPa. Such a phenomenon considerably and irreversibly reduces the properties of the superconducting layer.

Although impregnation is used in most traditional windings to provide good mechanical stability, its presence in 2G HTS windings increases the risk of damages during the magnet life time. Indeed, the radial stress caused during the cooling process exceeds the delamination limit of the conductor, generating cracks or delamination. One possibility is to adapt the impregnation to avoid delamination. Another possibility is to make windings without impregnation, called dry windings. I will consider this technique in my work.

I. 2. 2. 2 Anisotropy of REBCO tape caused by its crystal lattice

Superconducting ceramic materials are complex oxides with a crystallographic structure belonging to the Perovskite family. Each perovskite unit cell contains a Y (Yttrium) atom and Ba (Barium) in the center. Ba is in the lower and upper unit cell, Y in the middle one. Thus, Y and Ba are stacked in the sequence [Ba-Y-Ba] along the "c" axis. The crystal structure, available on the left of Figure I-5, is formed by a set of layers, which makes the material anisotropic and explain the epitaxial requirement: the ab planes must be aligned to maximize the critical current I_c .

In the center of Figure I-5, the plot shows that anisotropy is a significant factor. The critical surfaces were obtained using a fit reproducing the critical surface of a REBCO FUJIKURA conductor [6]. Indeed, a factor ~ 5 is observable at 4.2 K between the values of J_c for $\theta = 90^\circ$ and $\theta = 50^\circ$. The anisotropy thus strongly reduces the current densities of the superconducting material.

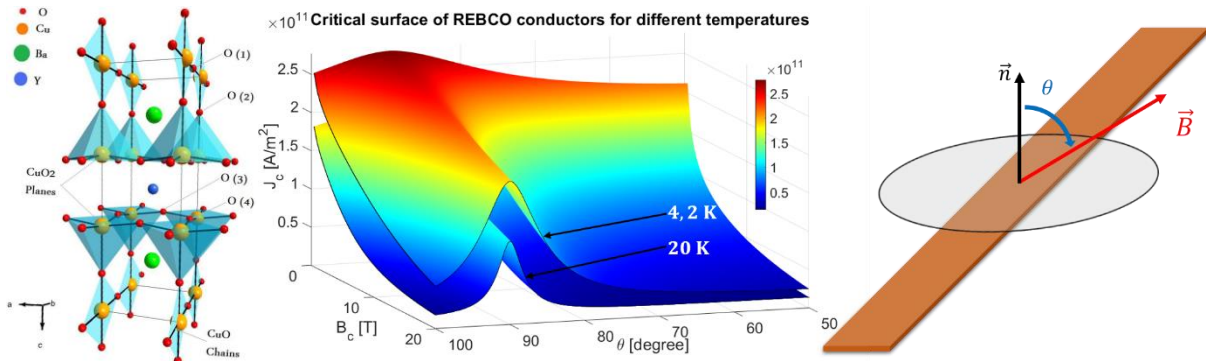


Figure I-5: On the left, crystal lattice of a YBCO superconductor [20]. In the middle, evolution of the critical surface of a REBCO FUJIKURA tape. On the right, ab plane and c axis of an HTS tape to take into account anisotropy.

In addition to anisotropy and delamination problems, REBCO HTS tapes have a non-homogeneous critical current along the length, increasing the complexity to estimate the operating magnet margins.

I. 2. 2. 3 Non-homogeneous critical current along the length of the HTS tape

Another disadvantage of HTS is the inhomogeneous critical current along the tape. Today, a tape can measure several hundred meters without interruption, but with variations of up to $\pm 10\%$ [18]. An example of the critical current along a Theva HTS tape is shown in Figure I-6. Some areas of the tape have lower critical values than others, which induces a problem in the design of the magnet. Especially in the choice of the nominal values and on the margins of the magnet protection. Given the uncertainty in the local assessment of the critical current and the inhomogeneous critical current along the tape, there is a significant risk that the critical current will be exceeded locally, causing damaging local hot spots.

Although the critical current value seems to be homogeneous for lengths of the order of a hundred meters, obtaining a tape of several hundred meters with a homogeneous critical current is complex. Indeed, as can be seen from the Theva manufacturer's data in Figure I-6, the presence of critical current below 700 A at approximately 20 m, 110 m, 120 m, 325 m and 400 m limits the length of the tape without defect. It might add uncertainties in the magnet margin estimation and protection. The NI/MI coils are an answer to this issue.

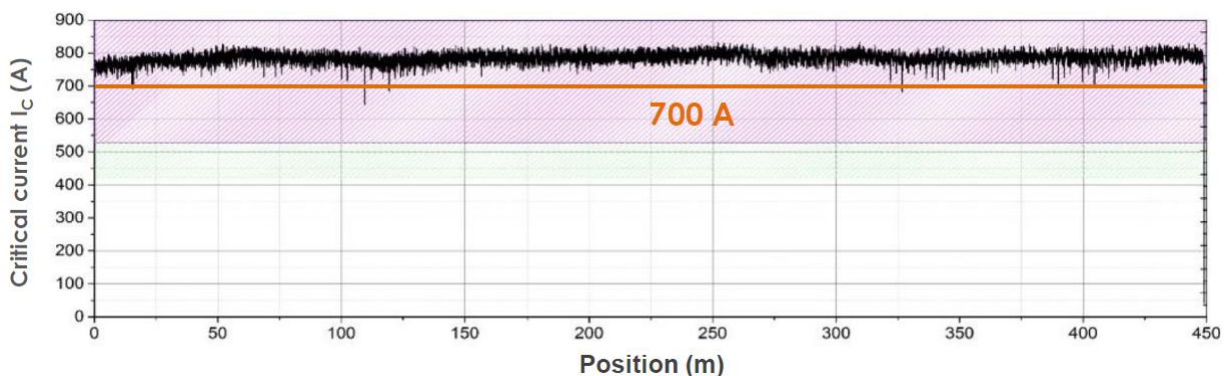


Figure I-6: Variation of the critical current along a 12 mm wide Theva superconducting tape at 77 K in self-field [18].

I. 2. 3 High-field electromagnets using HTS superconductors

The most common superconducting materials used today for different windings are NbTi and Nb₃Sn for LTS. Next come REBCO and BSCCO, which push the limits of LTS and generate very high magnetic fields (>25 T). Concerning the HTS, the use is still quite limited, and the product is not yet commercialized on a large scale because the technology is still partly at the

R&D stage, the technology is not yet fully controlled. Nevertheless, their use is very interesting, notably for the use of liquid nitrogen instead of liquid helium, for better critical currents and magnetic inductions, and finally for reducing the size and weight of applications. Thus, future applications in power grids, motors, generators, and in particle accelerators are to come. However, the protection of these HTS materials against quench remains a problem. This is the subject of the next paragraph I. 3.

It is possible to generate electromagnets that produce very strong magnetic fields using HTS superconductors. However, some very high field magnets are made of both LTS and HTS superconductors. These are called "hybrid magnets". The LTS form the outer coil. They are sufficient to carry high current densities where the magnetic field is lower (≈ 10 T), at the outer coil. This allows to avoid using HTS and thus to reduce the cost of the magnet. The HTS are only positioned where the magnetic induction is stronger, where they are unavoidable, so the HTS form the inner coil. In particular, the NOUGAT hybrid magnet (resistive-HTS) uses this technology to produce a record field strength of 32.5 T in a 38 mm aperture [21], [22].

HTS materials open the way for very high field superconducting magnets avoiding the huge power consumption of today resistive magnets. For the superconducting/resistive hybrid magnet in Grenoble [23], the power of the resistive magnet reaches 24 MW. HTS magnet could reduce this value by at least three orders of magnitude. Significant advances in very high field electromagnet with second-generation HTS have been made over the past decade, notably using REBCO. Today, various magnets consisting of several pancakes supplied in series generate more than 30 T in apertures with diameters of about 30 mm. Table I-1 lists several high field magnets using REBCO HTS superconductors.

Although the mechanical property of REBCO tapes is higher than that of BSCCO tapes, degradation due to delamination with the presence of impregnation poses problems for the development of REBCO superconducting coils. Finally, P. Trociewitz [24] observed delamination of superconducting tapes on a hybrid resistivity-superconducting magnet generating 35.4 T.

Table I-1: Very high field electromagnet with LTS and HTS superconductors.

Laboratory	HTS	Inner diameter	Background field	HTS field	Reference
NHMFL	YBCO	24.5 mm	31 T (resistive)	2.8 T	[25]
NHMFL	REBCO	14 mm	31.2 T (resistive)	4.2 T	[24]
MIT	REBCO	91 mm	11.7 T (LTS)	18.8 T	[26]
HFLSM	BSCCO	95.8 mm	14 T (LTS)	11 T	[27]
MIT-SuNAM	GdBCO	35 mm	26.4 T (All HTS)		[28]
NSFC	YBCO	41 mm	15 T (LTS)	15 T	[29]
LNCMI-CEA-Néel Institute	REBCO	50 mm	18 T (resistive)	14.5 T	[22]

With HTS superconductors, current density is no longer a limiting parameter. Nevertheless, other problems are generated with the presence of strong fields. This is the case, for example, with the cooling of the coil using helium. This is degraded by the accumulation of helium gas trapped around the coil due to the diamagnetic effect of high field helium at 4.2 K. This phenomenon was first observed in 1986 by L. G. Rubin [30] and in 1988 by E. J. McNiff [31], but also by W. D. Markiewicz [25] on a YBCO insert generating 2.8 T inside an external field of 31 T generated by a resistive magnet.

My work deal with REBCO HTS magnets, in particular their protection. I shall then present now the different existing ways to protect REBCO magnet, focusing on HTS REBCO coils without the electrical insulation between the superconducting tapes.

I. 3 Protection of superconducting coils

When a local area of the superconductor loses its superconducting state, when it becomes dissipative, local heat dissipation occurs by Joule effect. This heat spreads by conduction to other superconducting zones, which enlarges the dissipative zone. The more dissipative the zone, the higher the temperature of the conductor. This phenomenon continues to propagate until an event stops the energy dissipation. This may be a break in the magnet due to too high a temperature or thermal gradient, a triggering of a protection system to discharge the energy outside the magnet or the energy dissipation inside the magnet volume in the cryogenic environment. This loss of superconducting state can be due to a local manufacturing defect (Figure I-6), a handling defect, a cooling issue or a local energy deposition due to a movement (for example, a conductor motion or radiation coming from experiments). This phenomenon can occur anywhere, but it usually appears in areas with smaller margins, where the magnetic induction is mainly stronger.

If the cooling of the coil allows the resistive area to cool down without any additional action to make it superconducting again, we speak of a resistive transition. If the local heating is above the cooling heat extraction capabilities, the resistive volume will increase and we are speaking of a quench: an irreversible propagation in the winding, which generates a local thermal runaway. In this case, a protection is required to avoid a local thermal damage of the magnet.

One phenomenon to be taken into account when designing a magnet is its lifetime. Given the cost of an installation, their use should be as long as possible (this is the case for particle accelerators or MRIs, for example). When designing a superconducting magnet, one of the objectives is to avoid the generation of quench during operation of the magnet. Quench can usually occur as a result of poor cooling or a severe mechanical shock. In order not to damage the coil, a protection system must be implemented.

I. 3. 1 The different methods of protection against the quench phenomenon

When a defect occurs, the stored magnetic energy of the coil will turn into heat where the superconductor is in its resistive state. If this energy is too great, the superconductor can burn locally and irreversibly damage the magnet. There are several methods for protecting superconducting coils. They differ depending on the superconducting material.

- In the case of LTS, the temperature margin between the superconducting and normal state is very small. A slight rise in temperature is sufficient to make the material resistive. Thus, heaters can be installed throughout the coil, allowing it to be quickly made fully resistive when a quench is detected by sending energy to heat the superconducting coil. All the initial magnetic energy is dissipated throughout the coil. This is an active protection: the addition of the heaters allows the energy to be dissipated in a larger volume when a transition is detected. This method is used to protect the LHC dipoles. The heaters placed in the coil allow the temperature to increase by 10 K in 25 ms [8]. Although this protection method is more suitable for LTS, it has been tested by W. Denis Markiewicz [32] on a REBCO coil. As the temperature margin for HTS is higher, the energy input to the HTS coil is much higher than for LTS, making the method less suitable for HTS. Simulations of heater protection for high fields HTS insert coils operated at low temperature have been made by W. Denis Markiewicz [33], using a heat power between 20 and 80 kW.
- To limit the impact on the cryogenics environment and reduce the local hot spot temperature, an active protection scheme can be implemented. The so-called "detect and

dump" scheme is often used: a Magnet Safety System (MSS) detect the local transition and activate an electrical breaker in order to discharge most of the energy in an external dump resistor. One of the issue is the high voltage required to discharge quickly the magnet at the beginning of the discharge, which limit the discharge time and protection efficiency.

- Another method is to add a diode in the protection circuit. This blocks the current and thus prevents unwanted losses during a slow load, but more importantly it allows an efficient bypass of the coil by a low diode voltage [34].
- Detection methods have been developed to effectively protect HTS coils. This is the case of the BOSSE project, a 12 T REBCO solenoid used as a SMES with the objective of reaching an energy of 1 MJ [35]. A sensitive protection system based on magnetic flux compensation, presented by J. Vialle [36], [37], makes it possible to detect the quench phenomenon at a very early stage. The protection is based on the suppression of the inductive voltage to detect the small voltage of the resistivity transition.

Other precautions are taken to limit the risk of a quench. Safety margins are put in place during the design of the magnet. The current margin on the load line is a parameter indicating the operating point of the superconducting coil. It is defined by the value of the current versus the magnetic field (at a fixed temperature). If the operating point is below the critical surface, superconductivity is maintained. Having a larger current margin reduces the risk of quenching during operation of the magnet.

I. 3. 2 The quench propagation velocity for HTS

Although protection against the quench phenomenon is effective and well controlled for magnets with LTS, the protection of HTS magnets is more complex. The normal zones propagate much more slowly for HTS. The quench propagation velocity for HTS is about 10 mm/s [36], [38], [39], [40], [41], whereas it is about 20 m/s [42] for LTS (for different temperatures and magnetic inductions). In the case of HTS coils, the voltage signal during a quench is more difficult to measure because the dissipative zone remains local. The time between the start of the transition and the moment when the quench is observable is relatively long. This causes a local dissipation, which leads to a very high local temperature rise, making the protection method very complex and expensive to implement for large magnets, but feasible. This increase the risk of local hot spots.

The low quench propagation velocity in HTS is explained by a larger temperature margin and a higher heat capacity compared to LTS. A larger amount of energy is required to switch from the superconducting to the dissipative state. This influences the quench propagation velocity, and therefore the volume over which the energy will be dissipated. Thus, having a high propagation velocity is beneficial in having a larger dissipation volume, allowing lower temperatures, but also in the detection of the quench with the appearance of high voltages in the magnet. Finally, the damage of HTS is not only due to high temperatures, but also more precisely to a high temperature rise rate and temperature gradient. As early as 150 K, 1000 K/s can be reached [43]. It must be ensured that a transition does not damage the magnet.

Because the short length of the resistivity zones makes it difficult to detect a quench, other protection methods need to be developed for the protection of coils using HTS superconductors. One solution is to improve the quench propagation velocity by modifying the structure of HTS tapes. This is proposed C. Lacroix [44]: adding a highly resistive layer between the HTS and shunt layers allowing a better spatial distribution of the heat production when a normal zone appears. Simulations have shown quench propagation speeds of about 20 m/s which is in the same order of magnitude that for LTS magnets.

Another solution is to achieve passive protection by removing the insulation between the turns of the coil. It highly simplifies the detection and protection scheme of HTS magnets.

I. 3. 3 No-Insulation pancake: a method of protection for REBCO coils

Since about ten years, many groups have been working on novel windings consisting in removing the classical electrical insulation between turns. The idea of removing the electrical insulation between the turns of a coil was first proposed for HTS coils by R. Gupta [45] and S. Hahn [46] in 2011. Removing the insulation between the turns is possible due to the high thermal stability of HTS tapes, which prevents the tape from quenching prematurely. Indeed, removing the electrical insulation between the superconducting tapes generates radial currents during transient regimes (charging, discharging...), which leads to heat sources. HTS tolerate local dissipation because they have a high thermal stability, which is not the case for LTS. This solution improves the thermal stability, and it avoids local degradations in case of a quench. The current can flow radially from one turn to another thus bypassing the local defect.

One named them as “self-protected” coils as they do not need a complex Magnetic Safety System (MSS) to ensure the quench protection. If such coils are much less sensitive to local burnings, the drawback is the loss of the control of the current path and all linked magnet aspects. It also induces new mechanical forces and stresses distribution, which have to be known and controlled for designing a reliable magnet from a mechanical point of view. Some NI magnets have been destroyed through mechanics (Figure I-8). For some applications like SMES, the magnet should be isolated for pulse discharges. By setting appropriate contact resistivity value and the technology to obtain it, this solution is suitable for most of the applications. Various tests have already been carried out on NI (No-Insulation) and MI (Metal-Insulation) pancake where the electrical insulation has been fully removed or replaced by a resistive material [47], [48], [49], [50]. Experimentally, the thermal stability of the pancake during a quench was improved, protecting the pancake from thermal overheating. Other technologies were tested: soldered MI [51], PI (Partial-Insulation) [52], [53] and SI (Smart-Insulation) [54], [55], allowing to modify the behavior of the pancake during a transient regime. With these different solutions, several contact resistivity values are possible. They are presented in the following paragraphs.

I. 3. 3. 1 No-Insulation pancake (NI)

One of the first methods of making the pancake self-protecting and thermally stable when a quench is present is to remove only the electrical insulation on the surface of the superconducting tape and to wind without the addition of any further elements. Thus, there is no insulation between the turns of the pancake. This allows a redistribution of the current when a local defect occurs. The current can flow radially over adjacent turns, thus avoiding the area of the local defect where superconductivity is lost. By bypassing the local defect, the Joule heat dissipation is less important, thus avoiding a thermal overheating. In reality, the current does not flow radially at a point as shown in Figure I-7, but uniformly over a full turn of the pancake. The behavior of the current in a NI coil is explained in II. 2.

The equivalent electrical circuit that best approximates a NI pancake, proposed by D. G. Yang [48], is available in Figure I-7. Where R_c is the contact resistance, $L_{S,coil}$ the inductances of the superconducting coil. The time constant τ of an NI pancake is $\tau = L_{S,coil}/R_c$. However, this equivalence is not strictly accurate because in the case of a pancake with a low contact resistivity value, the current redistribution will be important. This means that the current "path" is different from the one generating the value of the inductance of the pancake.

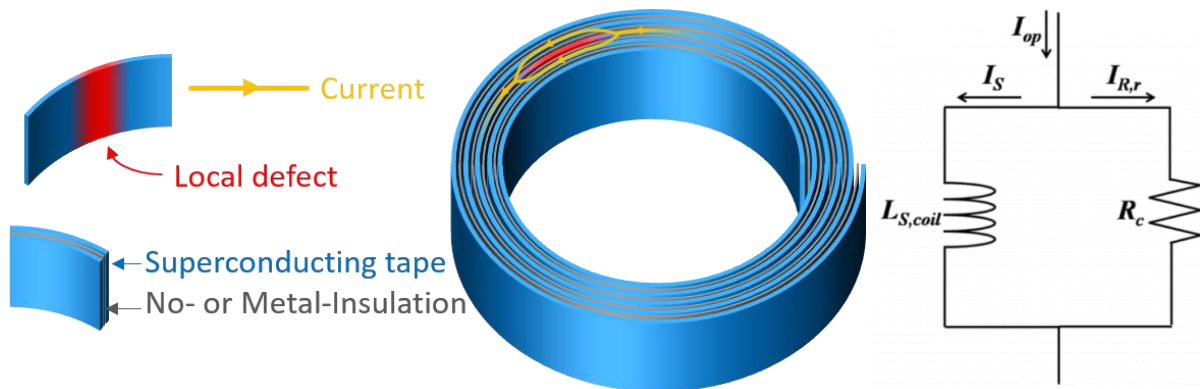


Figure I-7: On the left, sketch of a No- or Metal-Insulation simple pancake, current redistribution due to a local defect. On the right, equivalent diagram of a NI, MI or insulated pancake [48].

Thus, by removing the insulation, the pancake is thermally stable and self-protecting. However, this has an influence on its electrical behavior. The current path is no longer controlled, which leads to new Lorentz forces that can damage the coil. With strong magnetic inductions, the mechanical constraints are increasingly important. This can break the structure of the coil. This was observed by Philip C. Michael [26] in a test with a HTS NI magnet generating about 20 T in a 90 mm opening. The HTS NI pancakes rotated and moved vertically, breaking the pre-load bolts. Figure I-8 clearly shows the need for modeling during transient regimes and optimizing the contact resistance R_c to insure a safe operation: that is the objective of this PhD. The contact resistance R_c plays a large part and extensive measurements have been carried out during this PhD as well.

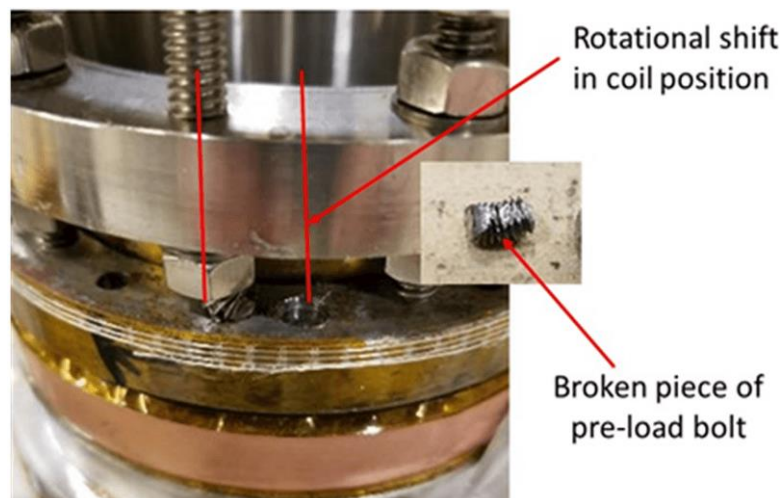


Figure I-8: Rotated and translated view of HTS insert pre-load plate and broken pre-load bolt following H800 quench [26].

Furthermore, without the presence of insulation between the turns, current can easily flow radially between the turns during charging or discharging of the coil, making its charging time constant relatively high compared to an insulated coil. Various solutions exist to reduce the charging time constant while keeping the self-protected character of a NI pancake. One way is to add a metallic tape between the superconducting tapes.

I. 3. 3. 2 Metal-Insulation pancake (MI)

Making a pancake without insulation and adding a metallic tape between the turns protects it from a quench and makes it mechanically stronger. Having a metallic co-wound tape is possible due to the high thermal stability of HTS tapes. This increases the contact resistivity of the coil and therefore the value of the contact resistance R_c , which decreases the charging time constant.

This is the protection method used for the NOUGAT insert developed in collaboration by the LNCMI, CEA and Institut Néel [22]. The pancakes of the insert are co-wound with a metallic tape. This is the first REBCO solenoid of this size using this technology and has been extensively tested at magnetic fields up to 32.5 T. The presence of a metallic co-wound tape improves the thermal stability and the mechanics of the magnet.

One of the advantages of the MI winding is the redistribution of current to the turns adjacent to the turn with a localized defect. Thus, when a quench occurs, voltages in the order of a volt (two to three orders of magnitude higher than the measurement of the resistive area in an insulated winding) are observable due to the contact resistivity R_{ct} . This makes protection easier and less dependent to the noise and prone to false detections.

MI pancakes can be co-wound with different types of metallic tape (copper, brass, steel...). They have a lower charge and discharge constant than a NI pancake, but higher than an insulated pancake (the insulation is mainly made of Kapton or Nomex). Experimental measurements by D. G. Yang [48] on a simple NI and MI (brass tape) pancake with 60 turns during a ramping rate of 1 A/s and a sudden discharge at 77 K show the charging and discharging time of MI pancakes shorter than NI pancakes. The same behavior is also observed by T. L crevisse [56] on a simple NI and MI (stainless steel 304 tape) pancake with 100 turns during a sudden discharge at 77 K in self-field. The experimental data is shown in Figure I-9. The higher contact resistivity means that the current flows less radially, accelerating the charge or discharge of the pancake.

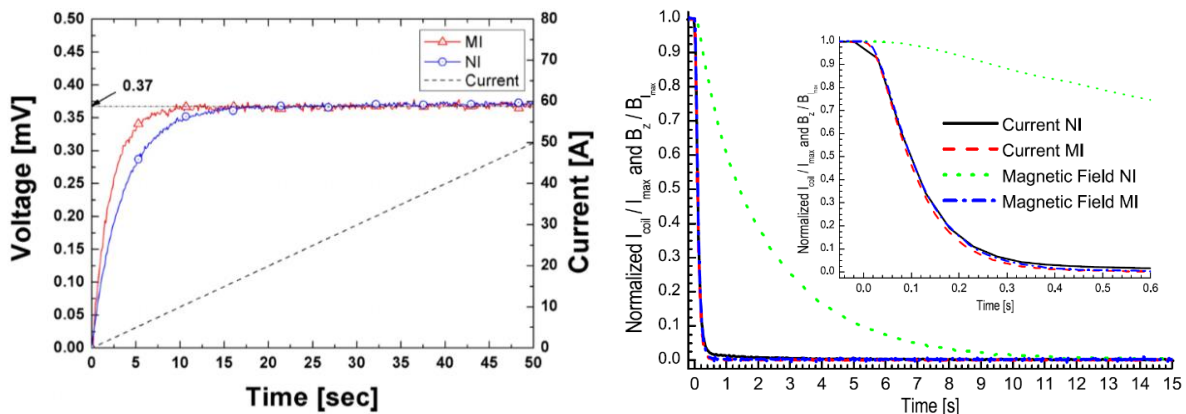


Figure I-9: On the left, experimental voltages of MI and NI simple pancake with 60 turns at 77 K in self-field during charging [48]. On the right, rapid discharge of simple NI and MI pancake with 100 turns at 77 K in self-field during rapid discharge, beginning of the behavior [56].

MI pancakes have the same objective as NI pancakes: to make it possible to redistribute the current when a local defect occurs. The area of the local defect where superconductivity is lost is bypassed, the pancake is thermally stable. Indeed, even with a current above the critical current, the pancake does not thermally overheat. This was observed by D. G. Yang [48] when testing the same insulated, NI and MI pancakes with a supply current higher than the critical current ($I_c = 1.1 I_c$), shown on the left in Figure I-10. When the current exceeds the local minimum, part of the current flows radially over the adjacent turns, generating a voltage across the pancake. The presence of radial currents generates Joule effect source terms, which heat up the pancake. If the supply current is slightly higher than the critical current and the cooling of the pancake is sufficient to absorb the heat generated by the radial currents, then the pancake is maintained in its superconducting state. With the insulated coil, the current is not be able to redistribute itself; it continues to pass through the resistivity zone, which causes a local temperature rise generating a burned-out.

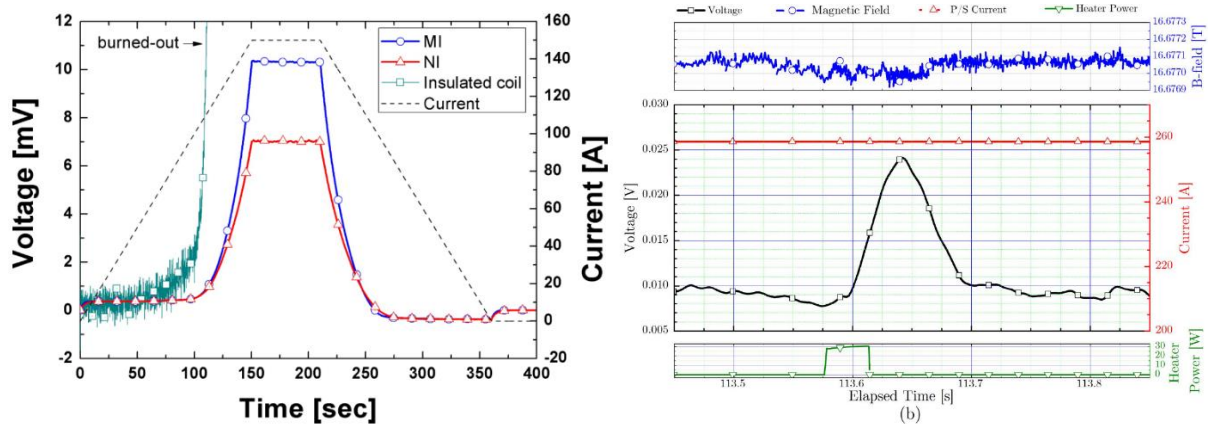


Figure I-10: On the left, over-current test results of MI, NI and insulated simple pancake with 60 turns at 77 K in self-field [48]. On the right, recovery of a quench at 260 A, 4.2 K and 16 T background field, thermal stability in a simple MI pancake with 238 turns [49].

The self-protected behavior is also highlighted by T. Lécresse in the case of an MI (stainless steel 304 tape) simple pancake with 238 turns at 4.2 K in 16 T background field subjected to a heat pulse (≈ 2 J) locally within the pancake [49], available on the right of Figure I-10. This causes a decrease in the critical current, and thus a redistribution of the current to adjacent turns, hence the increase in transient voltage. The cooling of the pancake allows the heated sector to return to its initial state. The redistribution of the current in the pancake during the introduction of the source term could be seen in the value of the magnetic induction. If the current flows radially and not azimuthally, then the field generated by the pancake is lower. However, the noisy environment given by the resistive background magnetic field of 16 T does not confirm the origin of the fluctuation. S. Choi [57] observed saturation of magnetic fields in NI pancakes due to the redistribution of current to adjacent turns during a local quench caused by an operating current above the critical current.

In the case of MI and NI windings, and in the case of several pancakes, if a quench occurs in one of the pancakes, it causes a change in the magnetic induction generated by the pancakes. The quench can quickly spread to the other pancakes by magnetic coupling. J. Song [58] observed the behavior experimentally on a coil of 13 NI MW (No-Insulation, Multi-Width) double REBCO pancakes at 4.2 K, but also with the help of simulations carried out by S. An [59], also on a coil of 13 NI double pancakes. This will be observed using the developed PEEC model in the Chapter II.

MI coils greatly reduce the charging time constant compared to NI coils, although this depends on the materials and conditions. However, the charging and discharging time of MI coils is still longer than that of insulated pancakes. Other winding techniques exist and have been experimentally tested in order to keep the self-protective behavior of NI pancakes during a quench, while having the behavior of an MI or insulated pancake during a charge: Partial-Insulation (PI), Smart-Insulation (SI) and Varistor-Insulation (VI). These techniques will be described now.

I. 3. 3. 3 Partial-Insulation pancake (PI)

Partial winding involves co-winding a no-insulation tape with an insulator only between some turns. This has the effect of improving the charge and discharge times of the pancake while acting as a thermal self-protection, thus ensuring electrical and thermal stability. The Partial-Insulation (PI) winding technique thus achieves a behavior closer to that of an insulated pancake, improving the charging and discharging times of the pancake, while maintaining the characteristics of a NI pancake. J. Song [52] and Y. H. Choi [53] conducted experimental tests

on NI, PI and insulated pancakes with 60 turns showing the faster charge and discharge time of the PI pancake compared to NI and MI pancakes. A comparison of fast discharge between NI, PI and insulated pancakes is available in Figure I-11.

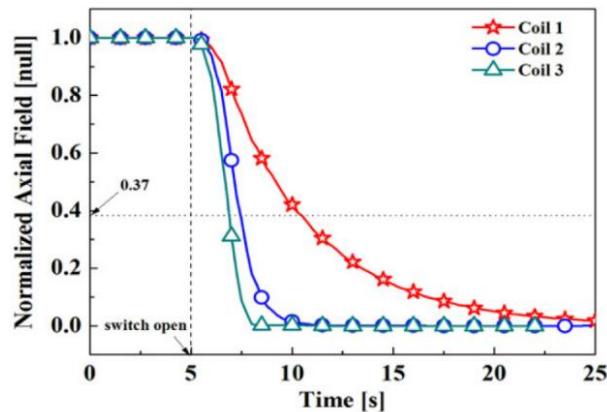


Figure I-11: Sudden discharge testing for NI (Coil 1), PI (Coil 2) and insulated coil (Coil 3) [53].

The presence of the partial insulation limits the presence of radial currents, accelerating the discharge of the pancake. The equivalent circuit of the partially insulated pancake proposed by Y. H. Choi [53] is a series of equivalent circuits of the no-insulation turns separated by the electrical insulation. A mutual inductance must be taken into account between each series connected circuit. The thermal stability of the PI pancake is however less efficient as current redistribution is limited on some turns of the pancake. Simulations of this phenomenon were done in II. 2. 4. 2.

I. 3. 3. 4 Smart-Insulation pancake (SI)

The objective here is therefore to have an insulated pancake during charging or discharging to get short charging/discharging times, and a NI pancake during the occurrence of a quench or a local defect. For this purpose, another pancake technology without insulation has been developed, called Smart Insulation (SI). The principle is to wind a tape without insulation but to add vanadium (III) oxide (V_2O_3) between each turn. Vanadium (III) oxide is an inorganic compound, which is in an electrically conductive state for temperatures above 150 K, and in an insulating state for temperatures below 150 K. The difference in resistivity of the material as a function of temperature is 7 orders of magnitude. The behavior of this material is therefore, in short, the opposite of a superconducting material.

The property of the material is therefore interesting in that it allows a high resistivity between turns when the pancake is stable, and a low resistivity when a local defect occurs. However, the presence of a defect that increases the temperature only modifies the resistivity of the vanadium oxide locally. The current redistribution is therefore limited to a portion of the turn, unlike a full turn for NI and MI pancakes. Experimental measurements by H. Kim [55] have shown this behavior for an SI pancake. Although the properties of Vanadium (III) oxide are interesting, this type of insulation is not suitable for protecting HTS tape pancakes.

I. 3. 3. 5 Varistor-Insulation pancake (VI)

The use of a varistor is another tested method of changing the value of the contact resistivity during a quench. The varistor has a high resistivity when the voltage across it is low and a lower resistivity when the voltage increases. This makes it possible to obtain a high and then a low contact resistivity when radial currents appear to generate a voltage in a pancake. G. Kirby [60] proposed this solution in 2022.

By including the behavior of the varistor into the insulation of the coil, it behaves as if it were insulated during a power ramp-up, thus reducing the charging time compared to NI and MI pancakes. This is an advantage over NI, MI and PI coils, and especially over fully insulated coils, where quench speeds are slow and protection difficult. As this technology is very new and promising, the characterization and application of varistor insulation is under development. Further work is required to verify and optimize the characteristics of the insulation, as well as to develop a reliable and simple application method.

I. 3. 3. 6 NI and MI modeling

The behavior and electrical scheme of a NI coil is more complex to study than that of an insulated coil. In order to study the electrical behavior of a pancake during a transient regime, I shall use a PEEC model to simulate the behavior of these pancakes. K. Katsumata [61], A. Ikeda [62] and Y. Wang [63] use the PEEC model to simulate the case of a simple pancake when a normal-state transition occurs. This model is also used by Y. Liu [64], T. Wang [65] and Y. Wang [66] to simulate the charge-discharge process, or even the sudden discharge, of a simple pancake. It is also applied to observe the behavior when the current is exceeded by T. Wang [65]. This model allows studying the influence of the contact resistivity and optimizing it. He is also used to understand the behavior of a NI pancake during a transient regime, but also for the purpose of coil optimization. The complexity of this model makes the simulation time important.

I. 3. 3. 7 Conclusion

NI and MI HTS coils are an attractive solution to improve the thermal stability, and it avoids local degradations in case of a quench. The behavior of SI and VI pancakes will not be studied mainly through modeling because SI is not suitable for protecting HTS tape pancakes, and the VI technology was proposed after the beginning of this thesis. Only the behavior of NI, MI and PI pancakes will be studied in the Chapter II, i.e. only with or without the presence of a metallic tape. Depending on the chosen technology, the value of the contact resistivity varies, which modifies the quench dynamics.

I. 4 Objectives of this work

The high stability and low quench propagation velocity for High-Temperature Superconductors (HTS) makes detection of the quench before deterioration difficult, but not impossible. Very complex active protection methods have to be implemented to protect the magnet, such as sensitive protection system based on magnetic flux compensation or heaters to limit the hot spot during discharge. Another method to protect the coil is to remove the insulation between the turns. This solution improves the thermal stability, avoiding local degradations in case of a quench.

NI-MI solutions clearly limit the risk of local damage during a quench due to overheating. This greatly simplifies the protection and viability of the magnets but induces a major problem related to radial currents: the path of the current is no longer controlled. This leads to a loss of the electromechanical and magnetic behavior of the magnets. From this phenomenon, we can ask the following question: **how to control the behavior of No-Insulation or Metal-Insulation coils in the HTS magnets?**

In order to answer this question, an existing PEEC model was first adapted and improved to simulate the behavior of simple pancake, racetrack and multi-pancakes coil constructed from

REBCO tapes in Chapter II. Different operating cases were implemented in order to study the transient behavior of REBCO coils. These include loading, unloading, resistivity transitions, and local defects due to heat sources or degradation of the superconducting properties of the tapes. Finally, a specific model to study the limitation has been implemented and used to optimize the protection of these magnets.

A very important parameter to study this type of coil is therefore the contact resistivity between the turns of the coil, which depends on several parameters. It has been studied experimentally in order to adjust the parameters of the models and to find technological solutions to obtain different ranges of values. In a second part, the control of the contact resistivity has been investigated using ALD (Atomic Layer Deposition). These experimental developments are described in Chapter III.

The Chapter IV aims to study coil protection using numerical tools developed but also from experimental points of view. Magnetic shielding due to additional turns of NI superconducting tape inside the overbanding is studied as well.

Chapter II

Behavior of superconducting coils during transient regimes, influence of the contact resistivity

REBCO No- or Metal-Insulation magnets open the way for very high field magnets, but their transient operation must be understood and optimized. In this chapter, a PEEC (Partial Element Equivalent Circuit) program simulating the case of a simple pancake subjected to a quench was used. The model, already developed [67], [68], is coupled with a 2D finite difference thermal model and with a 3D magnetic model. This program was then modified to simulate the behavior of a coil consisting of n pancakes subjected to a quench, or during other transient regimes (ramp-up operation, rapid discharge) [110]. This model makes it possible to observe locally the values of the radial and azimuthal currents (for each sector of each turn) within the pancakes as a function of time.

The first part focuses on the construction and modifications performed in this PEEC model. In a second part, the thermoelectric and magnetic behavior simulations of HTS pancakes, with different values of the radial contact resistivity, during different transient regimes will be studied. Finally, the behavior of a coil consisting of several pancakes powered in series during a quench will be analyzed. This PEEC code was also implemented to study the case of a simple NI-MI racetrack.

This model makes possible to investigate the influence and optimize the turn-to-turn contact resistivity. Indeed, the behavior of an NI-MI coil during a transient regime is mainly based on the value of the contact resistivity between each turn. With low contact resistivity, the current flows radially from one turn to another, bypassing the local defect, but the charging time increases and dissipation may high. With high contact resistivity, the current flows through the resistive zone, causing a local thermal overheating, but the magnet charging time is reduced. A compromise must be found.

II. 1 Partial Element Equivalent Circuit (PEEC) model

To simulate different geometries of a simple pancake during transient cases other than a quench (charge-discharge process, sudden discharge or when the critical current is exceeded), a PEEC (Partial Element Equivalent Circuit) program already developed [67], [68] simulating the case of a pancake with a heater has been modified and completed. The PEEC model is coded with the MATLAB software [69]. The principle of the PEEC model is to divide each turn of a pancake into several identical angular sectors (Figure II-1). Each sector created is defined by a variable azimuthal resistance R_θ (superconducting or not), a self-inductance and several mutual inductances regrouped in the matrix $M_{k|i}$. R_θ depends on the temperature, the amplitude and direction of the magnetic induction, and the current density. It is calculated at each time step. Details of the calculation of R_θ are available in [68]. The configuration of the critical surface of the superconducting tape is done using a fit based on Fujikura tapes [6] (more details in II. 1. 5) depending on field magnitude, orientation and temperature. This model can simulate electrically insulated pancakes, as well as No- or Metal-Insulation pancakes. A fixed radial resistance R_r characterizes the inter-turn insulation. It does not depend on any parameter.

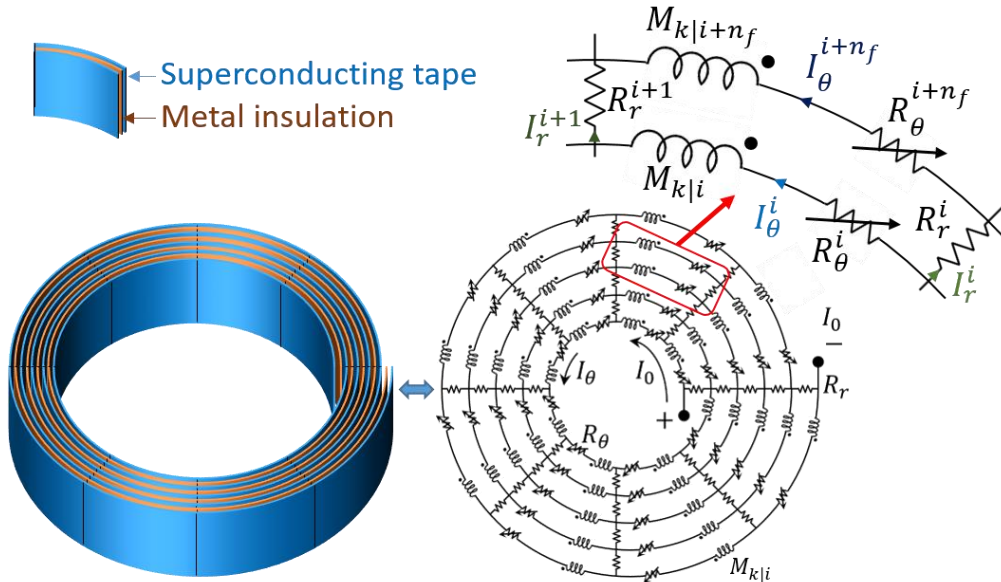


Figure II-1: Sketch and electrical circuit of a NI-MI simple pancake. On the top right, a mesh of the electrical circuit.

II. 1. 1 Electrical equation

II. 1. 1. 1 Simple pancake

From the electrical diagram of the simple pancake (Figure II-1), it is possible to obtain the electrical equation of the radial current I_r as a function of time using the Kirchhoff's laws:

$$M_{SP} H_{passSP} \frac{dI_{rSP}}{dt} + (R_{\theta SP} H_{passSP} - R_{rSP}) I_{rSP} = R_{\theta SP} K_{\theta SP}^{-1} I_0 \quad (1)$$

M_{SP} the constant matrix taking the set of the mutual inductances values and I_{rSP} , $R_{\theta SP}$ and R_{rSP} matrices to write the equations for each mesh. R_{rSP} is a constant matrix, even if it actually depends on several parameters such as temperature, mechanical stress for example. The transfer matrix from $I_{\theta SP}$ to I_{rSP} is $H_{passSP} = K_{\theta SP}^{-1} K_{rSP}$. $K_{\theta SP}$ and K_{rSP} are constant matrices consisting only of 0 and 1. Details regarding the construction and composition of these electrical equation matrices are available in [67], [68] and in the Appendix VI. 1. 1. 1.

II. 1. 1. 2 Multi-pancake

In order to consider two or more pancakes, modifications have been made. The model is built on the principle of a double pancakes. The odd-numbered pancakes are wound from the inside turn to the outside, while the even-numbered pancakes are wound from the outside turn to the inside (Figure II-2). The differential equation of the radial current is the same as in the case of a pancake, only the dimension of the matrices changes:

$$M_{DP} H_{passDP} \frac{dI_{rDP}}{dt} + (R_{\theta DP} H_{passDP} - R_{rDP}) I_{rDP} = R_{\theta DP} K_{\theta DP}^{-1} I_0 \quad (2)$$

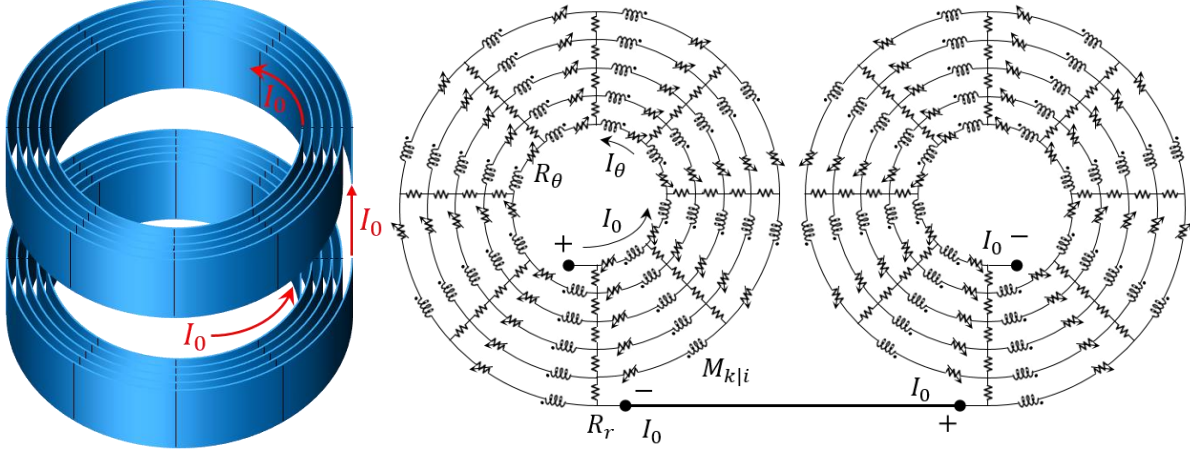


Figure II-2: Sketch and electrical circuit of a double NI-MI pancake.

Adding a second pancake with the same number of turns n_a and division per turn n_f as the first pancake automatically squares the dimension of each matrix. In the case of a double pancakes, the matrix M of the mutual inductances $M_{k|i}$ is thus composed of four sub-matrices:

$$M = \begin{pmatrix} M_{P_1 \leftrightarrow P_1} & M_{P_1 \leftrightarrow P_2} \\ M_{P_2 \leftrightarrow P_1} & M_{P_2 \leftrightarrow P_2} \end{pmatrix}$$

In the case of a simple pancake, all the self and mutual inductances are grouped in the matrix $M = M_{P_1 \leftrightarrow P_1}$. $M_{P_1 \leftrightarrow P_j}$ groups all the mutual inductances of the sectors of the pancake i with respect to the sectors of the pancake j . By adding a second pancake, new mutual inductances must be computed, i.e. the sub-matrices $M_{P_1 \leftrightarrow P_2}$; $M_{P_2 \leftrightarrow P_1}$; $M_{P_2 \leftrightarrow P_2}$.

In the case of equation (2), the construction of the M_{DP} matrix for a double pancakes is essentially identical to the matrix M_{SP} in equation (1). The construction of this matrix allows the mutual inductances between the two pancakes to be taken into account in the case of the mesh equations of the first pancake, and vice versa. Modifications to the matrices defining the radial and azimuthal resistance, as well as the node law matrices, have been made:

$$R_{\theta DP} = \begin{pmatrix} R_{\theta P_1} & 0 \\ 0 & R_{\theta P_2} \end{pmatrix}; R_{r DP} = \begin{pmatrix} R_{r P_1} & 0 \\ 0 & R_{r P_2} \end{pmatrix}$$

$$K_{\theta DP} = \begin{pmatrix} K_{\theta P_1} & 0 \\ 0 & K_{\theta P_2} \end{pmatrix}; K_{r DP} = \begin{pmatrix} K_{r P_1} & 0 \\ 0 & K_{r P_2} \end{pmatrix}$$

The details of the construction of M_{DP} to consider the magnetic coupling between the two pancakes, as well as the matrices $R_{\theta DP}$, $R_{r DP}$, $K_{\theta DP}$ and $K_{r DP}$, are available in Appendix VI. 1. 1. 2.

The electrical connection between the pancakes is made using the supply current vector I_0 because it can simulate the current input or output for each sector of the coil. More explanation and an example are available in Appendix VI. 1. 1. 2. By changing the coefficients of I_0 , it is possible to connect the azimuthal and radial current values of the last sector of the first pancake with the azimuthal and radial currents values of the first sector of the second pancake.

To generate the equations of a coil with n pancakes, the construction principle is similar to the step from one to two pancakes. Thus, adding one or more pancakes increases the size of the matrices, which greatly increases the simulation time of the code.

II. 1. 1. 3 Racetrack

This section add the possibility to simulate other types of geometry by approaching the case of an electromagnet. The principle for simulating a racetrack subjected to a quench is broadly the same as for a pancake coil. The electrical differential equation is strictly identical.

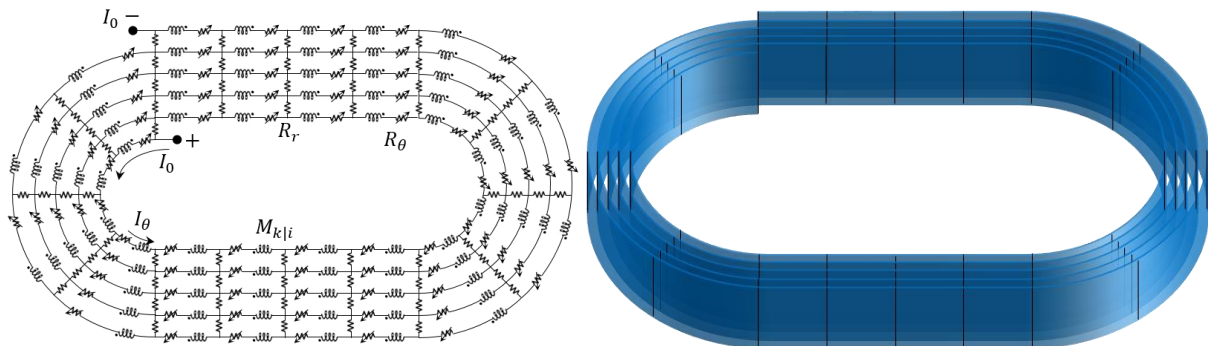


Figure II-3: Electrical circuit and sketch of a NI-MI racetrack.

No important modification is necessary: the electrical equations are obtained in the same way via Kirchoff's laws with the electrical circuit of the NI-MI racetrack (Figure II-3). Adding straight sectors in this electrical circuit simply increases the size of the matrices of the electrical equations.

For the simulation of the racetrack, new parameters are introduced:

- n_{fc} : the number of divisions per half turn.
- n_{fd} : the number of divisions per straight section.
- $n_{st} = 2(n_{fc} + n_{fd})$: the number of divisions per turn (formerly n_f).
- $n_s = n_a \times n_{st}$: the total number of sectors.

Thus, the dimensions of the matrices constituting the electrical equation (1) for the racetrack case are:

- $[n_s - n_{st} + 1 ; n_s]$ for M_{SP} et $R_{\theta_{SP}}$.
- $[n_s - n_{st} + 1 ; n_s - n_{st} + 1]$ for $R_{r_{SP}}$.
- $[n_s ; n_s]$ for $K_{\theta_{SP}}$.
- $[n_s ; n_s - n_{st} + 1]$ for $K_{r_{SP}}$.

The electrical behavior of one or more pancakes, as well as that of a racetrack, is now implemented in the PEEC model. I will now present the thermal part.

II. 1. 2 Thermal equation

II. 1. 2. 1 Simple and multi-pancake

The heat distribution in the simple and multi-pancake is calculated using the heat equation in cylindrical coordinates and solved numerically using finite difference method. This is a 2D model where the sectors of each turn have the same radius.

$$\rho C_p \frac{\partial T}{\partial t} = \text{div}(k\nabla T) + S \rightarrow \rho C_p \frac{\partial T}{\partial t} = \frac{k_r}{r} \frac{\partial T}{\partial r} + k_r \frac{\partial^2 T}{\partial r^2} + \frac{k_\theta}{r^2} \frac{\partial^2 T}{\partial \theta^2} + S \quad (3)$$

With ρ the density of the material, C_p is its thermal capacity, k_r and k_θ are the radial and azimuthal thermal conductivities respectively and S is the source term. These three parameters vary with the temperature, and k_θ depends on the amplitude of the magnetic induction. The properties of the REBCO tape used for the simulations are developed by P. Fazilleau [68] and available in Appendix VI. 1. 2. 1. The electrical and thermal equations are solved with MATLAB ODE solvers [69]. Using finite differences and the heat equation, it is possible to obtain the expression for $\rho C_p \frac{\partial T}{\partial t}$ for each sector of the pancake.

$$\left\{ \begin{array}{l} \frac{\partial T}{\partial r} = \frac{T(r + \delta r) - T(r - \delta r)}{2\delta r} + O(\delta r^2) \leftrightarrow \frac{\partial T_i}{\partial r} = \frac{T_{i+n_f} - T_{i-n_f}}{2\delta r} + O(\delta r^2) \\ \frac{\partial^2 T}{\partial r^2} = \frac{T(r + \delta r) + T(r - \delta r) - 2T(r)}{\delta r^2} + O(\delta r^2) \leftrightarrow \frac{\partial^2 T_i}{\partial r^2} = \frac{T_{i+n_f} + T_{i-n_f} - 2T_i}{\delta r^2} + O(\delta r^2) \\ \frac{\partial^2 T}{\partial \theta^2} = \frac{T(\theta + \delta \theta) + T(\theta - \delta \theta) - 2T(\theta)}{\delta \theta^2} + O(\delta r^2) \leftrightarrow \frac{\partial^2 T_i}{\partial \theta^2} = \frac{T_{i+1} + T_{i-1} - 2T_i}{\delta \theta^2} + O(\delta r^2) \end{array} \right. \quad (4)$$

A convective exchange between both inner and external turns of the pancake and the outer environment of the coil (Figure II-4) is implemented in the heat equation, but only radially ($\phi_r \neq 0$). The tape thickness is considered too small to generate convective exchange between the first sector and the outside of the pancake following \vec{e}_θ ($\phi_\theta = 0$). The same is true with the last sector of the pancake. No convective exchange along the z axis is implemented.

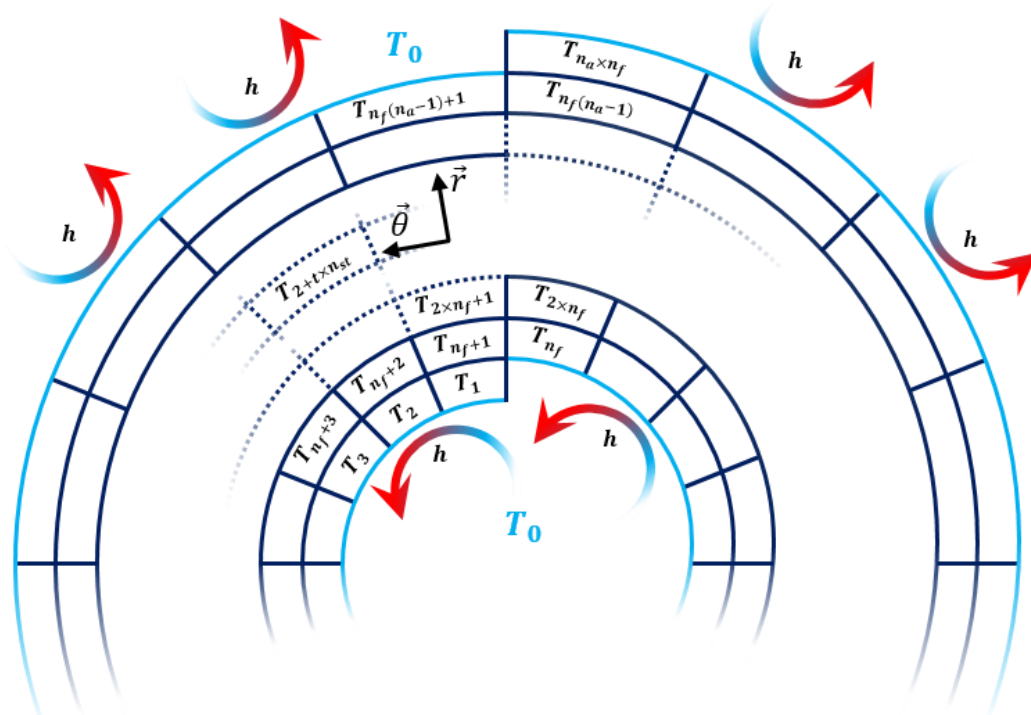


Figure II-4: Convective exchange and NI-MI pancake mesh for solving the heat equation.

The law for convective exchange is as follows:

$$\vec{\phi} = h(T_{side} - T_{fluid})\vec{n} \quad (5)$$

With $\vec{\phi}$ the convective heat flow between the solid and cryogenic fluid, h the heat transfer coefficient (in $W/m^2/K$) and $T_{side} - T_{fluid}$ the temperature difference in K between the two bodies. The value of h can be adjusted according to the operating mode of the coil. The details, as well as the expressions for each sector to obtain the thermal behavior of a simple pancake or a coil consisting of several pancakes, are available in the Appendix VI. 1. 2. 2.

In the heat equation (3), the term S groups the joule losses generated by the radial resistance R_r and the azimuthal resistance R_θ during a transient regime. It also allows a temperature rise, like a heater for instance, to cause a quench. In the case of joule losses generated by the azimuthal resistance R_θ , the power $S_s = R_\theta^k I_\theta^{k^2}$ is directly injected into the sector having azimuthal resistance R_θ^k . Regarding the joule losses generated by the radial resistance R_r , the power $S_c = R_r I_r^{k^2}$ is distributed in the four sectors adjacent to the radial resistance R_r^i (three sectors for the first and last contact resistor of each pancake).

No modification is necessary for the thermal part in the case of multi-pancake. We consider that each pancake are thermally decoupled from each other's. However, for the racetrack, modifications are required to achieve heat diffusion in the straight sections. This is the subject of the next paragraph. The thermal ODE systems of each pancake are solved in parallel to reduce calculation time.

II. 1. 2. 2 Racetrack

In the case of the racetrack, the thermal differential equation is solved in Cartesian coordinates for straight sections and in cylindrical coordinates for half-turns.

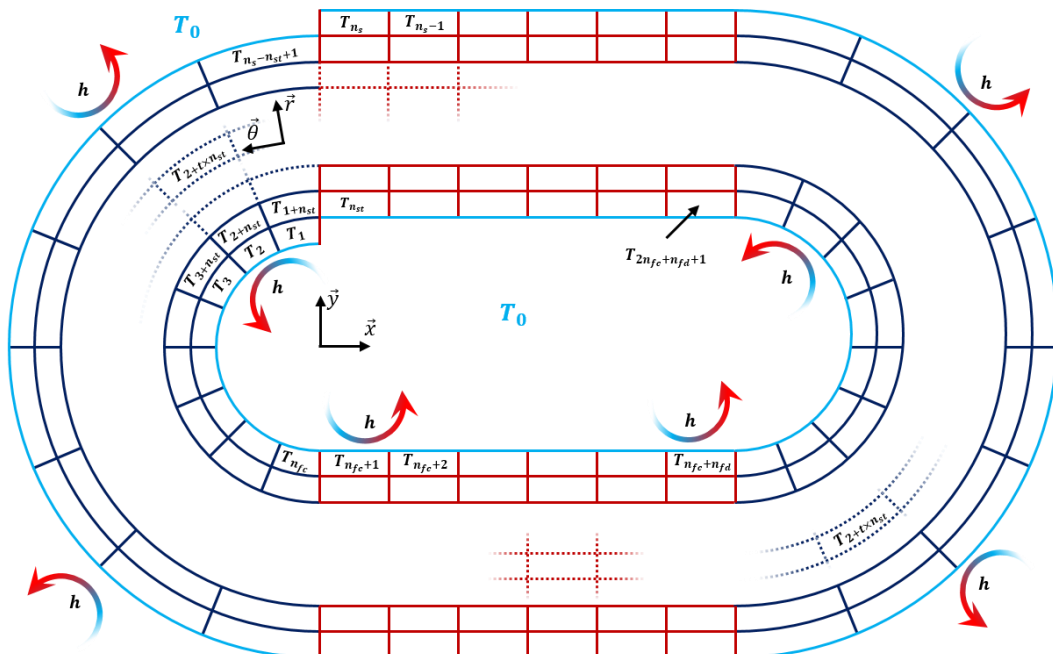


Figure II-5: Convective exchange and NI-MI racetrack mesh for solving the heat equation.

The resolution of the heat equation is already implemented for the half turns of the racetrack (dark blue parts, in Figure II-5). For the straight sections, the resolution is done in Cartesian coordinates (red parts, in Figure II-5). As for the case of one or more pancakes, a convective exchange with the outside of the pancake (only for the first and last turn) can be simulated.

In the pancake or racetrack case, each row of the matrix differential equation gives the heat equation in finite difference for each element of the coil. The objective is to keep the same matrix system but inserting coefficients in the matrices to take into account the heat diffusion in Cartesian coordinates in the right sectors. With the heat equation and assuming no heat diffusion along the z axis, we obtain in Cartesian coordinates:

$$\rho C_p \frac{\partial T}{\partial t} = k_x \frac{\partial^2 T}{\partial x^2} + k_y \frac{\partial^2 T}{\partial y^2} + S \quad (6)$$

In the case of a racetrack for straight sectors, the thermal conductivity along the x axis noted k_x , is the same as the thermal conductivity along the tape. Thus, for straight sectors, $k_x = k_\theta$. Similarly, the thermal conductivity passing from one tape to another along the y axis is the same as the radial thermal conductivity, hence $k_y = k_r$. The details, as well as the expressions for obtaining the thermal behavior of a racetrack, are available in the Appendix VI. 1. 2. 3.

One of the important points in this PEEC model is the magnetic coupling between the different sectors of each turn of each pancake. For this, obtaining the mutual inductances between each sector is essential in the case of one or more pancakes, but also for the racetrack. This is the subject of the next section.

II. 1. 3 Mutual inductance

II. 1. 3. 1 Simple pancake

The calculation of mutual inductance $M_{k|i}$ between the sector k and i is essential for the simulation because it allows taking into account the magnetic coupling between each sector of the pancake, or even between the pancakes of the coil in the case of a simulation of several pancakes. The value of the mutual inductance of a sector (in the case of thin solenoid arc) with respect to another sector has been mathematically developed by G. Aubert [70] and programmed in a MATLAB function by P. Fazilleau following the equations:

$$M_{k|i} = \frac{\mu_0}{4\pi} \frac{r r'}{(z_2 - z_1)(z_2' - z_1')} \int_{z_1'}^{z_2'} \int_{z_1}^{z_2} \int_{\phi_1'}^{\phi_2'} \int_{\phi_1}^{\phi_2} \frac{\cos(\phi - \phi') d\phi d\phi' dz dz'}{\sqrt{r^2 + r'^2 - 2rr' \cos(\phi - \phi') + (z - z')^2}} \quad (7)$$

With r , z_1 , z_2 , ϕ_1 et ϕ_2 respectively the radius, the width and the angular opening of the sector k . The notations with " ' " correspond to the second sector (Figure II-6, on the left). G. Aubert makes mathematical calculations to reduce the expression to a simple numerical integral (analytical with incomplete elliptic integrals).

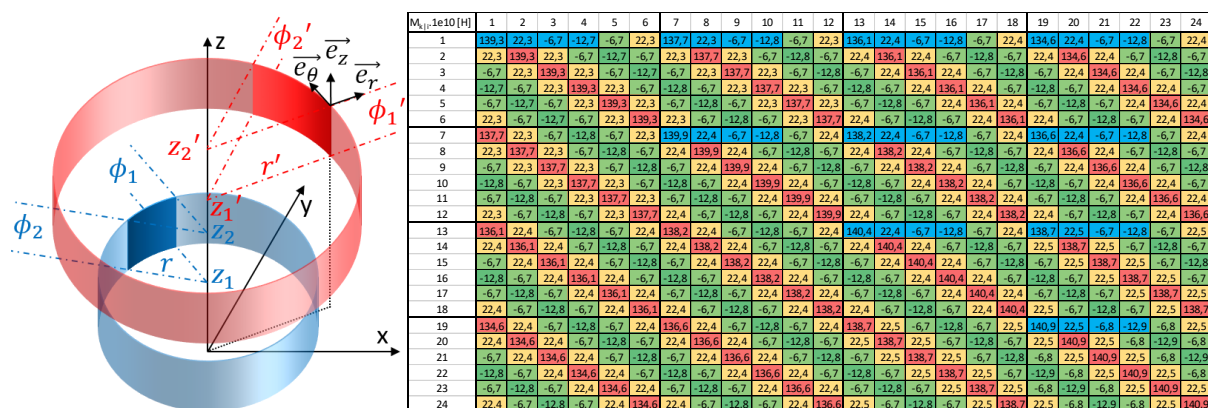


Figure II-6: On the left, sketch for the calculation of the mutual inductance between two coaxial fine angular sectors. On the right, example of M regrouping the self and mutual inductances of a simple pancake of 4 turns and 6 divisions per turn.

Figure II-6, on the right, is an example of a matrix M grouping the mutual inductances of a simple pancake of $n_a = 4$ turns and $n_f = 6$ divisions per turn. Many symmetries are present in the matrix M grouping the mutual inductances between all the sectors of the simple pancake. Indeed, in the generation of the coordinates of the sectors, all the sectors of the same turn have the same radius r_c and the same angular radius. Thus, considering $M \in M_{n_a \times n_f}(\mathbb{R})$, the matrix of mutual inductances M of order $n_a \times n_f$ is symmetric: ${}^tM = M$.

The matrix M is composed of symmetric sub-matrices. The two sub-matrices grouping the mutual inductances between the sectors of the l turn and the k turn are identical:

$$M_{S_l|S_k} = M_{S_k|S_l}, \forall l, k \in [1, n_a], \text{ with } l, k \in \mathbb{N}.$$

$$M = \begin{pmatrix} M_{S_1|S_1} & M_{S_1|S_2} & M_{S_1|S_3} & M_{S_1|S_4} \\ M_{S_2|S_1} & M_{S_2|S_2} & M_{S_2|S_3} & M_{S_2|S_4} \\ M_{S_3|S_1} & M_{S_3|S_2} & M_{S_3|S_3} & M_{S_3|S_4} \\ M_{S_4|S_1} & M_{S_4|S_2} & M_{S_4|S_3} & M_{S_4|S_4} \end{pmatrix} \text{ in the case of the example in Figure II-6 on the right.}$$

These symmetric submatrices $M_{S_l|S_k}$ have common coefficients. In the case of the mutual inductances between the sectors of the first turn ($M_{S_1|S_1}$):

$$\forall j \in [1, n_f - 1] \text{ and } \forall i \in [1, n_f - j], M_{i|j} = M_{i+1|j+1}, \text{ with } i, j \in \mathbb{N}.$$

A final symmetry in this submatrix $M_{S_1|S_1}$ can be noted: $\forall m \in [1, n_f - 1], M_{1|m+1} = M_{1|n_f-m+1}$, with $m \in \mathbb{N}$. The same is true for the set of submatrices $M_{S_l|S_k}$ of M .

Computing the mutual inductances $M_{1+n_f(l-1)|j+n_f(k-1)} \forall j \in [1, \lfloor \frac{n_f}{2} \rfloor + 1]$ in the submatrices $M_{S_l|S_k}$ with $l \in [1, n_a]$ and $k \in [l, n_a]$ allows us to completely fill the matrix M by duplicating the value of the calculated coefficients. In the example, only 40 coefficients are calculated (in blue in Figure II-6), out of the 576 coefficients that make up the matrix of mutual inductances M . This makes it possible to reduce the calculation time of the mutual during the initialization of the program.

II. 1. 3. 2 Multi-pancake

Concerning the calculation of the mutual inductance, the formula (7) allows to calculate the value of the mutual inductance between two thin coaxial angular sectors having different heights. Such modifications leads to a larger mutual inductance matrix and to an increased simulation time.

For a coil consisting of four identical pancakes, $M_{4P} \in M_{4n_a \times n_f}(\mathbb{R})$ and ${}^tM_{4P} = M_{4P}$:

$$M_{4P} = \begin{pmatrix} M_{P_1|P_1} & M_{P_1|P_2} & M_{P_1|P_3} & M_{P_1|P_4} \\ M_{P_2|P_1} & M_{P_2|P_2} & M_{P_2|P_3} & M_{P_2|P_4} \\ M_{P_3|P_1} & M_{P_3|P_2} & M_{P_3|P_3} & M_{P_3|P_4} \\ M_{P_4|P_1} & M_{P_4|P_2} & M_{P_4|P_3} & M_{P_4|P_4} \end{pmatrix}$$

With $M_{P_l|P_k} = M_{P_k|P_l}, \forall l, k \in [1, n_a]$, with $l, k \in \mathbb{N}$, where $M_{P_l|P_k}$ is the submatrix of M_{4P} grouping the mutual inductances between the sectors of the pancake l with those of the pancake k . The construction of the matrix M_{4P} is based on the same principle as with a simple pancake ($M = M_{P_1|P_1}$). Some coefficients are calculated and then duplicated.

II. 1. 3. 3 Racetrack

The major difference between the racetrack and the pancake case is in the values of the mutual inductances between thin sectors, due to the presence of straight sections. Thus, the mutual inductance between two thin straight sectors (M_{S-S} , in blue in Figure II-7); two non-coaxial thin angular sectors ($M_{A-A,nc}$, in red in Figure II-7); and between a thin straight sector and a thin angular sector (M_{S-T} , in green in Figure II-7) must be calculated numerically.

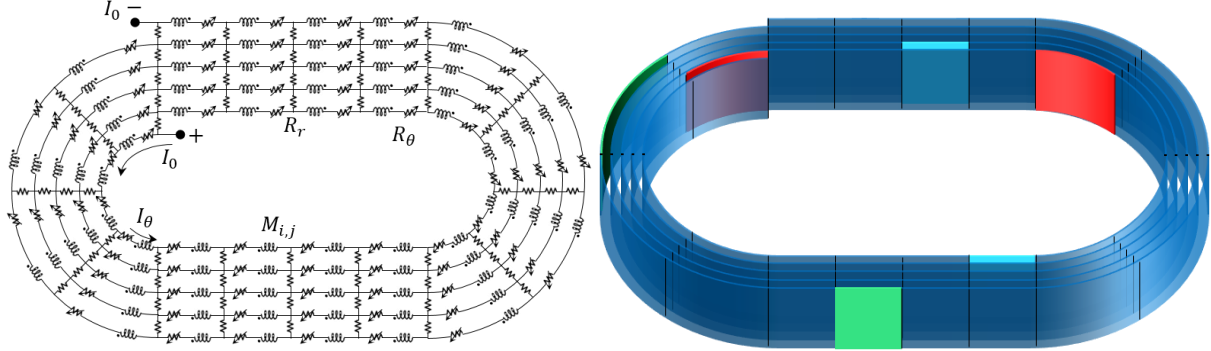


Figure II-7: On the left, electrical circuit of a NI-MI racetrack coil. On the right, sketch of the cases of the mutual inductances to be determined.

II. 1. 3. 3.1 Mutual between a thin straight sector and a thin angular sector

The expressions for the numerical values for calculating the mutual inductance in the different configurations between a thin straight sector and a thin angular sector is:

$$M_{S-A} = \frac{\mu_0}{4\pi} \frac{r_c}{(z_{r2} - z_{r1})(z_{c2} - z_{c1})} \int_{\phi_1}^{\phi_2} \int_{z_{c1}}^{z_{c2}} \int_{z_{r1}}^{z_{r2}} \int_0^{L_r} -\frac{\sin(\theta_c)}{d} d\theta_c dz_c dZ_r dX_r \quad (8)$$

With:

$$d = \sqrt{(Z_r - Z_c)^2 + r_c^2 + D_y^2 + (D_x + X_r)^2 - 2r_c \sqrt{D_y^2 + (D_x + X_r)^2} \cos(\alpha)}$$

And

$$\alpha = \theta_c - \text{atan}\left(\frac{D_y}{D_x + X_r}\right)$$

With for the angular sector the angles ϕ_1 ϕ_2 , the radius r_c and the heights z_{c1} z_{c2} . For the right sector, the heights z_{r1} z_{r2} , the length L_r and the displacements D_x D_y (Figure II-8, on the left). The details of these calculations are available in the Appendix VI. 1. 3. 1.

II. 1. 3. 3. 2 Mutual between two thin non-coaxial angular sectors

The expressions for the numerical values for calculating the mutual inductance in the different configurations between two thin non-coaxial angular sectors is:

$$M_{A-A,nc} = \frac{\mu_0}{4\pi} \frac{r_c r_c'}{(z_2 - z_1)(z_2' - z_1')} \int_{z_1'}^{z_2'} \int_{z_1}^{z_2} \int_{\phi_1'}^{\phi_2'} \int_{\phi_1}^{\phi_2} \frac{\cos(\phi - \phi')}{d} dz' dz d\phi' d\phi \quad (9)$$

With

$$d = \sqrt{r_c^2 + r_c'^2 + D_x^2 + 2D_x(r_c' \cos(\phi') - r_c \cos(\phi)) - 2r_c r_c' \cos(\phi - \phi') + (z - z')^2}$$

With for the two angular sectors the angles $\phi_1 \phi_2 \phi_1' \phi_2'$, the radius $r_c r_c'$, the heights $z_1 z_2 z_1' z_2'$ and the translation D_x (Figure II-8, on the right).

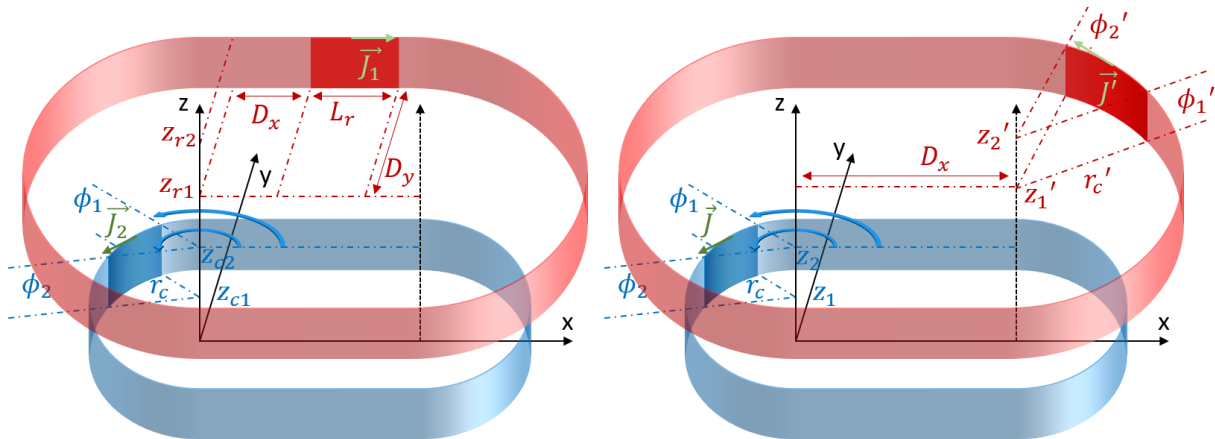


Figure II-8: On the left, mutual inductance between a thin straight and a thin angular sector. On the right, mutual inductance between two non-coaxial angular sectors.

With a value of $D_x = 0$, we find the expression of the mutual of two coaxial thin angular sectors, i.e. equation (7). For the expression of M_{S-A} and $M_{A-A,nc}$, the value of the quadruple integral is calculated using the `nag_quad_md_mcarlo` MATLAB function which returns an approximation of the integral using a Monte Carlo method. The details of these calculations are available in the Appendix VI. 1. 3. 2.

II. 1. 3. 3. 3 Mutual between two thin parallel straight sectors

A last case of calculation of mutual inductance is to be performed: the case of two thin parallel straight sectors. The value of the mutual inductance between two straight and thin sectors has been proposed by Z. Piatek in 2013 [71].

As in the previous case, starting from the generalization of the mutual induction coefficient between two non-wire-shaped circuits, it is also possible to determine the expression of the mutual inductance between two parallel thin straight sectors with the same method as the previous paragraphs.

$$M_{S-S} = \frac{\mu_0}{4\pi} \frac{1}{H_1 H_2} \int_{X_1}^{X_1+L_1} \int_{Z_1}^{Z_1+H_1} \int_{X_2}^{X_2+L_2} \int_{Z_2}^{Z_2+H_2} \frac{1}{d} dx_1 dz_1 dx_2 dz_2 \quad (10)$$

With $d = \sqrt{(x_2 - x_1)^2 + (Y_2 - Y_1)^2 + (z_2 - z_1)^2}$ and (Figure II-9):

- $X_1; Y_1; Z_1$ the coordinates of the right sector $n^{\circ}1$ in the Cartesian coordinates.
- L_1 the length and H_1 la height of the right sector $n^{\circ}1$.
- $X_2; Y_2; Z_2$ the coordinates of the right sector $n^{\circ}2$ in the Cartesian coordinates.
- L_2 the length and H_2 la height of the right sector $n^{\circ}2$.

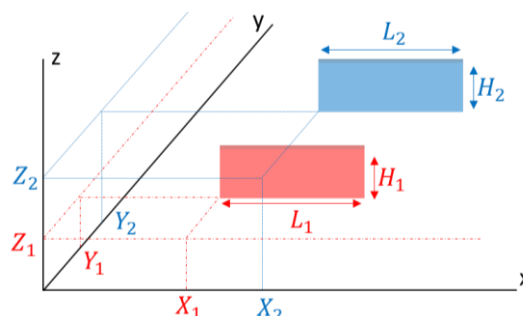


Figure II-9: Mutual inductance between two thin parallel straight sectors.

Comparisons between the expression for the mutual inductance proposed by Z. Piatek [71] and equation (10) have been performed. The results are identical; the computation time is significantly longer for equation (10) using the Monte Carlo method (a broad class of computational algorithms that rely on repeated random sampling to obtain numerical results). For the mutual induction calculations, the mutual expression proposed by Z. Piatek will be used. The racetrack mutual matrix can now be constructed.

II. 1. 3. 3. 4 Self-inductance of a racetrack

In the case of a racetrack of $n_a = 20$ turns, $n_{fc} = 10$ divisions per half turn and $n_{fd} = 5$ divisions per straight section, with an inner radius of $r_c = 50$ mm and a straight section length of $L = 100$ mm, and a tape width of 4 mm (Figure II-10), the self-inductance of the racetrack is the sum of the coefficients of the matrix M . The thickness of the tape, more precisely the distance between two turns, is $75 \mu\text{m}$. With $L = 0$, we find the case of a simple pancake. Self-inductance values were compared between analytical solutions calculated with MATLAB and the OPERA simulation software (Figure II-10). OPERA is a finite element analysis software that allows users to perform 2D and 3D simulations of electromagnetic and electromechanical systems. The values of the calculations between MATLAB and OPERA are relatively close; the obtaining of the mutual inductance for each sector of the electric circuit is operational.

Method	OPERA	MATLAB	OPERA	MATLAB
Geometry	Complete racetrack		Racetrack without straight section \rightarrow pancake	
Mutual [H]	$1.699 \cdot 10^{-4}$	$1.702 \cdot 10^{-4}$	$9.68 \cdot 10^{-5}$	$9.70 \cdot 10^{-5}$

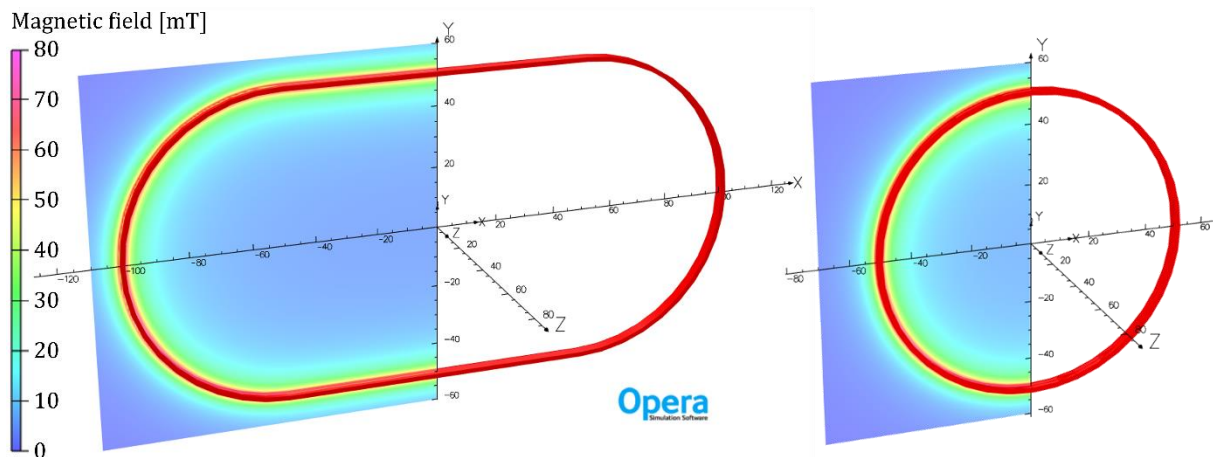


Figure II-10: Calculation of self-inductance with OPERA on a complete racetrack on the left and on a simple pancake on the right.

The thermoelectric and magnetic behavior is now implemented in the PEEC model. However, in order to simulate the behavior of a superconducting pancake, it is necessary to obtain the amplitude and orientation of the magnetic induction at the conductors, as this changes the value of the critical current. This is discussed in the next two sections.

II. 1. 4 Components of magnetic induction

II. 1. 4. 1 Simple and multi-pancake

The magnetic induction is calculated with analytical Biot-Savart formulas defined by G. Aubert in the case of thin solenoid arc. In this model, the components of the field are calculated only at one point, at the center of each angular sector (at mid-height, and at the middle of the angular

opening). In the case of a simple pancake, the field at the point of calculation is only parallel to the surface of the tape. Actually, the field generated by the simple pancake is not parallel to the surface of the tape over the entire height. Thus, in the case of a simple pancake, the critical current value is overestimated in our simulations.

In the case of n pancakes, the field is no longer parallel to the tape surface. The components of the field (B_r, B_θ, B_z) are calculated at the centers of each sector in order to obtain the angle between the field and the tape surface. Indeed, in addition to the amplitude of the magnetic induction, the influence of the angle is to be taken into account to determine the value of the critical current of each sector (additional explanations in II. 1. 5).

II. 1. 4. 2 Racetrack

In the case of a rectangular thin plate with a linear current density along \vec{e}_x , the expression for the vector potential is as follows:

$$\vec{A} = \frac{\mu_0}{4\pi} \int \int \frac{\vec{k} \cdot dS}{r} = \frac{\mu_0 k}{4\pi} \int \int \frac{dS}{r} \vec{e}_x \quad (11)$$

With (see Figure II-11):

- k the linear current density in A/m.
- $dS = da dc$ and $r = \sqrt{(x - a)^2 + (y - b)^2 + (z - c)^2}$
- a_1, a_2 intervals according to x of the right sector.
- c_1, c_2 intervals according to z of the right sector.
- b the y -coordinate of the right sector.
- x, y, z the coordinates of the calculation point of the components B_y and B_z of the magnetic induction.

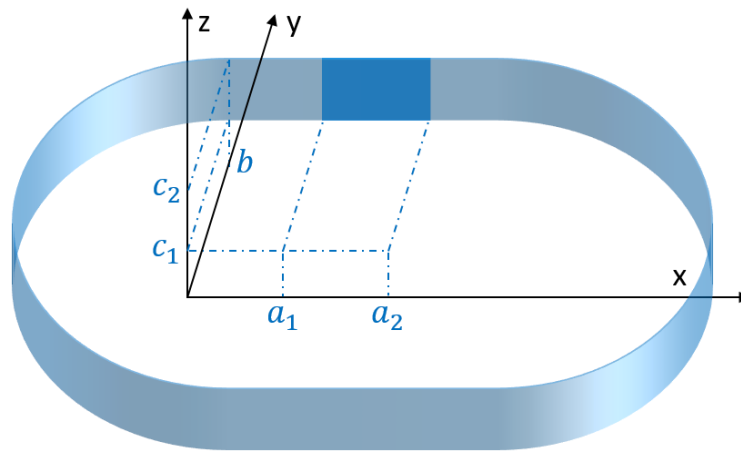


Figure II-11: Coordinates of the straight thin sector in the case of a racetrack.

With calculations made by E. Rochepault [72] and with integration method in Gradshtein [73], we obtain:

$$\iint \frac{dx dy}{r} = y \operatorname{arcth} \left(\frac{x}{r} \right) + x \operatorname{arcth} \left(\frac{y}{r} \right) - z \operatorname{arctan} \left(\frac{xy}{zr} \right)$$

The double integration leads to:

$$A_x = \frac{\mu_0 k}{4\pi} \left[(c - z) \operatorname{arcth} \left(\frac{a - x}{r} \right) + (a - x) \operatorname{arcth} \left(\frac{c - z}{r} \right) - (a - x) \operatorname{arctan} \left(\frac{(a - x)(c - z)}{(b - y)r} \right) \right]_{a_1, c_1}^{a_2, c_2}$$

The components of the induction are then obtained with $\vec{B} = \overline{rot}(\vec{A})$:

$$B_y = -\frac{\mu_0 \kappa}{4\pi} \left[\operatorname{arcth} \left(\frac{a-x}{r} \right) \right]_{a_1, c_1}^{a_2, c_2} \quad (12)$$

$$B_z = -\frac{\mu_0 \kappa}{4\pi} \left[\operatorname{arctan} \left(\frac{(a-x)(c-z)}{(b-y)r} \right) \right]_{a_1, c_1}^{a_2, c_2} \quad (13)$$

Using these calculations, it is possible to obtain the value of the magnetic induction generated by each sector at any point in space. The magnetic field measurements are made at the center of each sector of the pancakes in order to take into account the influence of the amplitude and the field angle to determine the value of the critical current of each sector.

II. 1. 5 Parameterization of the critical surface of REBCO conductors

In the model, the superconducting character of the tape must be implemented. In the case of HTS tapes, the critical surface depends on the current density J (in A/m²), the temperature T (in K), the amplitude of the magnetic induction B (in T) and the field angle from the tape surface θ (in radian). Above this critical surface, local zones of the tape are dissipative. Below, the tape is superconducting.

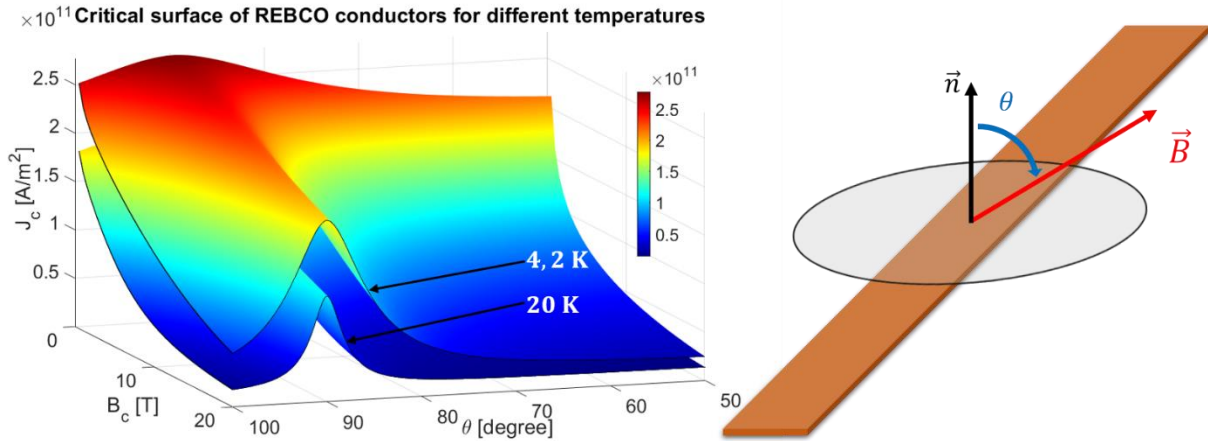


Figure II-12: On the left, critical surfaces of a HTS superconductor for different temperatures obtained using a fit based on Fujikura tapes [6]. On the right, sketch of the amplitude and orientation of the magnetic induction with respect to the tape surface.

The parameterization of the critical surface of the superconducting tape simulated in our code is based on work done with Fujikura tapes [6]:

$$J_c(B, T, \theta) = J_{c,c}(B, T) + \frac{J_{c,ab}(B, T) - J_{c,c}(B, T)}{1 + \left(\frac{\theta - \frac{\pi}{2}}{g(B, T)} \right)^\gamma} \quad (14)$$

With:

- θ the deviation of the field from the direction of the c axis,
- T the temperature,
- B the amplitude of the magnetic induction of the sector,
- γ a parameter allowing to fit the function and the experimental data,
- g the anisotropy factor defined by:

$$g(B, T) = g_0 + g_1 e^{-(g_2 e^{g_3 T}) B} \quad (15)$$

- $J_{c,c}$ and $J_{c,ab}$ are respectively the critical current densities in the planes perpendicular and parallel to the field :

$$J_c(B, T, \pi/2) = J_{c,c}(B, T) = \frac{\alpha_c}{B} b_c^{p_c} (1 - b_c)^{q_c} (1 - t^n)^{\gamma_c} \quad (16)$$

$$J_c(B, T, 0) = J_{c,ab}(B, T) = \frac{\alpha_{ab}}{B} b_{ab}^{p_{ab}} (1 - b_{ab})^{q_{ab}} [(1 - t^{n_1})^{n_2} + a(1 - t^n)]^{\gamma_{ab}} \quad (17)$$

with:

$$b_c = \frac{B}{B_{i0,c}(1-t^n)}; b_{ab} = \frac{B}{B_{i0,ab}((1-t^{n_1})^{n_2} + a(1-t^n))} \text{ and } t = T/T_{c0}$$

where $B_{i0,c}$ and $B_{i0,ab}$ are the maximum irreversibility fields in the perpendicular and parallel field orientations, respectively, and T_{c0} the critical temperature of the superconducting tape.

The parameter values used to plot the critical surfaces in Figure II-12 are as follows:

$g_0 = 0.03$	$g_1 = 0.25$	$\gamma = 1$	$p_c = 0.5$	$q_c = 2.5$	$\gamma_c = 2.44$
$g_2 = 0.06$	$g_3 = 0.058$	$a = 0.1$	$p_{ab} = 1$	$q_{ab} = 5$	$\gamma_{ab} = 1.63$
$n = 1$	$n_1 = 1.4$	$n_2 = 4.45$	$B_{i0,c} = 140 \text{ T}$	$B_{i0,ab} = 250 \text{ T}$	$T_{c0} = 93 \text{ K}$
$\alpha_c = 1.86 \text{ MA T/mm}^2$			$\alpha_{ab} = 68.3 \text{ MA T/mm}^2$		

Parameterization of the critical surface of other tapes made by P. Fazilleau are available for the manufacturers Theva, Shanghai Superconductor Technology, SuperPower and SuNAM.

All the parts generating the PEEC model have been presented. In the next section, we will see the overall functioning of the PEEC model.

II. 1. 6 Functioning and limitations of the PEEC model

The code is mainly built in two parts (Figure II-13). A first part allowing to generate the set of matrices and data according to the dimensions of the coil. It is mainly the matrices useful for the resolution of matrix systems:

- The matrix of the mutual inductances M ,
- The matrices for Kirchhoff's laws (K_θ and K_r),
- The matrices of radial and azimuthal resistivity (R_θ and R_r),
- The heat distribution matrix generated by the radial resistivity and the matrices for obtaining the magnetic induction components B_x, B_y and B_z at the center of each sector.

The resolution of the differential equations in matrix form is performed in the second part. First, the electrical equation is solved in order to obtain the azimuthal and radial currents for the next time step ($i + 1$). During the resolution of the electrical equation (calculation of the radial current I_r between i and $i + 1$), the value of the magnetic induction is obtained (link between the radial and azimuthal current), modifying the value of the critical current, which has an influence on the value of the azimuthal resistance R_θ . The temperature also influences the value of the azimuthal resistance. But unlike the magnetic induction, the temperature is fixed (at time i) when solving the electrical differential equation between time i and $i + 1$. The resolution of the electrical equation allows us to obtain the radial and azimuthal currents of each sector at time $i + 1$. The source terms are thus obtained and injected into the thermal equation to determine the temperature evolution of each sector of the coil, causing a change in the azimuthal resistivity of each sector for the next time step. The electrical equation between the instants $i + 1$ and $i + 2$ can now be solved.

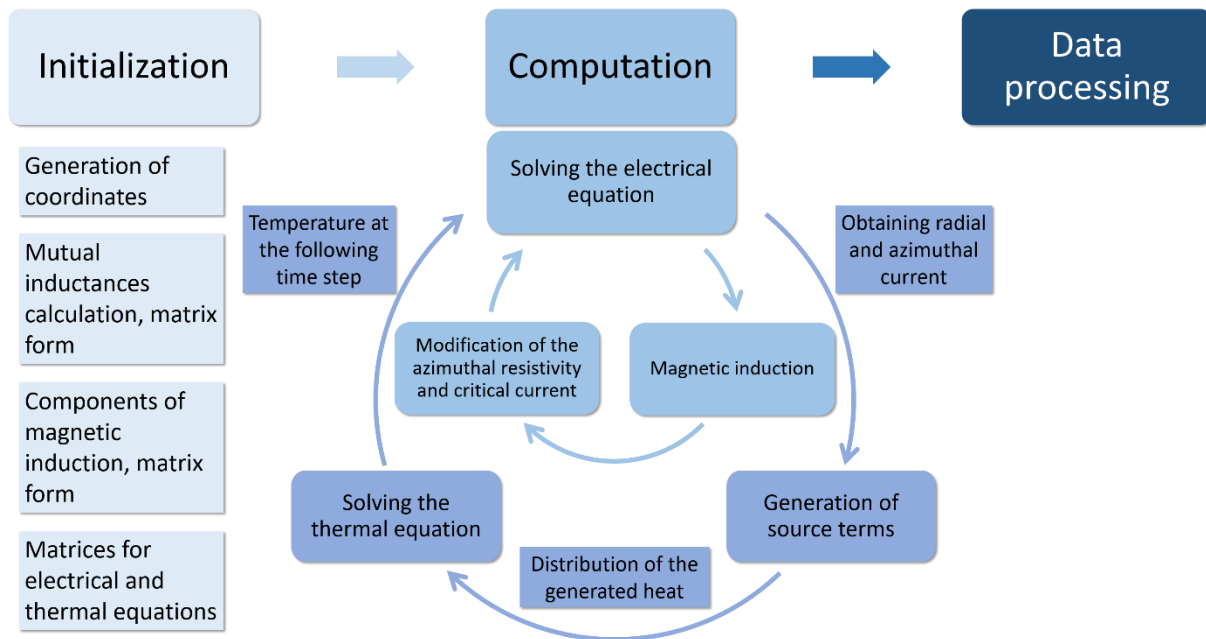


Figure II-13: Simulation diagram of the PEEC model.

The main drawback of this model is the computation time, which is important to simulate large magnets. The computation time depends strongly on the size of the matrices of the electrical equation. Thus, having a large number of turns (n_a) and division per turn (n_f) slows down the resolution.

It is not possible to solve in parallel the electrical equation for each pancake (and thus reduce the size of the matrix equation which would save a lot of time) because the pancakes are magnetically coupled together. However, it is possible to solve in parallel the heat equation for each pancake since they are thermally isolated in this PEEC model, which would slightly decrease the computation time.

In order to decrease the calculation time, a possible method would be to use the fast multipole method (FMM). This method has not been implemented in the previously presented model due to complexity and time constraints. A more detailed explanation is nevertheless available in the next paragraph.

II. 1. 7 An opening for a reduction of the computation time of the PEEC model

To decrease the calculation time, one possible method is to use the fast multipole method (FMM). The FMM is a method that is able to provide an approximate solution to the calculation of forces, potentials or energies within a given accuracy target. The method has a linear computational complexity, mainly due to its sophisticated algorithmic structure. The essential aspects of the FMM are the spatial grouping of the different elements, the hierarchical subdivision of space, the multipolar expansion of the loads and a special interaction scheme.

This algorithm makes it possible to differentiate the interactions between relatively close and distant elements. It avoids the need to build a large part of the linear system, reduces the number of operations and therefore saves a lot of computing time. The latter then evolves linearly with the number of elements.

During the 80's, Greengard and Rokhlin introduced the Fast Multipole Method to accelerate the matrix-vector product for the calculation of potential fields in systems with large numbers of particles [74]. Moreover, the FMM can reduce the prohibitive computation time through an iterative solver. The Fast Multipole Method has been widely studied to efficiently decrease the

prohibitive computation time. He has subsequently been extended to acoustical problems and Helmholtz equation [75] and elastodynamics [76], [77]. This method is also used by J. Van Nugteren [78] for the calculation of mutual inductance to simulate larger geometries. Using a Fast Multipole Method reduces the computational complexity of the resulting N-body problem, from $O(N_2)$ to $O(N)$.

In the case of a simple pancake, the mutual inductances between the sectors are not identical. Sectors radially and azimuthally adjacent to the reference sector have 5 to 10 times higher mutual values compared to sectors that are further away (Figure II-14). Thus, in order to save computation time, it might be possible to group sectors in order to generate only one mutual inductance between the reference sector and a set of relatively distant sectors. The idea would be to modify the method of calculating the mutual inductances in order to obtain the values between the reference sector and a set of sectors. In order to perform the calculations of the electrical equations, the azimuthal current of the grouped sectors could be averaged in order to see a set of sectors as a single sector with respect to the reference sector. This method seems adequate because as we have seen in the simulations, the value of the azimuthal current is mainly continuous between the sectors of a same turn.

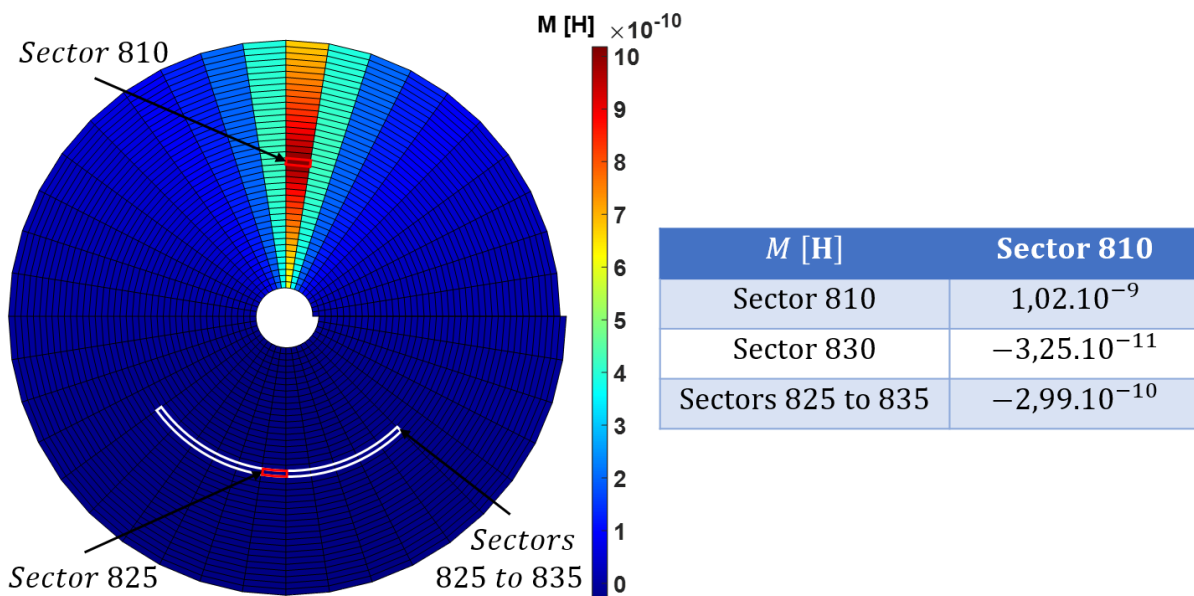


Figure II-14: Values of the mutual inductances between sector n°810 (10th sector of the 21st turn) and all other sectors of a pancake of 40 turns and 40 divisions per turn.

This method has not been developed due to the complexity of the code to be implemented. Firstly, a modification of the calculation of the mutual inductances is necessary because there will not be the same symmetries in the matrix M compared to the case without grouping of the mutual values. Moreover, it would be necessary to write the electrical equation for each mesh, taking into account the values of the azimuthal currents corresponding to the grouped sectors. As the operation is complex to implement, and other work is planned, this method was not carried out.

All these elements (without the FMM method) were implemented and coded with MATLAB software. The results of the simulations are presented in the next two parts of this chapter. The second part is only devoted to simulations of a simple pancake during different transient regimes (quench, ramp-up operation, rapid discharge) with different contact resistivity values. The aim is to understand the behavior of a simple pancake without electrical insulation during a transient regime but also to study the influence of this contact resistivity.

II. 2 Simulation of a No- or Metal-Insulation simple pancake

II. 2. 1 Influence of the contact resistivity during a quench

II. 2. 1. 1 Quench via the introduction of a heat source

The developed PEEC model allows to compare similar pancake geometries with different turn to turn contact resistivity values (R_{ct}). For the first simulations, the pancakes are operating in steady state with a constant power supply current I_0 . They are subjected to a local heat source S to study the stability and thermal overheating behavior. To do it, a power $p_{quench} = 200$ W is applied to one sector of the pancakes (20th sector of 21st turn) during a time $t_{quench} = 7$ ms (corresponding to a heater energy of 1.4 J). It induces redistribution of radial and azimuthal currents within the pancakes as presented in Figure II-15. Indeed, the local temperature exceeds the critical temperature T_c , and it leads the HTS layer to the dissipative state. The pancakes are under adiabatic conditions here and there is no external magnetic field. In this paragraph, a simple NI and MI pancake are simulated with the same properties except for the contact resistivity. The NI Pancake has a low contact resistivity ($R_{ct} = 100 \mu\Omega.cm^2$), while the MI Pancake has a high contact resistivity ($R_{ct} = 100\ 000 \mu\Omega.cm^2$). The high order of magnitude of the MI Pancake corresponds to the experimental measurements made in Chapter III. Having too many divisions per turn n_f increases the size of the matrices and therefore increases the calculation time. Conversely, having a smaller n_f reduces the simulation time but the length of the sectors will be too long, reducing the accuracy of certain parameters such as the local temperature. In the case of the two simulated pancakes, choosing $n_f = 40$ is a good compromise between the calculation time and the accuracy of the parameters. The parameters are in the Table II-1.

Table II-1: Common parameters of the simple NI and MI pancake simulated in the case of a quench with introduction of a heat source.

Parameters	Units	Values
Turns (n_a)	—	40
Divisions per turn (n_f)	—	40
Tape width (h_0)	mm	6
Winding inner diameter (ID)	mm	50
Winding outer diameter (OD)	mm	55.6
Current margin	%	10
Supply current (I_0)	A	1617
Initial temperature (T_0)	K	4.2
Coil self-inductance	mH	0.14
Substrate thickness	μm	50
Copper thickness	μm	2×10
Superconductor thickness	μm	2
Convective exchange coefficient (h)	W/m ² /K	0
Contact resistivity NI Pancake (R_{ct})	$\mu\Omega.cm^2$	100
Contact resistivity MI Pancake (R_{ct})	$\mu\Omega.cm^2$	100 000

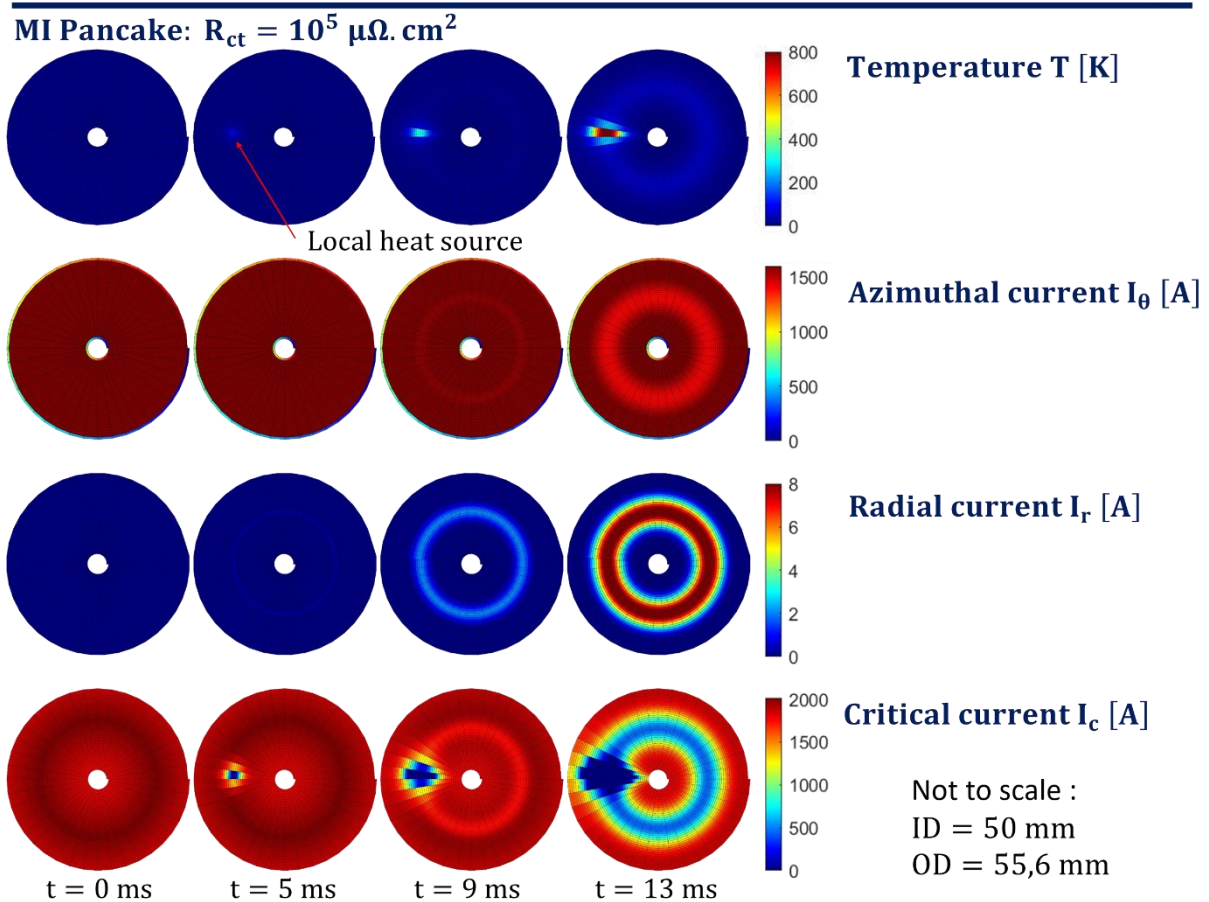
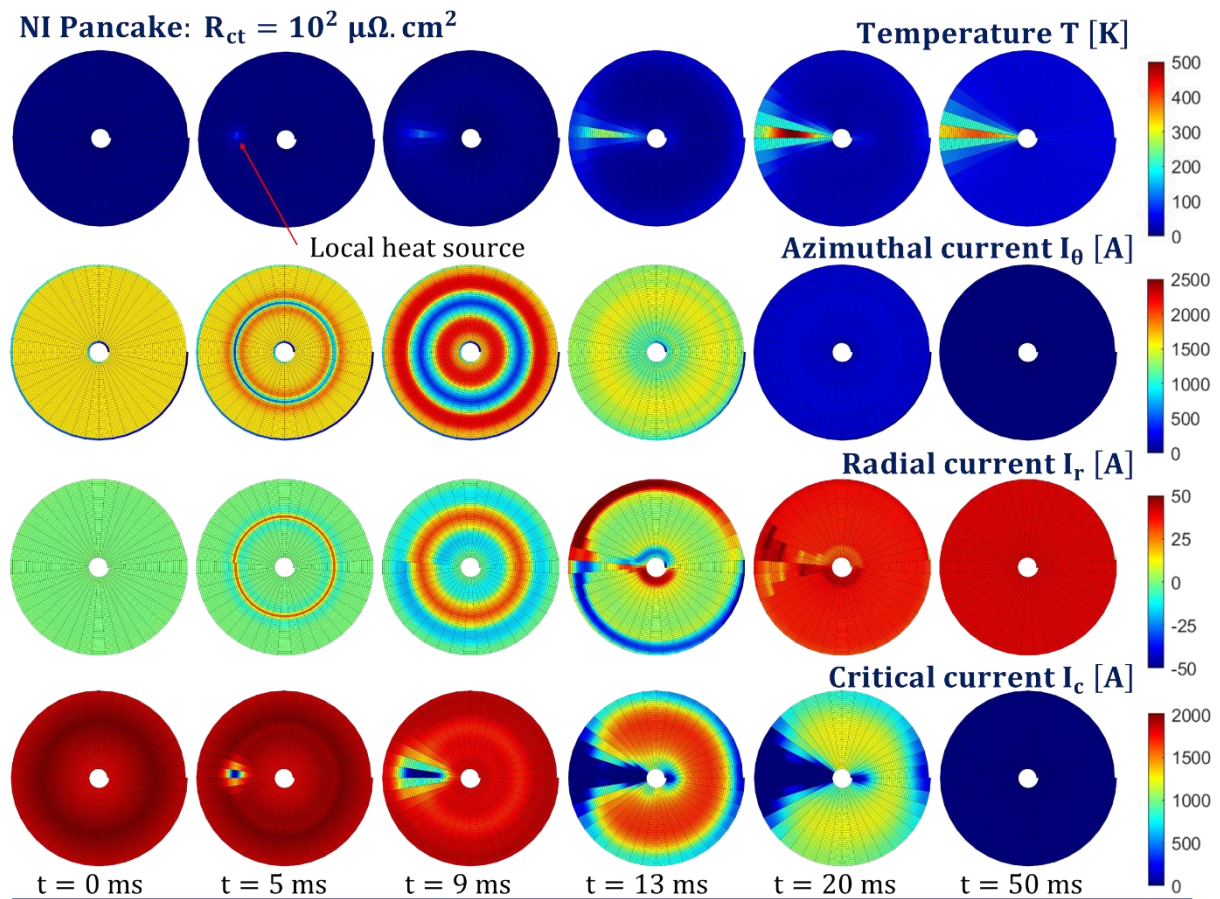


Figure II-15: Evolution of the distribution of the temperatures, azimuthal, radial and critical currents as a function of time in Pancake 1 and Pancake 2 during a quench (heater energy 1.4 J) under adiabatic conditions, with a different R_{ct} value.

In the case of the NI Pancake, the current by-passes radially from one turn to the other and thus avoids the local quenched zone (**between 0 and 10 ms**, in [Figure II-15](#)). It should be noted that the radial current from one turn to another is done over a full turn and not locally before or after the quenched zone. Thus, the current transfer length in the case of a NI pancake is one full turn. Indeed, the more the current is redistributed over a long length, the more the current will meet a low resistance. As the current redistributes to the adjacent turns of the quenched area, the azimuthal current value on the adjacent turns increases. However, in this simulation, the supply current I_0 is chosen to have 10% current margin in relation to the most critical sector of the pancake. The azimuthal current increase in adjacent turns causes the critical current to be exceeded, which results in quench propagation, in addition to heat diffusion by conduction.

At $t = 13 \text{ ms}$ in [Figure II-15](#), in the case of the NI Pancake, the azimuthal current value has exceeded the critical current value along the entire turn of the inner and external turns of the pancake. The values of the critical currents in these sectors are therefore lower. For a short time, the areas with the highest critical current are on the central turns of the pancake, apart from the areas where the heat source was introduced. Thus, the current will briefly favor the central turns to flow azimuthally, avoiding the inner and external turns where the critical current is lower than the central turns. This will cause the current to flow at the local hot spot, further increasing the temperature of the initially heated area.

After a few milliseconds ($t > 50 \text{ ms}$), the whole pancake is resistive. The current, therefore, flows exclusively radially. This uniform radial current causes a temperature rise in the whole NI Pancake. A part of the current now flows radially, which leads to a decrease of the field at the center of the pancake ([Figure II-16](#)).

The high turn-to-turn contact resistivity in the MI Pancake forces most of the current to flow azimuthally at the start of the quench. It leads to a higher heating of the quenched turn which also propagates by conduction to adjacent turns. Because the contact resistivity value is relatively high, the radial currents are low ([Figure II-15](#) and [Figure II-16](#)). Source terms are nevertheless generated by the presence of this low radial current over several full turns of the pancake, hence the decrease of the critical current over the whole circumference. There is no increase in azimuthal current in the turns adjacent to the sector that received a source term.

By allowing the current to redistribute in the NI Pancake, the maximum local temperature reached at $t = 20 \text{ ms}$ is lower for NI Pancake (~400 K) than MI Pancake (~900 K, [Figure II-15](#) and [Figure II-16](#)). It highlights the self-protective character of the pancake having a low turn-to-turn contact resistivity. In the case of the NI Pancake, the value of the hot spot reaches a peak at $t = 20 \text{ ms}$ before decreasing unlike MI Pancake, which reaches 900 K at the end of the simulation (the hot spot is constantly increasing). At this temperature, the conductor burns out. Therefore, no image of the MI Pancake is available for $t = 20$ and 50 ms in [Figure II-15](#). The very punctual peak at 400 K in the NI Pancake allows to say that in this case, the coil is self-protected because the maximum local temperature eventually decreases by homogenization. Therefore, contact resistivity has an important role in pancake protection. It is reminded here that the supply current remains constant, the simulations presented are mainly to understand the behavior and current redistribution of a simple pancake during a quench. Studies on contact resistivity measurements and work on the hot spot as a function of the passive protection imposed with voltage limitation on the pancake were conducted in the next chapters.

[Figure II-16](#) gives time evolution of the average radial and azimuthal current, local maximum temperature and magnetic induction at the center of the pancake. With a low contact resistivity, the average value of the azimuthal current drops when the source term is introduced. The current flows radially, which leads to a rapid decrease in the magnetic induction generated by the NI Pancake. With a higher contact resistivity, the current cannot be redistributed. This explains the

small decrease in azimuthal current and magnetic induction generated by the MI Pancake. The current does not redistribute, there are no radial currents. A thermal overheating occurs quickly.

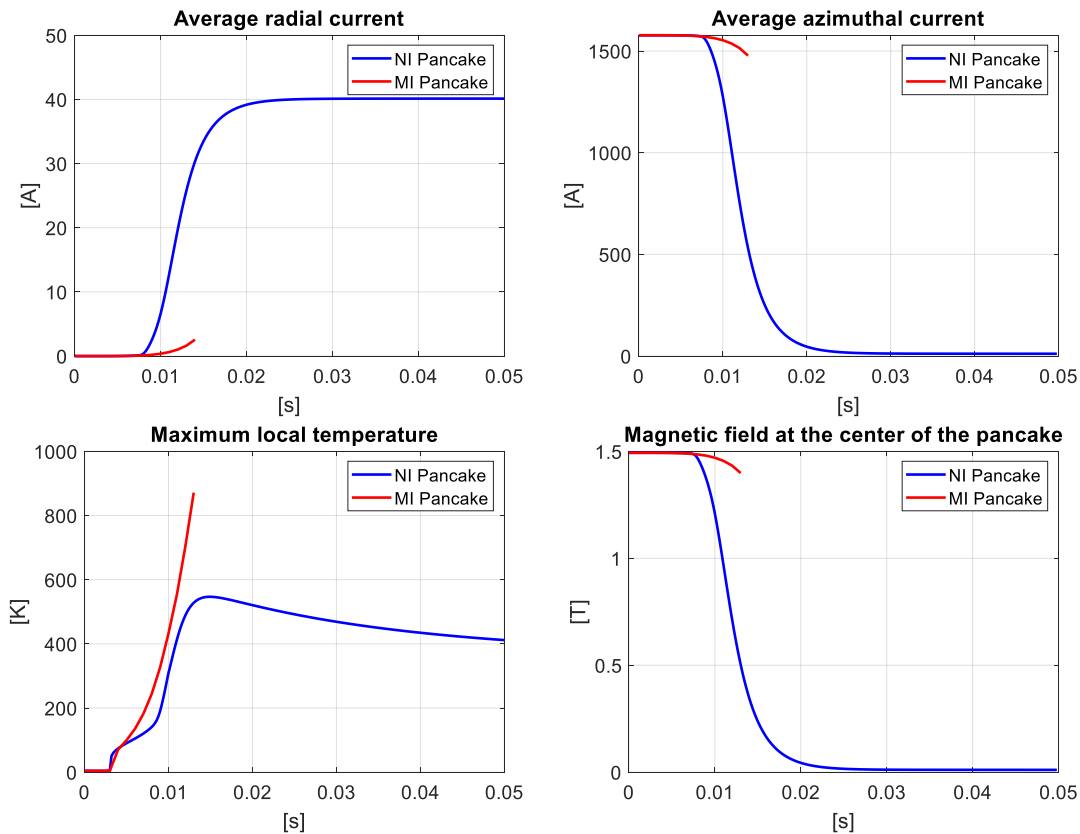


Figure II-16: Average values of the radial and azimuthal current, local maximum temperature and magnetic induction of the simple NI and MI pancake when introducing a source term causing a quench or thermal overheating.

II. 2. 1. 2 Quench caused by a local degradation of the critical current

Another simulation method is used to initiate a quench in the simple pancake case. The value of the critical current I_c of a single sector is deliberately degraded. No external energy is provided into the pancake. The properties of the simulated pancake are identical to the previous paragraph (Table II-1). The only difference comes from an instantaneous degradation of 50% on the same sector as the previous case (20th sector of the 21st turn) instead of the source term $S_{quench} = p_{quench} \times t_{quench}$. The introduction of this local degradation into the pancake, either NI or MI pancake, causes a redistribution of the current, i.e. the appearance of a radial current I_r , and therefore the generation of source terms causing a rise in temperature of the pancake. The pancake is always under adiabatic conditions, and its behavior differs according to the value of the contact resistivity.

II. 2. 1. 2. 1 Low contact resistivity: NI Pancake

During the first three milliseconds of the simulation, the pancake is in its steady state. The supply current I_0 is 1617 A (10% current margin) and the pancake is at 4.2 K. At $t = 3$ ms, an instantaneous 50% degradation on the 20th sector of the 21st turn is deliberately imposed ($I_{c\ min}$ at the bottom left of the Figure II-17). In the NI Pancake case ($R_{ct} = 100 \mu\Omega \cdot \text{cm}^2$), the 50% degradation from $t = 3$ ms of the sector leads to a redistribution of the current. The value of the critical current in the sector is not being directly at 0, a part of the azimuthal current continues to pass in the degraded sector. The appearance of a radial current I_r , combined with part of the azimuthal current I_θ flowing in the degraded sector leads to the generation of source

terms that increase locally, but slowly, the temperature of the degraded sector, as well as the adjacent sectors (for $3 \text{ ms} < t < 250 \text{ ms}$, in Figure II-17 and Figure II-18).

In the case of this simulation, the heat spreads azimuthally and radially in the pancake. Thus, the heat propagating radially from the degraded sector decreases the critical current of the sectors adjacent to the degraded sector. This decrease of the critical current is also explained by the value of the magnetic induction, which is more intense for the internal turns of the pancake. This decrease of I_c is observable for $t = 280 \text{ ms}$.

The decrease of the critical current at the adjacent turns will cause a new redistribution of the currents, mainly localized at the internal turns ($t = 284 \text{ ms}$ in Figure II-18). In the same way, more and more important source terms will be generated causing an increase in local temperature within the pancake ($t = 284 \text{ ms}$). This rise in temperature causes a local decrease of the critical current, mainly on the sectors adjacent to the initially degraded sector, for the internal turns. A decrease of the azimuthal current occurs on these internal turns, causing a rise of the azimuthal current on the external turns ($t = 286 \text{ ms}$, Figure II-17 and Figure II-18).

This increase in azimuthal current exceeds the value of the critical current I_c on the external turns ($t = 288 \text{ ms}$), thus generating a rise in temperature reducing the critical current for the external turns. The average value for each calculation time of the critical currents I_c of the pancake drops rapidly (bottom left of the Figure II-17). As the pancake is supplied with a constant current $I_0 = 1617 \text{ A}$, and all the sectors radially adjacent to the initially degraded sector have a zero critical current, the current flows mainly radially. This causes an increase in the average temperature of the pancake ($t > 300 \text{ ms}$) and a decrease in the magnetic induction (Figure II-17). The local maximum temperature thus has a temperature peak for $t = 294 \text{ ms}$, before decreasing by conduction heat transfer to adjacent sectors.

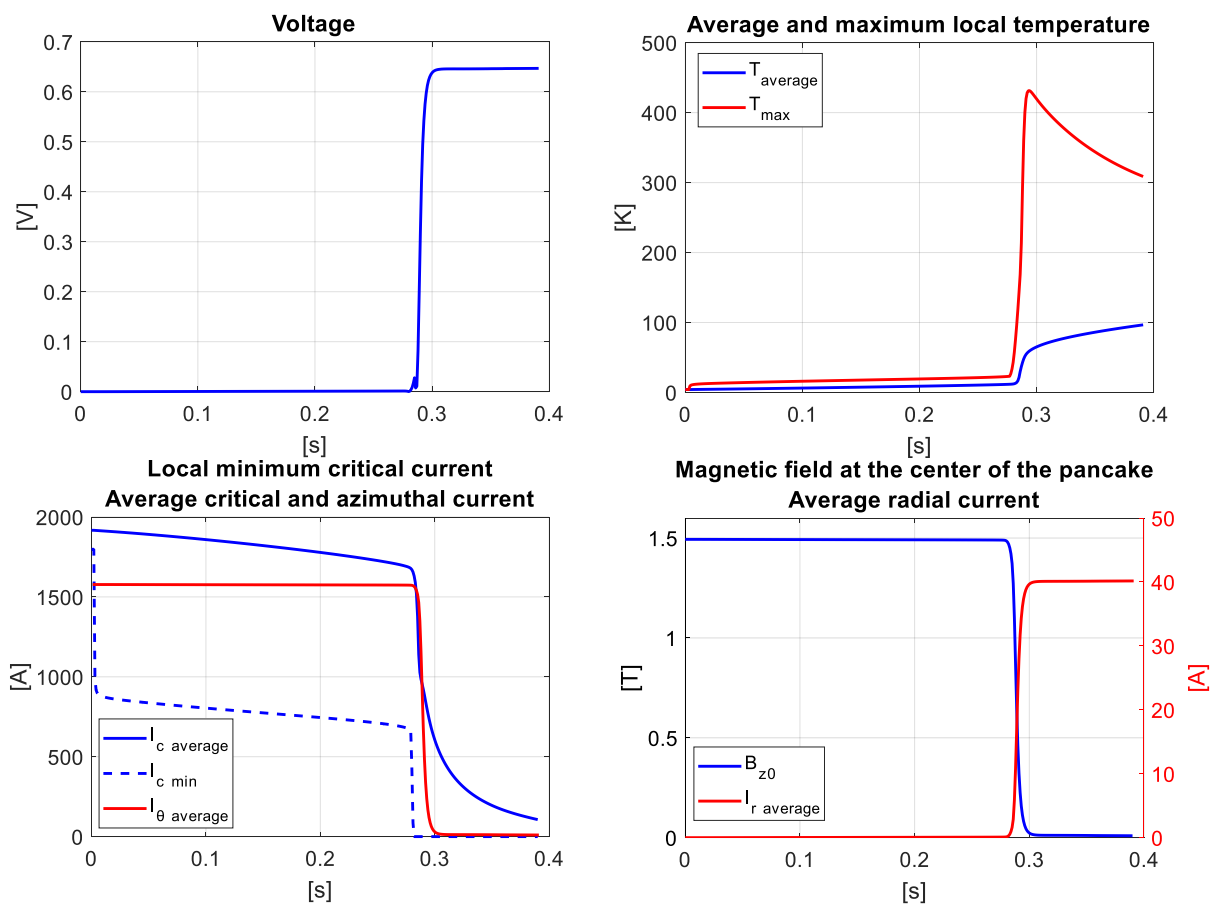


Figure II-17: Voltage, average and maximum local temperature, azimuthal and critical average current, minimum critical current, magnetic induction of the NI pancake subjected to local degradation.

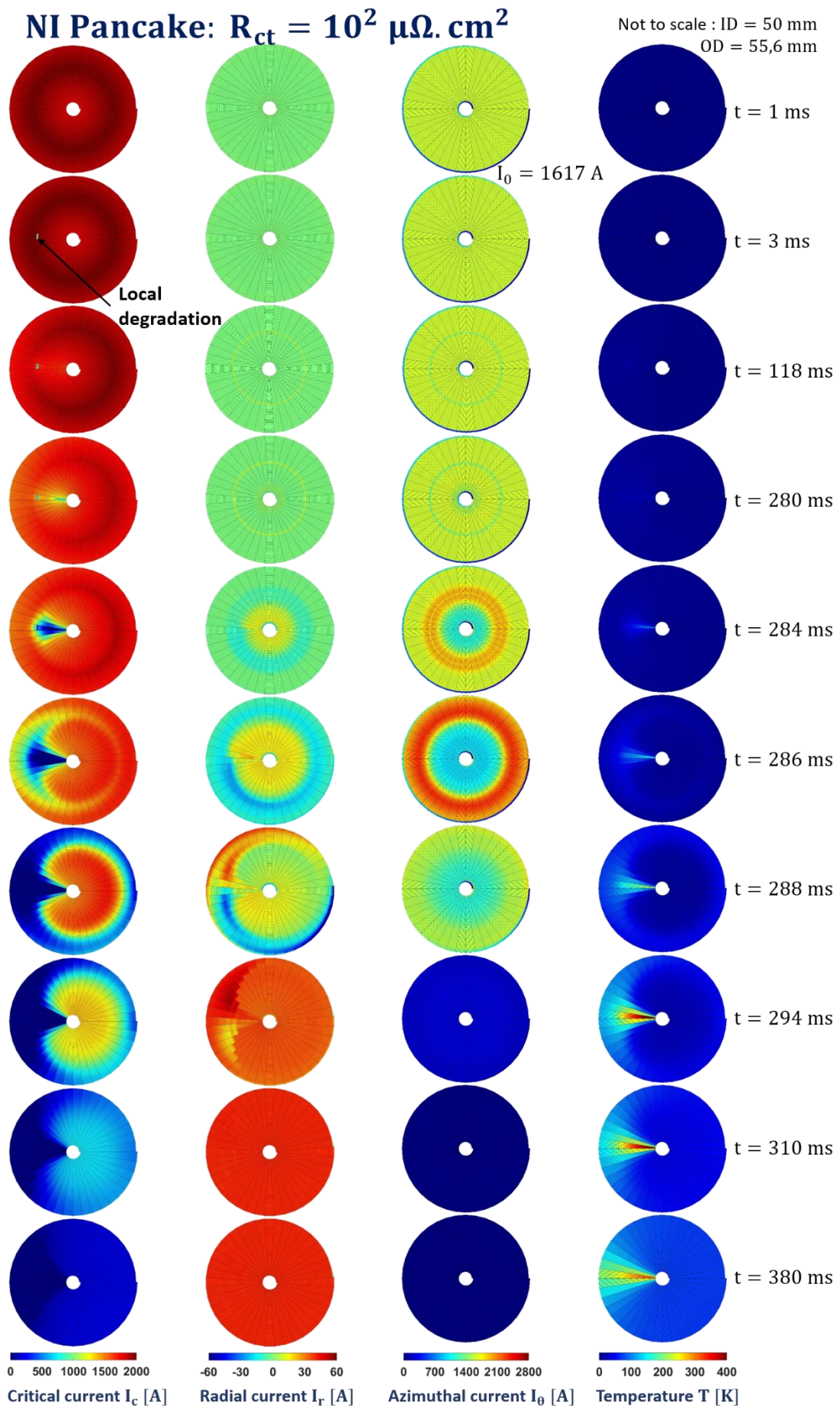


Figure II-18: Simple pancake during a quench caused by a local degradation of the critical current, low contact resistivity.

II. 2. 1. 2. 2 High contact resistivity: MI Pancake

In the case of the MI Pancake ($R_{ct} = 100 \text{ m}\Omega\cdot\text{cm}^2$), as for the case with the introduction of a source term, the behavior is significantly different compared to the case with the NI Pancake. For this new simulation, only the value of the contact resistivity has been changed. With the instantaneous 50% degradation from $t = 3 \text{ ms}$, still on the 20th sector of the 21st turn and with a high contact resistivity value, thermal overheating of the pancake is inevitable (Figure II-19). In the case of the simulation with a low contact resistivity value, the degradation of the sector causes a redistribution of the current in the pancake, thus allowing the current to bypass the local defect. However, in the case of a pancake with a high contact resistivity value, the current can hardly flow radially from one turn to another. Thus, a large part of the azimuthal current is forced to flow azimuthally, and thus through the degraded sector (Figure II-19 and Figure II-20).

In the case of the simulation with local degradation of the critical current of a sector, the thermal overheating is not direct, compared to the previous paragraph (quench caused by the introduction of a source term). Indeed, by degrading the sector by 50%, it is still partly superconducting. A proportion of the current continues to flow in the superconducting part, the other proportion flows in the copper matrix, thus generating source terms. These source terms cause a rise in temperature, decreasing more and more the value of the critical current I_c of the degraded sector, causing the thermal overheating of the pancake. This thermal overheating is faster and takes place at the degraded sector (compared to the case with a low contact resistivity value) because the heat generation is mainly due to the current I_θ higher than the critical current I_c . A high contact resistivity R_{ct} , forcing the current to flow azimuthally, causes this. Indeed, at the end of the simulation, the azimuthal current is still quite high (Figure II-19 and Figure II-20), which was not the case with a low value of contact resistivity: the value of I_θ was almost zero (Figure II-17).

Radial currents can be observed, but they are much lower in the case of a high contact resistivity. These radial currents are nevertheless responsible for the decrease of the critical current only on the sectors of the turn of the initially degraded sector (from $t > 113 \text{ ms}$, Figure II-19 and Figure II-20).

In this simulation, the maximum local temperature is much higher ($T_{max} \approx 900 \text{ K}$) than in the case with a low contact resistivity value ($T_{max} \approx 400 \text{ K}$), because much of the pancake's energy is concentrated in a small area. Another noticeable difference can be seen in the voltage of the two pancakes. Since the MI Pancake has a much higher contact resistivity than the NI Pancake, its voltage is higher when the current flows radially (more than 60 V in the case of the MI Pancake compare to less than 1 V for the NI Pancake, in top left of Figure II-17 and Figure II-20). The average value of critical, azimuthal and radial current, as well as temperature, as a function of time is the average of all sectors of the pancake:

$$\left\{ \begin{array}{l} I_{\theta,aver}(t) = \frac{1}{n_a \times n_f} \sum_{k=1}^{n_a \times n_f} I_\theta^k(t) \\ I_{c,aver}(t) = \frac{1}{n_a \times n_f} \sum_{k=1}^{n_a \times n_f} I_c^k(t) \\ I_{r,aver}(t) = \frac{1}{(n_a - 1) \times n_f + 1} \sum_{k=1}^{(n_a - 1) \times n_f + 1} I_r^k(t) \\ T_{aver}(t) = \frac{1}{n_a \times n_f} \sum_{k=1}^{n_a \times n_f} T^k(t) \end{array} \right. \quad (18)$$

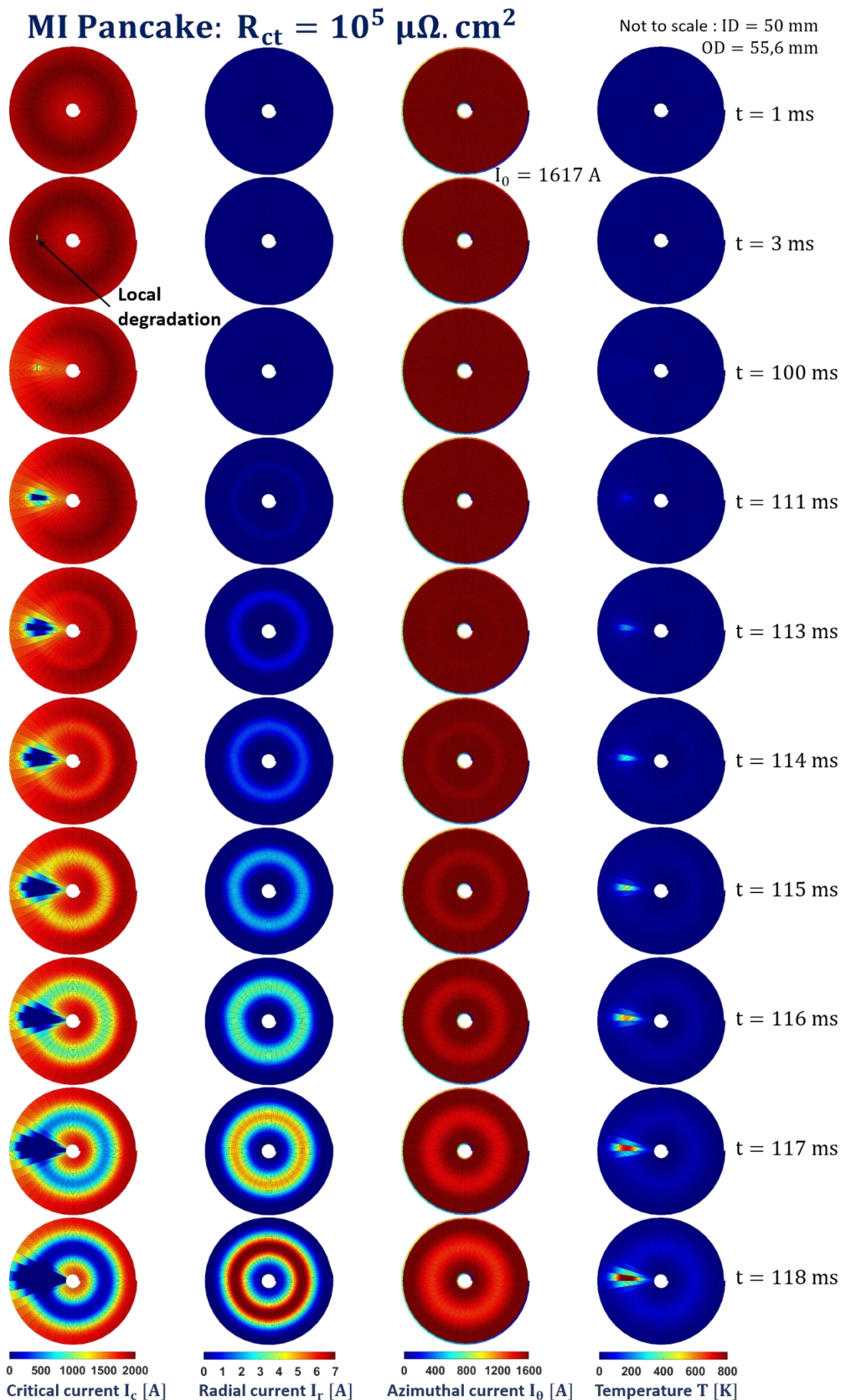


Figure II-19: Simple pancake during a quench caused by a local degradation of the critical current, high contact resistivity.

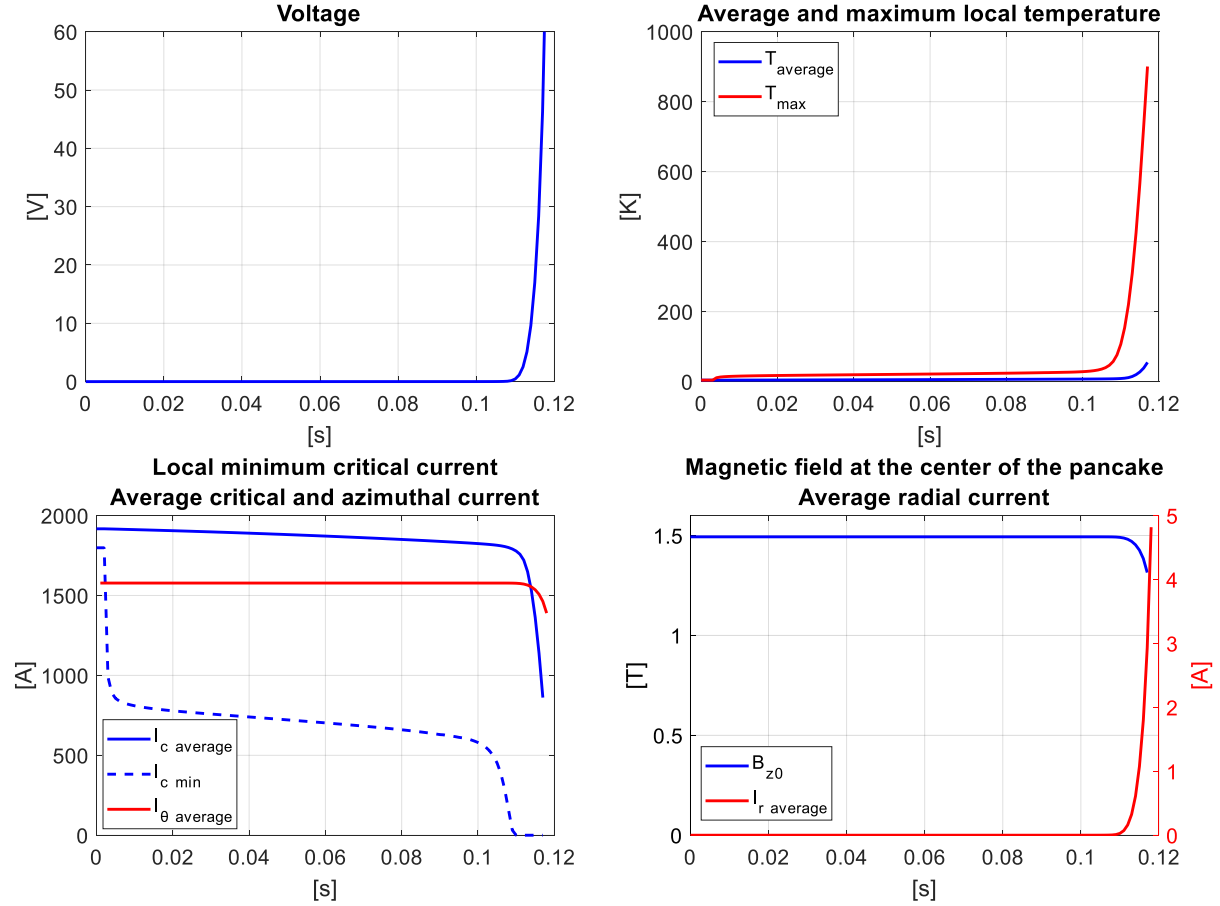


Figure II-20: Voltage, average and maximum local temperature, azimuthal and critical average current, minimum critical current, magnetic induction of the MI pancake subjected to local degradation.

The contact resistivity value influences the behavior of a simple pancake during a quench, making the pancake more or less self-protected. It also changes its behavior when powered with a non-constant current. This will be discussed in the next section, where the contact resistivity value is again studied.

II. 2. 2 Simple pancake in ramp-up operation, influence of the contact resistivity

For this mode of operation, the notable difference to the equation (1) and (2) comes from the fact that the supply current I_0 is time-dependent, so a modification of the electrical equation is required. In the case of a simple pancake:

$$M_{SP} H_{passSP} \frac{dI_r}{dt} + (R_{\theta SP} H_{passSP} - R_{rSP}) I_r = R_{\theta SP} K_{\theta SP}^{-1} I_0(t) + M_{SP} K_{\theta SP}^{-1} \frac{dI_0(t)}{dt} \quad (19)$$

$M_{SP} K_{\theta SP}^{-1}$ is a constant matrix. This model is mainly used to simulate the behavior of a NI/MI pancake during current ramping, and therefore to calculate the source terms generated by the pancake during transient phases. With this model, it is also possible to observe the influence of the turn-to-turn resistance R_{ct} . It also highlights the self-protective behavior when the current I_0 exceeds the local minimum I_c .

The parameters of the two pancakes are the same as in the previous paragraph (Table II-1), except for the value of the contact resistivity, the supply current (not constant) and the initial temperature of the two pancakes (77 K instead of 4.2 K). Imposing an initial temperature of 77 K instead of 4.2 K allows the critical current of the pancake to be lower, thus decreasing the simulation time before the critical current is exceeded during a ramp-up operation. For this

reason, a temperature of 77 K was chosen in order to reduce the calculation time while understanding and observing the influence of the contact resistivity during this transient regime.

With a contact resistivity value $R_{ct} = 100 \text{ m}\Omega\cdot\text{cm}^2$, the behavior is close to an insulated pancake. In order to better understand the influence of the contact resistivity on the behavior of a coil during a ramp-up operation, without and with exceeding the critical current of the pancake, two values of contact resistivity comparable to NI will be simulated. The NI pancake from the previous section is used (NI Pancake-100), and a factor of 5 on the contact resistivity value will be imposed for the second pancake (NI Pancake-500). New and additional parameters for this study are detailed in Table II-2. Finally, a high current ramp is imposed (20 A/s) in order to obtain a higher inductive voltage, which makes it possible to better observe the behavior of the pancakes during a ramp-up operation.

Table II-2: Parameters of the NI Pancakes during ramp-up operation.

Parameters	Units	NI Pancake-100	NI Pancake-500
Turn-to-turn resistivity (R_{ct})	$\mu\Omega\cdot\text{cm}^2$	100	500
Coil turn-to-turn resistance (R_c)	m Ω	0.39	1.96
Equivalent time constant ($\tau = L/R_c$)	ms	363	72
Current ramping: below - above I_c (c)	A/s	20	
Initial temperature (T_0)	K	77	

Where R_c is related to R_{ct} via the radius of the sectors (r_i) and the width of the tape (h_0):

$$R_c = R_{ct} \times \sum_{i=2}^{n_a} \frac{1}{2\pi r_i h_0} \quad (20)$$

II. 2. 2. 1 Below critical current

When charging the pancakes, the inductive voltage across the pancakes generates radial currents. Such currents generate Joule heating and a warming up of the coil. The contact resistivity R_{ct} modifies the charging time of the pancake as well as the radial source terms. The higher the R_{ct} , the faster we can charge the pancake and the lesser heat is generated (Figure II-21).

This simulation consists of three phases, each with a duration three seconds: ramp-up, plateau and ramp-down of the current I_0 . The supply current is, in this first case, lower than the critical current of the pancake ($I_c \approx 101 \text{ A}$, in self-field). Imposing a non-constant supply current on the pancake causes the appearance of an inductive voltage across it and thus radial currents (the values of the azimuthal resistances are almost zero because each sector is in the superconducting state). These radial currents cause a rise in temperature of the pancake (Figure II-21). The pancake not being cooled (no convective exchange, $h = 0$); the temperature rises linearly as long as the current I_0 is increasing. At the plateau, the voltage across the pancake becomes zero, the radial currents become zero, and the temperature of the pancake increases slightly and then remains constant. Similarly, when the pancake is discharged, the inductive voltage across the pancake causes the temperature to rise again because of the negative radial currents in the pancake.

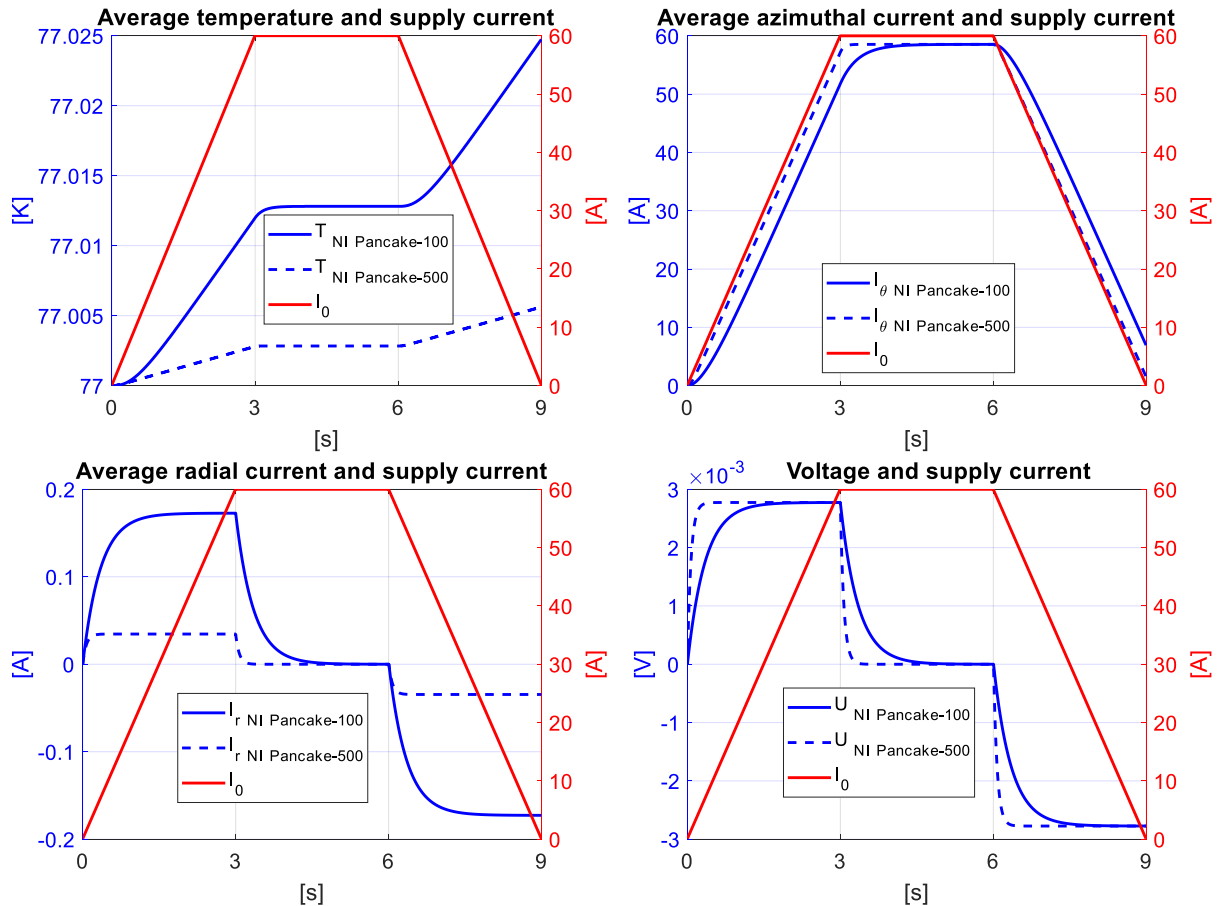


Figure II-21: Average temperatures, azimuthal and radial average currents, voltages of each pancake during a charging and discharge ramp without an excess of I_c .

At the plateau, the value of the average azimuthal current of the two pancakes is not equal to I_0 (Figure II-21, top right). This slight difference is explained by the fact that in the model, the current I_0 is uniformly distributed over the entire first and last turns (observable in Figure II-15). Since the displayed value is the average value of the azimuthal currents of all sectors, it is lower than I_0 . The average value of the azimuthal currents of all the sectors, except those of the first and the last turn, is equal to I_0 when I_0 is constant.

The equivalent circuit of a simple pancake can be modelled by a simple RL circuit (Figure II-22) connected in parallel [48]. In the case of a variable supply current not exceeding the critical current value, the azimuthal resistance values are almost zero.

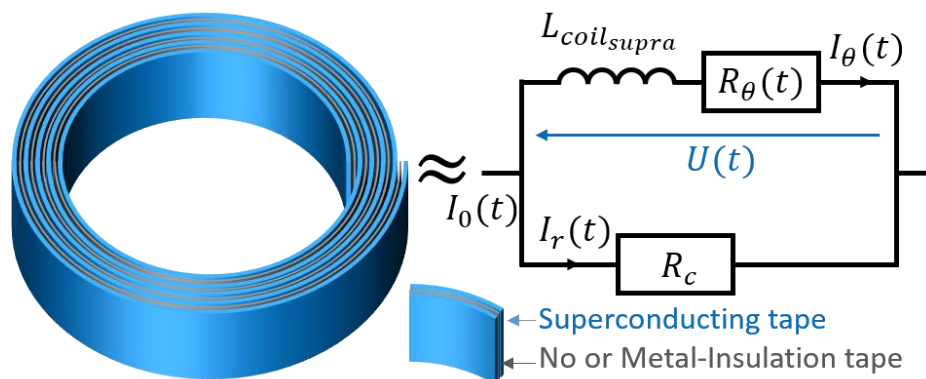


Figure II-22: Equivalent electrical circuit of a No- or Metal-Insulation simple pancake.

In the case of the electrical circuit in Figure II-22, and neglecting the value of $R_\theta(t)$ because the pancake is in its superconducting state:

$$U(t) = \begin{cases} L_{coil_{supra}} \frac{dI_{\theta}(t)}{dt} + R_{\theta}(t)I_{\theta}(t) \\ R_c I_r(t) = R_c (I_0(t) - I_{\theta}(t)) \end{cases} \text{ hence } \frac{dI_{\theta}(t)}{dt} + \frac{R_c}{L_{coil_{supra}}} I_{\theta}(t) = \frac{R_c}{L_{coil_{supra}}} I_0(t) \quad (21)$$

The solution of the equation when I_0 is linear with time is:

$$I_{\theta}(t) = I_0(t) - \tau c \left(1 - \exp\left(-\frac{t}{\tau}\right) \right) \quad (22)$$

With $\tau = \frac{L_{coil_{supra}}}{R_c}$ the time constant of the circuit and $c = \frac{dI_0(t)}{dt}$ the director coefficient of the current ramp. The values of these parameters for both pancakes are available in the Table II-2. Finally, we obtain equation (23):

$$I_r(t) = \tau c \left(1 - \exp\left(-\frac{t}{\tau}\right) \right) \text{ et } U(t) = R_c \times \tau c \left(1 - \exp\left(-\frac{t}{\tau}\right) \right) \quad (23)$$

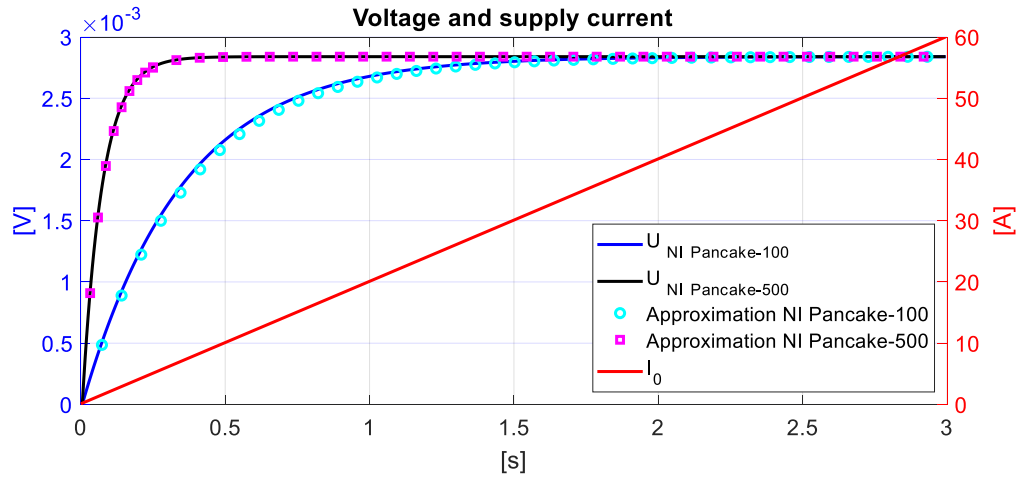


Figure II-23: Voltage of the NI Pancake-100 and the NI Pancake-500 during a ramp-up as a function of the contact resistivity.

In Figure II-23, the voltages of the NI Pancake-100 and NI Pancake-500 are superimposed with the expression in equation (23). The superposition of the solution of $U(t)$ and the results of the simulations are consistent. A maximum relative error of 5% is measurable between the two results for the NI Pancake-100, compared to a maximum relative error of 2% for the NI Pancake-500. The slight difference between the two results comes from the equivalent electrical circuit of the simple pancake (simple RL circuit) less complex than that of the PEEC model (voltage of the pancake is the sum of the voltage of each sector). Thus, from the PEEC model, it is quite possible to determine the source terms generated by the contact resistance during charging and thus to dimension a cryogenic system in order to cool the pancake or the coil during charging. The energy supplied by the power source during the ramp-up, the energy dissipated by Joule effect and the magnetic energy of each pancake at the end of the ramp-up ($t = 3$ s) are available in Table II-3.

The magnetic energy is higher for the NI Pancake-500 because it charges faster. The current flows more azimuthally compared to the NI Pancake-100. More of the energy supplied by the power source during the ramp-up is dissipated as heat by the NI Pancake-100 (0.05 J) compared to the NI Pancake-500 (0.01 J). Hence the higher temperature for the NI Pancake-100.

Table II-3: energy balance during a ramp-up operation for NI Pancakes.

At $t = 3$ s	NI Pancake-100	NI Pancake-500
Energy supplied by the power source [J]	0.24	0.25
Magnetic energy [J]	0.19	0.24
Energy dissipated by Joule effect [J]	0.05	0.01

In the next section, the self-protective behavior of a simple NI pancake during a ramp-up operation exceeding the critical current value is simulated. The contact resistivity value is again a parameter modifying the behavior of the pancake.

II. 2. 2. 2 Above critical current

The following model uses the same pancakes characteristics as the previous paragraph (Table II-1 and Table II-2) but with a final current 30% higher than the critical current ($I_c \approx 101$ A in self-field and $I_{0,max} \approx 132$ A). Through these simulations, we can observe the self-protective character of the NI pancake. During the first phase, when the supply current I_0 increases, the behavior is the same as in the previous paragraph. However, in the next two simulations, the supply current I_0 exceeds the critical current of the coil shown as a thin red dotted line in the top right of Figure II-24. The critical current values of both pancakes decrease during the ramp-up as the magnetic induction generated by the pancake, as well as the sector temperature, increases. The critical current value of the NI Pancake-500 is significantly lower than the NI Pancake-100 during the ramp-up because the charging is faster for the NI Pancake-500. The magnetic induction is higher than for the NI Pancake-100, which decreases the critical current.

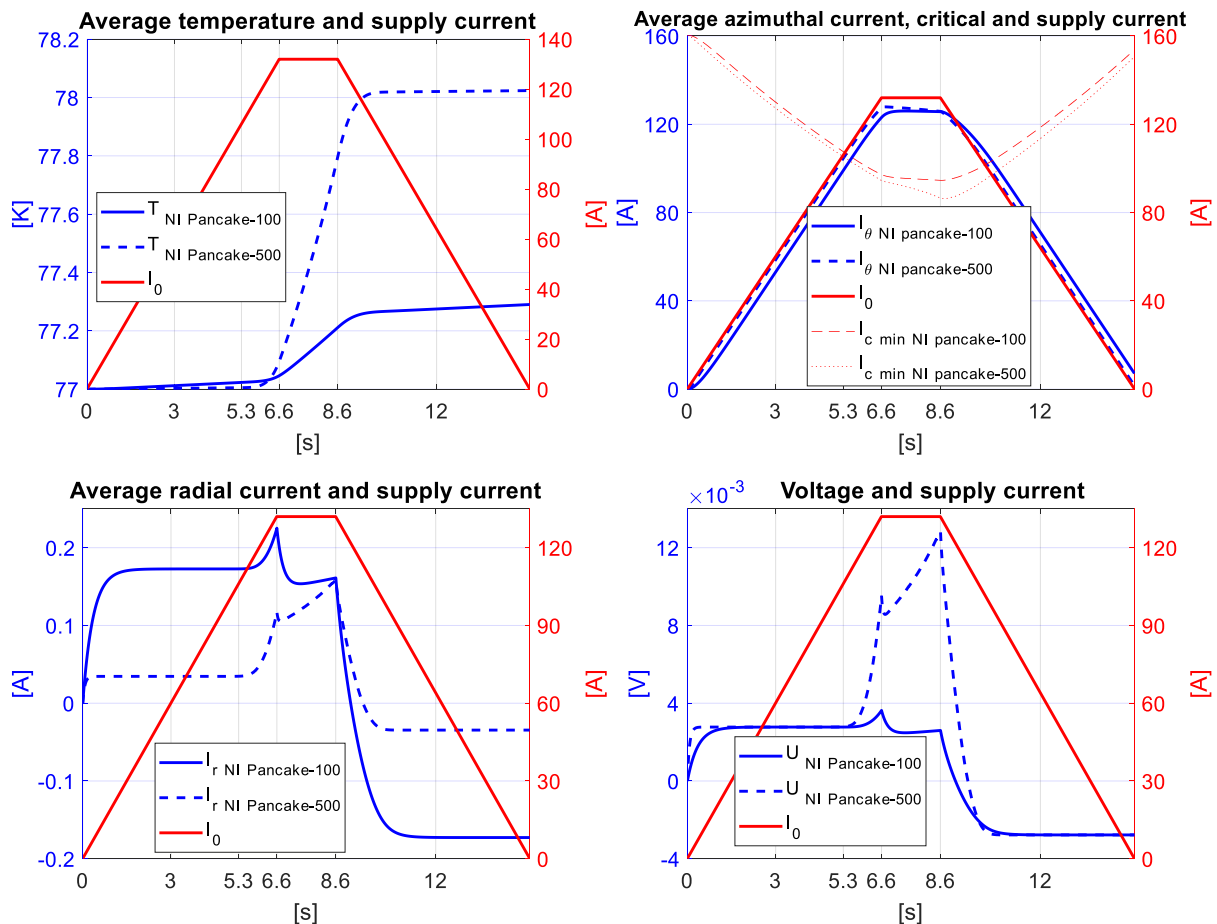


Figure II-24: Average temperatures, average azimuthal and radial currents, voltages of each pancake during a charging and discharge ramp with an excess of I_c .

The self-protected behavior is similar to the case of a local quench as explained previously in section II. 2. 1. 1 in the case of a low contact resistivity. The difference is that the transited sector's temperature in II. 2. 1. 1 was above the critical temperature (not anymore in superconducting state), whereas we are still in the current sharing mode here (not fully resistive sectors). It is observable that the voltage of NI Pancake-500 is higher than that of the NI

Pancake-100 when $I_0 > I_c$: this is due to the difference in the value of the contact resistivity R_{ct} , which is higher in NI Pancake-500, resulting in a higher voltage. During the overcurrent phase, a fraction of the current above the critical current will flow radially from one turn to another: the higher the contact resistivity, the higher the temperature of the pancake. By increasing the R_{ct} value, the current is forced to flow radially and azimuthally in resistive parts, causing an average increase of the pancake temperature (Figure II-24).

Through the results, we can observe that the average value of the azimuthal current of both pancakes is not equal to the supply current I_0 when $I_0 > I_c$ (Figure II-24). Indeed, one of the sectors of the pancake is in the case of current sharing. The current within the pancake is redistributed, which causes the appearance of radial currents, and therefore by Kirchhoff's law, a decrease in azimuthal current.

If the supply current remains constant and higher than the critical current, and considering that the pancake is under adiabatic conditions, the average and maximum temperatures will constantly increase which will cause a decrease of the critical current, and thus a thermal overheating of the pancake. In the case of these two simulations, the supply current is only constant for two seconds, the temperature of the pancake rises but does not thermally overheat.

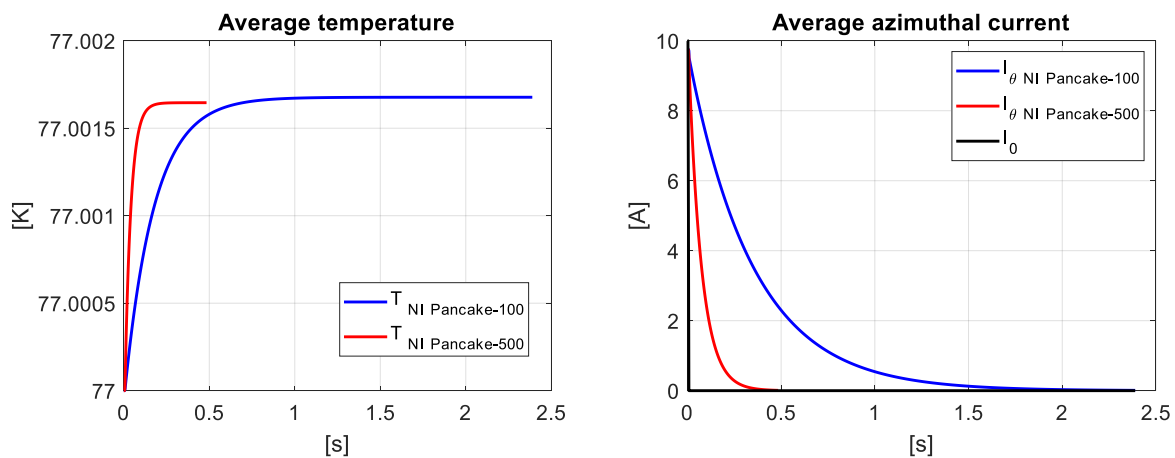
Finally, during the last phase (when $I_0 < I_c$, decrease of the supply current), the inductive voltage across the two pancakes generates a slight temperature rise. The negative inductive voltage causing the appearance of negative radial currents within the two pancakes explains this temperature rise.

II. 2. 3 Rapid discharge, influence of the contact resistivity

This model also allows simulating the case of a pancake subjected to a rapid discharge. In particular, it allows the evolution of the temperature increase of the pancake when it discharges into itself. The expression of the component $B_z(t)$ at the center of the pancake during the discharge is expressed by [48]:

$$B_z(t) = B_{z,0} \exp\left(-\frac{R_c \times t}{L_{coil_{supra}}}\right) = B_{z,0} \exp\left(-\frac{t}{\tau}\right) \quad (24)$$

A rapid discharge was simulated on the two pancakes of the previous paragraph (NI Pancake-100 and NI Pancake-500, parameters in Table II-1 and Table II-2). The initial current I_0 is 10 A.



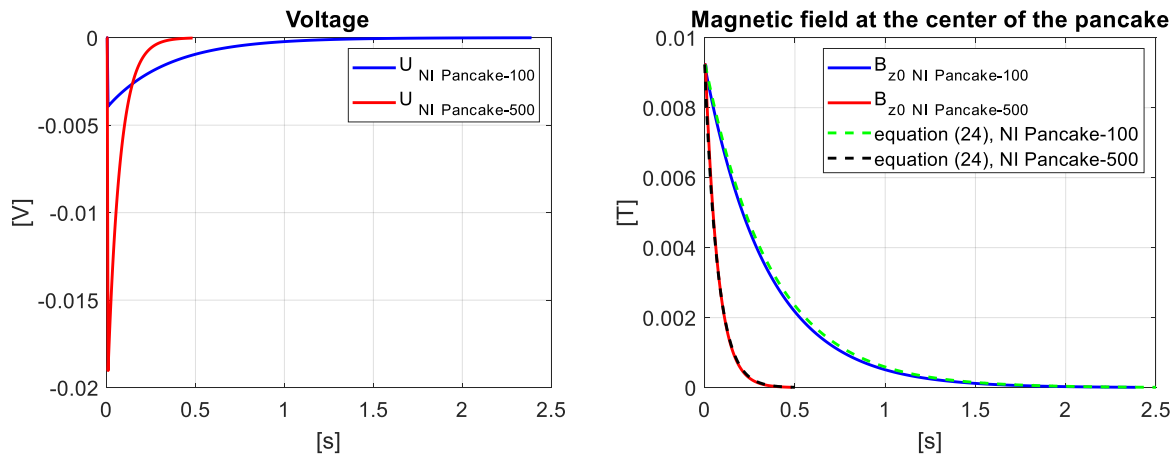


Figure II-25: Average temperature and average azimuthal current; voltage, magnetic induction and approximation of field decay at the center of the two pancakes during rapid discharge; different values of contact resistivity.

When the supply current I_0 becomes zero, the current loops back into the pancake, resulting in a negative voltage across the two pancakes and therefore negative radial currents. A homogeneous radial current during the discharge causes a uniform temperature rise in the whole pancake. Finally, the decrease of the azimuthal current causes an exponential decrease of the field component B_{z0} (Figure II-25). The magnetic energy of the pancake is converted into heat.

Having a low contact resistivity increases the discharge time constant of the pancake. Indeed, with a higher contact resistivity value, $\tau = R_c/L_{coil_{supra}}$ decreases, which causes the pancake to discharge faster. Concerning the temperature increase of the pancake, it is identical whatever the value of the contact resistivity R_{ct} . Indeed, changing the value of the contact resistivity does not change the amount of initial magnetic energy (≈ 7 mJ) that is transferred in heat during the fast discharge.

Through these first simulations, the self-protective character has been simulated for NI and MI pancakes. However, their fast charging and discharging time is higher compared to an insulated pancake. We have seen in the Chapter I that partially insulated pancakes have been experimentally tested in order to obtain a self-protective behavior while having a lower charging time compared to NI/MI pancakes (see I. 3. 3. 3). In the next section, the charging of a PI pancake, as well as its behavior during a local defect, will be the last simulations presented in this Chapter II for a simple pancake.

II. 2. 4 Partial-Insulation simple pancake

Adding electrical insulation between some of the turns of the pancake improves the dynamic response, decreasing for example the charge and discharge time of the pancake while keeping the No-Insulation character between most of the turns of the pancake. However, the thermal stability of the pancake is less pronounced, damage risks are possible with this type of winding [52], [53]. A simple modification of the R_r matrix values is required to simulate the behavior of a partially insulated coil using the PEEC model.

II. 2. 4. 1 Decrease in the charging time constant of the pancake

By adding electrical insulation between some of the turns of the pancake, the radial current when charging the pancake will be partially limited. The current will flow faster in an azimuthal way and not radially. The charging time will be reduced.

In the next simulation, a pancake with the same properties as NI Pancake-100 (parameters in Table II-1 and Table II-2) is again subjected to an increasing supply current I_0 without exceeding I_c . However, in this new simulation, electrical and thermal insulation is added every four turns, as experimentally proposed by Y. H. Choi [53]. The insulation simulated here is comparable to Kapton. A factor of 1.10^{10} is added on the contact resistivity value between the electrically insulated turns. In addition, the value of the thermal conductivity is divided by 100 in order to simulate the thermal behavior of the pancake. Indeed, Kapton is both an electrically and thermally insulating material. Further information and studies concerning the radial thermal conductivity k_r between tapes, with or without insulation, are available in the last chapter of this work: IV. 2. 3. 3.

The equivalent electric circuit of a partially insulated pancake proposed by Y. H. Choi [53] consists of several equivalent electric circuits of a No- or Metal-Insulation pancake in series. The calculation of the time constant is thus more complex.

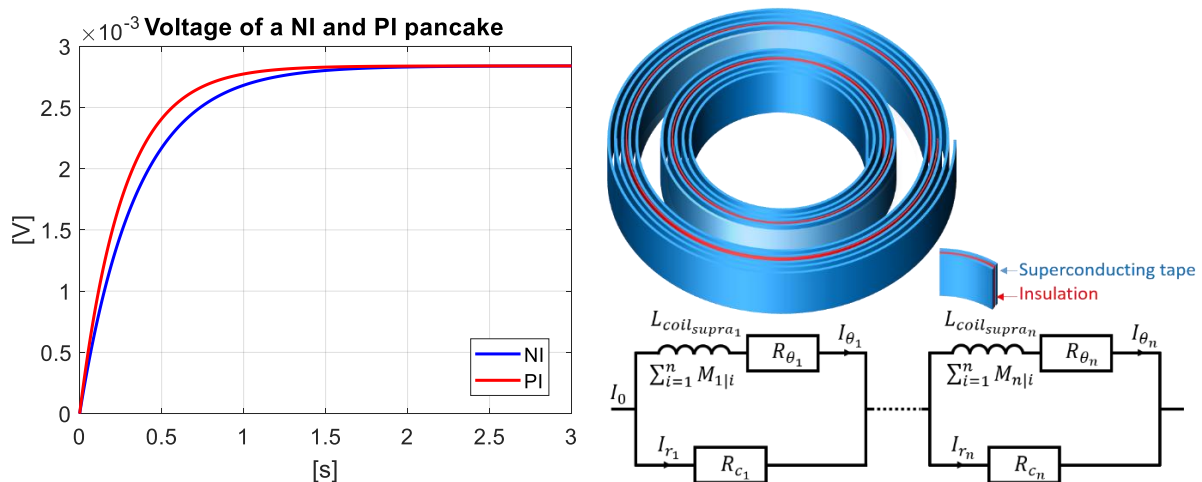


Figure II-26: Simulation of a NI and PI pancake in ramp-up operation; sketch and equivalent electrical circuit of a PI pancake.

In the case of the partially insulated NI Pancake-100, we clearly observe that the introduction of an electrical and thermal insulation between some turns decreases the charging time constant. We pass from a time constant of 340 ms to 263 ms with the addition of the partial insulation (obtained graphically via the simulations presented in Figure II-26). However, adding electrical insulation between some of the turns decreases the thermal stability of the pancake. This is investigated in the following paragraph, where different sectors with a critical current lower than the supply current are deliberately introduced.

II. 2. 4. 2 Behavior of a Partial-Insulation simple pancake during a quench

In the following simulations, the simulated pancake still has the same properties as NI Pancake-100 (properties in Table II-1 and Table II-2). In this simulation, the quench is caused by an instantaneous degradation of 100% on the 20th sector of the 21st turn. The objective here is to understand the current redistribution during a quench when it occurs on a turn electrically isolated from an adjacent turn as it seems to be the weakest location of the protection. For this purpose, in the simulation, an electrical and thermal insulation between two turns of the pancake is added (between 20th and 21st turn). This insulation prevents the current from flowing radially over a full turn in case of a local defect adjacent to the insulation. Thus, depending on the position of the local defect, the azimuthal and radial current redistribution is more or less pronounced: the maximum temperature varies (Figure II-27).

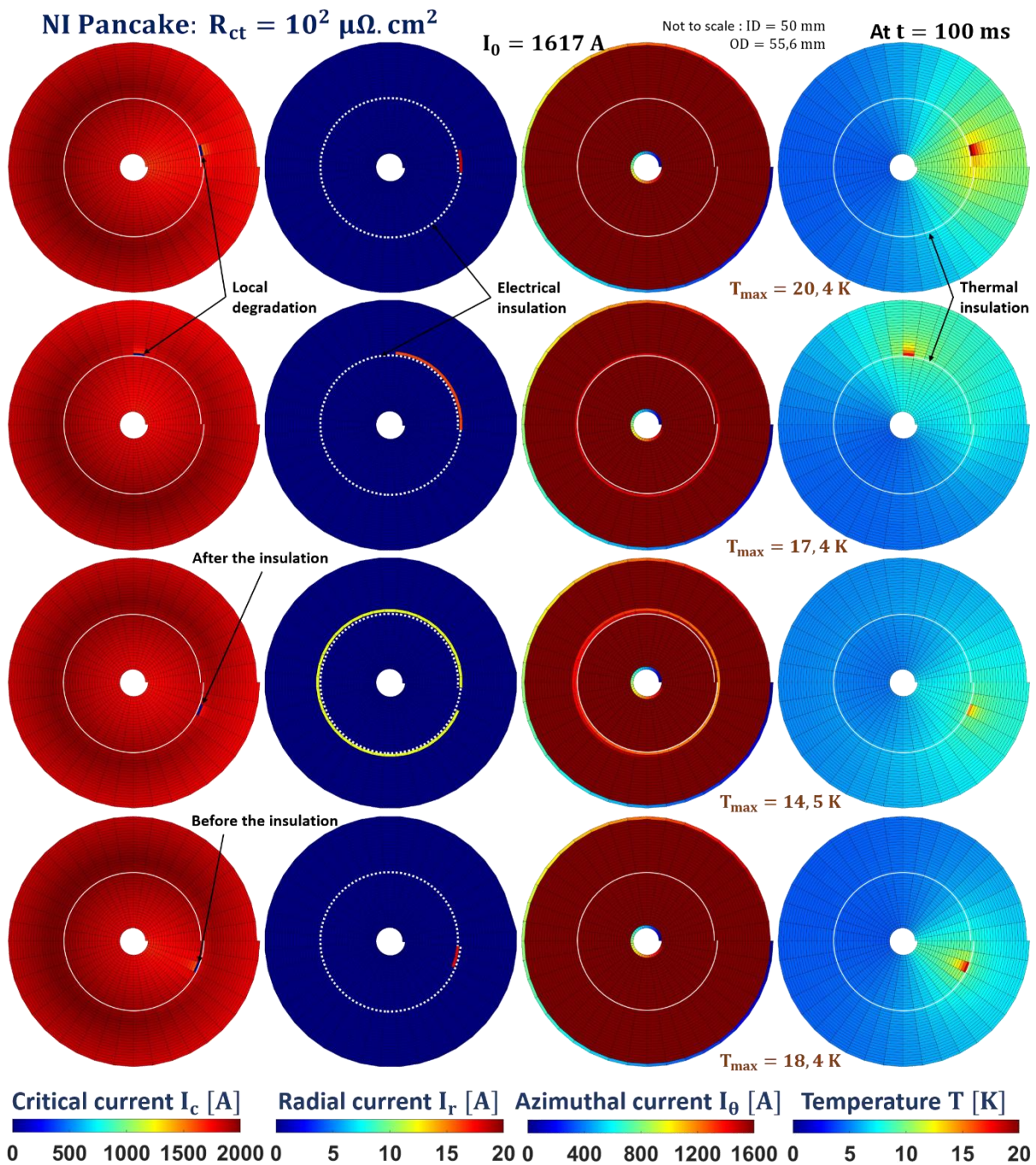


Figure II-27: Critical, radial and azimuthal current and temperature at $t = 100 \text{ ms}$ within a pancake with electrical and thermal insulation as a function of degraded location.

In the case without electrical insulation, the occurrence of a local degradation causes a redistribution of the current allowing the current to bypass the local defect (II. 2. 1. 2). The current redistributes radially and uniformly over a full turn before the degraded zone. Thus, if the local degradation is not adjacent to the insulation between the two turns, then redistribution can still take place without restriction. The current can bypass the local defect. However, adding electrical insulation increases the thermal insulation between the turns. The heat can thus diffuse less, increasing the local temperature of the degraded sector.

In the case where the degraded sector is adjacent to the insulation, the current will not be able to spread radially over a full turn (Figure II-27). The value of the radial current for each sector will increase as the area to pass radially is reduced. This prevents the current from completely

bypassing the degraded sector. Part of the current will continue to flow through the resistivity area, resulting in a higher local temperature rise. Moreover, this temperature increase is also explained by the lower value of the radial thermal conductivity between the two electrically insulated turns.

The closer the degraded area is to the beginning of the electrical insulation, the smaller the area available for current redistribution. This causes a more and more limited current redistribution, but also more radial currents locally, thus generating a higher local temperature (Figure II-27).

Making PI pancake decreases the time constant. However, this deteriorates the thermal stability of the pancake, even creating risk areas by adding electrical insulation on a full turn. Adding electrical insulation between some turns on half turns would reduce these risk areas. However, making PI pancake between turns on half-turns seems complex to achieve.

II. 2. 5 Conclusion

Using the PEEC model, the behavior of an NI/MI simple pancake during ramp-up, ramp-down and rapid discharge was simulated. The model also allows the self-protective behavior of a simple NI/MI pancake during a quench to be studied. In these simulations, the behavior of the simple pancake is greatly influenced by the contact resistivity value. With a low contact resistivity value, the current in the pancake can easily bypass the local defect, making the pancake self-protected but increasing the charging time of the pancake. Conversely, with a higher contact resistivity value, the pancake is less self-protected, but charging time is lower. The contact resistivity value is therefore an important parameter in the behavior of a simple pancake, but also for the behavior of a coil consisting of several NI/MI pancakes. In the third part of this Chapter II, the behavior of a coil consisting of several NI/MI pancakes powered in series during a quench will be analyzed, in particular on the propagation of the quench by magnetic coupling.

II. 3 Simulation of a multi-pancake coil

II. 3. 1 Quench propagation by magnetic coupling

In order to generate higher magnetic fields, it is possible to connect several pancakes in series. In the construction of a multi-pancake coil, the term "double pancakes" is used. The behavior during a quench of a coil consisting of several pancakes without insulation varies greatly depending on the common turn-to-turn contact resistivity between all the pancakes. The behavior of the initially quenched pancake is comparable to section II. 2. 1. In the simulations of this section II. 3, the supply current I_0 is always constant.

In this section, the influence of the contact resistivity on the behavior of a multi-pancake coil will be studied during a quench. For this purpose, two coils with the same properties but different contact resistivity values will be simulated (Table II-4). The pancakes of the first coil have a contact resistivity comparable to NI pancake ($R_{ct} = 900 \mu\Omega.cm^2$), it is called NI Coil. The pancakes of the second coil have a contact resistivity 10 times higher than the first coil ($R_{ct} = 9\,000 \mu\Omega.cm^2$). Although the R_{ct} is rather low compared to values for MI pancakes, it is named MI Coil to better differentiate the two cases. The values of $R_{ct} = 900 \mu\Omega.cm^2$ for the NI Coil and $R_{ct} = 9\,000 \mu\Omega.cm^2$ for the MI Coil were used in the first simulations performed during the thesis. The influence of the R_{ct} value on the behavior of the coil being highlighted with these two values, they have been kept for this part. To simulate the behavior of these two coils, the number of divisions per turn (n_f) is lowered to 10 in order to limit the calculation

time while keeping a certain precision on the local maximum temperature. A study concerning the number of divisions per turn on the PEEC model is available in section IV. 2. 1. 2. 4.

Table II-4: Common parameters of the NI and MI Coil simulated in the case of a quench with introduction of a heat source.

Parameters	Units	Values
Turns (n_a)	—	30
Divisions per turn (n_f)	—	10
Pancakes	—	4
Tape width (h_0)	mm	4
Quench heater element	J	3.75
Convective exchange coefficient (h)	W/m ² /K	0 / 500 / 1 000
Winding inner diameter (ID)	mm	100
Winding outer diameter (OD)	mm	105.6
Current margin	%	5 / 10
Supply current (I_0)	A	394
Initial temperature (T_0)	K	4.2
Coil self-inductance	mH	2.4
Contact resistivity NI Coil (R_{ct})	$\mu\Omega.cm^2$	900
Contact resistivity MI Coil (R_{ct})	$\mu\Omega.cm^2$	9 000

In this section, four simulations are presented:

- NI Coil with a low current margin: II. 3. 1. 1
- MI Coil with a low current margin: II. 3. 1. 2
- MI Coil with a low current margin, but with convective exchange (change of $h = 500$ or 1000 W/m²/K): II. 3. 1. 3
- MI Coil with a high current margin (modification of the current margin to 10%): II. 3. 1. 4

These simulations show the behavior of a coil during a quench as a function of the contact resistivity value, but also as a function of other parameters such as the current margin or the cooling of the coil. The current margin on the load line is a parameter indicating the operating point of the superconducting coil. It is defined by the value of the current versus the magnetic field. If the operating point is below the critical surface, superconductivity is maintained. Having a larger current margin reduces the risk of quenching during operation of the magnet.

II. 3. 1. 1 NI Coil: low contact resistivity, low current margin

II. 3. 1. 1. 1 Behavior during a quench in the NI Coil

The simulation results of the four pancakes of the NI Coil (referenced as A to D from the bottom to the top of the magnet, with $R_{ct} = 900 \mu\Omega.cm^2$) are shown in Figure II-28. A source term is imposed in the 5th sector of the 16th turn of the Pancake A (P_A): the resistive zone spreads and the P_A quenches thermally (with a constant current supply I_0). The current no longer flows azimuthally through the P_A , but mainly radially. The magnetic flux generated by the P_A will therefore decrease. In order to compensate this loss of magnetic flux, the currents in pancakes B (P_B), C (P_C) and D (P_D) re-loop (negative radial current) to increase the value of the azimuthal current I_θ of each pancake. However, the azimuthal current will loop back as it passes radially from one turn to another, generating radial source terms. The increase of the current exceed I_c of the pancakes, leading successively to a thermal overheating of the other pancakes (in the following order: P_A at 30 ms, P_B at 80 ms, P_D at 135 ms and P_C at 170 ms, in Figure II-28).

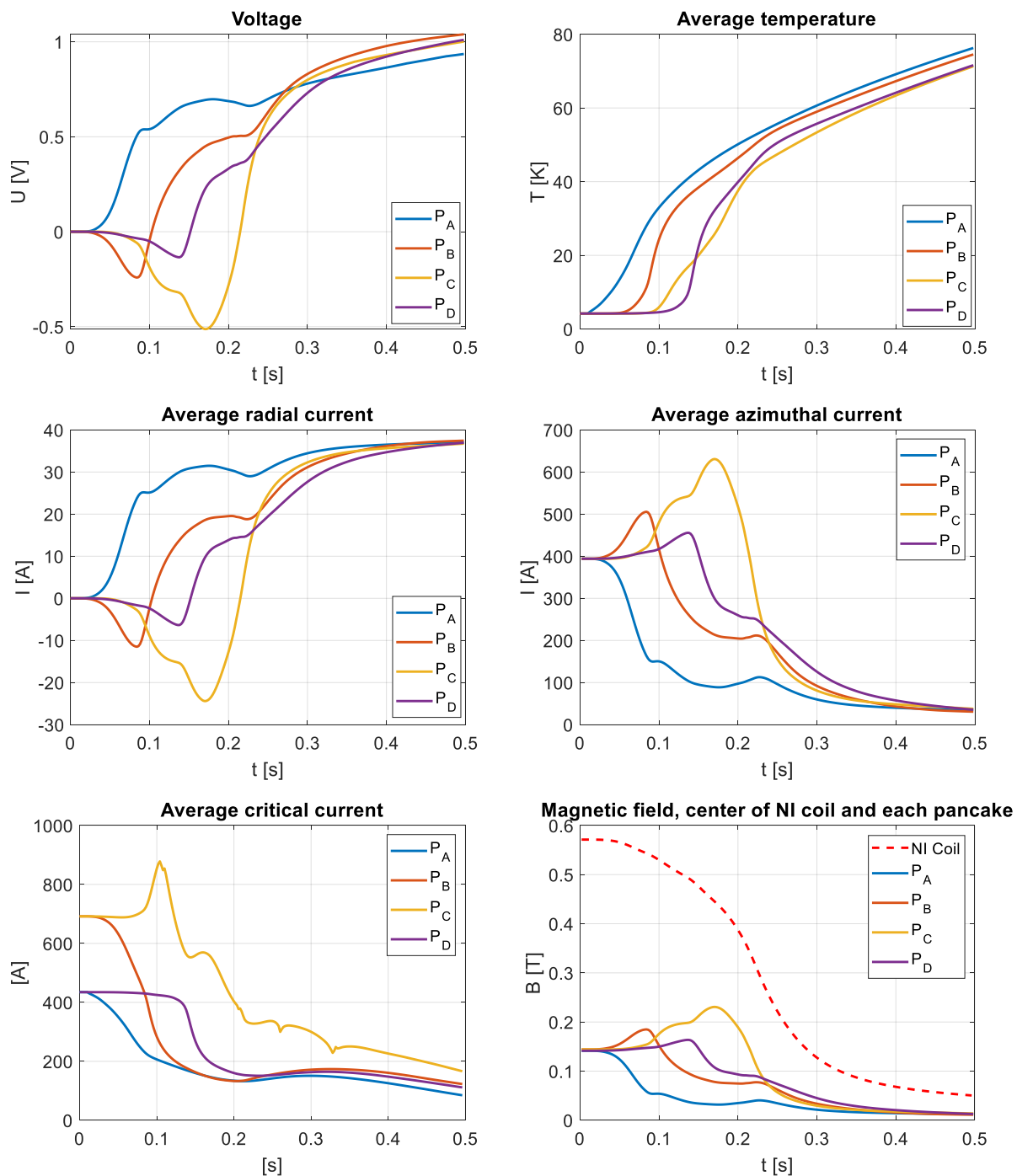


Figure II-28: Voltages; average temperatures; average radial, azimuthal and critical currents of the four pancakes of the NI Coil during a quench, $R_{ct} = 900 \mu\Omega.cm^2$; magnetic field at the center of the NI Coil and the four pancakes.

Note: In the bottom right of Figure II-28, the magnetic field at the center of each pancake is only the field generated by the pancake in question. The field generated by the other pancakes is not taken into account.

Concerning the values of the critical currents of each pancake (Figure II-28), various behaviors are observable:

- $t = 0$ ms: the initial values of the critical currents of the P_B and P_C are higher compared to the P_A and P_D because there is less radial field.

- $0 < t < 50$ ms: the average value of the critical current of the P_A drops rapidly. This is due to the introduction of a source term (at $t = 3$ ms) increasing the local temperature of the pancake.
- $20 < t < 100$ ms: the average value of the critical current of the P_B decreases significantly. This drop is mainly explained by two phenomena: the temperature increase due to the re-looping of azimuthal currents (thus the appearance of radial currents) and the modification of the magnetic field orientation on the conductors of the P_B .

P_A generates less and less magnetic induction since the current flows more and more radially than azimuthally. At $t \approx 100$ ms, P_A generates about ≈ 50 mT, which is small compared to the ≈ 150 mT generated by pancakes B, C, and D (Figure II-28). Approximately, at $t \approx 100$ ms, the magnetic field is mostly generated by pancakes B, C, and D. That is, the orientation of the magnetic field with respect to the surface of the tapes in the coil is changed. Initially, all four pancakes generate a magnetic field. At the center of the tape (depending on its width) of the first turn of the P_B , a non-zero angle α (the field angle from the tape surface) is measurable (Figure II-29). This angle degrades the value of the critical current of the sectors of the first turn of the P_B . At $t \approx 100$ ms, considering that the magnetic induction generated by the P_A is negligible, and thus the magnetic field is generated mainly by the pancakes B, C, and D, the angle between the magnetic field and the tape surface of P_C (at the center of the tape) is zero. If the magnetic field is parallel to the tape surface, then the critical current value for P_C increases at $t \approx 100$ ms (Figure II-12).

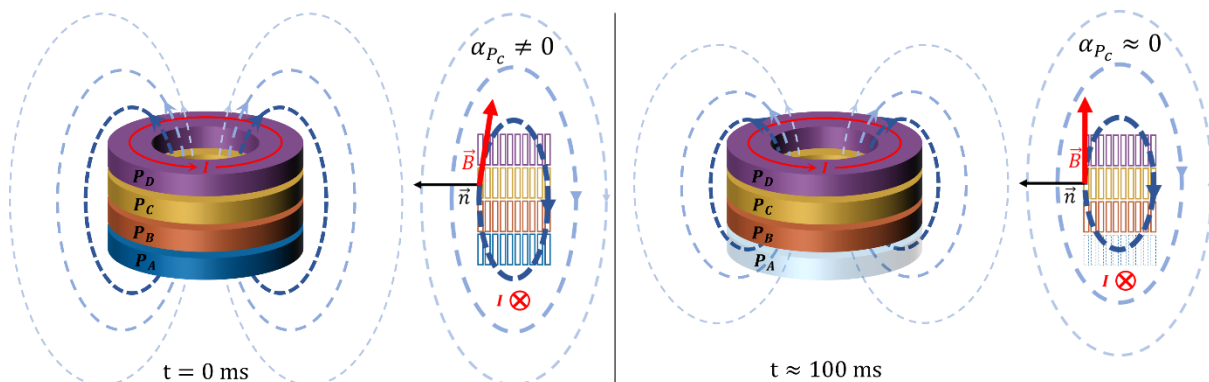


Figure II-29: Modification of the critical current on the tapes of the pancakes with the change of angle between the field and the surface of the tapes.

- $t > 100$ ms: the value of the critical current of the P_C decreases strongly. It is mainly explained by the appearance of radial currents responsible for the increase in temperature of the pancake, thus decreasing its critical current. P_B also generates less and less field, responsible for an angle $\alpha \neq 0$, decreasing the critical current of the P_C .
- $t \approx 135$ ms: P_D quenches. The magnetic induction is partly generated only by the P_C at $t \approx 160$ ms, hence the presence of a weak second peak of the critical current of the P_C in Figure II-28.
- $t > 160$ ms: the increase of the azimuthal current value exceeds the critical current value of the last non-transited P_C , it quenches.

II. 3. 1. 1. 2 Magnetic coupling in the NI Coil

We have seen previously (Figure II-22) that a NI or MI pancake can be assimilated to an equivalent parallel RL circuit. In the case of a coil made of four pancakes, the voltage of pancake i is:

$$U_{P_i} = R_{c_i} I_{r_i} = R_{\theta_i} I_{\theta_i} + \sum_{j=1}^4 \frac{d\phi_{j \rightarrow i}}{dt} \quad (25)$$

With $\phi_{j \rightarrow i}$ the fluxes of the magnetic inductions of the pancakes j through the pancake i , where $i \in L = \{1,2,3,4\}$.

In the initial case of the simulation, the azimuthal current of the pancakes is constant, and the value of the azimuthal resistance is zero. The voltage of the four pancakes is therefore zero.

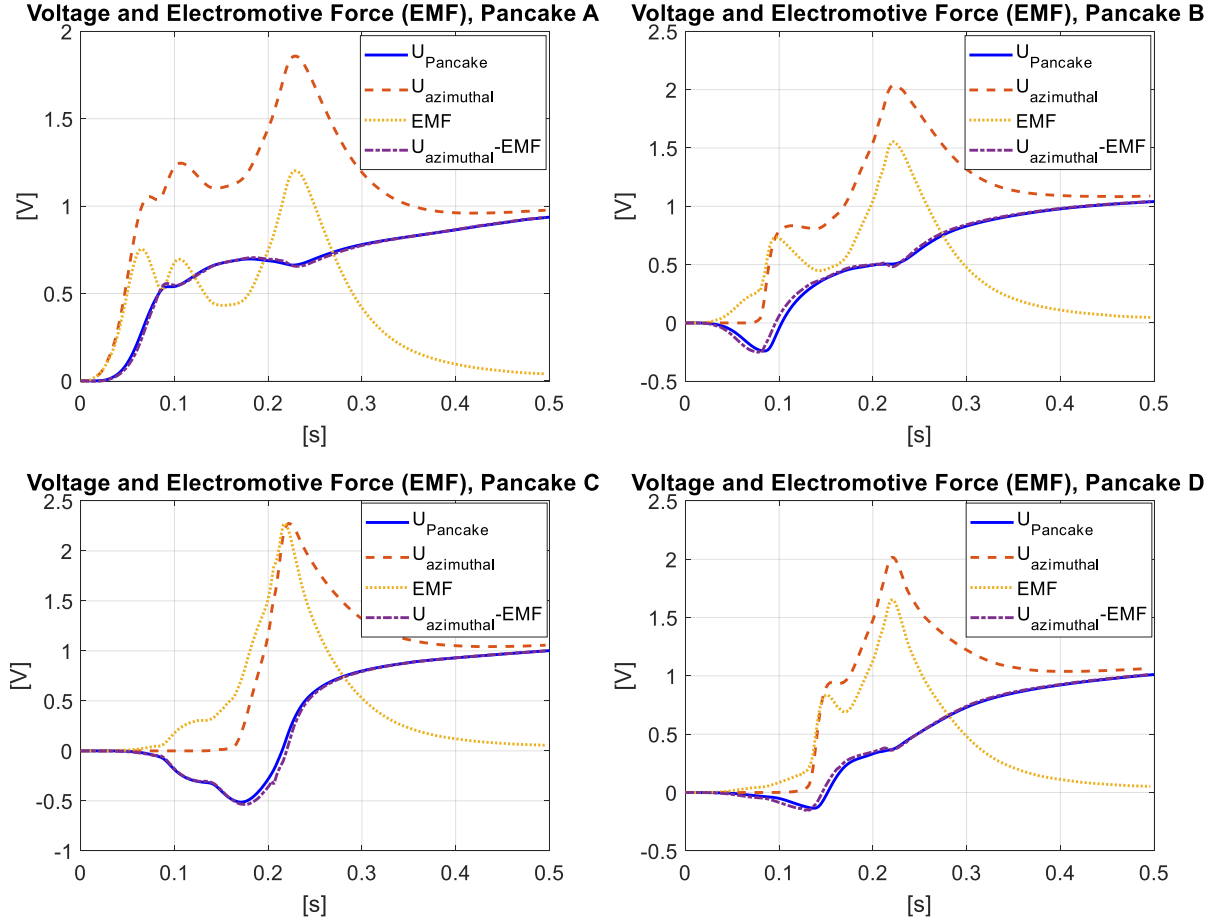


Figure II-30: Electromotive forces (EMF) of the four pancakes of the NI Coil, $R_{ct} = 900 \mu\Omega \cdot cm^2$, current margin at 5%.

In the plots of Figure II-30, several values are superposed for each of the four pancakes of the NI Coil:

- The total voltage across the pancake $U_{Pancake}$.
- The sum of the voltages of the sectors in the superconducting and resistive states $U_{azimuthal}$ (voltages along the turns in the azimuthal direction).
- The electromotive forces EMF (obtained by deriving the magnetic fluxes of each pancake: $EMF_i = -\frac{d\phi_i}{dt}$).
- The voltage $U_{azimuthal} - EMF$

The voltages $U_{Pancake}$ and $U_{azimuthal} - EMF$ are relatively identical. By introducing a source term, the P_A quenches. The current flows radially. Thus, for $25 \text{ ms} < t < 80 \text{ ms}$, the derivatives of the magnetic flux generated by the P_A passing through the surfaces of the pancakes B, C and D ($\frac{d\phi_{A \rightarrow B}}{dt}$, $\frac{d\phi_{A \rightarrow C}}{dt}$ and $\frac{d\phi_{A \rightarrow D}}{dt}$) become negative. This means that $\frac{d\phi_{ext}}{dt} < 0$ which causes a negative voltage for the pancakes B, C and D, and thus positive electromotive forces (Figure II-30). The increase of the azimuthal current in the magnetically coupled

pancakes causes an increase of the self-flux of each pancake, but it is smaller than the decrease of the magnetic flux caused by the quench of the pancake.

As the pancakes quench one after the other, successive changes in the voltage on pancakes B, C and D are observable:

- At $t \approx 40$ ms, the time when P_A quenches, the voltage becomes negative for all three pancakes.
- At $t \approx 80$ ms, the time when P_B quenches, the voltage becomes more negative for P_C and P_D .
- At $t \approx 140$ ms, the time when P_D quenches, the voltage becomes more negative only for P_C .

This phenomenon of quench diffusion by magnetic coupling occurs here because the current margin is low. With a higher current margin (change from 5% to 10% in II. 3. 1. 4), and under the same conditions, the increase in azimuthal current in the Pancake B, C and D not exceed the value of the pancake-specific critical current. The diffusion of the quench by magnetic coupling will not occur. The energy balance for this simulation is available in section II. 3. 2. The contact resistivity value can also limit the diffusion of the quench by magnetic coupling in the case of a coil consisting of several NI pancakes. In order to observe this phenomenon, the same coil with a 10 times higher contact resistivity is simulated in the next section.

II. 3. 1. 2 MI Coil: high contact resistivity, low current margin

II. 3. 1. 2. 1 Behavior during a quench in the MI Coil

The diffusion of the quench by magnetic coupling depends strongly on the contact resistivity R_{ct} . The higher the contact resistivity value, the lower part of current flows radially in the quenched P_A . It leads to a lower magnetic induction decrease and so to a lower increase of the azimuthal current in the other pancakes. In order to evaluate the effect of the contact resistivity, we present the same four pancakes coil but with a 10 times higher contact resistivity R_{ct} , the MI Coil. In the case of a quench, the energy stored in the MI Coil is mainly discharged in P_A and partially in P_B , and not on all the pancakes as seen in the case of the NI Coil. With a higher R_{ct} , the diffusion of the quench by magnetic coupling occurs only on P_B .

In the case of the MI Coil (Figure II-31), the quench caused by the introduction of a heat source on P_A has caused a drop in the magnetic induction generated by the P_A . Since the contact resistivity is higher, the current redistribution within the P_A is lower. The current will flow less radially compared to the simulation of the NI Coil. The decrease in azimuthal current during quenching will be smaller for P_A . Increasing the contact resistivity decreases the electromotive forces and thus reduces the looping of the currents in the pancakes magnetically coupled to the initially quenched pancake. Indeed, the transition of P_A in the case of the NI Coil causes an average azimuthal current rise of about 100 A (Figure II-28); while in the case of the MI Coil, the average azimuthal current rise is about 20 A (Figure II-31). This azimuthal current rise, combined with the heating of the pancakes by the appearance of radial currents, is sufficient to cause the P_B to quench, but too low to spread the quench to the P_C and P_D . This is why in this simulation, only the value of the voltage, the average temperature, and the average radial current increases for P_A and P_B . P_C and P_D did not quench. At $t = 0.9$ s, their voltage and radial current are zero, the average azimuthal current is equal to the supply current I_0 , the magnetic induction generated by the P_C and P_D is identical to that before quench. Two slight increases in temperature are visible on these two pancakes. These are due to the electromotive forces generated by the successive transition of the P_A and P_B .

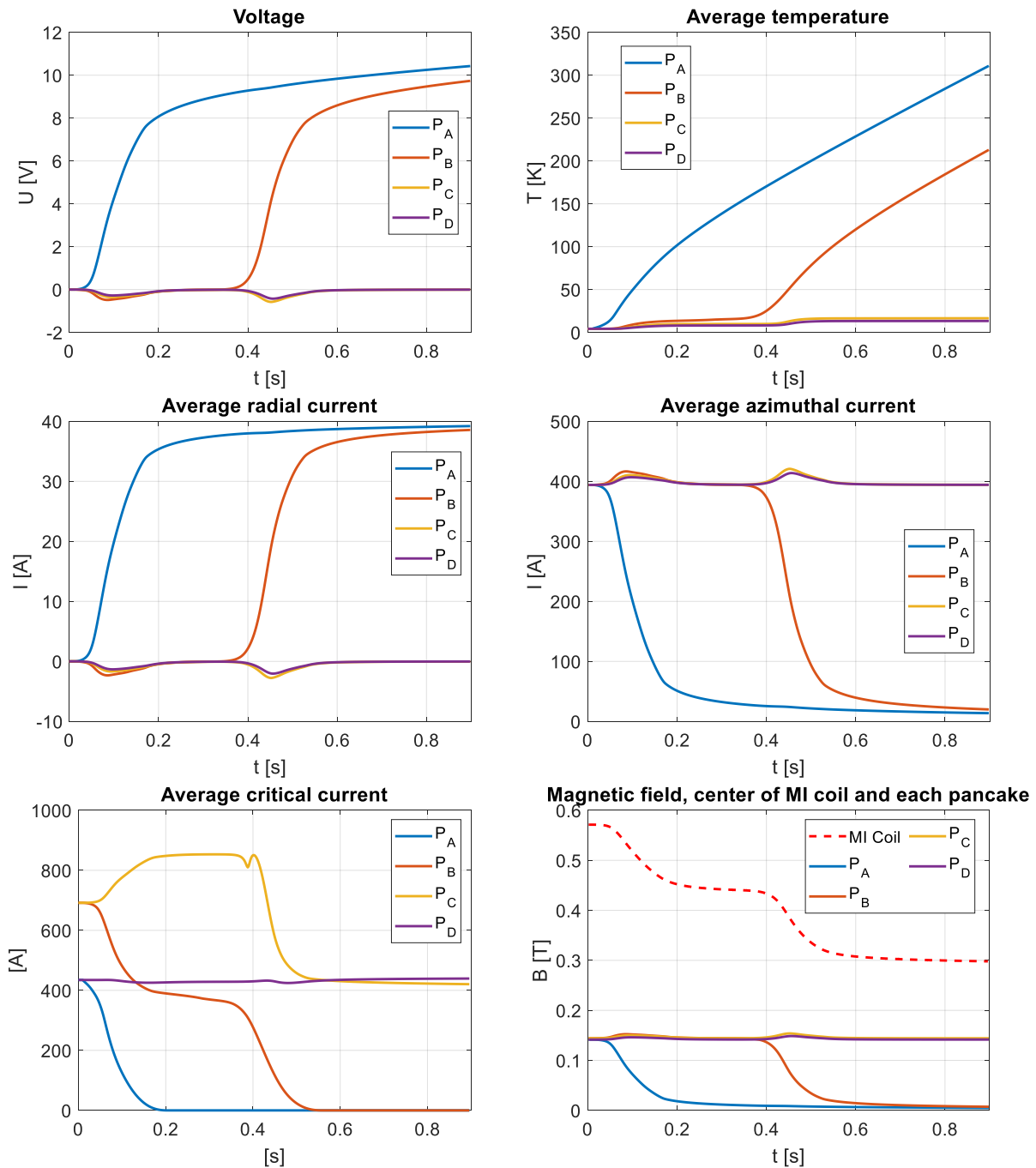


Figure II-31: Voltages; average temperatures; average radial, azimuthal and critical currents of the four pancakes of the MI Coil during a quench, $R_{ct} = 9\,000\ \mu\Omega\cdot\text{cm}^2$; magnetic field at the center of the MI Coil and the four pancakes.

In the case of the simulations of the two coils, the inductive voltage value of P_B with low contact resistivity is approximately equal to the inductive voltage of P_B with high contact resistivity (during the transition of P_A): $U_{P_B-R_{ct}=900} \approx -0.25\ \text{V}$ and $U_{P_B-R_{ct}=9000} \approx -0.5\ \text{V}$ (Figure II-28 and Figure II-31). With a higher contact resistivity value, the radial current value will be less important and thus a smaller increase in azimuthal current, which will limit the exceeding of the critical current. In addition, less radial current causes a lower temperature rise in P_B (Figure II-32). The other pancakes will be more difficult to quench. In the case of Figure II-31, the temperature rise is less rapid for P_B , which delays its thermal overheating.

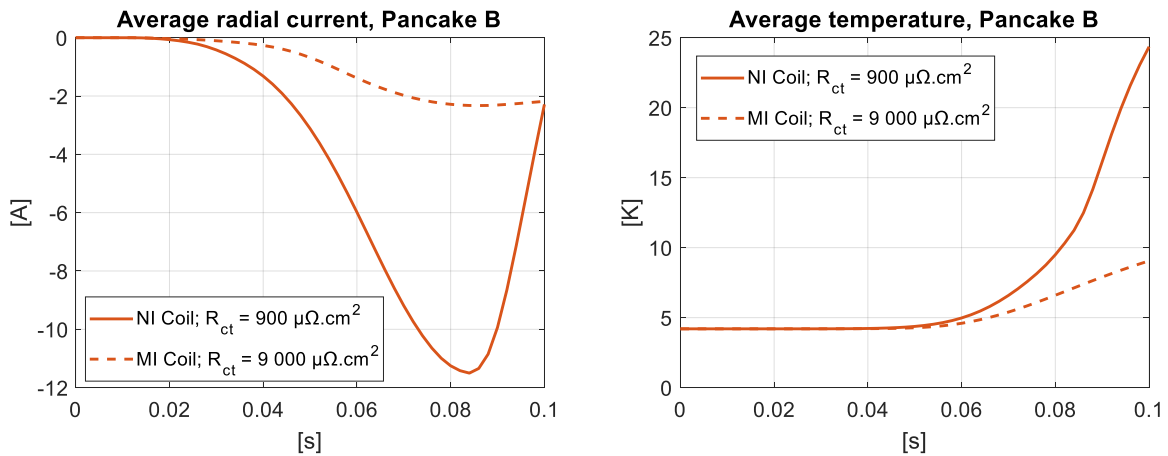
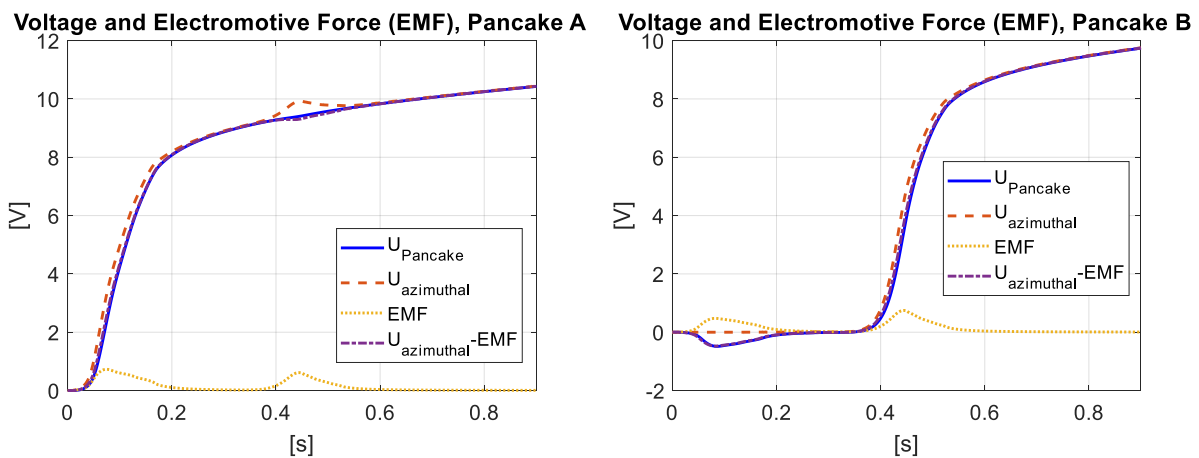


Figure II-32: Overlay of the average temperatures and average radial currents of the Pancake B during a quench, $R_{ct} = 900 - 9\,000 \mu\Omega.cm^2$.

II. 3. 1. 2. 2 Magnetic coupling in the MI Coil

For the MI Coil, the behavior of the quench diffusion by magnetic coupling, only on P_B , is clearer. Taking up the values of the critical currents (bottom left of the Figure II-31), three distinct phases are observable:

- **10 ms < t < 200 ms:** the P_A quenches after the introduction of the source term. The current flows more and more radially. It generates less and less magnetic induction.
- **200 ms < t < 400 ms:** the P_B , P_C and P_D are the only ones to generate a magnetic field. We find ourselves in the situation of Figure II-29: the orientation of the magnetic field is parallel to the surface of the tapes of the P_C . The value of the critical current is thus more important for this pancake. Pancakes B and D have approximately the same critical current values, due to the symmetry of this model coil. The increase in temperature and the modification of the orientation of the field on the conductors are responsible for the decrease of the critical current of the P_B between $t = 10$ ms and $t = 200$ ms.
- **t > 400 ms:** the drop in critical current causes a quench of P_B which generates new electromotive forces in the P_C and P_D (Figure II-33). The transition of the P_A and P_B cause both temperature increases. Since the critical current value of the P_C and P_D is larger than the supply current value I_0 (constant), both pancakes do not quench.



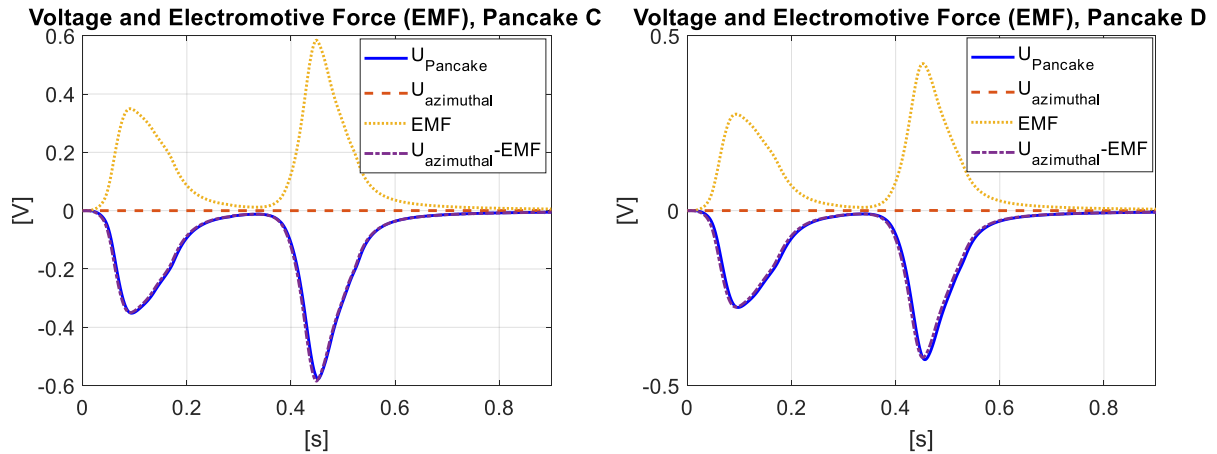


Figure II-33: Electromotive forces of the four pancakes of the MI Coil, $R_{ct} = 9\,000\ \mu\Omega.cm^2$, current margin at 5%.

The two successive peaks of EMF in Figure II-33 at $t \approx 0.1\text{ s}$ and $t \approx 0.45\text{ s}$ are responsible for the two successive increases in temperature of the P_C and P_D . Thus, having a diffusion of the quench by a magnetic coupling between the pancakes allows to distribute the magnetic energy on the whole coil during a thermal overheating. Having the energy distributed within the whole coil reduces the temperature increase in a simple pancake, which would be the only one to pass through. The energy balance for this simulation is available in section II. 3. 2.

So far, we have studied the influence of the contact resistivity on the behavior of the coil during a quench. As a reminder, the simulated NI and MI Coils are under adiabatic conditions. We will now study the effect of the convection cooling, but only on the MI Coil.

II. 3. 1. 3 MI Coil: high contact resistivity, low current margin and convection cooling

Previously, we have seen that decreasing the contact resistivity value allows to limit the propagation of the quench to the other pancakes of the coil. In the case of MI Coil, P_B has quenched due to an increase in temperature and an azimuthal current exceeding the critical current value. Taking into account a convective exchange between the coil and the cryogenic fluid, the temperature increase of the P_B will be less important, which will prevent the diffusion of the quench to the P_B . In this section, the influence of convective cooling (see II. 1. 2. 1) will be studied on MI Coil. All parameters are identical to section II. 3. 1. 2 (Table II-4). Only the value of the convective exchange coefficient becomes non-zero.

By simulating a convective exchange between MI Coil and the cryogenic fluid, the average temperature of the pancakes will increase less during the transient regime, causing the critical current to decrease to a smaller extent. In the case of the previous simulation, by adding a convective exchange $h = 500$ or $1000\text{ W/m}^2/\text{K}$ (values based on R. V. Smith measurements [79], [80]), the average temperature of the P_B has a smaller increase, which results in a higher average critical current (Figure II-34) compared to the simulation without convective exchange.

The transition of the P_A generates an inductive voltage across the P_B , which causes an increase in the azimuthal current. In the case of convection cooling, the value of the azimuthal current is lower than the critical current of the P_B . The azimuthal current does not exceed the critical current value in the case of P_B , so the azimuthal resistances generate no heat source, which does not lead to a thermal overheating of the P_B with a convective exchange $h = 500$ or $1000\text{ W/m}^2/\text{K}$ (Figure II-34).

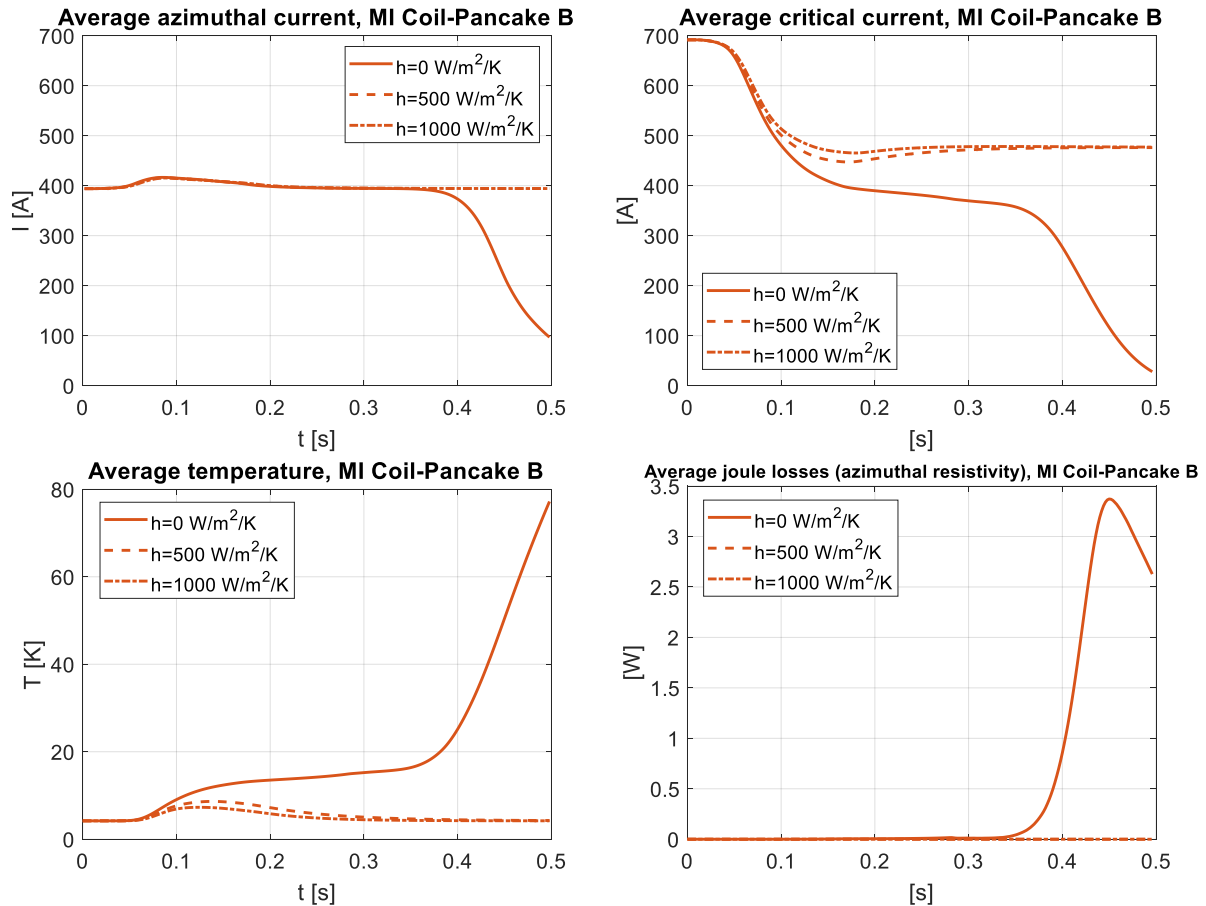


Figure II-34: Azimuthal and critical average currents only of the MI Coil-Pancake B during a quench, average temperatures, joule losses by generated by azimuthal resistivity; $R_{ct} = 9\,000\ \mu\Omega\cdot\text{cm}^2$ with different convective exchange.

In Figure II-34, it can be seen that part of the P_B without convective exchange becomes resistive at $t \approx 0.3$ s. Indeed, the average value of the joule losses generated by the azimuthal resistances increases and has a peak at $t \approx 0.45$ s. In the case of convective cooling, no Joule loss through the azimuthal resistance is observable, the pancake remains entirely in a superconducting state. The critical current of the P_B in the case of convective cooling is still noticeable. The transition of the P_A generates different flux lines, the angle between the field orientation and the tape surface of the P_B is larger. This is the main reason for the drop in the critical current. This decrease can also be explained by the increase in temperature of the P_B caused by the presence of radial currents. However, as the pancake is cooled, it returns to its initial temperature ($T_0 = 4.2$ K), which explains the slight rise in the average critical current after $t \approx 0.2$ s. Thus, keeping the same simulation parameters, but only adding convective exchange over the entire coil, the quench does not diffuse to the P_B . Only P_A quenches.

A final parameter prevents the diffusion of the quench by magnetic coupling to the P_B in the case of the MI Coil. This is the current margin. We will see that with this larger current margin, the quench does not diffuse to the P_B . This is the subject of this last section.

II. 3. 1. 4 MI Coil: low contact resistivity, high current margin

In the previous paragraphs, we have seen that it is possible to limit the diffusion of the quench by magnetic coupling to the other pancakes by increasing the contact resistivity and by taking into account a convective exchange between the coil and the cryogenic environment. High current margin also prevents a thermal overheating of the pancake when a local heat source is introduced into a pancake. Magnetically coupled quench diffusion occurs when the azimuthal

current value exceeds the critical current value of the magnetically coupled pancakes to the voluntarily quenched pancake. For this simulation, all parameters are identical to paragraph II. 3. 1. 2 (Table II-4). The coil simulated here is the MI Coil. The current margin magnitude is the only difference from previous simulations: it was 5%, while here it is set to 10%.

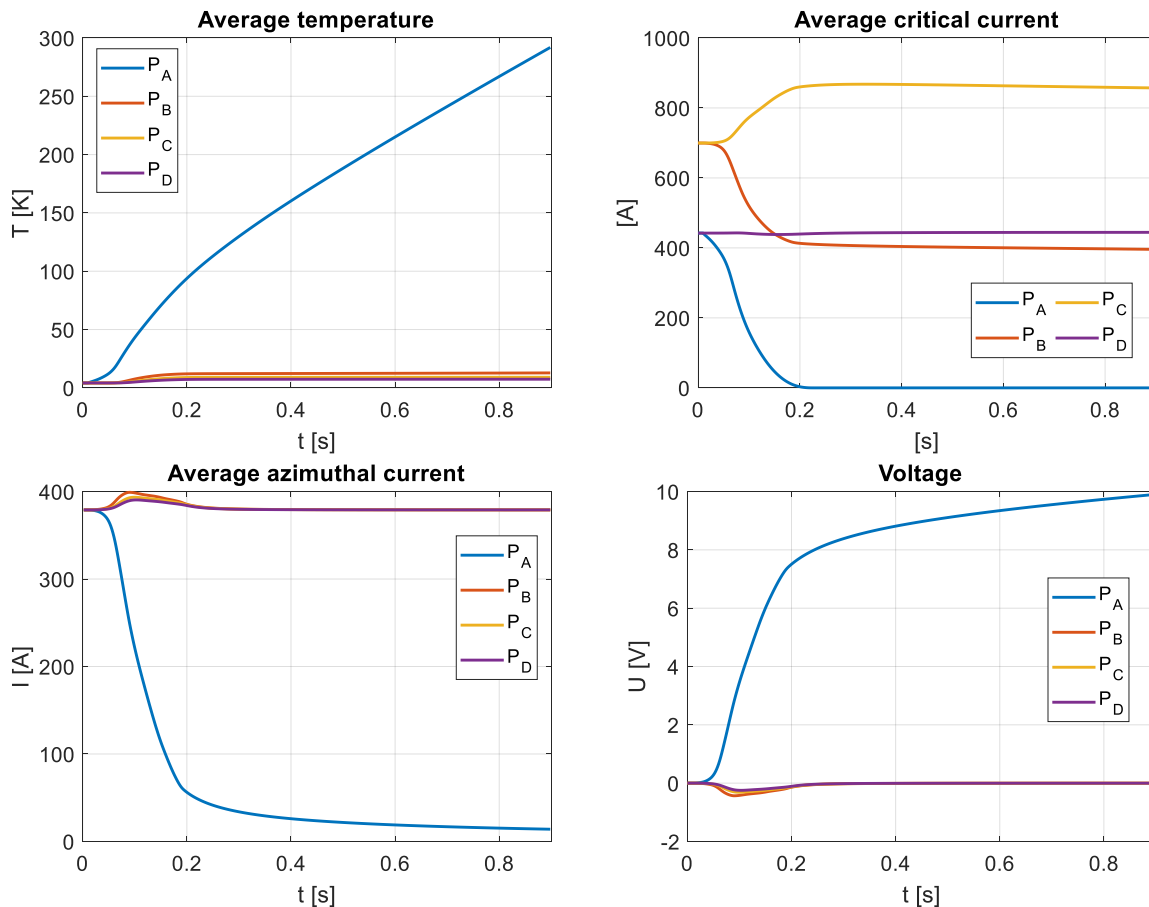


Figure II-35: Average temperatures; critical and azimuthal average currents of the four pancakes of the MI Coil during a quench, $R_{ct} = 9\,000\ \mu\Omega\cdot\text{cm}^2$ without convective exchange and with a high current margin ($I_0 = 0.9 I_c$).

The results of the simulation are available in Figure II-35. In this simulation, a source term is imposed, the maximum temperature of the P_A increases, which decreases the local critical current. The value of the azimuthal current of the heated sector is higher than the value of the critical current, so a redistribution of the current occurs and P_A quenches. The quenching of P_A generates EMF on the magnetically coupled pancakes. This causes an increase in azimuthal currents. However, with a larger current margin, the critical current of P_B is higher. The value of the azimuthal current of P_B remains below its critical current so P_B does not quench. The temperature, voltage, critical and azimuthal current of P_B become constant at $t = 0.3$ s. The behavior of the other pancakes has not been greatly modified with the introduction of a heat source on a sector of P_A .

Operating with a high current margin has two main effects:

- Reducing the risk of thermal overheating during a local defect in the coil.
- The critical current is less likely to be exceeded due to the increase in azimuthal current following an inductive voltage. The propagation of a quench by magnetic coupling will thus be more limited.

Thus, having a high current margin allows to limit the quench phenomenon. In return, the performance of the magnet is reduced. The MI Coil with a 5% current margin generates about 0.57 T at the center of the coil, compared to about 0.55 T with a 10% current margin.

Through these simulations, we have seen that several parameters influence the behavior of the coil during a quench. This is the case for the current margin, the convective cooling and especially the contact resistivity value. Depending on these parameters, the magnetic energy of the coil is converted into heat in itself. However, in some cases, the energy is dissipated either in the whole coil or only in one or more pancakes. The local maximum temperatures are therefore different. An energy balance on the previous simulations was carried out. The results are presented and available in the following section: II. 3. 2.

II. 3. 2 Energy balance

The energy balances of the simulations of NI and MI Coil with a low current margin (II. 3. 1. 1 and II. 3. 1. 2) and of the simulation of the MI Coil with a high current margin (II. 3. 1. 4), are available in Table II-5.

In this table, we find:

- The value of the magnetic energy of each pancake at the initial and final times of the computation.
- The magnetic energy of the coil at the initial and final times of the computation.
- The energy dissipated by Joule effect of each pancake at the final time of the computation.
- The average and maximum local temperatures of each pancake at the final time of the computation.
- The proportion of energy dissipated in each pancake at the final time of the computation.
- The energy from the power supply and the heat source.
- The energy balance at the initial and final states.

→ The magnetic energy of each pancake is obtained using the self and mutual inductances and azimuthal currents I_θ flowing in each sector of the coil. As a reminder, for a coil consisting of four identical pancakes, $M_{4P} \in M_{4n_a \times n_f}(\mathbb{R})$:

$$M_{4P} = \begin{pmatrix} M_{P_1|P_1} & M_{P_1|P_2} & M_{P_1|P_3} & M_{P_1|P_4} \\ M_{P_2|P_1} & M_{P_2|P_2} & M_{P_2|P_3} & M_{P_2|P_4} \\ M_{P_3|P_1} & M_{P_3|P_2} & M_{P_3|P_3} & M_{P_3|P_4} \\ M_{P_4|P_1} & M_{P_4|P_2} & M_{P_4|P_3} & M_{P_4|P_4} \end{pmatrix}$$

With $M_{P_l|P_k} = M_{P_k|P_l}, \forall l, k \in \{1, 2, 3, 4\}$, where $M_{P_l|P_k}$ is the submatrix of M_{4P} grouping the self and mutual inductances between the sectors of the pancake l with those of the pancake k . The magnetic energy of the pancake P_i at time t , with $i \in \{1, 2, 3, 4\}$, is:

$$E_{mag_{P_i}}(t) = \begin{cases} \left((M_{P_i|P_1} & M_{P_i|P_2} & M_{P_i|P_3} & M_{P_i|P_4}) \times I_\theta^2(t) \right) / 2 \\ \sum_{j=1}^{n_a \times n_f} \sum_{k=1}^{4n_a \times n_f} M_{k|j} \times \left(I_\theta^k(t) \right)^2 / 2 \end{cases} \quad (26)$$

With $I_\theta(t) \in \mathbb{R}^{4n_a \times n_f}$, the column vector of azimuthal currents in the coil at time t .

→ The energy dissipated by Joule effect by the pancake P_i during a time t_f is obtained by:

$$E_{J_{P_i}}(t_f) = \int_0^{t_f} \sum_{j=1}^{n_a \times n_f} S_{P_i}(t) \cdot dt \quad (27)$$

With S_{P_i} the source term from the azimuthal resistance R_θ and contact resistivity R_{ct} .

→ The energy delivered by the power supply during a time t_f is:

$$E_{PS}(t_f) = \int_0^{t_f} U_{coil}(t) \times I_0 \cdot dt \quad (28)$$

The total energy in the initial state in Table II-5 is the sum of the magnetic energy in the coil, the energy of the heat source, and the energy supplied by the power supply. The total energy in the final state is the sum of the remaining magnetic energy in the coil and the Joule energies dissipated from the four pancakes.

In the case where the current margin is 5%, the energy balance differs depending on the contact resistivity value. Indeed, in the previous sections (II. 3. 1. 1 and II. 3. 1. 2), the quench diffusion by magnetic coupling takes place on P_B , P_C and P_D when $R_{ct} = 900 \mu\Omega \cdot \text{cm}^2$ (NI Coil), but only at P_B when $R_{ct} = 9\,000 \mu\Omega \cdot \text{cm}^2$ (MI Coil). In the case of low contact resistivity, the energy stored in the coil is distributed almost uniformly throughout the four pancakes ($\approx 25\%$ per pancake) during the quench. The temperature rise of the four pancakes is relatively the same (local maximum temperature T_{max} of about 120 K for each pancake, available in Table II-5).

In the case where the contact resistivity is higher ($R_{ct} = 9\,000 \mu\Omega \cdot \text{cm}^2$) with 5% current margin, the magnetic energy stored in the coil and the energy supplied by the power supply discharges mainly in P_A (65%) and partly in P_B (35%). Therefore, the temperature increase is larger for P_A ($T_{max} \approx 410$ K) and for P_B ($T_{max} \approx 290$ K), while the temperature increase for P_C and P_D is relatively small ($T_{max} \approx 15$ K). In both simulations (II. 3. 1. 1 and II. 3. 1. 2), the magnetic energy and the energy supplied by the power supply was mainly converted into heat within the coil. Having a low contact resistivity improves the distribution of the stored energy in the case of a coil during a quench. This avoids a local increase in temperature that could locally and irreversibly deteriorate the value of the critical current.

Table II-5: Energy balance of the NI and MI Coil; influence of the contact resistivity and the current margin.

R_{ct} [$\mu\Omega \cdot \text{cm}^2$]	NI Coil: 900		MI Coil: 9 000		MI Coil: 9 000		900	9 000	9 000	
Current margin [%]	5		5		10		5	5	20	
Time [s]	0	0.5	0	0.9	0	0.9	0.5	0.9	0.5	
Magnetic energy in P_A [J]	44.2	0.5	44.2	16.1	40.9	26.0	T_{max} local P_A [K]	124.0	408.0	212.2
Magnetic energy in P_B [J]	49.2	0.6	49.2	21.1	45.5	34.4	T_{max} local P_B [K]	115.6	287.0	10.3
Magnetic energy in P_C [J]	49.2	0.6	49.2	28.4	45.5	37.4	T_{max} local P_C [K]	131.3	16.5	7.7
Magnetic energy in P_D [J]	44.2	0.5	44.2	28.4	40.9	34.4	T_{max} local P_D [K]	112.5	13.3	6.5
Magnetic energy of the Coil [J]	186.8	2.2	186.8	94.0	172.8	132.2				
Energy dissipated, Joule effect P_A [J]	0	156.4	0	2937.4	0	2655.7	Part of energie dissipated P_A [%]	26.3	65.1	99.9
Energy dissipated, Joule effect P_B [J]	0	154.3	0	1566.3	0	0.8	Part of energie dissipated P_B [%]	26.0	34.7	0.0
Energy dissipated, Joule effect P_C [J]	0	139.5	0	1.4	0	0.4	Part of energie dissipated P_C [%]	23.5	0.0	0.0
Energy dissipated, Joule effect P_D [J]	0	136.8	0	0.9	0	0.3	Part of energie dissipated P_D [%]	23.0	0.0	0.0
Energy of the heat source [J]	3.8		3.8		3.8		T_{av} P_A [K]	76.3	310.9	164.9
Energy of the power supply [J]	406.0		4413.6		2614.3		T_{av} P_B [K]	74.5	212.9	10.2
Total energy, initial state [J]	596.6		4604.2		2790.9		T_{av} P_C [K]	71.3	16.5	7.7
Total energy, final state [J]	589.2		4600.0		2789.4		T_{av} P_D [K]	71.6	13.3	6.5

In the case of the simulation with a high current margin (10%), the initial magnetic energy stored in the coil is lower (172.8 J versus 186.9 J in the case of a 5% current margin).

In addition, the larger current margin avoided P_B to quench. The coil voltage is therefore lower compared to the simulation with a 5% current margin. The energy injected by the power supply is lower (2612.3 J with a 10% current margin, compared to 4413.6 J with a 5% current margin). The sum of the magnetic and power supply energy is thus lower for the case with a 10% current margin. This is why the maximum temperature of P_A is lower ($T_{max} \approx 210$ K), although it is the only one to quench, compared to the case with the 5% current margin ($T_{max} \approx 410$ K) where both P_A and P_B quench.

II. 3. 3 Conclusion multi-pancake coil

The PEEC model developed during this thesis allows to simulate the behavior of a coil consisting of several pancakes in series and to study the influence of the contact resistivity R_{ct} . The lower the value, the more magnetic energy is dissipated as heat in the pancakes during a quench. This reduces the risk of excessive local temperatures that could cause local damage to the coil. However, as in the case of a simple pancake, if the contact resistivity is too low, the charging time becomes significant. This type of model therefore allows the contact resistivity value to be optimized according to the geometry of a coil made up of several NI/MI pancakes, with the aim of protecting it as well as possible during a quench.

A model for NI-MI simple racetrack has also been implemented in the code. This geometry is presented in the next and last part of this Chapter II.

II. 4 Simulation of a simple racetrack coil

The objective of this section is to simulate other types of geometry than pancakes. The principle for simulating a simple racetrack coil subjected to a quench is broadly the same as for a simple pancake coil. The electrical ode system is strictly identical (II. 1. 1. 3). The thermal ode system is solved in Cartesian coordinates for straight sections and in cylindrical coordinates for half-turns (II. 1. 2. 2). The major difference between the racetrack and the pancake case is in the values of the mutual inductance between thin sectors, due to the presence of straight sections. Thus, the mutual inductance between two thin straight sectors; two thin non-coaxial angular sectors; and between a thin straight sector and a thin angular sector has been calculated numerically (II. 1. 3. 3). Modifications have been made to the electrical and thermal equations, as well as to the magnetic induction in the case of a thin straight sector in order to calculate the total magnetic induction generated by the racetrack. The parameters for the simulation of a quench in a simple racetrack are available in Table II-6.

Table II-6: Simulated simple racetrack parameters in the case of a quench with the introduction of a heat source and with convective cooling.

Parameters	Units	Values
Turns (n_a)	—	30
Divisions per half turn (n_{fc})	—	16
Divisions per straight section (n_{fd})	—	10
Divisions per turn $n_{st} = 2(n_{fc} + n_{fd})$	—	2(16 + 10)
Tape width (h_0)	mm	6
Quench heater energy	J	8
Convective exchange coefficient (h)	W/m ² /K	1000
Winding inner (ID) and outer (OD) diameter	mm	100 – 104.2
Length right section (L)	mm	200
Supply current (I_0)	A	1000
Initial temperature (T_0)	K	4.2
Coil self-inductance	mH	0.49
Contact resistivity (R_{ct})	$\mu\Omega\cdot\text{cm}^2$	10 000

In this simulation in Figure II-36, the source term generates a local increase of the temperature, leading to a redistribution of the current within the racetrack. The observed behavior is similar to that of a simple pancake: the higher the contact resistivity R_{ct} , the higher the local

temperature. For more information on the behavior and redistribution of the current during a quench, refer to the paragraph concerning a quench in a simple pancake (II. 2. 1).

This paragraph is mainly an opening on the possibilities of the PEEC model. This type of simulation shows that this simulation method is not only intended for pancake geometries. By knowing the expression of the mutual inductance between sectors with complex geometries, it is possible to reproduce the electrical circuit of any geometry of a superconducting coil (No- or Metal-Insulation). As the work in this thesis does not have the direct objective of simulating coils made of racetracks, simulation work concerning a racetrack, or other geometries, has not been further developed.

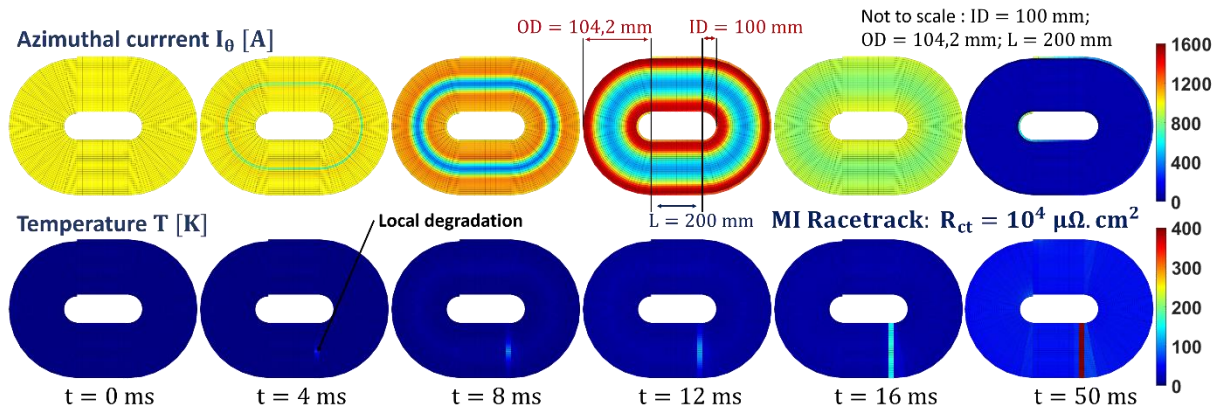


Figure II-36: Evolution of temperatures and azimuthal currents as a function of time in a racetrack during a quench.

This code can of course be developed and improved in order to simulate the behavior of a coil made up of several racetracks during a quench, a charging or during a fast discharge. The method to be applied is the same as the one used for a simple or multi-pancake. However, with the presence of straight sections in this geometry, the number of sectors per turn is more important, increasing the computation time. To study a complete magnet, a modification of the resolution method is necessary in order to decrease the computation time (FMM for example).

II. 5 Conclusion

A complete magneto-thermo-electric model has been greatly improved and used to observe and understand the phenomenon of current redistribution in coils of several types (pancake, multi-pancakes and racetrack coil) during a quench and transients of the current (ramp-up, ramp-down, abrupt cut in the supply current). As explained in this chapter, the contact resistivity value plays an important role in the behavior of these NI-MI coils. It strongly influences the quench dynamic in a pancake, making it less susceptible to local burnings. The optimal contact resistivity depends on the geometry of the coil but also on the protection method used. There is no ideal value for any type of geometry. Our multi-pancake PEEC model allows us to include this critical parameter in the design phase of a specific magnet and find the best technological solution for each application.

In this Chapter II, a passive protection has been simulated. In reality, during a quench in a coil, the value of the supply current does not remain constant, which is the case in the previous simulations. During a local defect, an active protection with a discharge resistance can be used. Another method is to realize a passive protection to make the magnet self-protected. A self-protected magnet means that the electrical circuit is not modified to actively or passively protect the magnet. The idea is to use the high voltage in an MI coil during a quench to passively protect the magnet during the transient. The principle is to consider the power supply as a voltage

source when the coil is quenching. The behavior of a coil during a quench with passive protection with voltage limitation is the subject of the Chapter IV.

Through this Chapter II, we have seen that it is possible to make a pancake self-protected depending on the contact resistivity value between the superconducting tapes. This contact resistivity value is studied experimentally in the next chapter.

Chapter III

Understanding and control of the contact resistivity between HTS tapes

In order to have a reasonable charging time and to protect the magnet as well as possible, the value of the contact resistivity between turns (R_{ct}) must be controlled. In this Chapter III, a literature review of contact resistivity measurements, mainly in NI and MI, is presented in the first part.

In a second part, I present my experimental setup allowing measuring the contact resistivity between No-Insulation (NI) 6 mm HTS superconducting tapes cooled at 77 K in a liquid nitrogen bath, as a function of the mechanical stress. Then, I introduce the different types of winding pack measured in addition to NI: Metal-Insulation (MI), Soldered No-Insulation (SNI), Soldered Metal-Insulation (SMI) and double Metal-Insulation (2xMI). These technologies are tested with superconducting tapes from different manufacturers: SuperPower (SP), Theva, Shanghai Superconductor Technology (SST) and SuperOx. Changing the nature of the insulation between the turns changes the value of the contact resistivity and thus the behavior of a coil during transient regimes. In a second part, I introduce and explain the different parameters of the superconducting and metallic tapes to have a turn-to-turn contact resistivity R_{ct} between 1 and $10^7 \mu\Omega.cm^2$ and I discuss about the influence of the HTS and metallic tapes properties allowing different contact resistivity values.

In a third part, an ALD (Atomic Layer Deposition) of a few hundred nanometers on superconducting or metallic tapes was tested in order to modify the contact resistivity R_{ct} . The idea is to deposit an insulating material on a tape in order to significantly increase the contact resistivity and then to control this contact resistivity value.

III. 1 Contact resistivity in NI and MI coils from the literature

The contact resistivity is one of the key parameters in NI-MI coil technology. Several works, mainly on NI or MI pancakes, report contact resistivity values between 10^2 and $10^4 \mu\Omega \cdot \text{cm}^2$ at 4.2 K or 77 K. They are listed in Table III-1 from the work of T. Lécrevisse [81]. These contact resistivity values depend on the quality of the tape surface, the hardness of the materials and the mechanical stress.

Table III-1: Overview of the R_{ct} published values for NI and MI windings.

Technology	Sample type	Temperature	$R_{ct} [\mu\Omega \cdot \text{cm}^2]$	Reference
NI	Small pancakes	77 K	70.7-71.3	[82]
NI Thermal Grease insulation (TG)	Small pancakes	77 K	NI: 15.2 TG: 23.1	[83]
NI	Small coil	-	12.8	[84]
NI ; MI brass	Small pancake	77 K	25.5 ; 46.8	[48]
NI	Stack 2 tapes $25 \times 4 \text{ mm}^2$	77 K	26-100	[85]
NI	Small pancake	77 K	48.3-56.8	[86]
MI SS (SuS) - MI copper	Small pancakes	77 K	155-60	[87]
NI ; MI SuS 304 1	Small pancake	77 K	19.2 ; 1100-9800	[56]
MCI	2 DPs magnet	4.2 K	130-280	[88]
MI Durnomag [®]	2 DPs magnet	4.2 K	207	[50]
MI Durnomag [®]	Simple pancake	4.2 K	615-810	[49]
MI Durnomag [®]	Double pancakes and magnet	4.2 K	1000	[89]
NI SuperOx	Small pancake	-	29.2-33.2	[90]
NI (oxide removal) MI Sus 316 MI CuZn37	Stack 2 tapes $12 \times 4 \text{ mm}^2$	77 K	80-100 (2-3) 3000-4000 120-900	[91]
MI SuS MI SuS pre-tined MI SuS soldered	Small pancakes	77 K	>293 292.7 25.5	[51]

Several observations can be made from this data:

- Having MI pancake increases the contact resistivity value, which decreases the time constant of the pancake. On the other hand, soldering the tapes decreases the contact resistivity, thus increasing the charging time of this type of coil.
- The thickness of the added metallic tape ($\sim 50\text{-}100 \mu\text{m}$) is not responsible for the increase in contact resistivity.
- The publications giving the values in the Table III-1 do not always provide information on the experimental conditions of the measurements carried out (number of mechanical cycles, level of oxidation on the surface of the tapes), which may modify the contact resistivity.
- The method to obtain the contact resistivity with a rapid discharge of the coil is more complex to achieve. Indeed, with a low contact resistivity, the value of the radial currents is high. The path of the current within the coil is no longer strictly the same as the path defined by the turns of the tapes. The value of the coil inductance is modified, which implies discrepancies between experimental measurements and theoretical values from numerical models. On the other hand, with a high contact resistivity, the time constant is relatively low, making acquisition during discharge complex.

The measurement of contact resistivity with a stack of superconducting tapes thus seems more suitable.

- The mechanical stress, as well as the number of mechanical cycles, modify the value of the contact resistivity. J. Lu [85], [92], observes this behavior on a stack of two REBCO tapes in NI and MI configuration. Loading and unloading a pancake leads to mechanical stresses, which therefore change the contact resistivity with the number of uses.

Finally, it should be noted that oxidation on the tape surface plays an important role in the value of R_{ct} . This phenomenon was observed during the work of this thesis, but also in the work of J. Lu [92]. All these remarks (values of the contact resistivity depending on the technology, influence of the load, presence of oxidation) will be studied in this Chapter III.

III. 2 Experimental measurements of contact resistivity between superconducting tapes with or without metallic co-wound tape

III. 2. 1 Presentation of the experimental setup

III. 2. 1. 1 Setup overview

The objective is to measure different turn-to-turn contact resistivity values R_{ct} (in $\mu\Omega.cm^2$) between No- and Metal-Insulation 6 mm wide HTS superconducting tapes as a function of the mechanical stress applied on a tape stack (measurements up to 70 MPa - corresponding to 121 kN - in our study) in a liquid nitrogen (LN_2) bath at 77 K. We chose this value which is high enough to reach a stable R_{ct} value and far below a critical value evaluated around 400 Mpa [14]. Several samples were tested (different manufacturers, NI or MI, soldered tapes).

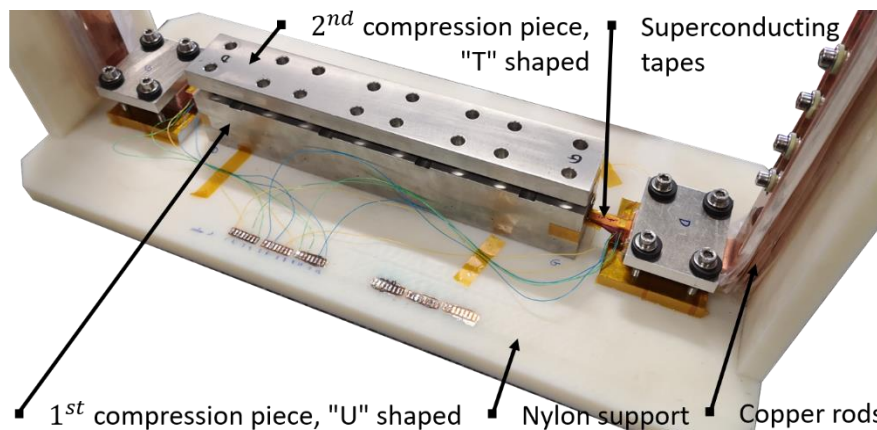


Figure III-1: Plate for measuring contact resistivity values between superconducting tapes as a function of mechanical stress.

The superconducting tapes are placed in the “U” shaped stainless steel part (Figure III-1 and Figure III-2). In order to carry out the measurements according to the mechanical stress, another part in stainless steel, with a “T” shape, is placed on the tapes stack. Copper parts allow injecting current (few tens amps) in the stack. The whole assembly (the “plate”) is fixed on an insulating-Nylon support. The stress is applied on a 300 mm stack length. With the fillets (Figure III-3) at both ends of the “U” and “T” shaped part, the real length is 290 mm for a 6 mm wide tapes ($S_{sample} = 1740 \text{ mm}^2$). These fillets allow to avoid important over-stresses due to edge effects which could locally degrade the superconducting layer. This length of about 300 mm is representative of a typical small pancake coil turn length (as for the NOUGAT insert [22] where the length of a turn is between 150 mm and 320 mm). We chose this length to mitigate the local surface defaults and have a more reliable R_{ct} value.

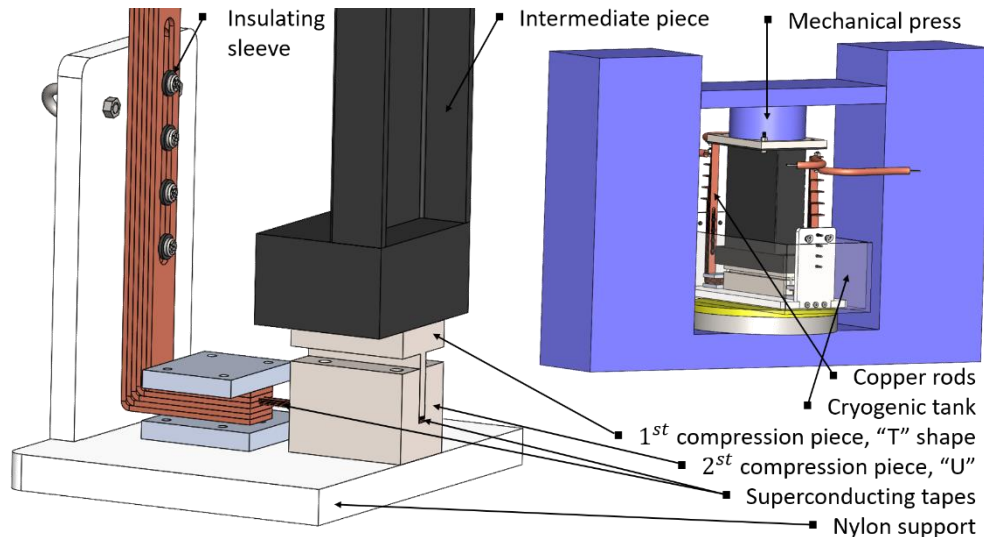


Figure III-2: On the left, cross-section of the plate. On the right, CAD of the experimental setup.

In order to impose a mechanical stress on the tapes, a press generating up to 300 kN is used. Finite element calculations using GetDP [93] and ANSYS software [94] have been performed in order to design an intermediate part (in black on Figure III-2) in stainless steel rectangular tube shape (upper part) to thermally isolate the deformation cell from the press. The objective is to maintain this cell at room temperature (≈ 293 K) after at least four hours of test in order to accurately measure the stress imposed by the press (the cryogenic tank is at 77 K). The intermediate part is full (lower part) in order to obtain a uniform stresses distribution over the whole length of the stack. This intermediate part is included between the plate and the press. Parts in G10 fiberglass (yellow) are placed under the cryogenic tank in order to thermally insulate the press frame. Another G10 insulation layer is placed between the "T" shape part and the stainless steel press block.

III. 2. 1. 2 Preliminary tests: mechanical stress distribution and thermal insulation

III. 2. 1. 2. 1 Simulations with GetDP and ANSYS

Several iterations were done with GetDP (only thermal part) and ANSYS (thermal and mechanical part) in order to optimize the geometry allowing a good thermal insulation of the press cell and an good stresses repartition over the stack surface (Figure III-3).

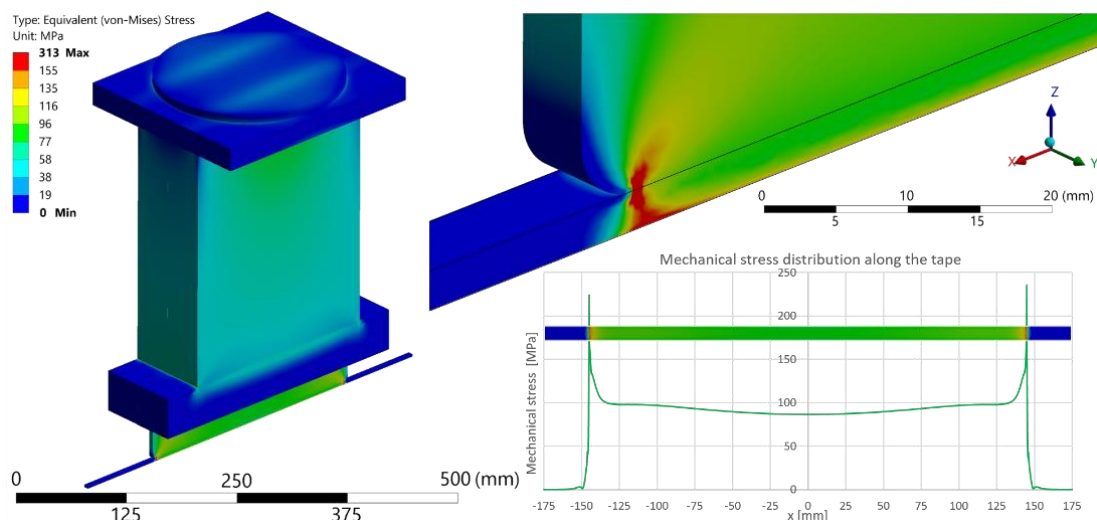


Figure III-3: On the left, ANSYS simulation of the mechanical stress distribution along the tapes. On the top right, fillet and zoom on the edge effect. At the bottom right, mechanical stress distribution along the tape.

With this geometry, the stress imposed on the tapes is between $\pm 10\%$ between $x = -135$ mm and $x = 135$ mm compared to the average value of the stress over the whole length. This means that the stress variation is $\pm 10\%$ over 93% of the total length. From a thermal point of view, the stainless steel tube of the intermediate piece fulfills its role of thermal insulation (Figure III-4). The calculations performed with ANSYS and GetDP simulated the worst case (no convective exchange with the outside, Dirichlet boundary condition for the sides and the bottom face of the intermediate piece). The press cell is maintained at room temperature (≈ 293 K) after 4 hours, it will not change temperature during testing.

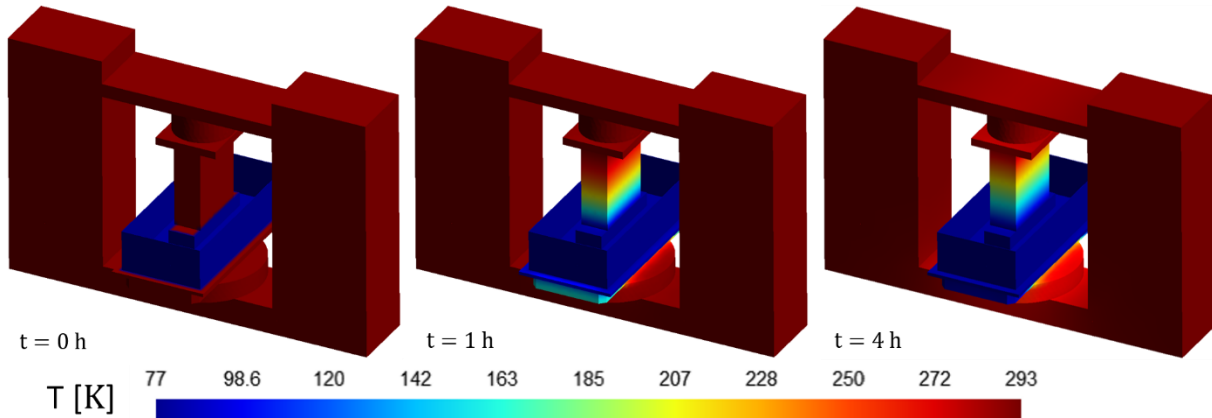


Figure III-4: Simulation of thermal diffusion via GetDP.

III. 2. 1. 2. 2 Experimental verifications

In order to confirm the proper stress distribution on the tapes, we conducted loads up to 90 MPa on a stack of 30 stainless steel tapes (properties in Table III-2) at room temperature. Fujifilm "HS" paper tapes [95] were placed on, under and in the middle of the tape stack.

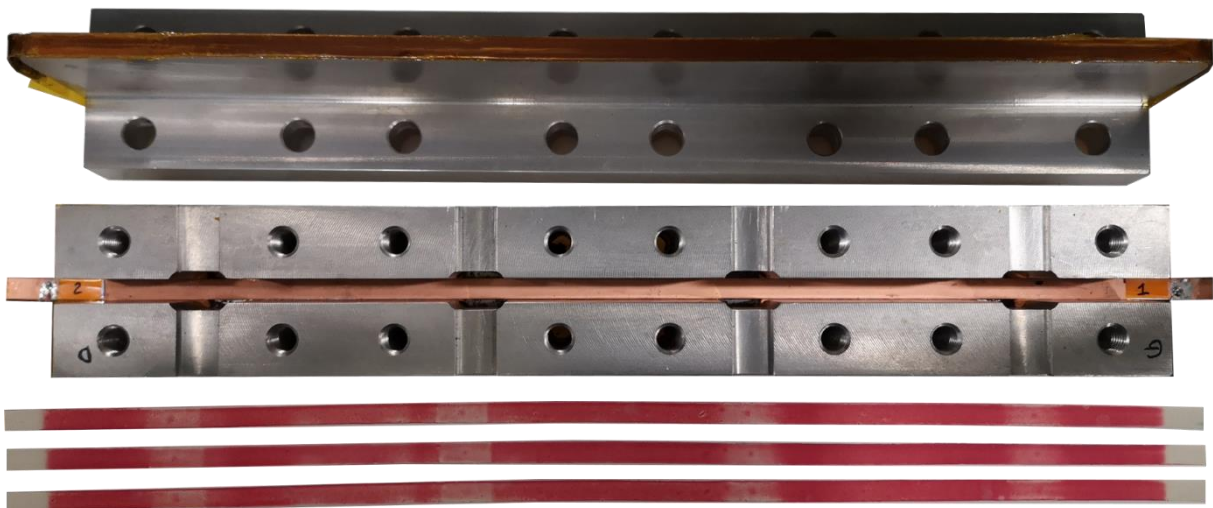


Figure III-5: On the top, "T" shaped part. In the middle, "U" shaped part with superconducting tapes and position of the gaps for the strain gauges (not used). At the bottom, 90 MPa compression of stainless steel and Fujifilm paper tapes.

A homogeneous distribution over the whole length and width of the stack can be observed on the Fujifilm paper tapes (Figure III-5). However, four areas have a lower compression values. This decrease is caused by the four places initially planned to insert strain gauges. Since the stress value is given by the press cell, the gauges are no longer necessary. These gaps cause the tapes to creep, generating less local stress. We perform the same test on SuperPower tapes (properties in Table III-3). The stress distribution is good along the length but uneven along the width of the tape (see Fujifilm paper pressed with SP tapes, Figure III-6). This difference is due

to the thickness variation (only observed with SP tapes from 2016) over the width of the superconducting tape. With the help of a cross-sectional view of SP tape and a surface analysis made with a confocal microscope (Figure III-6), it has been observed that the copper layer is responsible for the thickness variation. This behavior has also been observed in different papers [85], [96]. SP has since improved the thickness uniformity of the copper stabilizer [96].

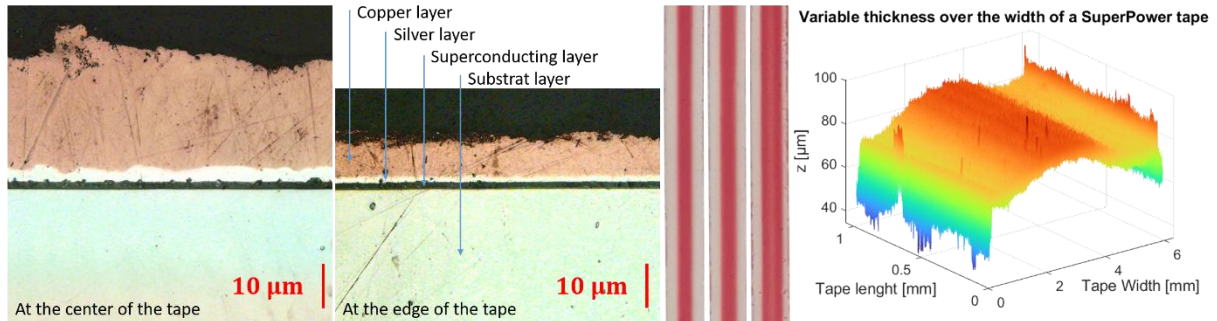


Figure III-6: From left to right; cross-sectional view of an SP HTS tape at the center and the edge of the tape; Fujifilm paper pressed with SP tapes; thickness variation made with a confocal microscope across the width of a SP tape.

Concerning the thermal part, a first liquid nitrogen cooling without stress and without the plate was performed in order to observe and validate the thermal insulation of the press cell (Figure III-7). After four hours of cooling, the decrease of the press cell temperature is consistent with the simulation results. During all measurements, the temperature probe (present in Figure III-7) is present to ensure that the temperature of the press cell is always close to the ambient temperature. In the case of the measurements, the experimentally measured temperature is higher (about 3 ~ 4 K) compared to the simulations. This difference is due to the absence of convective exchange at the surface of the intermediate piece, in the case of ANSYS and GetDP calculations. In reality, the room is slightly heated by the ambient air in the room, which causes a smaller temperature decrease.

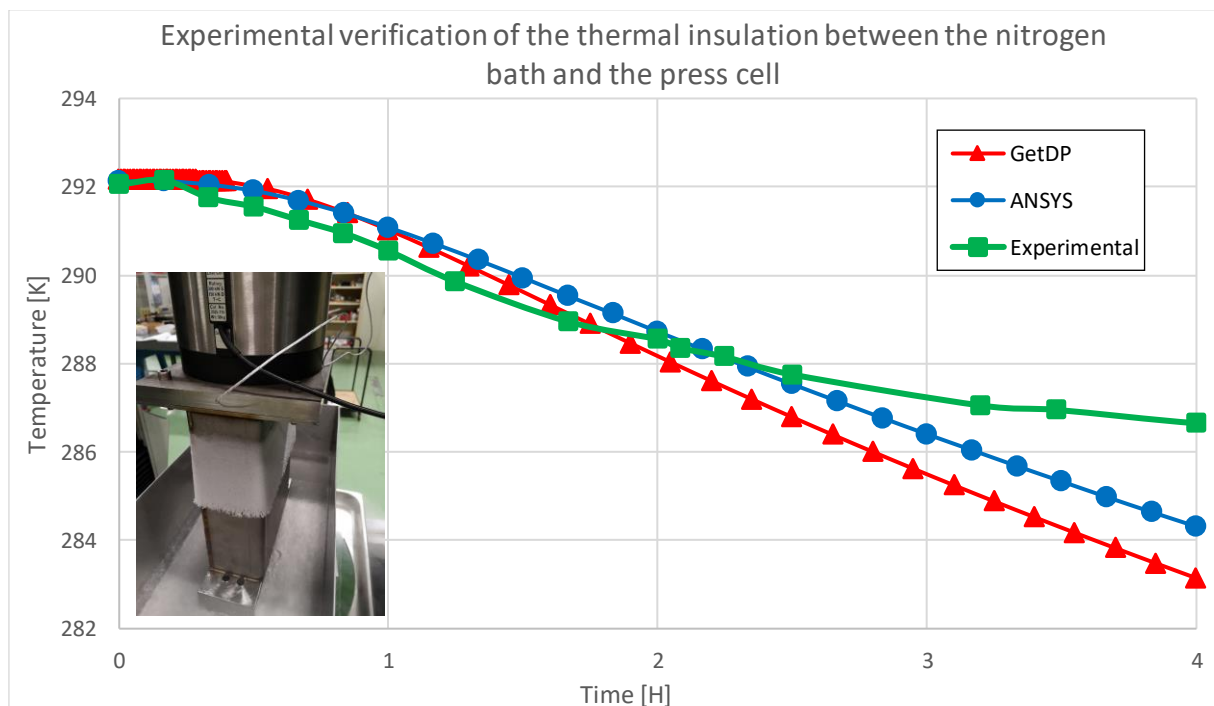


Figure III-7: Experimental verification of the thermal insulation between the nitrogen bath and the press cell.

With the thermal and mechanical part operational, measurements were carried out. These are presented in the following section.

III. 2. 2 Contact resistivity measurements between superconducting tapes

The signals were recorded using the National Instrument *cDAQ* – 9178 chassis [97] comprising three modules. Two *NI* 9238 modules with a range of ± 0.5 V for the seven signals (the six potential taps and the shunt resistor) and one *NI* 9269 module allowing sending a voltage to the power source. This card allows controlling the 8 V / 600 A *TDK Lambda* power supply via a LabVIEW program. This LabVIEW program makes it possible to acquire the contact resistivity values at any time but also to read and record all the data during the measurements. The potential taps are placed at the ends of the “U” shaped part.

This setup allows to measure up to six samples simultaneously placed in the “U” shaped part. A sample is a set of two superconducting tapes, with possibly of one or more metallic tapes between the two superconducting tapes (Figure III-8). For this purpose, six copper rods on each side of the plate are insulated from each other with Mylar film. Insulating sleeves around the screws prevent electrical contact between the copper rods (Figure III-1 and Figure III-2). The six samples (sample 1 \leftrightarrow tape #1 and #2; sample 2 \leftrightarrow tape #3 and #4; ...) are powered in series. Kapton tapes are inserted between each sample (in red in Figure III-8) to ensure electrical insulation. Kapton is also added at the bottom and sides of the “U” shaped part, to ensure perfect insulation. With this setup, it is also possible to measure an average contact resistivity between several superconducting tapes. However, all the contact resistivity values presented are from samples consisting of only two superconducting tapes (and possibly metallic tapes). The superconducting tapes used have not been treated to remove the oxide layer. They are used as received.

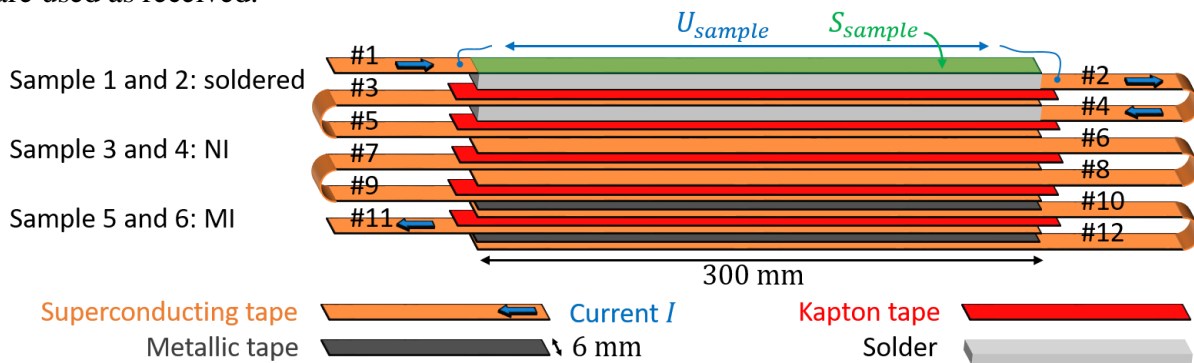


Figure III-8: Sketch showing an example of superconducting tapes and metallic tapes placed in the “U” shaped part.

The contact resistivity R_{ct} is defined by:

$$R_{ct} = \frac{U_{sample}}{I} S_{sample} \quad (29)$$

With U_{sample} the voltage measured between the beginning and the end of the contact area between the two tapes. S_{sample} the contact area of the two tapes and I the current value.

For each measurement made, the superconducting tapes are 385 mm long (85 mm allowing for connection to the copper parts). The dimensions of the metallic co-wound tapes are in Table III-2. With this setup, different technologies have been tested: with or without metallic co-wound tapes (in soft or extra hard state), but also by soldering the superconducting tapes with tin-lead. These different techniques were performed with different manufacturers: SuperPower (SP), Theva, SuperOx and Shanghai Superconductor Technology (SST). With these solutions, it is possible to obtain different contact resistivity values R_{ct} : from $1 \mu\Omega.cm^2$ to $10^7 \mu\Omega.cm^2$. All contact resistivity values presented in this chapter correspond to Superconductor – Hastelloy® side contact which is representative of a NI-MI winding. The properties of the superconducting tapes are available in Table III-3.

Table III-2: Properties of the metallic co-wound tapes.

	Stainless steel	Beryllium copper	Durnomag®
Reference	EN 1.4301–AISI 304	CuBe ₂	EN 1.4369
Length [mm]	300	300	300
Width [mm]	6	6	6
Thickness [m]	50	50	30
Vickers hardness [kgfmm ⁻²]	Soft, HV=160	Hard, HV=210	Extra Hard, HV=410
Surface roughness [μm]	0.08	0.15	0.05
Number of peaks per unit area [mm ⁻²]	1.2×10 ⁶	3.9×10 ⁶	2.5×10 ⁶
Main curvature of the peaks [mm ⁻¹]	1.3×10 ³	10.9×10 ³	0.7×10 ³

III. 2. 2. 1 Without electrical or metallic tape insulation

We firstly tested NI samples. The objective was to measure a contact resistivity characteristic of NI windings. Tapes from SP, Theva, SuperOx and SST were tested. The current values used for all the measurements in this chapter are available in the Appendix (VI. 2). Having a high current value allows to improve the accuracy of the measurements. However, a too high current heats the samples, which leads to an increase of the contact resistivity, and eventually to the loss of superconductivity, which might distort the measurements. This is due to the presence of copper on the surface of the tapes as indicated by J. Lu [85]. For each sample, a search for the optimal current is performed. The values of R_{ct} and sample voltage as a function of current are in the followings parts. The optimal current value is chosen to remain in the linear region of the voltage, to be in the constant part of R_{ct} . The curve allowing to estimated the best current value is presented in Figure III-9 for the second sample type, which is the soldered NI case. As it can be seen, the linear part is valid up to about 100 A for the sample number 2 (dotted line), whereas it is valid above 140 A for sample number 1. In this case, we limit the current at 70 A to avoid any effect on the measurements. A too low current would cause a lower accuracy on R_{ct} .

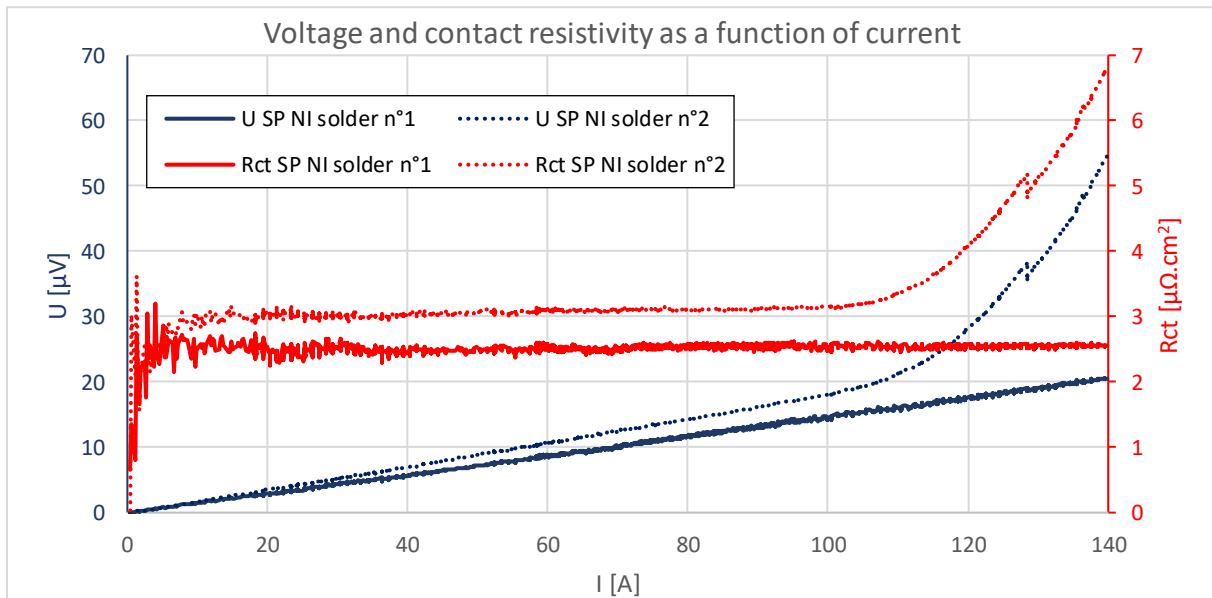


Figure III-9: Evolution of voltage and contact resistivity as a function of current in the soldered SuperPower NI case.

III. 2. 2. 1. 1 Influence of the mechanical stress

During the measurements, several load cycles were performed. A load cycle corresponds to a stress increase from 2 to 70 MPa, then a decrease to 2 MPa. As the contact resistivity value depends on the number of load cycles [85], [92], the results presented and compared are those

of the first phase of the second load cycle. For each manufacturer, several samples were tested simultaneously (between two and six samples depending on the manufacturer). The results in Figure III-10 are the averages of the samples from each manufacturer.

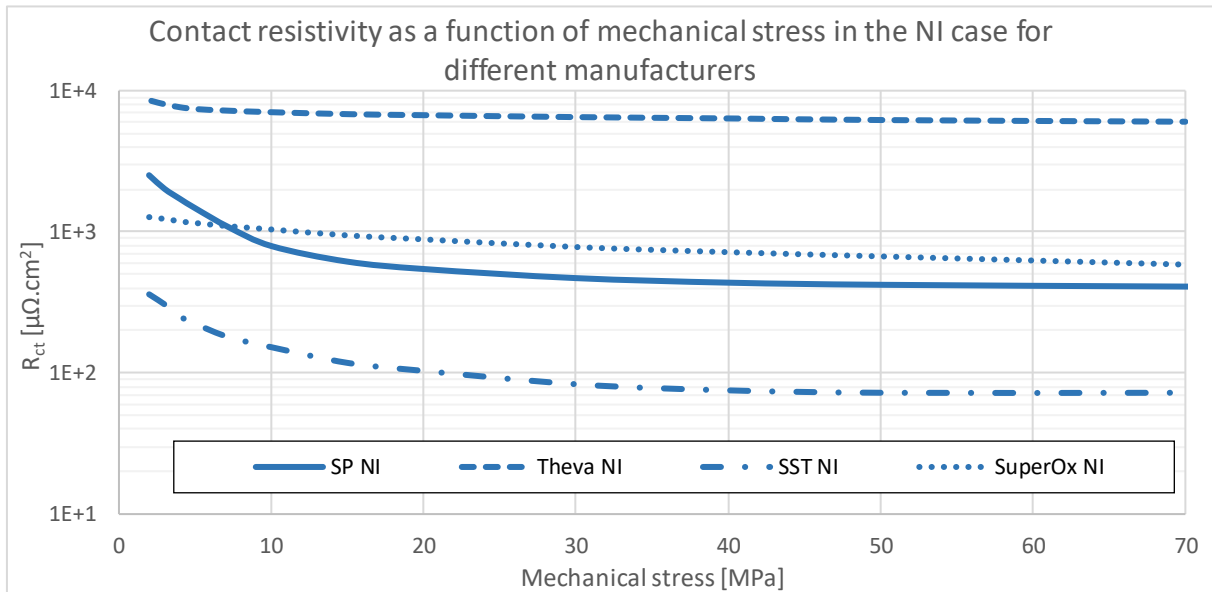


Figure III-10: Contact resistivity as a function of mechanical stress in the NI case for different manufacturers.

Figure III-10 shows the contact resistivity values in the NI case as a function of the mechanical stress applied to the stack for the four manufacturers. The principal property is the variation of R_{ct} as a function of the mechanical stress, a phenomenon also observed by J. Lu [85], [92] on REBCO conductors made by SP and SuNAM. Indeed, the higher the stress, the more local plastic deformation occurs at the surface of the two tapes in contact. The contact area between the tapes increase, which decreases R_{ct} . This change in the contact area between the tapes as a function of mechanical stress is due to the rough surface condition of the tapes (Figure III-11). The local plastic deformation is observed via the hysteresis cycle of contact resistivity generated by the charging and discharging load of a sample. The contact resistivity during discharge is lower than during loading because the contact area between the two tapes is larger during discharge due to the plastic deformations caused during the loading of the tapes. This phenomenon is also observed by J. Lu in [85].

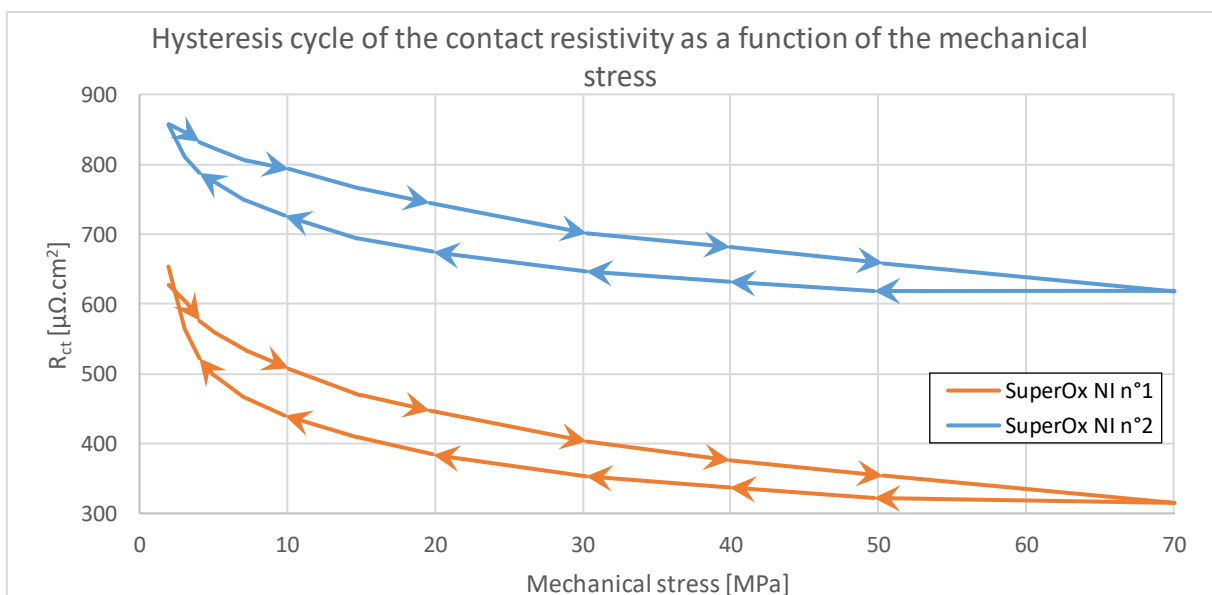


Figure III-11: Hysteresis cycle of the contact resistivity as a function of the mechanical stress.

In the case of NI tapes, differences in R_{ct} values are observable between manufacturers (factor of 10 to 100). One might think that the difference is due in part by the surface condition of the tapes not being identical between the manufacturers (leading to different copper surface quality, Figure III-12), thus generating variations in R_{ct} . However, the surface condition is not the only parameter to take into account. Indeed, the contact resistivity between NI tapes also depends on its oxidation, on the hardness of the copper layer coating the tape and on the composition of the superconducting tape (mainly between Theva and other manufacturers). No direct link between the R_{ct} values and the surface condition of the tapes of the different manufacturers is observable (Table III-3). The surface condition measurements are performed using a confocal microscope with a lateral resolution of 130 nm and a depth resolution of 0.5 nm. For the surface condition and hardness of the superconducting tapes, these are averages of measurements made on the superconducting and Hastelloy[®] sides of several tapes. Measurements are made on areas of approximately $\sim 7 \times 10^3 \mu\text{m}^2$.

The surface condition, and more precisely the roughness, has more of an influence on the behavior/shape of the R_{ct} curve as a function of the mechanical stress. The greater the roughness, the greater the elastic deformation, which will result in a greater variation of the contact surface, and therefore a more pronounced decrease in R_{ct} with an increase in stress. This phenomenon is relatively visible between SP-SST and SuperOx tapes: the decrease is more important between 2 and 70 MPa on the R_{ct} of SP (- 84%) and SST (- 80%) compared to SuperOx (- 54%).

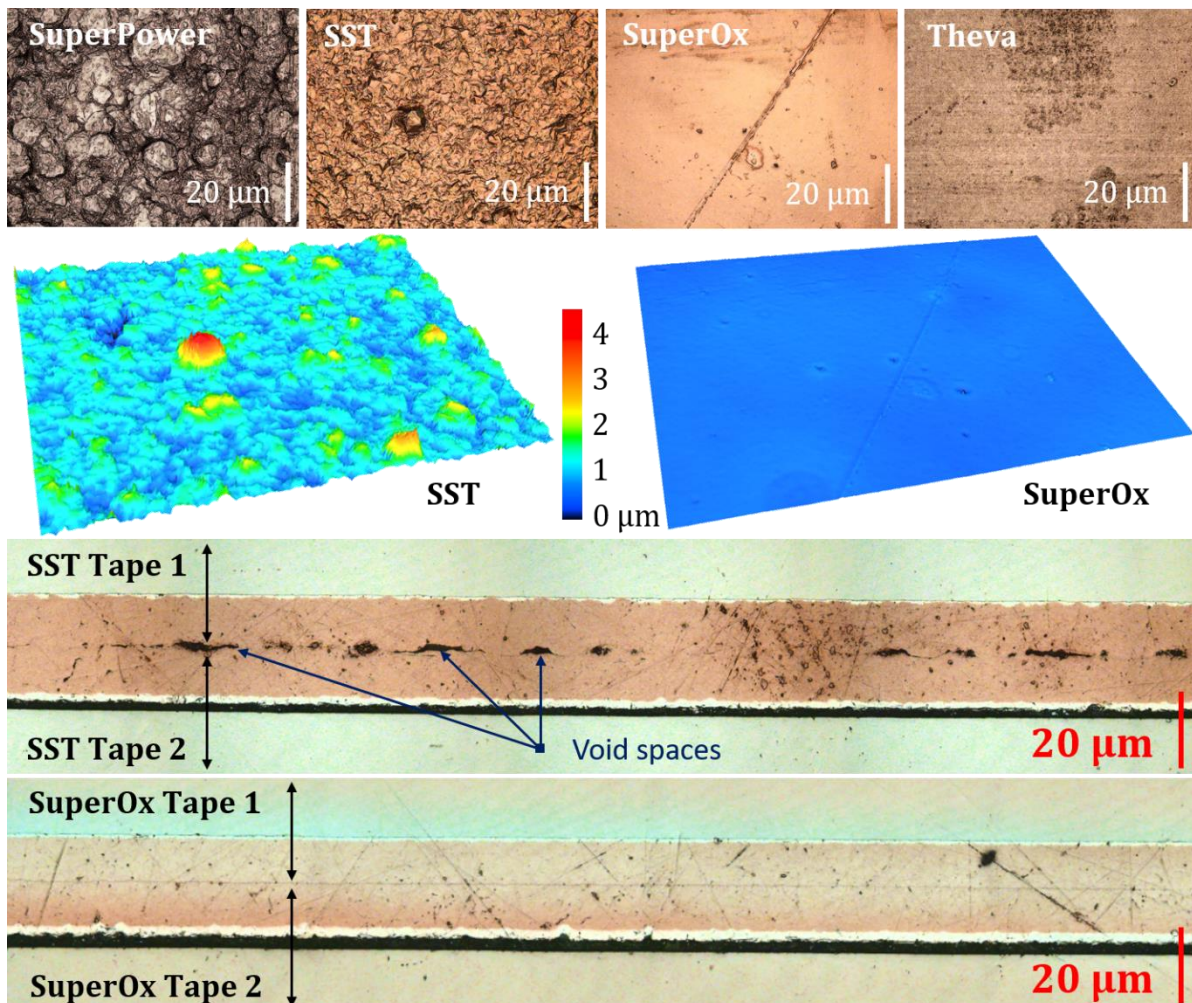


Figure III-12: On the top, surface condition on the superconducting side of SP, SuperOx, Theva and SST tapes. In the middle, 3D views of the SST and SuperOx tape surface obtained with a confocal microscope. At the bottom, cross-sectional views of two SuperOx and SST tapes compressed under a mechanical stress of about 15 MPa.

Using the confocal microscope, we measured a rougher contact surface for SP and SST tapes compared to Theva and SuperOx tapes (Figure III-12 and Table III-3). This rougher surface condition of SST compared to SuperOx can also be observed with the cross-sectional view of two superconducting tapes compressed under a mechanical stress of about 15 MPa. Because the asperities of the SST tape are larger, void spaces are more massive compared to compressed SuperOx tapes. Theoretically, the more void spaces there are, the higher the contact resistivity. However, the contact resistivity measurements for SuperOx are higher than that of SST. These results can be explained by the other properties of the superconducting tapes that are predominant on the R_{ct} value. For example, the copper layer for SST tapes is softer compared to the SuperOx tapes (Table III-3). The contact area for the different zones is larger, thus generating a lower contact resistivity for SST tapes. Thus, there may be fewer contact areas between the SuperOx tapes to a very small scale.

Table III-3 groups for each manufacturer the contact resistivity value at 20 MPa associated with the parameters of the surface state, the hardness and the thickness of the buffers layer of the tapes. Through Table III-3, it is observable that some parameters have more influence on the R_{ct} value than others. The values of the thicknesses of the different layers are taken from different papers [17], [96], [98], [99], [100] and from measurements of cross-sectional views of the tapes (Figure III-13, Figure III-14 and Figure III-20).

Table III-3: Properties of superconducting tapes.

	SST	SuperPower	SuperOx	Theva
Reference	–	SCS6050-AP	ST-6-150-100	TPL 4601C
R_{ctNI} @ 20 MPa [$\mu\Omega\cdot\text{cm}^2$]	104	544	888	6 702
Surface roughness [μm]	0,50	0,59	0,05	0,04
Number of peaks per unit area [mm^{-2}]	3.3×10^6	4.7×10^6	4.0×10^6	4.5×10^6
Main curvature of the peaks [mm^{-1}]	51.4×10^3	50.1×10^3	1.5×10^3	2.2×10^3
Vickers hardness [$\text{kg}\cdot\text{mm}^{-2}$]	125	132	156	153
MgO / buffer layer thickness [nm]	5 / 325	40 / 200	5 / 150	3 000 / 3 500
Copper thickness [μm]	$\sim 2 \times 10 - 20$	$\sim 2 \times 10 - 20$	$\sim 2 \times 10 - 20$	$\sim 2 \times 10 - 20$
Silver thickness [μm]	1 – 2	$\sim 2 \times 2$	1 – 2	$\sim 2 \times 1.5$
Superconductor thickness [μm]	1.5 – 2.5	~ 1.6	1 – 3	$\sim 3 - 5$
Substrate thickness [μm]	50	50	60	100
Tape thickness [μm]	$\sim 80 - 90$	$\sim 75 - 85$	~ 100	$\sim 140 - 150$

A high value of the number of peaks per unit area indicates a greater number of contact points with other objects. Regarding the average of the main curvature of the peaks on the surface, a low value indicates that the contact points with other objects are rounded, increasing the contact between the tapes. A high value indicates that the points of contact with other objects are sharp. Although the value for Theva is low, R_{ct} is high compared to other manufacturers due to a higher buffer layer thickness (see next paragraph III. 2. 2. 1. 2).

It is difficult to observe the impact and the preponderance only of these two parameters on the contact resistivity. Indeed, in Table III-3, other quantities (surface roughness, Vickers hardness, composition of the superconducting tape) modify, with more or less importance, the contact resistivity. In order to evaluate the influence of these two parameters, it would be necessary to vary the number of peaks per unit area and the main curvature of the peaks and have the other properties of the tape fixed, which is relatively complex to obtain in our case. Among our results, it is difficult to know the importance of each tape parameter on the contact resistivity value, but the thickness of the **MgO layer** and the **hardness** of the copper layer are the two preponderant parameters concerning the contact resistivity values in the NI case. These two parameters are explained in the next two subsections.

III. 2. 2. 1. 2 Influence of the composition of the tapes / soldered NI samples

Although the roughness of the SP and SST tapes are higher than the Theva tapes or the SuperOx tapes, the R_{ct} as a function of mechanical stress is not only dependent on the surface condition. Indeed, with the R_{ct} values between the tapes (soldered with tin-lead) of the different manufacturers, it is observed that the soldered Theva NI tape has a quite high R_{ct} value compared to the other three manufacturers. Although the Theva tape is mechanically smoother (and thus theoretically the contact area should be larger and thus decrease R_{ct}), this one has a higher R_{ct} . This relatively high value can be explained by the composition of the tape. In the case of the Theva tape, a magnesium oxide buffer layer (MgO) of about 3 μm is deposited on the substrate before the superconducting layer [17]. This insulating layer is thinner in the case of SP, SuperOx and SST tapes [98], [99], [100]. These differences can be observed with cross-sectional views made on the superconducting tapes with a microscope (Figure III-13). The thickness, and thus the composition of the tape layers, has an influence on the R_{ct} values, but mainly in the NI case. Through these cross-sectional views, we can clearly see a surface with more asperities in the case of SST and SP (rougher) compared to the Theva and SuperOx tapes (less rough).

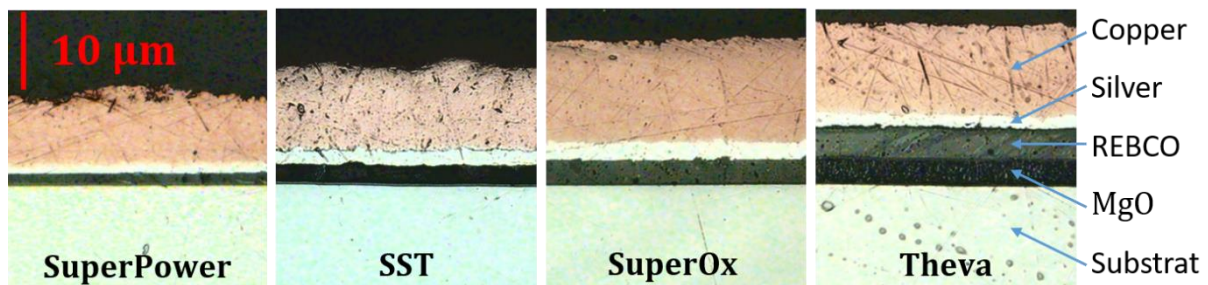


Figure III-13: From left to right, cross-sectional view of SP, SuperOx, SST and Theva tapes; MgO layer influence.

Moreover, by soldering the superconducting tapes together, we observe a significant decrease of the contact resistivity. The soldering between the two superconducting tapes is done manually with a soldering iron. Tinning for the tin-lead solder ($\text{Sn}60/\text{Pb}40$) is carried out on both superconducting tapes using liquid Tixflux[®] flux at a temperature of 230°C. Indeed, soldering the tapes maximizes the contact area and flux pickling for soldering removed the oxidation layer on the surface of the tapes. The R_{ct} of the soldered tapes (excluding Theva) are relatively low (Figure III-15). This low R_{ct} values are observable in fully soldered pancakes, generating relatively large charging time constants [51], [101]. This thicker MgO layer therefore explains the factor 1000 between Theva and other manufacturers.

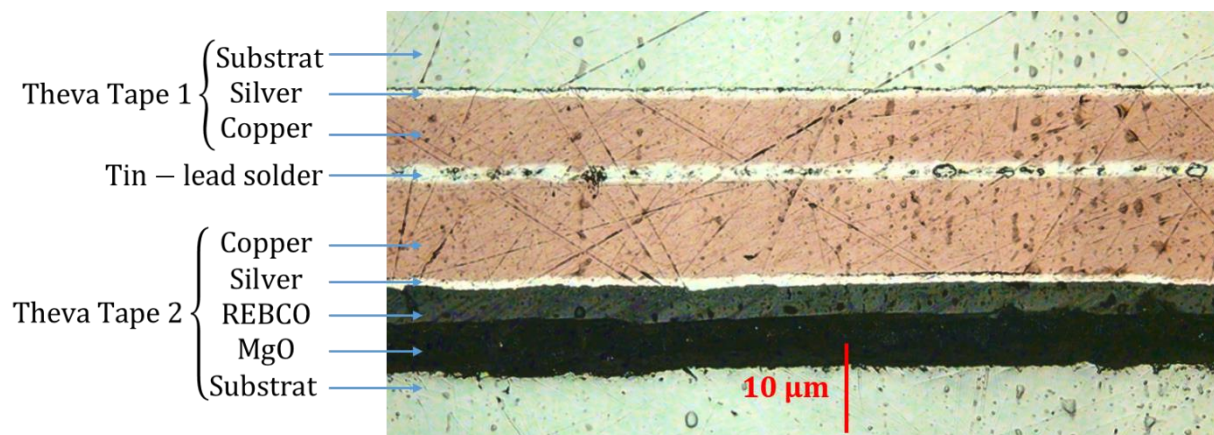


Figure III-14: Cross-sectional view of Theva tapes soldered with tin-lead.

The presence of the solder between the two HTS tapes fills in the large majority of the holes of the asperities present on the tape surface (Figure III-14). Thus, with an increase in mechanical stress, the surface condition remains the same: the solder makes the contact surface between the soldered tapes invariant. Since the conduction surface is maximum, the R_{ct} values become relatively low, hence the values of $1\sim 10 \mu\Omega\cdot\text{cm}^2$, except for the Theva case, where the MgO layer is responsible for an increase of three orders of magnitude compared to the other three manufacturers. Finally, the presence of the solder will prevent any form of oxidation between the two tapes. In addition, the soldering process removes the oxidation layer on the copper, which reduces the contact resistivity value.

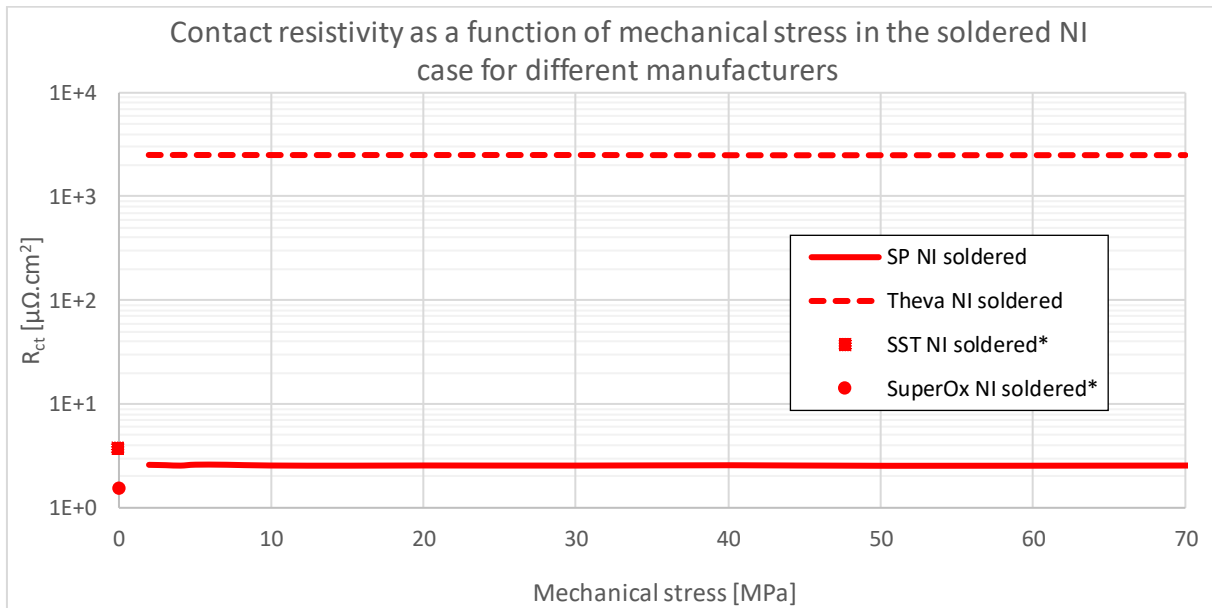


Figure III-15: Contact resistivity as a function of mechanical stress in the soldered NI case for different manufacturers.

*: Since the contact resistivity of SuperPower and Theva in the soldered NI case are independent of mechanical stresses, contact resistivity measurements were conducted without applying a mechanical stress on the SST and SuperOx samples. The values obtained are of the same order of magnitude as the first two manufacturers tested under different compressions.

Thus, R_{ct} is mainly generated by the interfaces between the tapes: soldering is the same as getting over this interface resistance, which reduces R_{ct} .

In addition, in the NI case, the current flows from one tape to another mainly at the edges of the superconducting tapes. This was explained by S. Noguchi in a study of the current flow between the turns using the 2D finite element method [102]. Thus, the thicknesses of the different layers of the superconducting tapes should explain the difference in contact resistivity values measured between the manufacturers.

For this purpose, cross-sections of the tapes were taken at the edges. The 6 mm tapes do not have the same structure on both edges. Indeed, a cut on a larger tape without copper and silver results in different edges. In Figure III-16, the thickness of the copper and silver layer is thicker for SuperOx than for SST. This should generate a lower contact resistivity for SuperOx compared to SST. However, the R_{ct} measurements in the NI case do show a higher R_{ct} for SuperOx compared to SST.

Thus, the thicknesses of the different layers at the edges of the tapes should change the R_{ct} value, but this is not the main reason for the difference in value between the manufacturers. The more rounded shape of SuperOx compared to SST may be responsible for the difference in value.

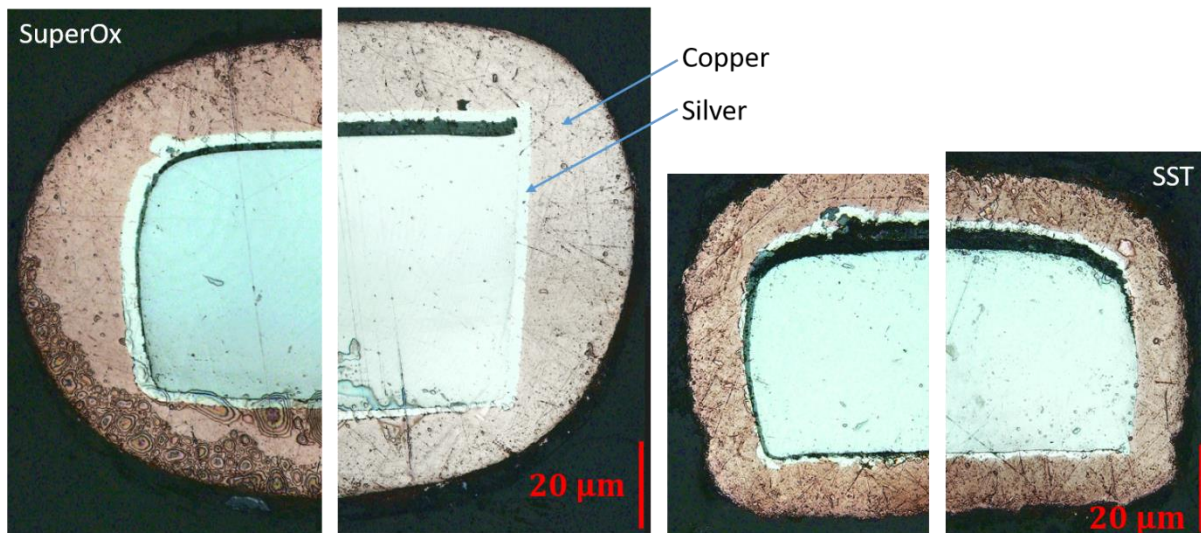


Figure III-16: Cross-sectional views of the edges of SuperOx (left) and SST (right) superconducting tapes.

III. 2. 2. 1. 3 Influence of the hardness of the copper layer on the superconducting tapes

Omitting the Theva R_{ct} values (presence of the MgO layer which is largely responsible for the increase in R_{ct} in the NI case), we can observe a decrease in R_{ct} of the other manufacturers with a decrease in Vickers hardness. The properties of the buffer layers are relatively identical for SP, SST and SuperOx tapes. Micro Vickers hardness measurements are made using the Wilson Instruments 401/402 MVD. The softer the copper on the surface of the tapes, the greater the contact between the tapes will be, thus decreasing the R_{ct} value (Table III-3).

In addition to the hardness and composition of the tape, oxidation on the surface of the tape greatly affects the value of the contact resistivity in the NI case. This is explained in the next paragraph.

III. 2. 2. 1. 4 Influence of the oxidation

The presence of oxidation on the tapes is also one of the important parameters modifying the R_{ct} values. Three measurements of R_{ct} on the same samples (SP NI tapes) were conducted, with a warming in the open air and without stress between each measurement (generating oxidation). Through these measurements, an increase of R_{ct} after each heating is clearly observed. This increase is due to the appearance of an oxidation deposit on the surface of the tape (Figure III-17).

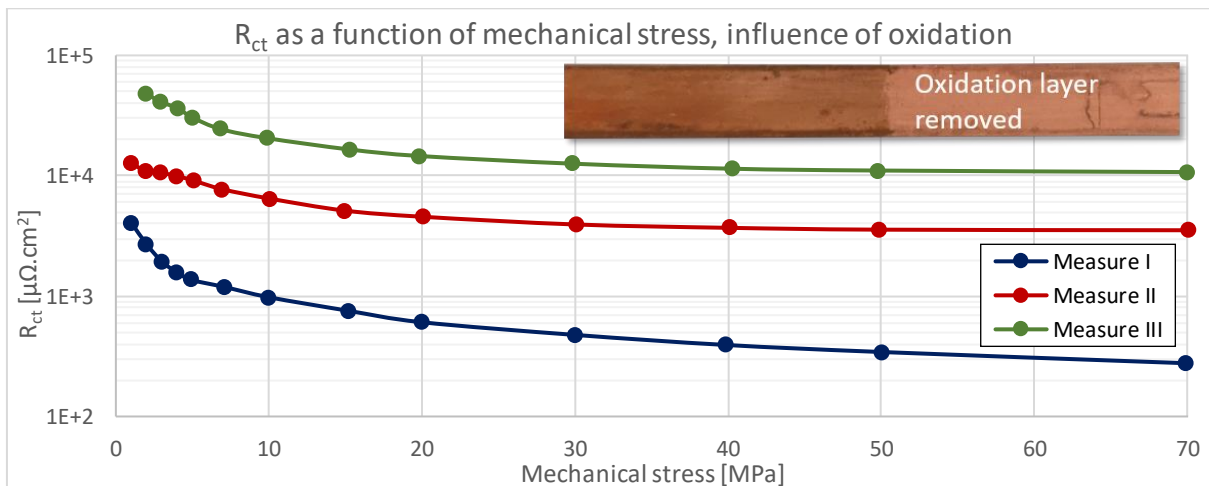


Figure III-17: Contact resistivity as a function of mechanical stress in the NI case, influence of oxidation.

Ortho phosphoric acid easily removes the oxidation present on the surface of the tapes (the tape on the top right of Figure III-17 was cleaned with ortho phosphoric acid on the right side only). Table III-4 groups measurements of R_{ct} in a stack consisting of ortho phosphoric acid cleaned (1 to 4) and uncleaned (5 to 12) tapes. The disappearance of the oxide layer causes a decrease of a factor of 10 in the R_{ct} at 30 MPa. This decrease in contact resistivity with the disappearance of the oxide layer is also observed by J. Lu in [92] where a large number of load cycles is responsible for the degradation and destruction of the oxide layer on the copper surface.

Table III-4: Contact resistivity with a mechanical stress of 30 MPa between oxidized and non-oxidized SuperPower tapes.

30 Mpa	tape 1 to 4 cleaned				tape 5 to 12 not cleaned						
Connection	1 ↔ 2	2 ↔ 3	3 ↔ 4	4 ↔ 5	5 ↔ 6	6 ↔ 7	7 ↔ 8	8 ↔ 9	9 ↔ 10	10 ↔ 11	11 ↔ 12
R_{ct} [$\mu\Omega\cdot\text{cm}^2$]	84	180	84	274	854	1840	1740	1261	1797	1073	1290
Average [$\mu\Omega\cdot\text{cm}^2$]	116			274	1408						

III. 2. 2. 1. 5 Conclusion contact resistivity between superconducting tapes without insulation

In the NI case, by increasing the mechanical stress on the tapes, the contact surface increases which leads to a decrease of R_{ct} . The R_{ct} values depend mainly on the oxidation, on the hardness of the tapes and on the composition of the different layers of the tape, which generates variations of R_{ct} between manufacturers. These parameters have a more or less important influence on the R_{ct} values. It is difficult to observe separately the influence of each parameter on the R_{ct} values because to vary only one parameter at a time is complex. However, through these results, we can deduce that the composition of the tape is one of the parameters influencing the most R_{ct} in the NI case, responsible for the difference between Theva and other manufacturers.

In the NI case, it is possible to obtain contact resistivity values between $10^2 \mu\Omega\cdot\text{cm}^2$ and $10^4 \mu\Omega\cdot\text{cm}^2$ for mechanical stress between 2 and 70 MPa. Moreover, soldering two HTS tapes greatly decreases the contact resistivity value ($1 - 10 \mu\Omega\cdot\text{cm}^2$, except for Theva) and makes the contact resistivity independent of the load. In order to obtain higher contact resistivity, the addition of one or more metallic tapes is necessary. In the following section, several samples with different metallic tapes and for different manufacturers have been tested.

III. 2. 2. 2 Metallic co-wound tape

In the NI and soldered NI case, the R_{ct} values are between $1 \mu\Omega\cdot\text{cm}^2$ and $10^4 \mu\Omega\cdot\text{cm}^2$ for mechanical stress between 2 and 70 MPa. In order to obtain higher contact resistivity values, a stainless steel 304 (StS) or Durnomag[®] metallic tape (Table III-2) is inserted between the two superconducting tapes, reproducing the case of an MI pancake winding. Having a pancake with a co-wound metallic tape allows to obtain compact and mechanically robust magnets and to decrease the magnet charging time. In this section, we will look at the influence of the nature and hardness of the metallic tape, as well as the soldered metallic co-wound tape.

III. 2. 2. 2. 1 Influence of the hardness of the metallic tape with soft and extra hard stainless steel

New R_{ct} measurements are made by adding a StS tape between two superconducting tapes for each sample type, and for each manufacturer. As for the NI case, the results in Figure III-18 are the averages of each manufacturer's samples from the first phase of the second load cycle. The behavior of R_{ct} as a function of the imposed mechanical stress is the same as in the NI case: the higher the mechanical stress, the lower the R_{ct} value (in the form of a nonlinear way).

Concerning the MI cases with StS, we observe that R_{ct} strongly increases (Figure III-19, from 1 to 3 orders of magnitudes with comparison to NI, depending on the manufacturer). Adding a StS tape allows to obtain quite similar R_{ct} values between the different manufacturers, and thus to get rid mostly of the parameters having an influence on the R_{ct} value in the NI and soldered NI case (Figure III-18). Indeed, the composition of the tape, or even the condition and surface hardness of the superconducting tapes, have less influence on the total R_{ct} value in the case of MI StS. In other words, adding a StS tape increases the R_{ct} value. This increase is much larger compared to the R_{ct} values of the NI case, making the intrinsic properties of the superconducting tapes negligible.

In the case of metallic co-wound tape, the nature of the metallic tape plays a role in the contact resistivity value. Indeed, as in the NI case, the hardness influences the R_{ct} value. New measurements of R_{ct} are made with new metallic co-wound tape. A Durnomag[®] tape, a special extra hard StS alloy, is added between two superconducting tapes of each sample.

Thus, changing the hardness of the co-wound tape increases the R_{ct} value by a factor of 2 to 5. The contact between the tapes is worse with Durnomag[®] than with StS, which explains why $R_{ct_{MI_{StS}}} < R_{ct_{MI_{Durnomag}^{\text{®}}}}$ (Figure III-18).

As a reminder, the thickness of the StS tape is greater than that of the Durnomag[®] tape. In the case of thin metallic tapes (below 100 μm), the thickness of the co-wound tape is not responsible for the increase in R_{ct} . The increase in R_{ct} is caused by the change in contact interfaces between the tapes.

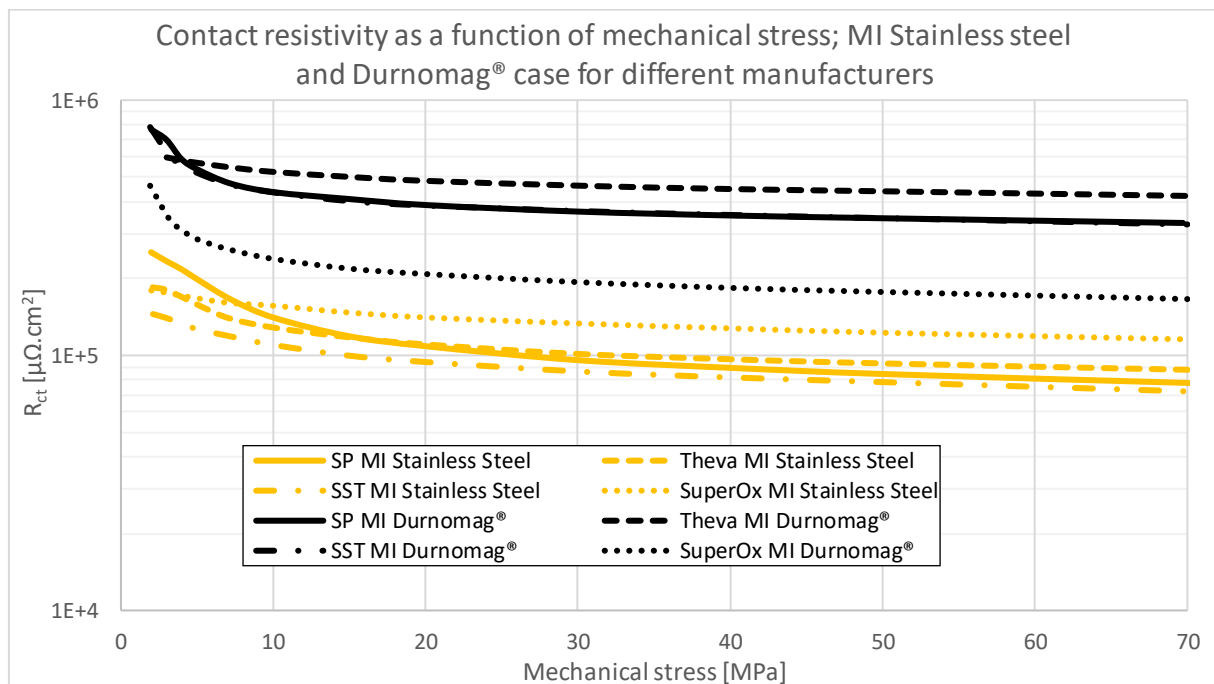


Figure III-18: Contact resistivity as a function of mechanical stress in the MI Stainless steel and Durnomag[®] case for different manufacturers.

III. 2. 2. 2. 2 Influence of the nature of the tape

The increase in contact resistivity also depends on the nature of the contact interface added by the metallic co-wound tape. If the tapes in contact are made of the same material, then the contact resistivity will increase only slightly, in the case of copper-copper contact for example. Measurements in the case of MI with beryllium copper (CuBe_2) were performed. Co-winding with CuBe_2 was tested only with SP tapes (Figure III-19). The addition of a CuBe_2 tape does

not significantly increase the R_{ct} values; we find the values comparable to the NI case. Indeed, adding a CuBe_2 tape initially changes from one Copper-Copper interface (NI case) to two Copper-Copper interfaces (MI CuBe_2 case), which does not significantly increase R_{ct} because it is only a copper-copper like contact.

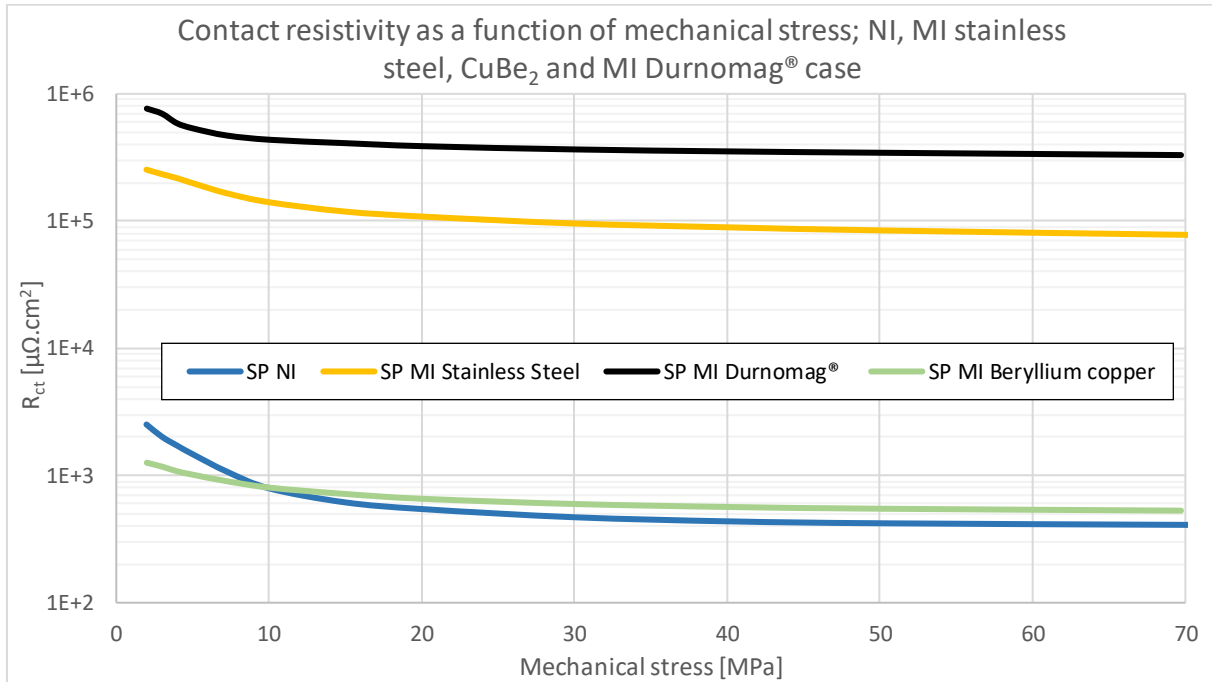


Figure III-19: Contact resistivity as a function of mechanical stress in the NI, MI Stainless steel, MI CuBe_2 and MI Durnomag® case with SuperPower tapes.

III. 2. 2. 2. 3 Soldered metallic co-wound with stainless steel tape

Previously, it was stated that the increase in R_{ct} in the MI StS or Durnomag® case is not due to the thickness of the metallic tape, but to the change in the contact interface between the superconducting and metallic tapes. This assumption is verified with the MI StS soldered case for SP and Theva. By soldering our tapes, the two "Copper-Stainless steel" interfaces generated by adding a StS tape is neglected. The R_{ct} value is the same order of magnitude as the soldered NI case: $\sim 10 \mu\Omega \cdot \text{cm}^2$ for soldered SuperPower MI StS and $\sim 10^3 \mu\Omega \cdot \text{cm}^2$ for soldered Theva MI StS (Table III-5). The addition of resistive material is not the only reason for the increase in R_{ct} . Thus, the 100 μm thickness of the substrate in the case of the tape Theva is therefore not responsible for the higher R_{ct} values compared to SP or SST, which has a 50 μm substrate.

Table III-5: Contact resistivity for soldered NI and MI StS – Durnomag® – CuBe_2 .

Soldered case	Theva NI	Theva MI StS	SP NI	SP MI CuBe_2	SP MI StS	SP MI Durnomag®
R_{ct} [$\mu\Omega \cdot \text{cm}^2$]	2 501	3 737	2.6	3.7	6.6	8.0

The contact resistivity of SP and Theva in the soldered NI case are independent of mechanical stresses, the contact resistivity measurements were conducted without applying a mechanical stress on the samples.

Considering a resistivity of StS at 77 K $\rho_{ss@77K} = 600 \cdot 10^{-9} \Omega \cdot \text{m}$ and assuming perfect contact, adding $l = 50 \mu\text{m}$ of StS should increase the R_{ct} value by $R_{ct} = \rho_{StS@77K} \cdot l = 600 \cdot 10^{-9} \times 50 \cdot 10^{-6} \Omega \cdot \text{m}^2 = 0.3 \mu\Omega \cdot \text{cm}^2$, which is small in front of the value of $R_{ct_{MI-soldered}} \approx 10 \mu\Omega \cdot \text{cm}^2$. Experimentally, the measured value of $R_{ct_{MI-soldered}}$ is higher than the theoretical value. This slight increase is explained by the presence of some asperity holes not filled with solder (Figure III-20).

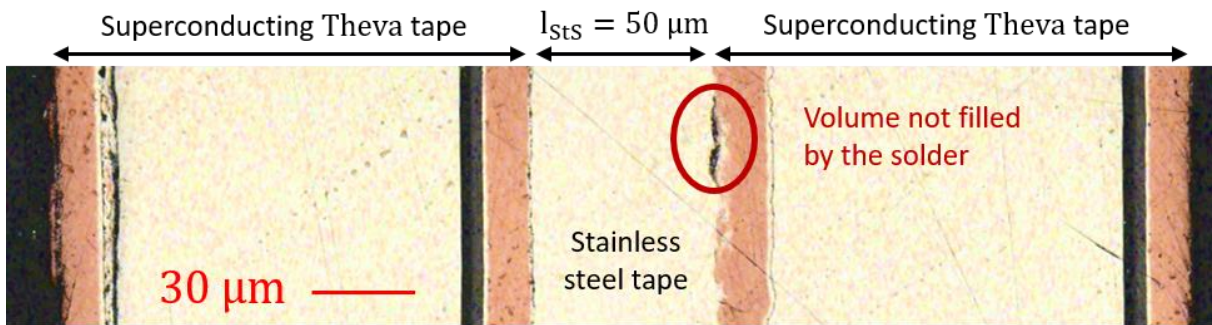


Figure III-20: Cross-sectional view of soldered Theva MI stainless steel tapes.

III. 2. 2. 2. 4 Double metallic co-wound tape

A final solution was tested: doubling the number of metallic tapes (2xMI) with the objective of increasing R_{ct} . Over the range of [2 MPa; 70 MPa], the R_{ct} was increased by a factor of 5 in the case of Durnomag[®] and by a factor of 8 in the case of StS co-wound tape. Indeed, co-winding a second metallic tape adds an extra contact interface. We pass from two Copper-StS interfaces (MI StS) to two Copper-Stainless steel interfaces + one StS-StS interface (2xMI StS). This StS-StS interface significantly increases the R_{ct} value. The behavior is similar with the Durnomag[®] tape.

In the case of a double metallic co-wound tape with a CuBe₂ tape, the increase in R_{ct} is very small (Figure III-21). We remain in a range of R_{ct} characteristic of the NI case. This can be explained by the addition of a new Copper-Copper interface which does not strongly increase R_{ct} . It should be noted that measurements with higher contact resistivity are not possible. Increasing the stack electrical resistance causes an increase in the temperature of the samples, which will distort the R_{ct} values. Indeed, the R_{ct} value depends on the temperature of the sample [85].

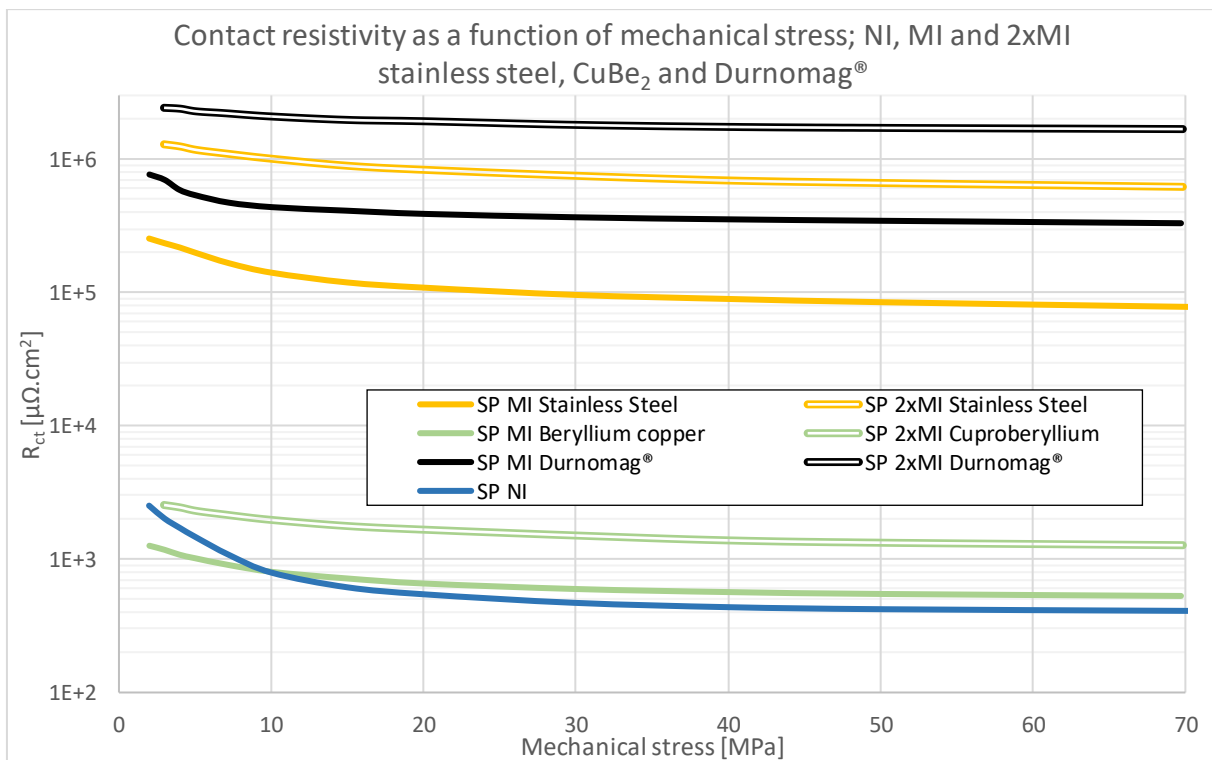


Figure III-21: Contact resistivity as a function of mechanical stress in the NI, MI and 2xMI stainless steel, CuBe₂ and Durnomag[®] case with SuperPower tapes.

III. 2. 2. 3 Influence of the number of mechanical cycles

It is important that fluctuations in contact resistivity during the life of the magnet do not alter its electromagnetic and mechanical behavior. The measurements made in this section allow us to understand and estimate these fluctuations over a few hundred/thousand cycles, which is typical of the number of cycles a magnet will undergo in its lifetime. The contact resistivity R_{ct} in NI and MI configuration (stainless steel, beryllium copper and Durnomag[®] metallic tapes) is measured between superconducting tapes as a function of the number of mechanical cycles, always at 77 K and for different manufacturers (SuperOx, Theva and SST). For NI and MI CuBe₂ samples, the imposed current is 50 A. For MI Durnomag[®] and MI StS, it is 10 A. With the same device, it is possible to measure up to six samples at the same time. For each manipulation, the device consists of three samples of one type of insulation and three other samples of another type of configuration. We alternate the two configurations in the stack in order to limit the position in the stack in the measurement of R_{ct} .

A pre-load up to 3 MPa and then mechanical cycles from 3 to 40 MPa are performed. In the previous measurements, the decrease in the contact resistivity value as a function of mechanical stress is small from 40 MPa. Mechanical cycling above 40 MPa is not necessary. A cycle lasts about 30 s (Figure III-22), i.e. about 960 cycles in 8 h. A constant displacement speed is imposed on the press until it reaches the value of 40 MPa. The displacement speed is the same during the discharge.

The results presented are plotted in semi-log for each configuration and are the average of the three samples tested simultaneously. These are the contact resistivity values of the samples at maximum load (40 MPa).

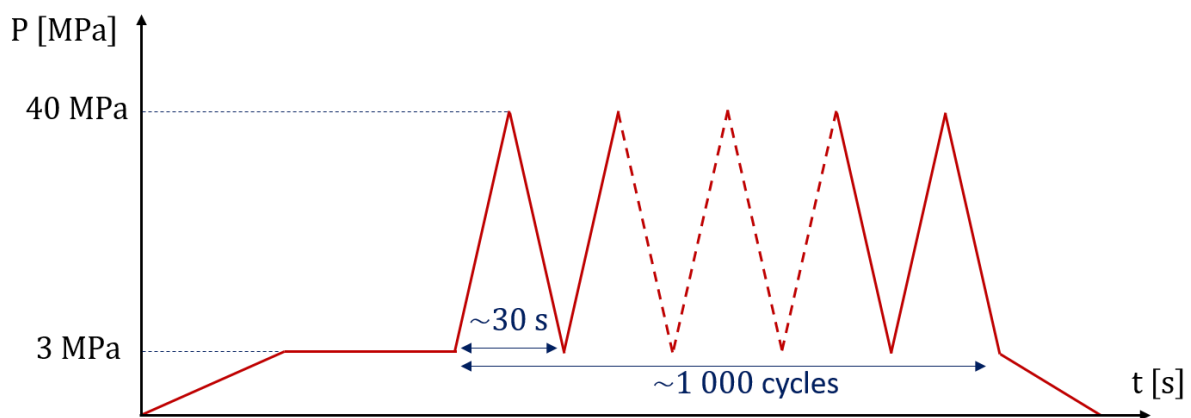


Figure III-22: Profile of the mechanical stress applied to the tapes.

III. 2. 2. 3. 1 SST and SuperOx NI at 23 MPa

First measurements were made with a maximum mechanical stress of 23 MPa with SuperOx and SST (free tapes given by Shanghai Superconductor Technology) NI samples (Figure III-23) in order to study the influence of the maximum mechanical stress during cycles. A slight increase in contact resistivity during the first five cycles is measurable with SST NI samples, and only with the second cycle for SuperOx. This behavior was also observed by J. Lu who attributes this effect to cryogenic work hardening of copper under cyclic load (up to 25 MPa) [85]. A decrease in R_{ct} then occurs for SST, before stabilising at around $15 \mu\Omega \cdot \text{cm}^2$ after about 100 cycles. For the SuperOx NI samples, a decrease is also visible (from 2000 to $200 \mu\Omega \cdot \text{cm}^2$, i.e. a decrease of 90%), but unlike the SST NI samples, it continues to decrease even after 100 cycles. J. Lu speculates that this decrease in R_{ct} with the number of mechanical cycles may be due to a destruction of the oxidation layer on the surface of the tapes.

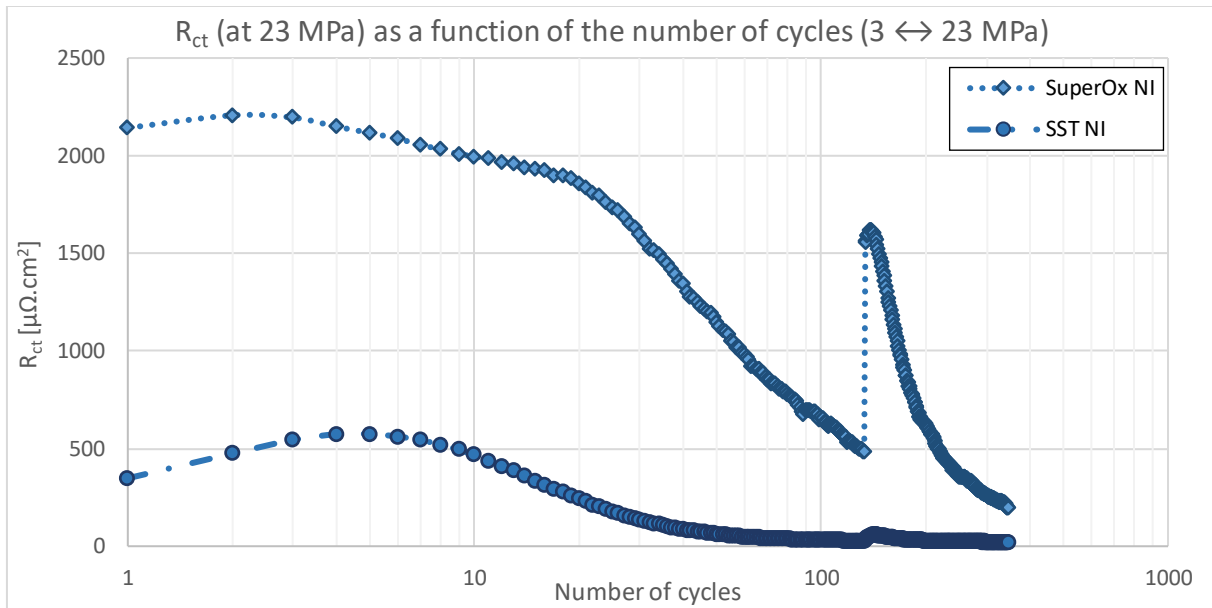


Figure III-23: Evolution of R_{ct} (at 23 MPa) as a function of the number of cycles (3 ↔ 23 MPa) for SST and SuperOx NI.

A second possible effect may be a plastic deformation occurs with each compression cycle, increasing the contact area between the tapes, thus decreasing the contact resistivity. The higher the number of cycles, the less plastic deformation there will be for each compression cycle. Elastic deformations also occur, but these are increasingly small as the repeated compression of the tapes increases the plastically deformed areas.

To see this phenomenon, surface roughness was measured on several areas of SST and SuperOx tapes before and after compression. For SST tapes, a decrease in roughness is measurable using a confocal microscope, on the superconducting or Hastelloy® side of the tape. For the sample in Figure III-24, the roughness is 0.64 μm before compression compared to 0.63 μm after compression. Visually, a difference can be seen at the top of the "crystals" on the copper surface of SST tape, mainly on the Hastelloy® side. Plastic deformations are clearly visible. As the yield strength of copper is 33 MPa, this limit is exceeded locally in the contact areas even at an average stress of 23 MPa imposed on the stack. As the SuperOx tape is flat compared to SST, no difference is observable or measurable with the confocal microscope. This is due to the roughness being lower for SuperOx than for SST (see Table III-3 and Figure III-12).

However, the order of magnitude decrease in contact resistivity, due to the number of charge cycles, for SuperOx and SST would imply an order of magnitude increase in the contact area between the superconducting tapes, which is relatively large. The change in contact area does cause a decrease in R_{ct} , but other phenomena such as the destruction of the oxidation layer can explain this decrease in R_{ct} .

In Figure III-23, the contact resistivity value for SST stabilizes more quickly compared to SuperOx. This can be explained by the hardness of the copper layer on the surface of the SST tape, which is lower than that of SuperOx (see Table III-3). Larger areas are plastically deformed for SST compared to SuperOx. A lower number of mechanical cycles is sufficient to achieve a relatively constant value.

For the SST and SuperOx curve in Figure III-23, a rise in R_{ct} at the 130th cycle is observable. This peak corresponds to a problem that occurred during the cycle control, which led to the release of the mechanical stress on the sample. The value of the contact resistivity after this release is not equal to the values of the first load cycle because plastic deformations are present on the tape surface.

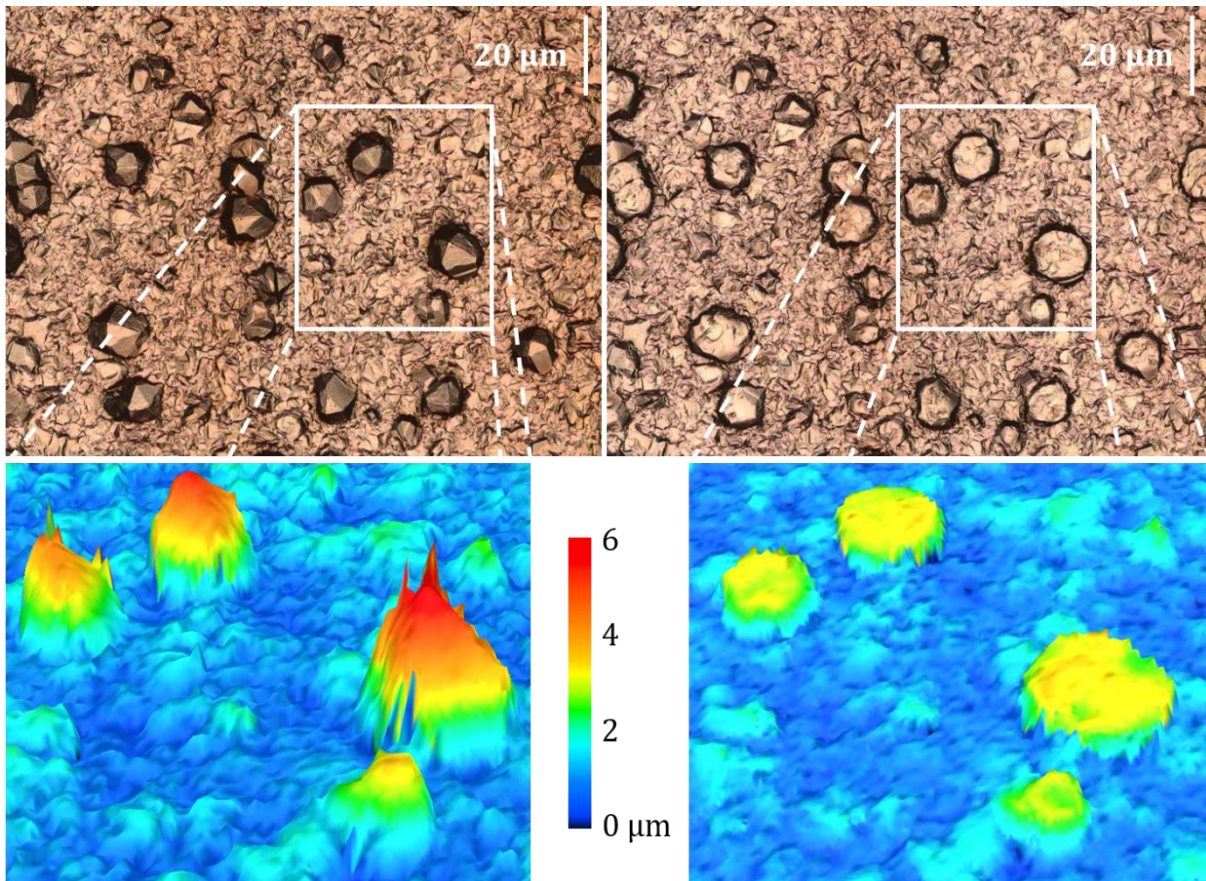


Figure III-24: Image and 3D representation of the surface condition of a SST tape on the Hastelloy® side before (left) and after compression (right).

III. 2. 2. 3. 2 SuperOx NI and MI beryllium copper alloy configuration at 40 MPa

Figure III-25 shows SuperOx NI and MI CuBe_2 . Concerning the SuperOx NI, a decrease in the contact resistivity is observable during the first 600 cycles (from 400 to 40 $\mu\Omega\cdot\text{cm}^2$, i.e. a decrease of 90%), to then remain relatively constant at 40 $\mu\Omega\cdot\text{cm}^2$ beyond 600 cycles. For SuperOx with the presence of a CuBe_2 tape, the R_{ct} variation is less significant (from 90 to 35 $\mu\Omega\cdot\text{cm}^2$, i.e. a decrease of 61%). The presence of the metallic tape reduces the R_{ct} variation with the number of mechanical cycles. In addition, in the case where the maximum mechanical stress for each cycle is increased (from 23 MPa to 40 MPa in the case of the SuperOx NI sample), the increase in R_{ct} for the first few cycles is less pronounced or even non-existent for the samples tested.

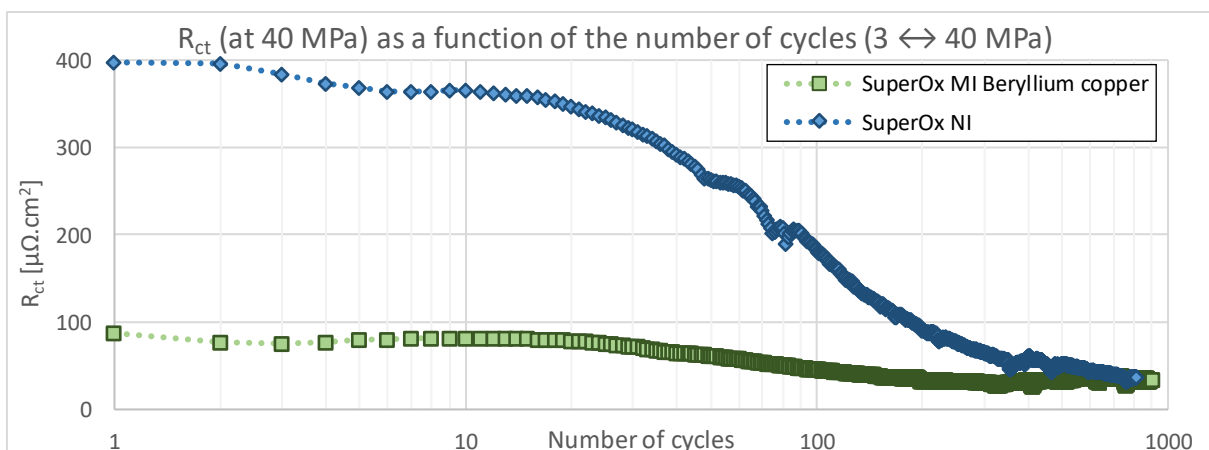


Figure III-25: R_{ct} (at 40 MPa) as a function of the number of cycles (3 \leftrightarrow 40 MPa) for SuperOx NI and MI beryllium copper.

The plastic deformation can be seen in Figure III-26, where the value of the contact resistivity as a function of the mechanical stress for different cycles is plotted. The higher the number of mechanical cycles, the more the contact resistivity decreases in part due to the increase of plastically deformed areas, until saturation is reached. The contact resistivity value no longer varies, i.e. there is no longer any plastic deformation generated by the mechanical cycles. Slight load-dependent fluctuations between 3 and 40 MPa can be observed for cycles above 600, which is explained by small elastic deformations.

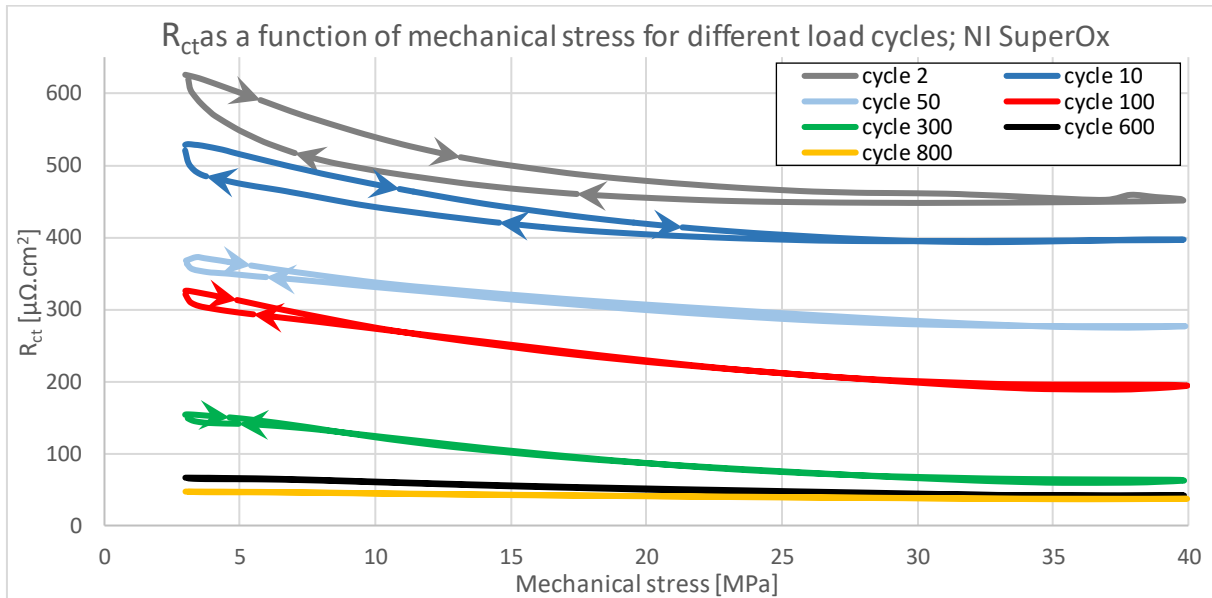


Figure III-26: Contact resistivity as a function of mechanical stress for different load cycles; SuperOx NI

III. 2. 2. 3. 3 Theva NI and MI beryllium copper alloy configuration at 40 MPa

The same measurements were made with Theva in NI and MI CuBe₂ configuration (see Figure III-27). Here again, a slight increase in contact resistivity is measurable during the first ten cycles before observing a decrease and stabilization at around 300 cycles. In addition, as with SuperOx, the presence of the CuBe₂ tape strongly reduces the R_{ct} decrease in with the number of mechanical cycles. As a reminder, the higher MgO layer for Theva compared to other manufacturers causes the increase in contact resistivity (see III. 2. 2. 1. 2).

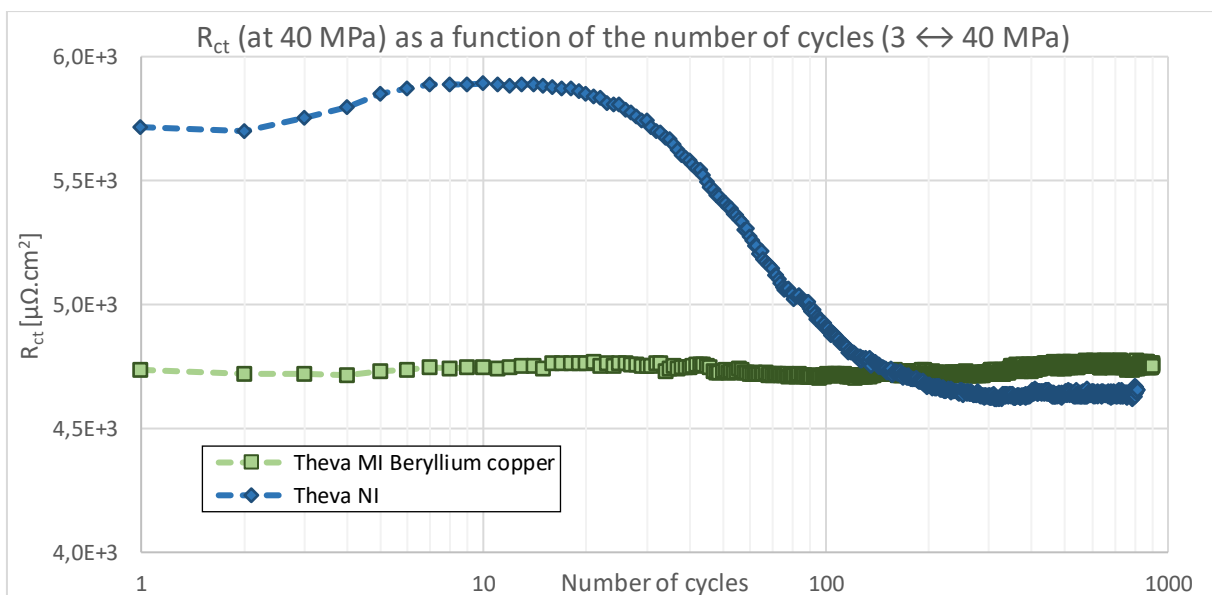


Figure III-27: R_{ct} (at 40 MPa) as a function of the number of cycles (3 ↔ 40 MPa) for Theva NI and MI beryllium copper.

III. 2. 2. 3. 4 SuperOx and Theva, MI stainless steel and Durnomag® configuration

With the presence of the CuBe² tape, the decrease in contact resistivity with the number of mechanical cycles is less pronounced. With the presence of a stainless steel or Durnomag® tape, variations are observed. Adding a metallic tape increases the number of mechanical cycles required before a globally constant value is reached. In the four different measurements (SuperOx and Theva in MI StS and Durnomag® configuration), a slight increase is measurable. After a few hundred cycles, R_{ct} starts and continues to decrease even after 1000 cycles. No constant value can be observed.

Although the hardness of Durnomag® tape is higher than of StS (Table III-2), which allows for higher contact resistivity values, this does not prevent R_{ct} from varying with the number of mechanical cycles. Nevertheless, this variation is not abrupt. Even in the worst case (SuperOx MI StS), R_{ct} drops by a maximum of one order of magnitude after about 1 000 cycles.

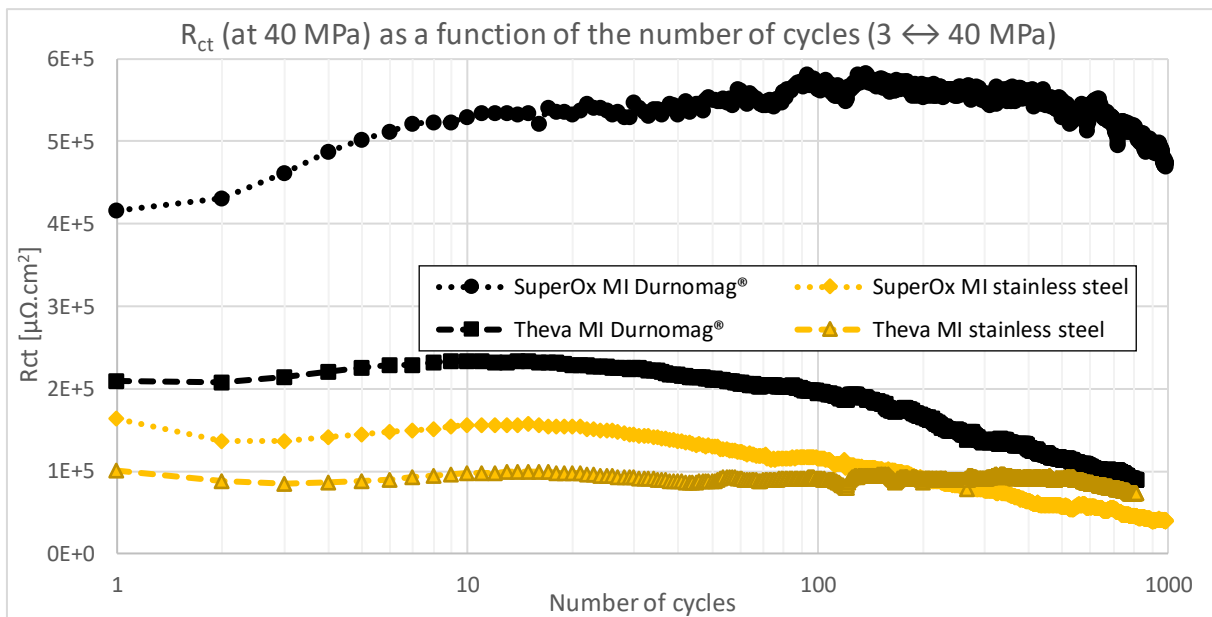


Figure III-28: Evolution of R_{ct} (at 40 MPa) as a function of the number of cycles (3 ↔ 40 MPa) for Theva and SuperOx MI stainless steel and beryllium copper.

Thus, whether in NI or MI configuration, R_{ct} decreases with increasing number of mechanical cycles, before being globally constant after about 500 cycles in the NI case. In the MI case, the presence of the metallic tape imposes a greater number of mechanical cycles before reaching a stable value, but the order of magnitude of R_{ct} is maintained and the variations are relatively small.

III. 2. 2. 4 Simulation and experimental comparison

Simulations of a double pancakes in case of rapid discharge are performed using our PEEC model [26] with two contact resistivity values: $0.1 \Omega \cdot \text{cm}^2$ and $0.3 \mu\Omega \cdot \text{cm}^2$. The results of the field decay are then compared to experimental values of the nine double 290-turn pancakes co-wound with a Durnomag® tape (CEA-LNCMI NOUGAT magnet [22]) at 77 K. The experimental plots are interleaved between the two simulations (only two of the nine double pancakes are displayed for better visibility). In the results of Figure III-29, the experimentally measured field decay does not go down to 0, contrary to the simulation. This is due to the screening currents (SCIF) which are not considered in our PEEC model. Experimentally, the discharge time constant is between 2.3 ms and 6 ms for the nine double pancakes (decreasing exponential fit); and having each an inductance of 26.46 mH, we obtain

a contact resistivity between $110 \text{ m}\Omega\cdot\text{cm}^2$ and $290 \text{ m}\Omega\cdot\text{cm}^2$ [81]. Both approaches give the same results: the contact resistivity for this type of coil is relatively high, $R_{ct} \in [100 ; 300] \text{ m}\Omega\cdot\text{cm}^2$. These results are consistent with the R_{ct} values measured on the superconducting tape stack with Durnomag[®] tapes ($R_{ct} \in [150 ; 1,000] \text{ m}\Omega\cdot\text{cm}^2$, for stresses ranging from 2 to 70 MPa, whatever the manufacturer).

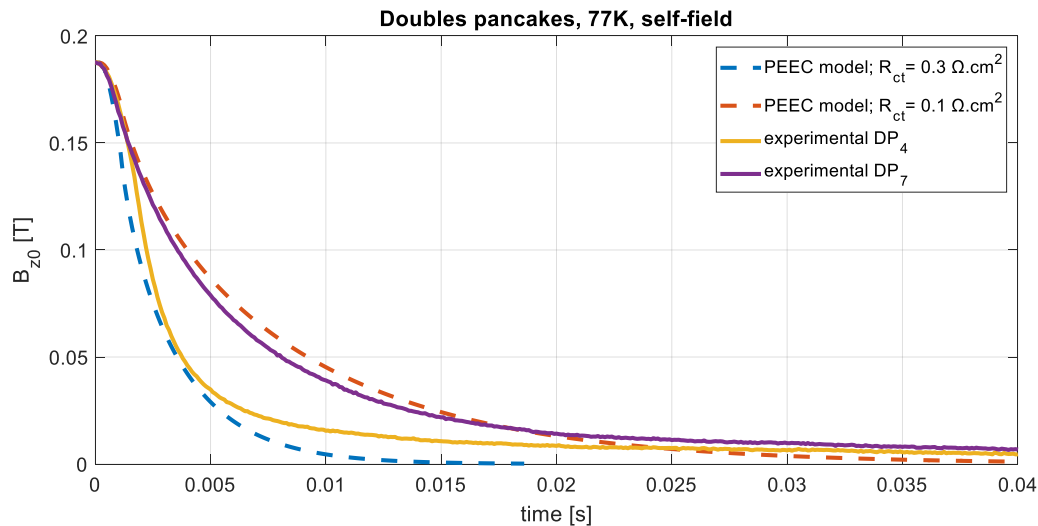


Figure III-29: Experimental results and simulations of double pancakes co-wound with a Durnomag[®] metallic tape [81].

III. 2. 3 Conclusion experimental measurements of contact resistivity between superconducting tapes

Through all these measurements, made at 77 K with 6 mm wide HTS tapes and for stresses ranging from 2 to 70 MPa, we can conclude that the contact resistivity R_{ct} between superconducting tapes depends on:

- The **thickness of the different buffer** layers that compose the superconducting tapes (mainly in the NI and soldered NI cases)
- The **surface condition** of the superconducting tapes (oxidation, roughness and hardness of the copper layer, mainly in the NI case, negligible in the MI case)
- The presence and number of **metallic tapes**
- The **mechanical stress**: high dependence at low stress and kind of stabilization at high stress
- The **hardness** of the metallic tapes in the case of a co-winding
- The **nature** of the materials in contact

Many parameters influence the R_{ct} value. It is difficult to accurately determine the importance of each parameter on the contact resistivity value, because it would be necessary to vary one parameter at a time, which is relatively complex to implement in the case of a superconducting tape. However, depending on the winding technology, it is possible to choose the order of magnitude of R_{ct} (between $1 \mu\Omega\cdot\text{cm}^2$ and $10^7 \mu\Omega\cdot\text{cm}^2$), mainly by adding a metallic co-wound tape in a dry wound coil. This in some cases makes parameters such as the hardness of the copper layer of the superconducting tape, or even the composition of the buffer layers, negligible. It also might reduce the relative influence of the radial stresses in a winding, which is of great importance to control the current path during transient step of a magnet run.

In the first part of this Chapter III, we have seen that the modification of the contact resistivity is possible by adding a metallic tape. In the second part, we will now see whether it is possible to modify and control this contact resistivity using an atomic layer deposition.

III. 3 Experimental measurements of contact resistivity between superconducting tapes with an Atomic Layer Deposition

III. 3. 1 Introduction

III. 3. 1. 1 Purpose of the Atomic Layer Deposition

The objective of this part is to perform an atomic layer deposition (ALD) of a few hundred nanometers directly on the superconducting or metallic tapes surface in order to modify and control the contact resistivity R_{ct} . The Atomic Layer Deposition is a synthesis method based on self-limiting and sequential surface reactions between chemicals in vapor form called precursors. ALD allows growth, atomic layer by atomic layer, in a compositionally and thickness compliant manner on objects with complex geometries and large surfaces. This deposition technique, developed since the 1970s, is slow (between 1 Å and 1 nm per minute) and is therefore reserved for the synthesis of films with a thickness of less than 1 μm.

The idea is to deposit an insulating material on the tape surface (superconducting or metallic) in order to significantly increase and control the contact resistivity by modifying the resistivity value of the deposited film. This will allow obtaining complex contact resistivity ranges to be generated with the different techniques presented in the previous chapter (soldered tapes, NI tapes, MI, soldered MI and double MI). In particular, values between 10^3 and 10^5 μΩ.cm² (Figure III-21). For this purpose, a deposit consisting of two precursors, with varying proportions, is used in order to vary the ALD thin film resistivity.

First, we will look at the choice of the ALD in order to obtain the desired values. Secondly, the experimental measurements of the contact resistivity with the presence of the ALD will be presented. Finally, we will see why the results obtained are different from the expected values.

III. 3. 1. 2 Choice of the Atomic Layer Deposition and the deposition support

The bench for thin film deposition consists of a 500 mm long chamber with a diameter of 50 mm. The deposition temperature can be adjusted between 100°C and 500°C and under a pressure of about $5 \cdot 10^{-3}$ mbar. A deposit consisting of zinc oxide (ZnO, conductive) and alumina (Al₂O₃, insulating) was chosen because it is possible to achieve an atomic thin film resistivity between 10^{-3} Ω.cm and 10^{16} Ω.cm (on the left, Figure III-30) depending on the proportion of precursors [103]. However, the deposition temperature, which is 177°C, is too high to directly deposit the thin film on a superconducting tape. Indeed, it is possible to apply temperatures around 230°C for a few hundreds of seconds, but imposing temperatures higher than 100°C for several hours will degrade the critical current value of the superconducting tape [18] (on the right, Figure III-30).

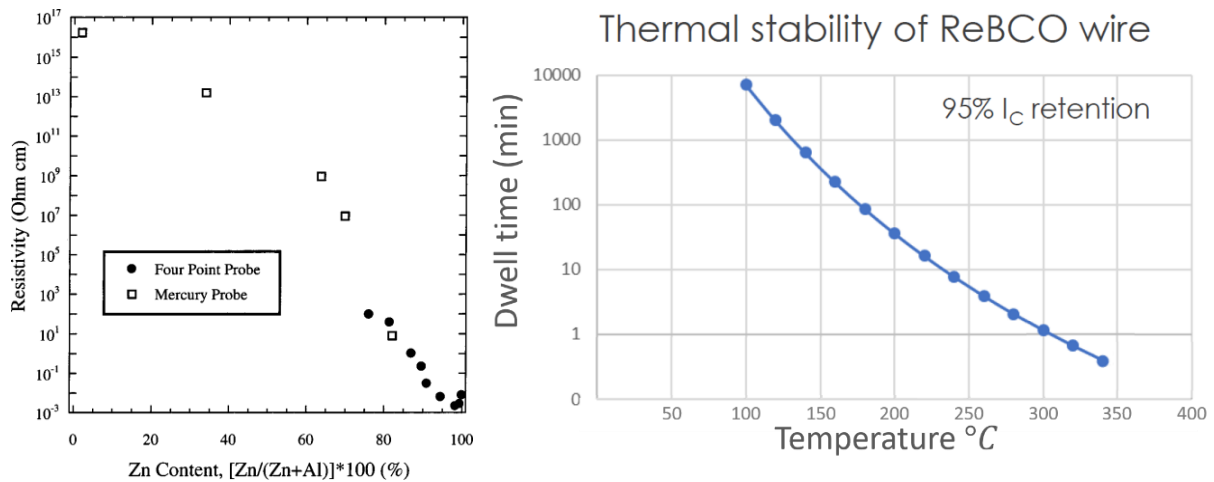


Figure III-30: On the left, evolution of the resistivity of the ZnO/Al₂O₃ ALD versus the precursor content [103]. On the right, degradation of the critical current of a Theva tape versus temperature and dwell time [18].

Tests were performed at 77 K and low atmospheric pressure ($\approx 5.10^{-3}$ mbar) on three 6 mm wide SuperPower superconducting tapes to measure the critical current decay when subjected to 130°C and 180°C during three hours (simulate ALD on superconducting tape). For each tape, four voltage measurements were taken on four 85 mm lengths before and after the simulated ALD (Figure III-31). The detection threshold is set at $E_0 = 10 \mu\text{V}/\text{cm}$ to properly observe the transition of the tape. The voltage giving the critical current value is 85 μV . In an HTS tape, the critical current value is variable along the length of the tape. In our measurements, the voltages of the four sectors are relatively identical.

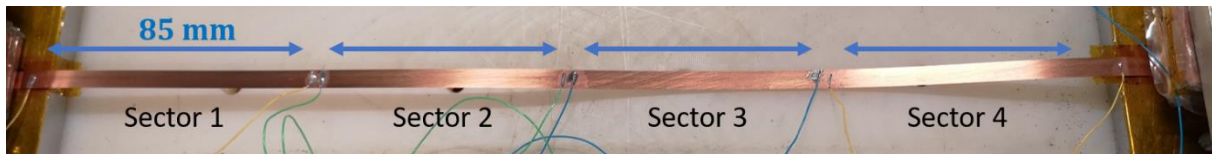


Figure III-31: Plate with four sectors for measuring the critical current after the simulated ALD.

The readings in Figure III-32 correspond to the voltage of the first of the four sectors. The results are available in the Table III-6. Without the simulated ALD, the critical current value is $I_{c-\emptyset \text{ simulated ALD}} = 201.1 \text{ A}$. With the tape placed at 130°C during three hours, the critical current value decreased by about 4%, $I_{c-130^\circ\text{C}} = 193.7 \text{ A}$. Finally, with a temperature of 180°C during three hours, the critical current value decreased by about 28%, $I_{c-180^\circ\text{C}} = 145.6 \text{ A}$. Therefore, it is not possible to directly deposit at 177°C on our superconducting tapes.

Table III-6: Influence of the useful temperature for the ALD on the SuperPower critical current tape.

	\emptyset simulated ALD	$T = 130^\circ\text{C}$	$T = 177^\circ\text{C}$
I_c [A] / decline [%]	201.1 / 0	193.7 / 4	145.6 / 28

One of the possibilities is to lower the deposition temperature to 130°C, this will have an influence on the thin film resistivity value but the critical current of the superconducting tape will be only slightly reduced. However, by performing several measurements with deposits having different precursor contents, it will be possible to modify the contact resistivity value, and thus to know the proportion of precursors to obtain the desired R_{ct} value.

A second possibility is to carry out the deposits directly on CuBe₂ tapes. Indeed, in the Chapter III, we have seen that adding a tape of CuBe₂ between superconducting tapes did not greatly modify the contact resistivity value. The measured values were comparable to the NI case (Figure III-19). Adding an ALD on the CuBe₂ tape and then interposing it between two superconducting tapes should make it possible to control the contact resistivity value.

After consideration, both possibilities have been realized at the same time: an **ALD at 130°C on CuBe₂ tapes** and then to intercalate them between the two superconducting tapes.

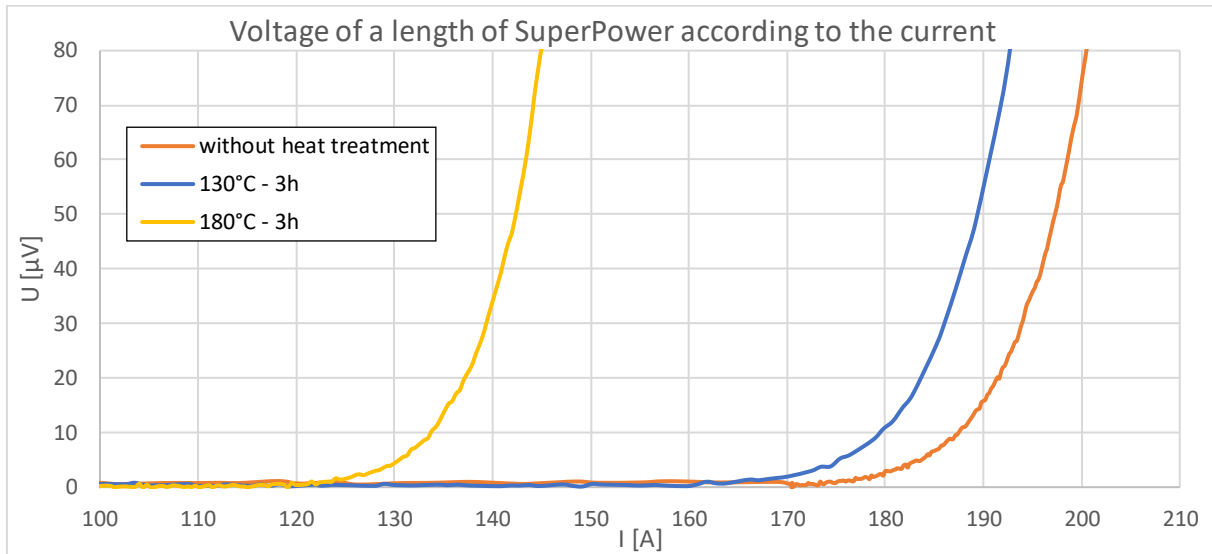


Figure III-32: Voltages of a length of SuperPower according to the current, influence of the useful temperature for the ALD.

III. 3. 1. 3 Expected values with Atomic Layer Deposition zinc and alumina oxide

A simple setup was designed to keep the CuBe₂ tapes spaced apart to properly deposit the thin film in the ALD chamber. This setup also allows for the insertion of a larger number of metallic tapes. For some deposits, StS and Durnomag[®] tapes were positioned with the CuBe₂ tapes. The tapes are then inserted into the ALD chamber (Figure III-33). The thickness of the targeted deposit is $l_{ALD} = 100$ nm, the operation takes about 10 hours.

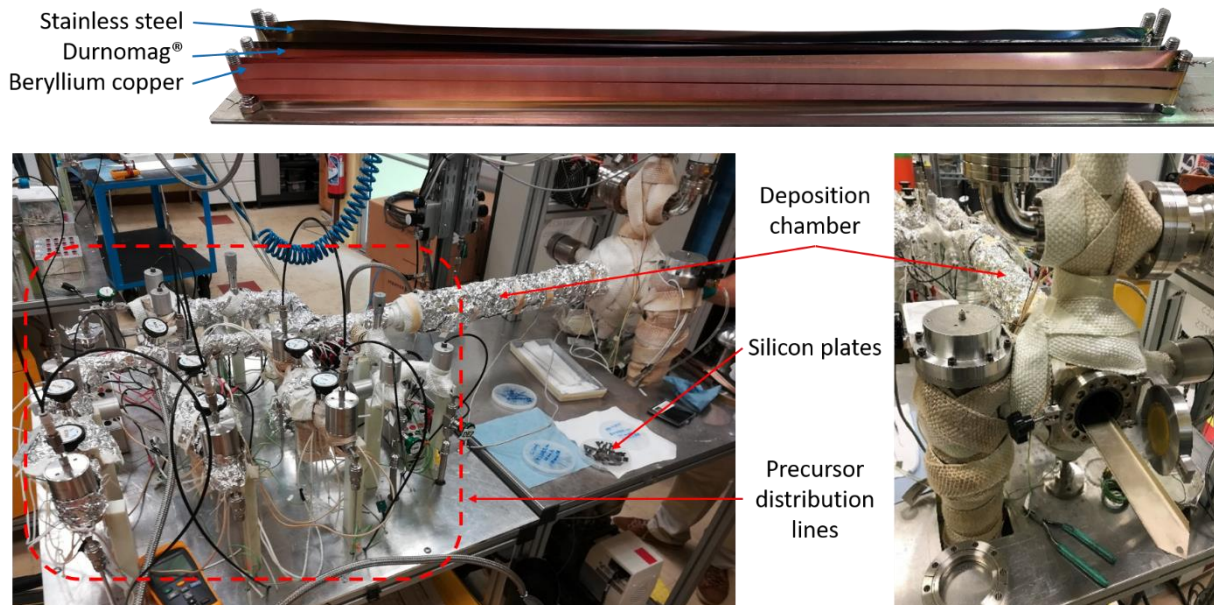


Figure III-33: On the top, stainless steel, Durnomag[®] and CuBe₂ tapes prior to ALD. At the bottom, thin film deposition bench consisting mainly of the deposition chamber and the various precursor distribution lines.

Three different deposits were performed with a deposition temperature of 130°C:

- 80% ZnO–20% Al₂O₃, only on CuBe₂ tapes.
- 75% ZnO–25% Al₂O₃, on CuBe₂, StS and Durnomag[®] tapes.
- 67% ZnO–33% Al₂O₃, on CuBe₂, StS and Durnomag[®] tapes.

Varying the content of the two precursors changes the deposited thin film resistivity value and thus theoretically changes the contact resistivity. From the resistivity measurements of the ZnO/Al₂O₃ deposit as a function of precursor content, a deposit with 80% ZnO generates a resistivity $\rho_{80\% \text{ ZnO}} \approx 10 \text{ } \Omega \cdot \text{cm}$ (Figure III-30). With 75% and 67% zinc oxide, resistivities $\rho_{75\% \text{ ZnO}} \approx 10^2 \text{ } \Omega \cdot \text{cm}$ and $\rho_{67\% \text{ ZnO}} \approx 10^8 \text{ } \Omega \cdot \text{cm}$ are obtained, respectively. As a reminder, in the case of two SuperPower MI CuBe₂ tapes, the contact resistivity value at 20 MPa is approximately $10^3 \text{ } \mu\Omega \cdot \text{cm}^2$.

In order to estimate the increase caused by the addition of the ALD, we consider a perfect contact over the entire tapes surface (over the 290 mm by 6 mm). With a resistivity $\rho_{80\% \text{ ZnO}} \approx 10 \text{ } \Omega \cdot \text{cm}$ and a thickness of the $l_{\text{ALD}} = 100 \text{ nm}$, we obtain a contact resistivity generated only by the ALD of: $\rho_{80\% \text{ ZnO}} \times 2l_{\text{ALD}} = 2 \cdot 10^{-4} \text{ } \Omega \cdot \text{cm}^2 = 200 \text{ } \mu\Omega \cdot \text{cm}^2$. The factor 2 takes into account the deposit thickness on both sides of the CuBe₂ tape (Figure III-34). Theoretically, the increase in contact resistivity in the case of a CuBe₂ tape with an 80% ZnO - 20% Al₂O₃ ALD at 130°C is relatively small compared to the contact resistivity value with a simple CuBe₂ tape. The difference between the two cases should not be observable. With 75% ZnO deposition, the resistivity $\rho_{75\% \text{ ZnO}} \approx 10^2 \text{ } \Omega \cdot \text{cm}$ should increase the contact resistivity by about 2 000 $\mu\Omega \cdot \text{cm}^2$. A slight increase should be observable, but the values obtained should be comparable to NI or MI CuBe₂ windings.

The third deposition with 67% ZnO is performed in order to obtain a significant increase in contact resistivity (compared to the NI or MI CuBe₂ case). With this zinc oxide and alumina content, the resistivity of the deposit is $\rho_{67\% \text{ ZnO}} \approx 10^8 \text{ } \Omega \cdot \text{cm}$. This should increase the contact resistivity by about $2 \cdot 10^9 \text{ } \mu\Omega \cdot \text{cm}^2$. The experimental measurements with these three different deposits are presented in the next section.

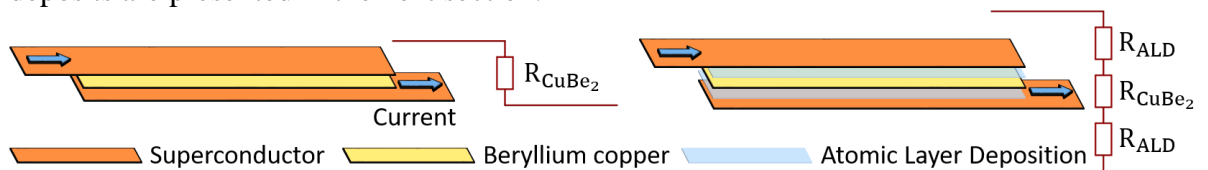


Figure III-34: Sketch of the modification of the contact resistivity by adding a thin atomic layer.

III. 3. 2 Contact resistivity with 100 nm Atomic Layer Deposition

Contact resistivity measurements for the three ALD are made on six samples supplied in series. Each sample consists of a CuBe₂ tape interposed between the two SP superconducting tapes (Table III-7). Among the six CuBe₂ tapes, four have received an ALD while the last two are without ALD: these are the reference samples (Figure III-35).

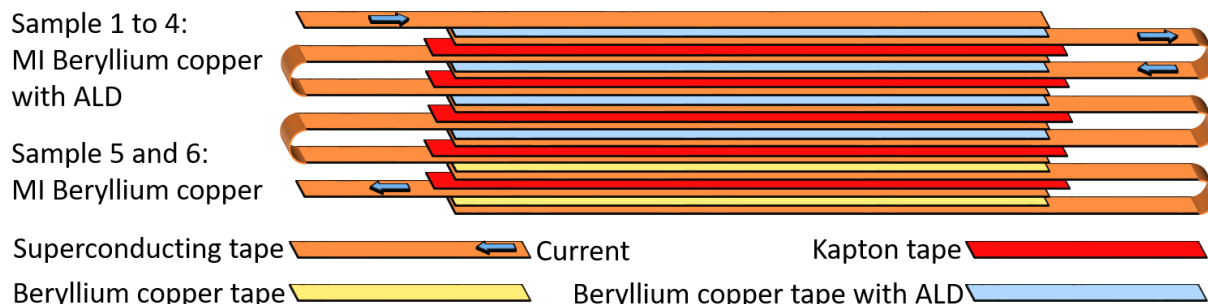


Figure III-35: Sketch of six samples for load-dependent R_{ct} measurements with and without the influence of the ALD.

The R_{ct} values will be measured as a function of the mechanical stress at 77 K (liquid nitrogen), with a current value $I_0 = 30 \text{ A}$ that is both high to have accurate measurements but without causing heating of the samples. As for the Chapter III, the results presented and compared are those of the first phase of the second load cycle. Each assembly was subjected to three load

cycles: a load ramp-up from 2 to 70 MPa, then a ramp-down to 2 MPa. The contact resistivity value for each of the three ALD (Figure III-36) is the average of the four samples. The contact resistivity value in the MI CuBe₂ case without ALD (the reference samples) is the average of the 2×3 samples present in the three assembly tested separately.

Table III-7: Metallic and superconducting tapes dimensions for R_{ct} measurements with ALD.

	Stainless steel	Beryllium copper	Durnomag®	SuperPower
Length [mm]	300	300	300	385
Width [mm]	6	6	6	6
Thickness [μm]	50	50	30	~75 – 85

As expected, there was a slight increase in the contact resistivity value for the 80% and 75% ZnO deposits (Table III-8 and Figure III-36). The values remain comparable to a NI or MI CuBe₂ winding. However, the 67% ZnO ALD should have generated relatively high contact resistivity values (having an order of magnitude approaching $10^9 \mu\Omega\cdot\text{cm}^2$) compared to the NI case. The measurements for this ALD have an order of magnitude of $10^3 \mu\Omega\cdot\text{cm}^2$, i.e. comparable to the NI case. There is indeed a factor of two increase in contact resistivity compared to the case without ALD. **The influence of the deposit is measurable, but six orders of magnitude separate the experimental values from the theoretical ones.** Different phenomena are responsible for this slight increase of R_{ct} , much lower than expected.

In the following sections, we will first list the parameters that could and should explain variations in contact resistivity values, but which in the end have no influence. Then we will present the observed phenomena responsible for the small increase of the contact resistivity.

Table III-8: R_{ct} at 20 MPa with and without the three different deposits ALD, @ 77 K, CuBe₂ tapes, $I = 30 \text{ A}$.

20 MPa, $I = 30 \text{ A}$	without ALD	80% ZnO	75% ZnO	67% ZnO
$R_{ct} [\mu\Omega\cdot\text{cm}^2]$	1 064	1 431	1 266	2 332

III. 3. 3 Parameters that could have explained the small increase in contact resistivity with Atomic Layer Deposition

In this section III. 3. 3, the deposit temperature in the ALD chamber, thermal shocks, the content of the two precursors and the thickness of the deposit are studied in order to verify that these parameters are not responsible for the low rise in contact resistivity measured with the presence of the ALD.

III. 3. 3. 1 The deposit temperature in the ALD chamber

It is important to remember that the deposition temperature in the ALD chamber has been set at 130°C while the required temperature is 177°C [103]. This difference in ALD growth temperature implies that:

- The growth rate of zinc oxide and thus of doping in the films is different.
- The zinc oxide resistivity is also different.

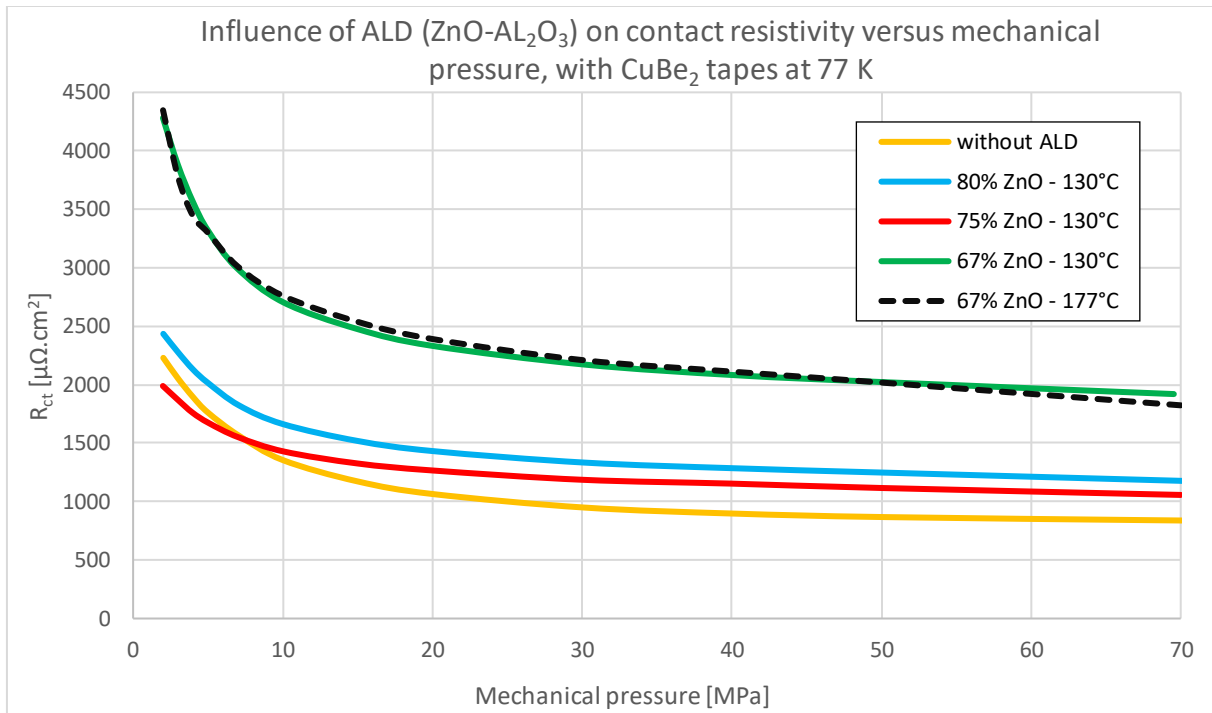


Figure III-36: Influence of ALD ($\text{ZnO}/\text{Al}_2\text{O}_3$) on contact resistivity versus mechanical stress, with CuBe_2 tapes at 77 K; $I=30$ A.

This temperature of 130°C was chosen because it does not change, or only slightly, the critical current of the superconducting tapes (III. 3. 1. 2). For CuBe_2 or StS tapes, the growth temperature can be 177°C . This is why, at first, it was thought that this important difference in measured value could come from the fact that our deposits were made at 130°C instead of the required 177°C , which could lead to a shift in the deposit resistivity depending on the content of the precursors. A new deposition of material was performed, again with a concentration of 67% ZnO, but with a deposition temperature of 177°C .

Experimentally, it is observable that **the change from 130°C to 177°C has no influence on the contact resistivity** (Figure III-36). The temperature used for the ALD of 130°C is not responsible for the small increase in contact resistivity with the presence of ALD.

III. 3. 3. 2 Thermal shock on the ALD during cooling with liquid nitrogen

The objective is to observe if cooling the tapes in liquid nitrogen has an influence on the R_{ct} generated by the ALD. Putting the metallic tapes with ALD in liquid nitrogen can eventually deteriorate the deposited thin layer due to a different thermal shrinkage between the ALD and the metallic tape. For this purpose, room temperature R_{ct} measurements on a tape with the uncooled deposit are performed in a first step. Then in a second step, the same measurements are made on the same samples cooled with liquid nitrogen.

During the 67% ZnO - 33% Al_2O_3 @ 130°C ALD, StS tapes, in addition to the CuBe_2 tapes, were placed in the ALD chamber. The setup consists of three MI StS samples with ALD 67% ZnO - 33% Al_2O_3 @ 130°C and three MI StS samples without ALD. The six samples are connected in series (the setup is relatively the same as in Figure III-35). They are electrically insulated with Kapton tapes. Since the measurements are initially made at room temperature, a low current must be imposed. Based on a value of $3 \text{ A}/\text{mm}^2$, and considering that our tapes have a conduction surface of $6 \times 0.075 = 0.45 \text{ mm}^2$, performing room temperature measurement with a current of 0.5 A is acceptable (current acquisition with the NI ± 0.5 V card instead of the ± 10 V card).

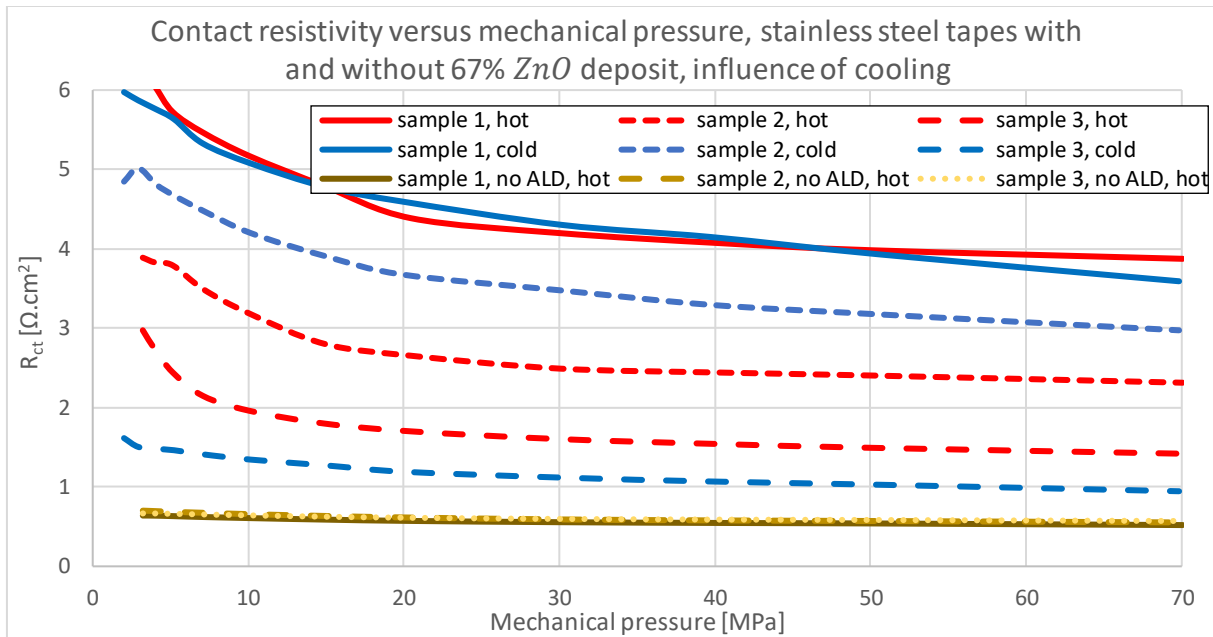


Figure III-37: Contact resistivity versus mechanical stress, stainless steel tapes with and without 67% ZnO deposit, influence of cooling; $I = 0.5 \text{ A}$.

By comparing the R_{ct} values of the StS tapes with and without ALD, we observe experimentally the presence of the ALD. Indeed, the R_{ct} values are higher with the deposit, which is consistent with the addition of a thin resistivity layer. Moreover, with a percentage of 67% ZnO, the ALD resistivity is about $\rho_{67\% \text{ ZnO}} \approx 10^8 \text{ } \Omega \cdot \text{cm}$, which should theoretically generate a contact resistivity of about $2 \times 10^3 \text{ } \Omega \cdot \text{cm}^2$. In the case of room temperature measurements (Figure III-37), the contact resistivity is about $1 \text{ } \Omega \cdot \text{cm}^2$. Therefore, the increase is not as high as expected without even cooling the samples.

Cooling with liquid nitrogen does not change the R_{ct} value for tapes with ALD by several orders of magnitude. For the three samples compared, sample 2 became more resistive (about +30%), sample 3 less resistive (about -32%) and sample 1 did not change much. A decrease in contact resistivity can be explained by a decrease in temperature while imposing an additional load cycle causes an increase in R_{ct} [85]. These two physical phenomena therefore generate variations on the R_{ct} . However, they are not responsible for a variation of two orders of magnitude on the contact resistivity value ($1 \text{ } \Omega \cdot \text{cm}^2$ measured experimentally against $100 \text{ } \Omega \cdot \text{cm}^2$ theoretically, in the case of StS tapes with ALD). **Therefore, the assumption of thin film degradation by thermal shock is not valid.**

III. 3. 3. 3 The zinc oxide and alumina content

To show that the problem does not come from the resistivity of the deposit but more from a deterioration of the thin film; a final ALD (0% ZnO - 100% Al_2O_3 @ 177°C) was performed. With this highly resistive deposit, $\rho_{0\% \text{ ZnO}} \approx 10^{16} \text{ } \Omega \cdot \text{cm}$, significant contact resistivity values should be obtained. The comparison is made between the ALD 67% ZnO - 33% Al_2O_3 @ 130°C , and the ALD 0% ZnO - 100% Al_2O_3 @ 177°C . R_{ct} measurements for both deposits are made separately. The reference samples (StS tapes without ALD) are also present in both measurement series. Figure III-38 shows and compares the results of the first phase of the second loading cycle (three samples with ALD, two samples without deposition) for both sets of measurements performed at room temperature ($\approx 290 \text{ K}$).

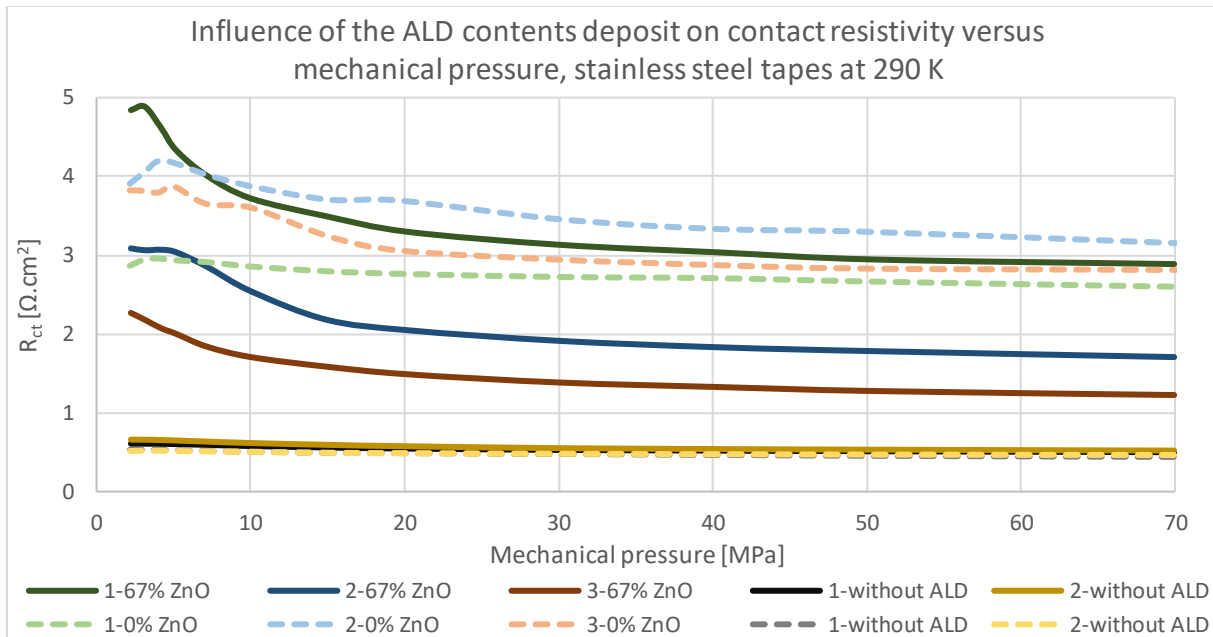


Figure III-38: Influence of the contents of ALD ($\text{ZnO}/\text{Al}_2\text{O}_3$) on contact resistivity versus mechanical stress, with stainless steel tapes at 290 K; $I = 0.5 \text{ A}$.

An increase in contact resistivity between the ALD 33% Al_2O_3 and the ALD 100% Al_2O_3 , about a factor of two, is generated by the resistivity value of the ALD 33% Al_2O_3 being much higher than the ALD 100% Al_2O_3 . However, this increase should have been much larger. The ALD is therefore not interposed on the entire contact surface between the different tapes (superconducting and StS), although it is present on the entire surface of the metallic tape. The zinc content in the deposit, therefore, influences the value of the contact resistivity but the order of magnitude is the same, although there are eight orders of magnitude between the resistivity of the 33% Al_2O_3 ALD and the 100% Al_2O_3 ALD. **The zinc oxide and alumina content is not responsible for the small increase in R_{ct} .**

III. 3. 3. 4 ALD thickness

A final hypothesis was based on a smaller than expected ALD thickness. In order to verify the presence of the 100 nm ALD, cross sections of the CuBe_2 tapes with ALD, as well as that of silicon plates previously installed with the CuBe_2 tapes, were prepared. These samples were observed using a Scanning Electron Microscope (SEM, Figure III-39).

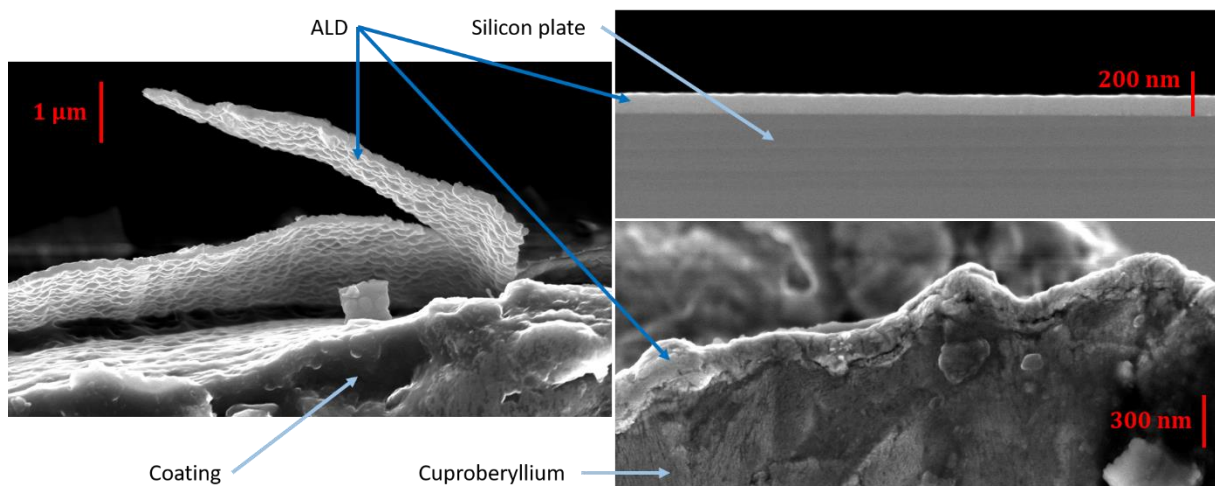


Figure III-39: SEM observation of the ALD 67% ZnO - 33% Al_2O_3 @ 130°C. On the left, thin delaminated layer. On the top right, ALD thickness on a silicon plate. At bottom right, ALD thickness on a CuBe_2 tape.

SEM allows observing a thickness of about 100 nm (more precisely 90 nm). **The thin film thickness is therefore not responsible for the small increase in contact resistivity with the ALD.**

Note: in order to make clear images of the ALD thickness, a large part of the coating necessary to prepare a cross sectional view, had to be removed in order not to charge our sample with electrons during the observation with the SEM. An insulating or poorly conducting sample is difficult to observe because of the electrons of the incident beam which are trapped and which cause an accumulation of charges in the sample. By breaking the excess coating around the CuBe₂ tapes, delamination between the ALD and the CuBe₂ tape was caused. The delaminated deposit alone is observable on the left side of Figure III-39. In addition, it was difficult to observe a thin layer on our tape: in most of the observed areas, the ALD was not clearly visible.

We have seen in this section III. 3. 3 that the deposit temperature in the ALD chamber, thermal shocks, the content of the two precursors and the thickness of the deposit are not responsible for the low rise in contact resistivity measured with the presence of the ALD. In the next section, we will see that this small increase is mainly due to delamination of the ALD at the contacts between the tapes. Then we will quickly see that the presence of the ALD causes a decrease in contact resistivity with an increase in current.

III. 3. 4 Phenomena responsible of the small increase in contact resistivity with Atomic Layer Deposition

III. 3. 4. 1 Deterioration and delamination between the ALD and the metallic tape

The deterioration of the ALD is one of the most likely hypotheses to explain the small R_{ct} increase with the presence of the zinc oxide and alumina thin film. Indeed, by observing the thickness of the ALD with the SEM (Figure III-39), delamination between the thin layer and the CuBe₂ tape are observable (other observations in Figure III-40). Thus, it is possible that the ALD is deteriorated at the level of the asperities during the compression of the tapes, causing contact zones between the metallic tape (StS or Durnomag[®]) and the superconducting tape without the presence of the ALD. This hypothesis would explain the small increase in contact resistivity with the presence of the ALD.

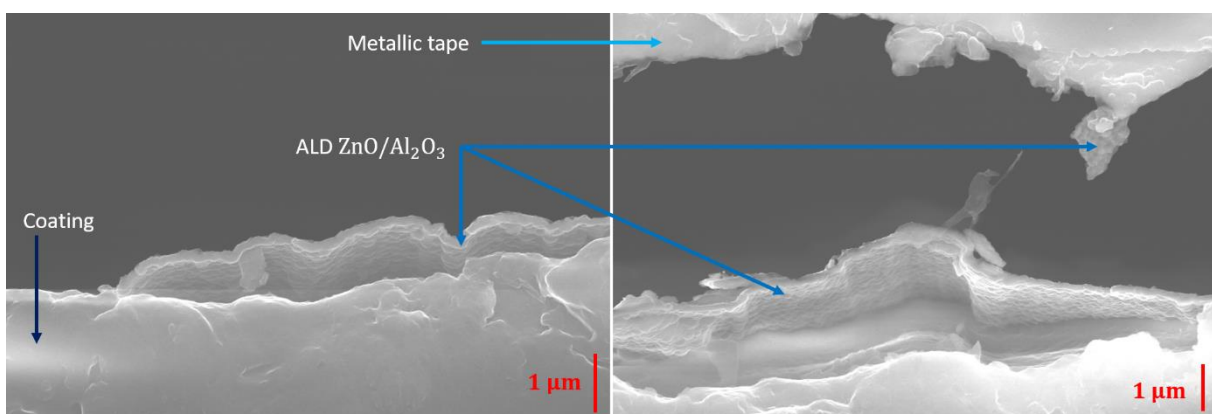


Figure III-40: ALD delamination SEM observation.

To validate this hypothesis, a simple device to compress tapes at room temperature and with a pressure of approximately ≈ 15 MPa (using Fujifilm paper [95]) was created (Figure III-41).

In order to observe the thin film behavior with a thickness of 100 nm, images of the cross-sectional views of the different tapes compressed were taken with SEM. The observed sample consists of three SST superconducting tapes, two StS tapes with the 67% ZnO - 33% Al₂O₃

ALD at 130°C and two StS tapes with an Yttrium oxide ALD (first test for this deposit, it will not be finally observed). The two StS tapes of the two deposits are inserted between the superconducting tapes in order to have stainless steel-superconducting contacts with the ALD between the tapes.

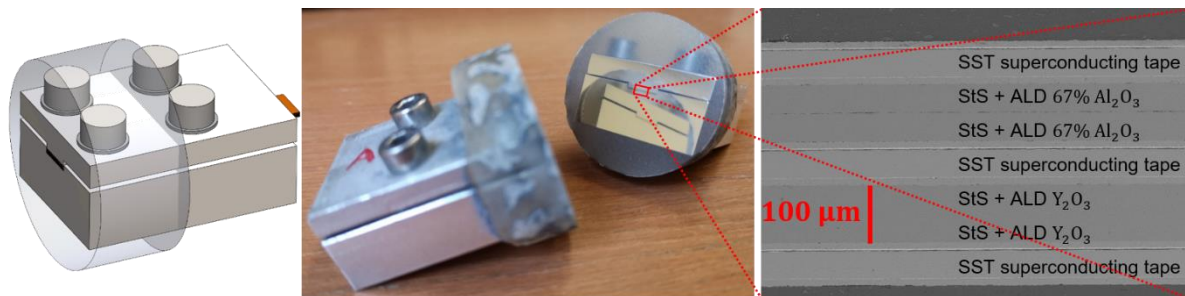


Figure III-41: Left to right, CAD; polished samples; cross-sectional view of the different tapes compressed observed by SEM.

Several images at different positions between the SST superconducting tape and the StS tape with the ZnO/Al₂O₃ ALD have been made in order to observe the behavior of the thin layer during the compression of the tapes. Under the effect of the load, a deterioration of the ALD is clearly visible (Figure III-42). Stainless steel-copper contact zones are significantly observable. The 100 nm thin layer is not uniformly present between the two tapes, which explains the small increase in contact resistivity with the presence of the ALD. This is why the R_{ct} value with ALD have the same orders of magnitude as the R_{ct} value without ALD.

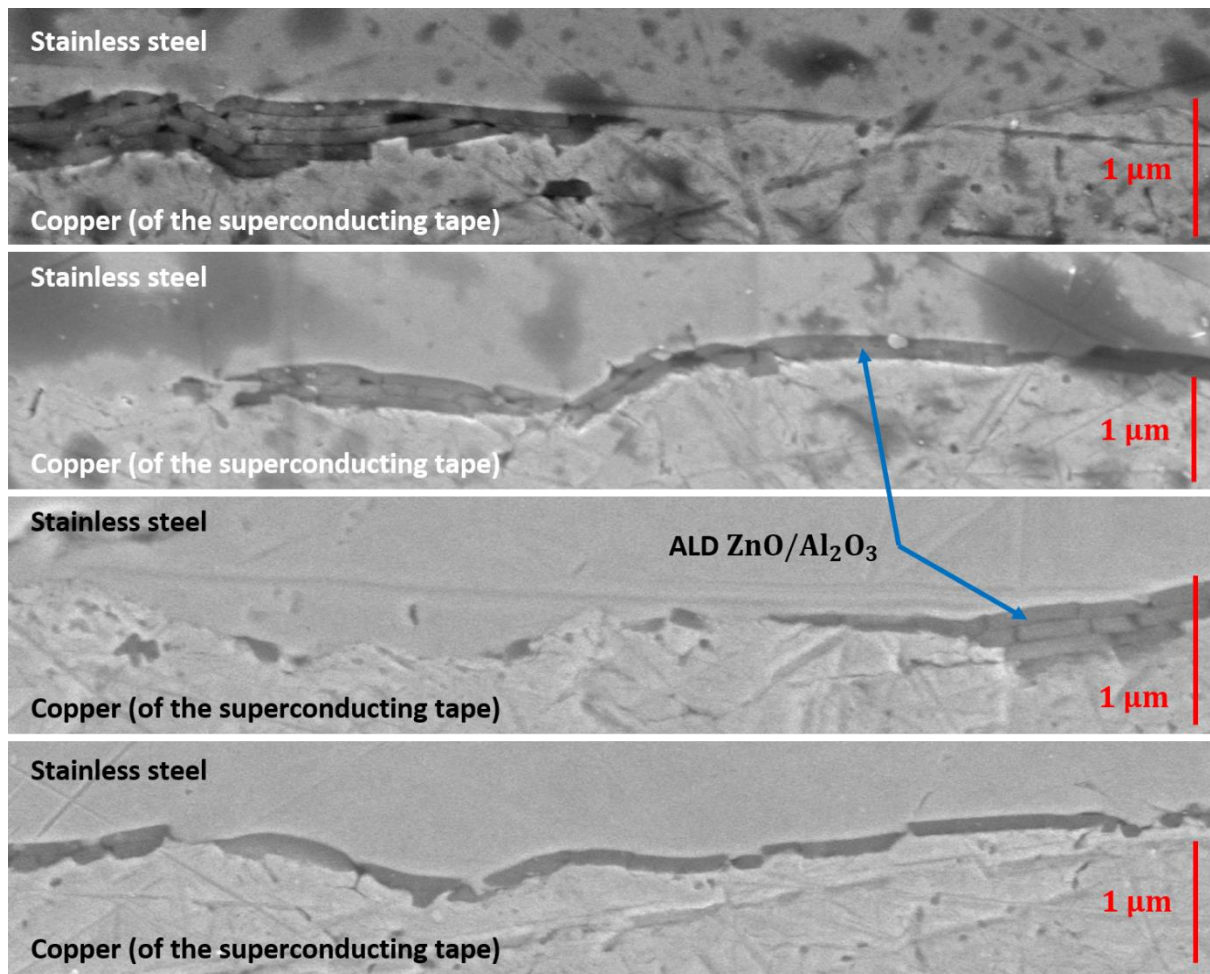


Figure III-42: cross sectional views of the contact between the stainless steel tape with the ALD and the SST superconducting tape; ALD deterioration and stainless steel-copper contact without the presence of the thin layer observed by SEM.

In the images of Figure III-42, the ALD is clearly observable between the StS tape and the SST superconducting tape, but several thicknesses are stacked giving the impression that several deposits have been made. When the tapes are compressed, the local mechanical stress at the top of the asperities causes delamination between the ALD and the StS tape. The delaminated ALD plates slide and position themselves in areas of lower compression, i.e., at the holes of the asperities (Figure III-43). Thus, with the migration of the delaminated ALD plates, some contact areas no longer have a thin layer interposed between the StS tape and the copper, greatly reducing the contact resistivity.

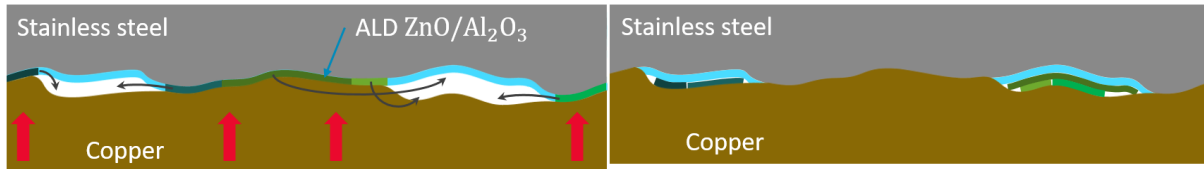


Figure III-43: On the left, sketch of deterioration, migration and local stacking of several plates. On the right, stainless steel-copper contact without ALD.

Note: Polishing the sample could cause delamination of the ALD observed on the surface of the tapes during sample preparation. However, this hypothesis is rejected because the stacking of the ALD observed in the top left of Figure III-42 is too orderly. Delamination during polishing would result in a much more disordered stacking of the ALD.

Two chemical studies using line-scan EDX analysis on a cross-sectional view were performed: on line **A** through a contact with observation of the 100 nm thickness of the 33% Al_2O_3 - 67% ZnO ALD at 130°C, and on a line **B** through a contact without observation of the ALD (Figure III-44). For both lines, the presence of copper (from the superconducting tape) and iron (from the StS tape) is observed. A peak is well measured on line **A** concerning the alumina and zinc oxide, justifying the presence of the deposit between the StS and the copper. On line **B**, no peak is measurable, there is no ALD at the level of the contact between copper and StS. The absence of the thin film on line **B** is also observable by the shift of about 0.1 μm between the iron measured on line **A** and line **B**.

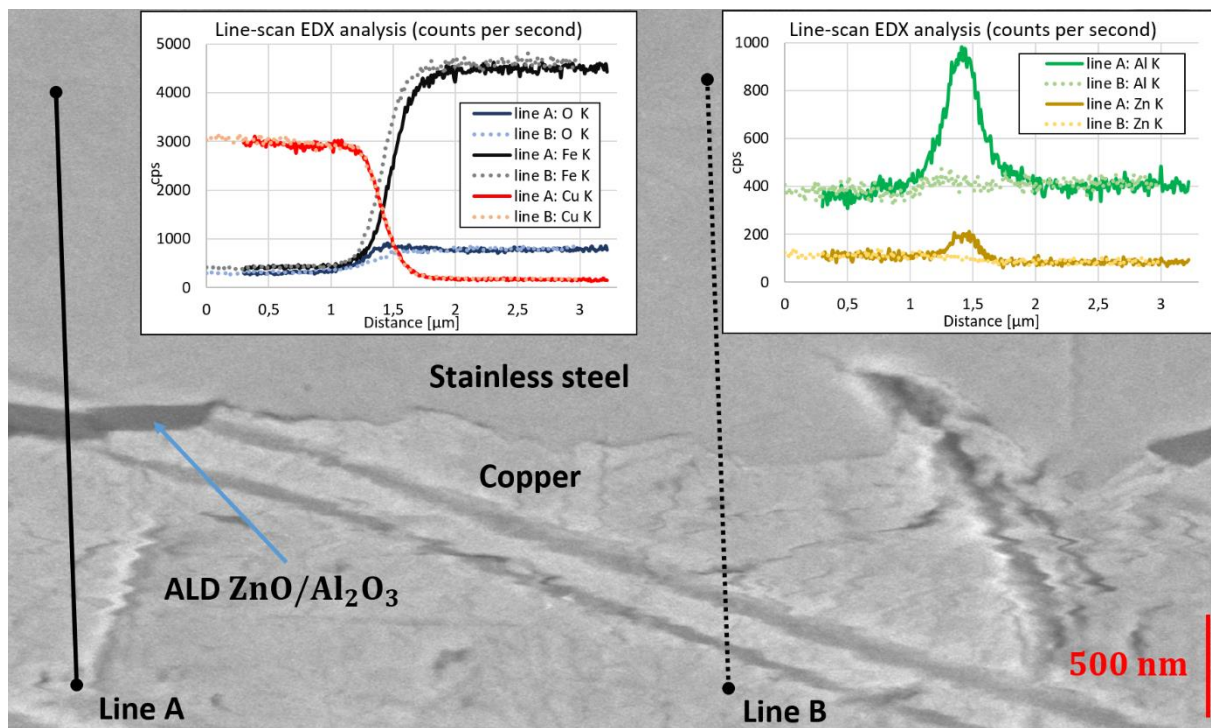


Figure III-44: Chemical studies via line-scan EDX analysis on a cross-sectional view of a stainless steel-copper contact with and without the presence of the ALD of zinc oxide and alumina.

III. 3. 4. 2 R_{ct} modification as a function of the current with the ALD

In addition to delamination of the ALD layer, the presence of the ALD causes a decrease in contact resistivity with an increase in current.

III. 3. 4. 2. 1 Decrease of the contact resistivity with an increase of the current

An unexpected behavior was observed during the R_{ct} measurements with ALD subjected to thermal shock. By placing the samples in liquid nitrogen, it is possible to increase the current value without damaging our samples, in order to obtain results that are more accurate. Contact resistivity measurements were performed with a current of 3 A, instead of the 0.5 A imposed to obtain the results of the section III. 3. 3. 2.

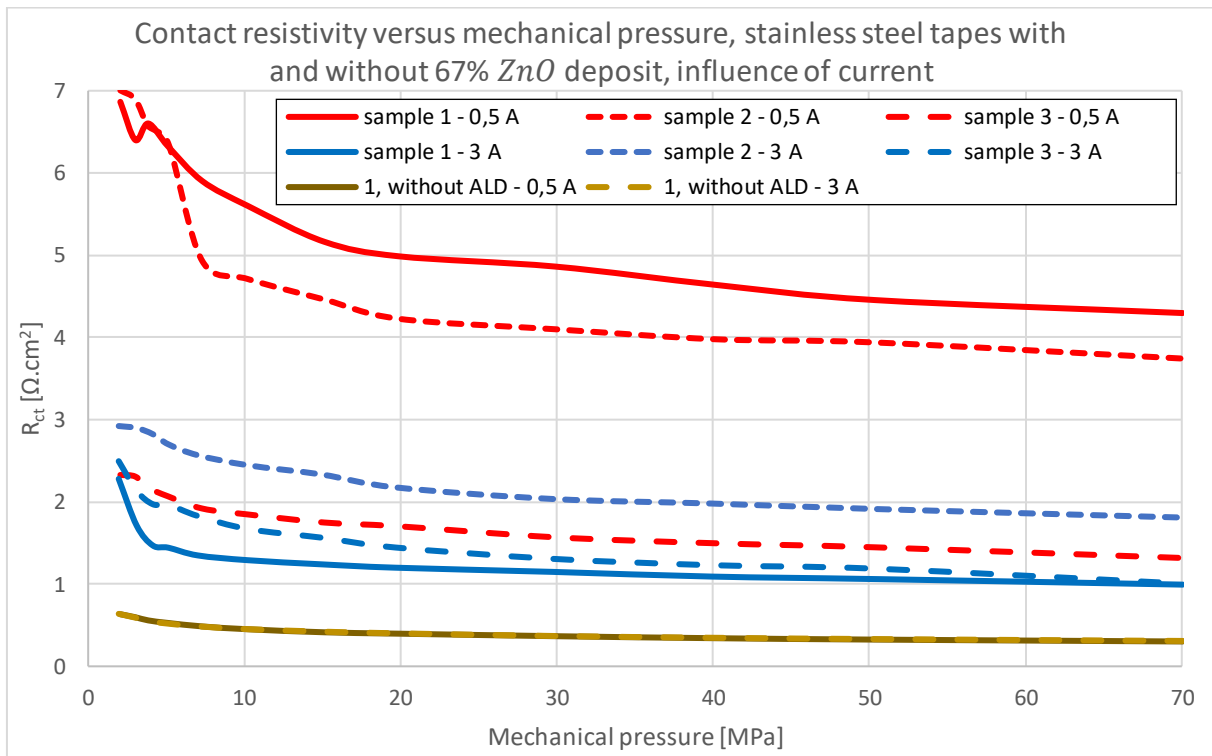


Figure III-45: Contact resistivity versus mechanical stress, stainless steel tapes with and without 67% ZnO deposit, influence of current, at 77 K.

An increase in current (from 0.5 A to 3 A) causes a clear decrease in contact resistivity on the StS tape samples with ALD, while the R_{ct} of the reference samples (StS without ALD) remains the same regardless of the current value (Figure III-45). Thus, the current flowing radially in the samples with ALD decreases the contact resistivity. This phenomenon explains in part the small increase in R_{ct} with the presence of the ALD composed of alumina and zinc oxide.

New measurements were made to confirm this decrease in R_{ct} with increasing current on StS tapes with the ALD 100% Al_2O_3 @ 177°C. Measurements are performed at room temperature (≈ 290 K) on six samples: four samples with StS tape with 100% Al_2O_3 @ 177°C ALD, and the reference samples StS tape without ALD (Figure III-35: CuBe_2 tapes are replaced by StS tapes). As the R_{ct} value varies with the number of load cycles, a fixed load of 70 MPa is chosen for the following measurements. This allows to have a resistivity of the stack as low as possible allowing to impose a more important current and thus to observe the influence of the current at best.

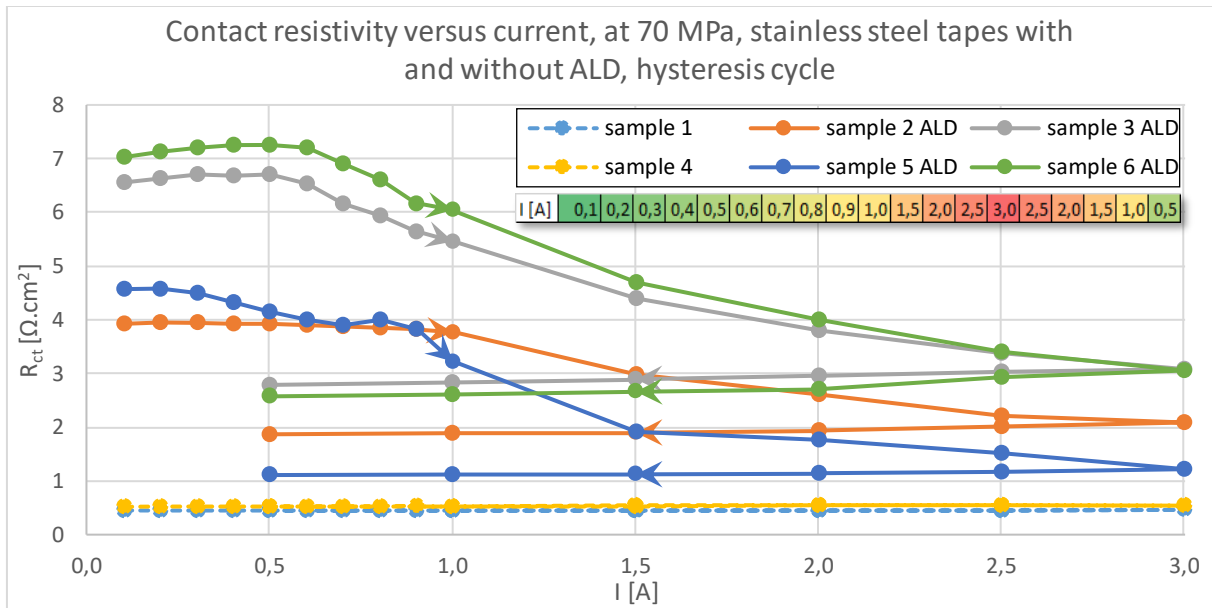


Figure III-46: R_{ct} versus current, at 70 MPa, stainless steel tapes with and without ALD 100% Al_2O_3 @ 177°C, hysteresis cycle; room temperature.

The results in Figure III-46 show a decrease in R_{ct} with an increase, from a certain value, of the current. This phenomenon is irreversible: a hysteresis cycle can be observed. However, this behavior is not observable with the two reference samples (MI StS without ALD): the R_{ct} value is invariant and fixed with the current. The same behavior is observed on Durnomag[®] tapes with the presence of the ALD 100% Al_2O_3 @ 177°C. In Figure III-47, two current cycles (0.5 → 2 → 0.5 A then 0.5 → 2.5 → 0.5 A) were conducted. Two steps in the R_{ct} value are observable as a function of the maximum value of the imposed current. This behavior can be explained by the appearance of micro soldering. This is the Branly effect.

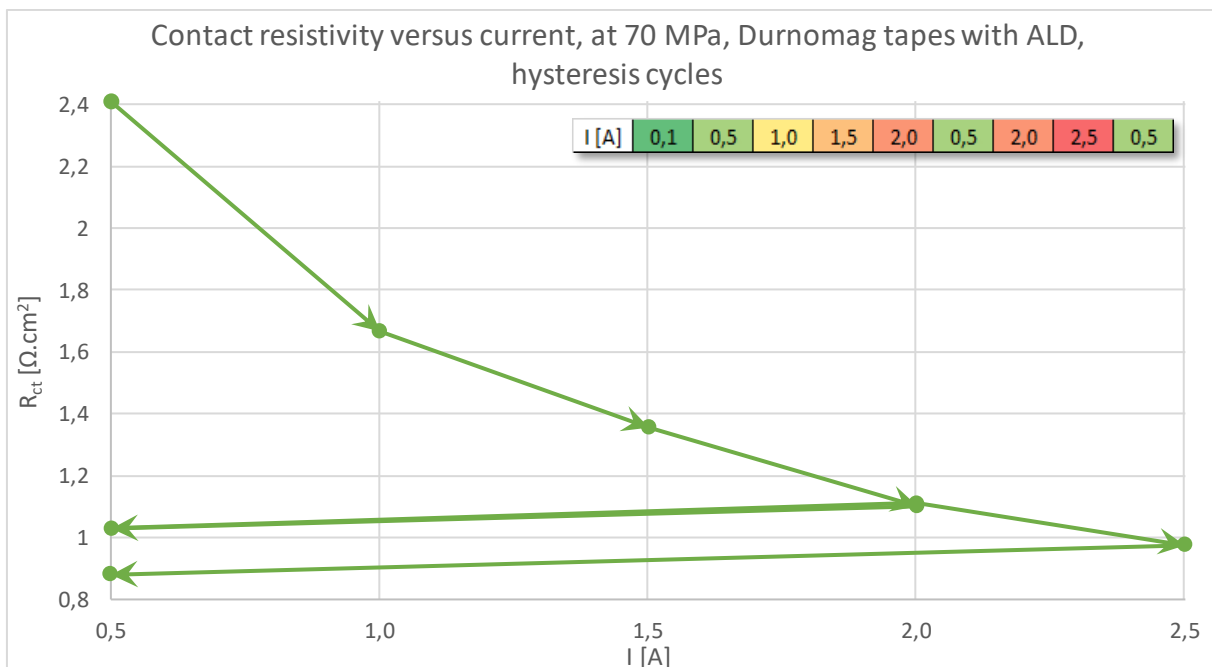


Figure III-47: Hysteresis cycles of R_{ct} versus current, Durnomag[®] tape with ALD 100% Al_2O_3 @ 177°C, room temperature measurement, constant load of 70 MPa.

III. 3. 4. 2. 2 Branly effect

This decrease in resistivity as a function of current, with hysteresis loops, was observed by C. Zhai [104] on a sample consisting of several rough alumina disks subjected to a constant load. This phenomenon of nonlinear conductivity on alumina disks can be explained by the Branly effect or the Coherer effect.

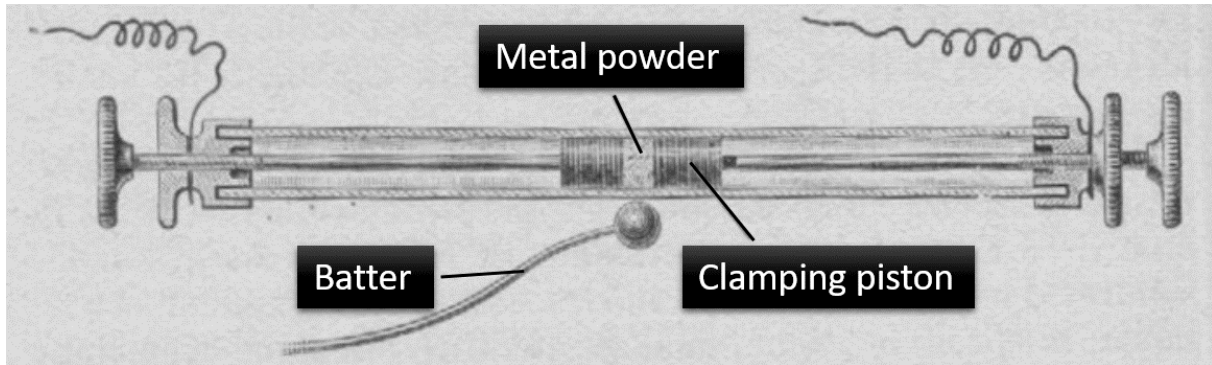


Figure III-48: Edouard Branly's "coherer" experiment, 1888 [105].

In 1888, Edouard Branly discovered that the metal powder resistivity (inserted in a glass tube, Figure III-48) varies by several orders of magnitude by causing an electric spark a few meters from the device. He also noticed that it was possible to restore the initial resistivity value by a mechanical shock on the glass tube. The appearance of micro soldering have been suggested by E. Falcon [106] to explain this phenomenon. From a high current, an electro thermal coupling generates a soldering of the micro contacts leading to conductive metallic links (constant surface). The soldering, and thus the contact surface, does not vary for a lower current compared to the maximum imposed current.

Thus, after having decreased the contact resistivity values by increasing the current on our samples with the presence of the ALD ZnO/Al₂O₃, it should be possible to restore the initial R_{ct} value by simply moving the tapes constituting the stack. The mechanical shock would then break the micro soldering, decreasing the electrical contact, which would restore the initial resistivity value. In order to verify this theory, new contact resistivity measurements before and after mechanical shock were carried out on StS samples with the presence of the ALD 100% Al₂O₃ @ 177°C. The decrease in contact resistivity with increasing current and an increase in contact resistivity following a mechanical shock has been observed experimentally. Details are available in Appendix: VI. 3.

III. 3. 4. 3 Deposition support nature of the ALD

Another major phenomenon explains the small R_{ct} increase in Figure III-36. The Branly effect is observable on StS and Durnomag[®] tapes with ALD, but not in the presence of CuBe₂ tapes subjected to treatment to receive a thin layer of zinc oxide and alumina (Figure III-49). Indeed, no contact resistivity variation as a function of the current is observable with CuBe₂ tapes submitted to ALD 100% Al₂O₃ @ 177°C. Since the ALD causes the Branly effect and it is not observable in this sample, then the thin film is not well deposited on the surface of the CuBe₂ tape. The nature of the deposit support is not negligible.

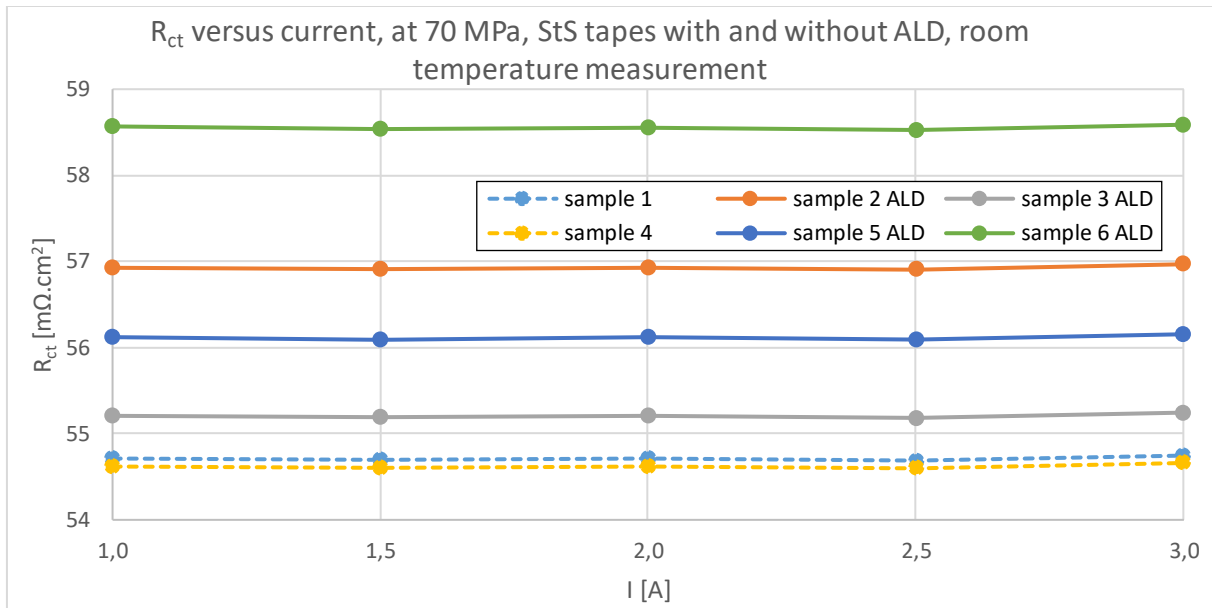


Figure III-49: R_{ct} fixed versus current, $CuBe_2$ tape with ALD $100\% Al_2O_3$, room temperature; load 70 MPa.

III. 3. 5 Modification of the contact resistivity behavior as a function of the load with Atomic Layer Deposition

As a reminder, the objective of adding the ALD was to modify, but also to control the contact resistivity value. However, in the previous section, we have seen that by adding a thin layer the contact resistivity value varied according to the current flowing radially. Such a behavior is not acceptable in the implementation of NI or MI windings. Adding an ALD also changes the contact resistivity behavior as a function of mechanical stress. Indeed, it increases the standard deviation of the contact resistivity compared to the samples without ALD, both in room temperature and cooling conditions (Figure III-37). This phenomenon can be explained by the deterioration of the ALD during the compression of the tapes. Since the surface condition of the tapes is not strictly identical, the deterioration of the thin layer causes greater variations in the contact resistivity for the same compression value. Similarly, since the deterioration of the ALD is greater with a higher load, the decrease in contact resistivity with increasing mechanical stress is more pronounced with the presence of the ALD than without (Table III-9).

Table III-9: R_{ct} decrease between 3 MPa and 70 MPa for 3 MI Stainless Steel samples with and without ALD 67% ZnO, room temperature measurements and with $I = 0.5$ A, third load cycle.

R_{ct} [$\Omega.cm^2$]	sample 1+ALD	sample 2+ALD	sample 3+ALD	sample 1	sample 2	sample 3
3 MPa	6,27	3,89	2,97	0,64	0,70	0,67
70 MPa	3,87	2,31	1,42	0,52	0,55	0,57
decline [%]	38	41	52	19	21	14

Still on the same sample (three MI StS samples with and without ALD 67% ZnO), at room temperature with $I = 0.5$ A, six load cycles ($2 \rightarrow 70 \rightarrow 2$ MPa) were performed. Figure III-50 plots the values for 70 MPa. As with the influence of mechanical stress, the number of load cycles causes much greater variations in contact resistivity with than without the presence of the ALD. This phenomenon of the contact resistivity variation according to the mechanical stress (load) is expected [85], [92] and observed, but this variation is more pronounced with the presence of the ALD. The objective of controlling the contact resistivity is clearly not achieved with the presence of the ALD.

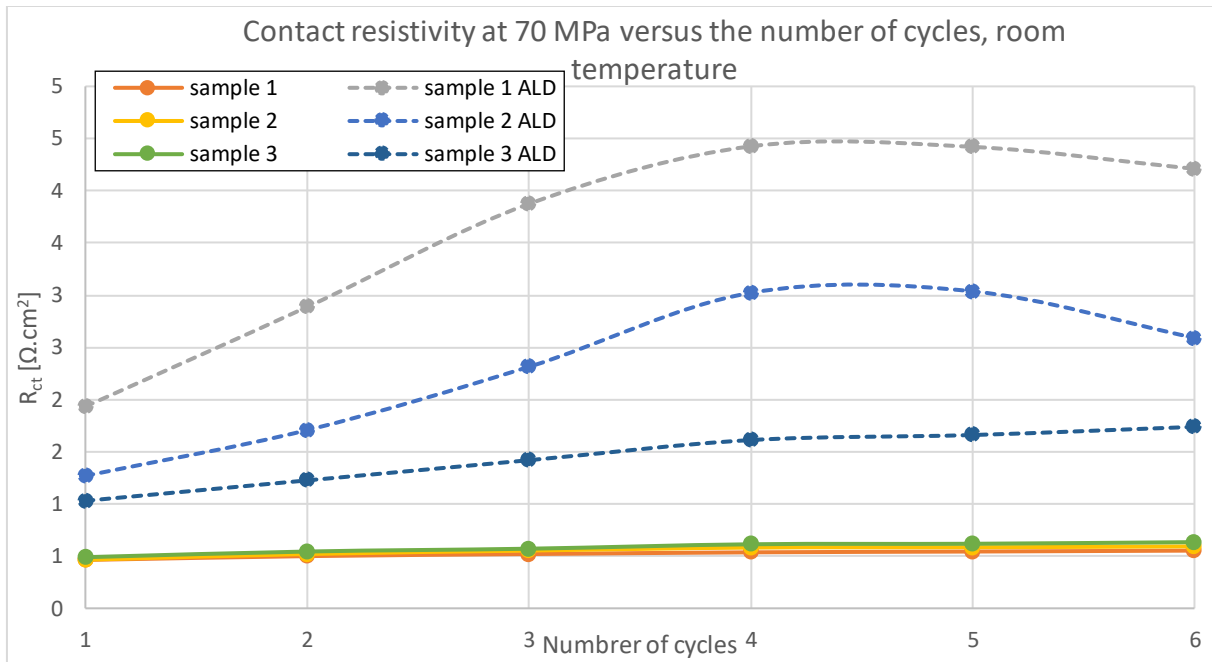


Figure III-50: Evolution of the R_{ct} versus the number of mechanical cycles at 70 MPa for three MI Stainless Steel samples with and without ALD 67% ZnO, room temperature measurements; $I = 0.5$ A.

III. 3. 6 Contact resistivity with 1 μm Atomic Layer Deposition

A last ALD with a thickness 10 times thicker was made in order to study and observe its influence on the contact resistivity value. Unfortunately, measurements of R_{ct} could not be performed, only observations of this last ALD during the compressing of the tapes were made. The set-up for the observations is the same as that presented in section III. 3. 4. 1. The deposit is composed only of alumina, and the deposition temperature is 177°C. The thin film is deposited on stainless steel tapes and then compressed with SST superconducting tapes (the compression of the tapes is always about 15 MPa). As the thickness of the deposit is greater, observation with a confocal microscope is sufficient.

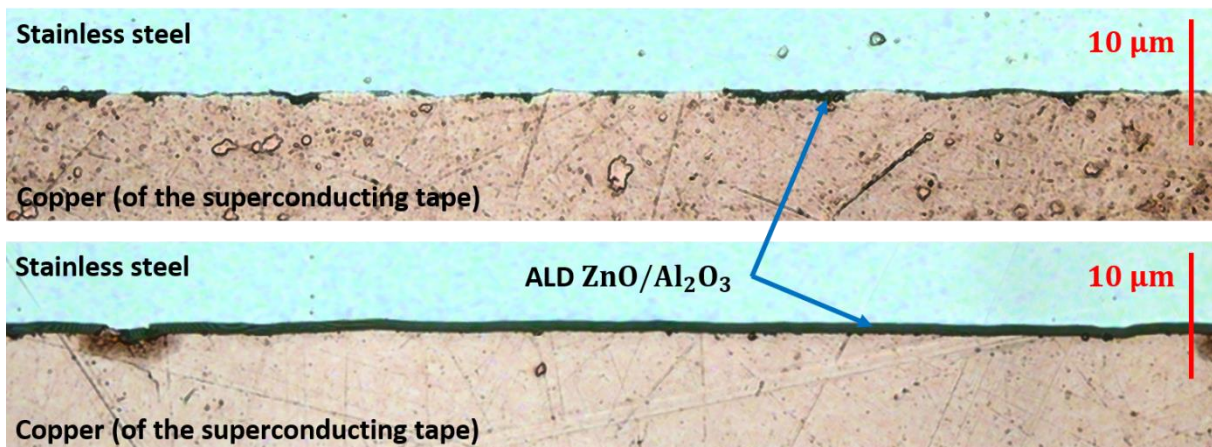


Figure III-51: cross sectional views of the contact between the stainless steel tape with the ALD and the SST superconducting tape observed by confocal microscope. On the top, ALD 100 nm deterioration and stainless steel-copper contact without the presence of the thin layer. At the bottom, very limited deterioration and delamination of the ALD 1 μm .

The presence of stainless steel-copper contact zones in the case of the 100 nm ALD is clearly observable in the top image of Figure III-51. However, with the 1 μm deposit, the deterioration and delamination of the thin layer is greatly reduced. Indeed, with a thicker deposit, the roughness of the superconducting tape is of the same order of magnitude compared to the

deposit, which reduces the deterioration of the ALD. In the bottom image of Figure III-51, the ALD is almost constantly interleaved between the stainless steel tape and the copper layer.

Making deposits with a thicker deposition thickness limit the deterioration and delamination of the thin film, but also make the contact resistivity invariant with the current. However, having a higher ALD thickness increases the deposition time, but it remains reasonable for a thickness of 1 μm (about 2 days). Controlling R_{ct} with ALD 1 μm therefore seems feasible.

III. 3. 7 Conclusion of the Atomic Layer Deposition

The main objective of this section was to carry out a 100 nm atomic thin film deposition on metallic tapes in order to modify and control the contact resistivity R_{ct} . The idea was to vary the proportion of precursors (alumina and zinc oxide) in order to modify the thin film resistivity and thus control the contact resistivity in an MI coil. However, the different measurements showed that the ALD precursor contents only slightly modified the R_{ct} . The influence of the ALD resistivity is not as pronounced as expected. The same is valid for the ALD chamber temperature used to carry out the deposition. It should change the thin film resistivity, although no difference was measurable on the contact resistivity.

Several measurements on different samples were made to understand why the contact resistivity measurements does not show the expected values. Through these results, the ALD is well present on the surface of the metallic tapes with the right thickness, and it is not deteriorated via a thermal shock (cooling the tapes in liquid nitrogen). The small increase in contact resistivity is mainly due to deterioration and delamination of the thin layer when compressing the superconducting and metallic tapes. Plates of the ALD migrate on the contact surface causing stainless steel-copper contacts without the presence of the deposit in between the two tapes.

The presence of the ALD is nevertheless observable: a slight increase in contact resistivity is measurable. The different measurements show that the standard deviation of the contact resistivity for a fixed load is greater with the presence of the deposit than without. Similarly, with the presence of the ALD, the contact resistivity varies more strongly with the load but also with the number of load cycles. Finally, with the presence of the ALD, the current also modifies the contact resistivity value and in a non-reversible way (except with a mechanical shock to break micro soldering). The ALD ZnO - Al_2O_3 100 nm does not allow controlling the R_{ct} .

Chapter IV

Coil protection

In the final chapter of this thesis, the PEEC model was completed to study the behavior of a simple or multi-pancake during a quench with voltage limitation by the power supply. The principle is to use the high increase in the resistivity of an MI pancake during a quench and to adjust the maximum voltage of the power supply to obtain an automatic decrease of the supply current to protect the coil. In the first part, simulations and experimental measurements were carried out on a coil made of four MI pancakes to demonstrate the use of MI technology with voltage limitation to improve the protection against quenches. In a second part, the PEEC model is again completed to simulate the presence of a magnetic shielding around the coil. The purpose of this magnetic shielding is to prevent a too high local temperature increase in the coil during a transient regime that could damage the magnet.

IV. 1 Introduction

In the simulations presented in Chapter II, the supply current I_0 remains constant when a quench occurs in a coil consisting of one or more pancakes. In reality, when a minimum voltage across a superconducting pancake is detected, a protection system is activated to limit the damage caused by the quench. Another method is to add a diode in the protection circuit. In this Chapter IV, the PEEC model is modified to best simulate the real behavior of a pancake during a quench with the implementation of a self-protection system. The presence of self-protection means that the electrical circuit of the magnet is not changed during a quench or any other transient. The objective of this section is to demonstrate that it is possible to use NI-MI technology, even with a high contact resistivity value, to protect a coil during a quench.

In this Chapter IV, the idea is to use the high resistance of the MI pancake during the start of a quench to passively protect the pancake with a voltage limitation. For this purpose, the power supply is a current source but with a voltage limitation when the coil quenches, it provides the necessary current for this voltage limit. By imposing a maximum voltage U_{max} , the supply current I_0 imposed on the pancake will automatically decrease when it becomes too resistive, i.e. when a quench occurs. A decrease in the supply current I_0 will thus prevent a thermal overheating of the coil, even with a high contact resistivity value (above $10 \text{ m}\Omega\cdot\text{cm}^2$) where the MI self-protected behavior is no longer valid.

A second method of improving the protection of the coil is to put additional superconducting turns inside the stainless steel overbanding around each pancake in the coil. This magnetic shielding is not electrically connected with superconducting tapes to the pancakes in the coil. The principle is to transfer part of the energy to the magnetic shielding during a transient regime in order to decrease the maximum temperature of the pancakes of the coil. Simulations using the PEEC model have been carried out to understand the behavior of the coil with the presence of additional superconducting turns in the overbanding. A part of this work has already been published in [81].

IV. 2 Protection with NI/MI and voltage limitation

In the first part of this Chapter IV, simulations of a simple pancake with voltage limitation are performed to study the maximum value of the local temperature during a quench as a function of the value of the contact resistivity and the value of the maximum imposed voltage. This protection method was then simulated using the PEEC model and experimentally tested on a coil of four MI pancakes.

IV. 2. 1 Simulation of a simple pancake with voltage limitation

IV. 2. 1. 1 Implementation of voltage limitation in the PEEC model

Modifications have been made in the PEEC model to simulate the voltage limitation when the coil quenches. Before it quenches, the supply current I_0 is constant and the introduction of a source term, or a degradation of the critical current of a sector, generates a local temperature rise within the pancake. This generates a redistribution of the currents and thus a voltage across the pancake. When this voltage is higher than the maximum imposed voltage U_{max} , the program does not go to the next time step. It remains at the current time step and modifies the value of the supply current I_0 in order to obtain a coil voltage U_{coil} between $0.99 \times U_{max}$ and U_{max} . To do this, several iterations are performed for the same calculation time, making

the simulation time longer. The dichotomy method is used to obtain the value of the supply current I_0 giving $0.99 \times U_{max} < U_{coil} \leq U_{max}$. Choosing a voltage between $0.99 \times U_{max}$ and U_{max} allows to have a voltage close to the maximum voltage imposed while limiting the number of iterations necessary to determine I_0 . The simulation diagram of the PEEC model with voltage limitation during a quench is shown in Figure IV-1. The operation is the same as in section II. 1. 6, but with the addition of voltage limitation. In order to avoid too many unnecessary iterations, the variation of the supply current I_0 at times $i - 1$ and i is obtained in order to estimate the value of the supply current at time $i + 1$ ($I_{0_{i+1}}$) and to carry out the dichotomy method around $I_{0_{i+1}}$, and not on the interval $[0, I_{0_i}]$. This limits the number of iterations and therefore reduces the calculation time.

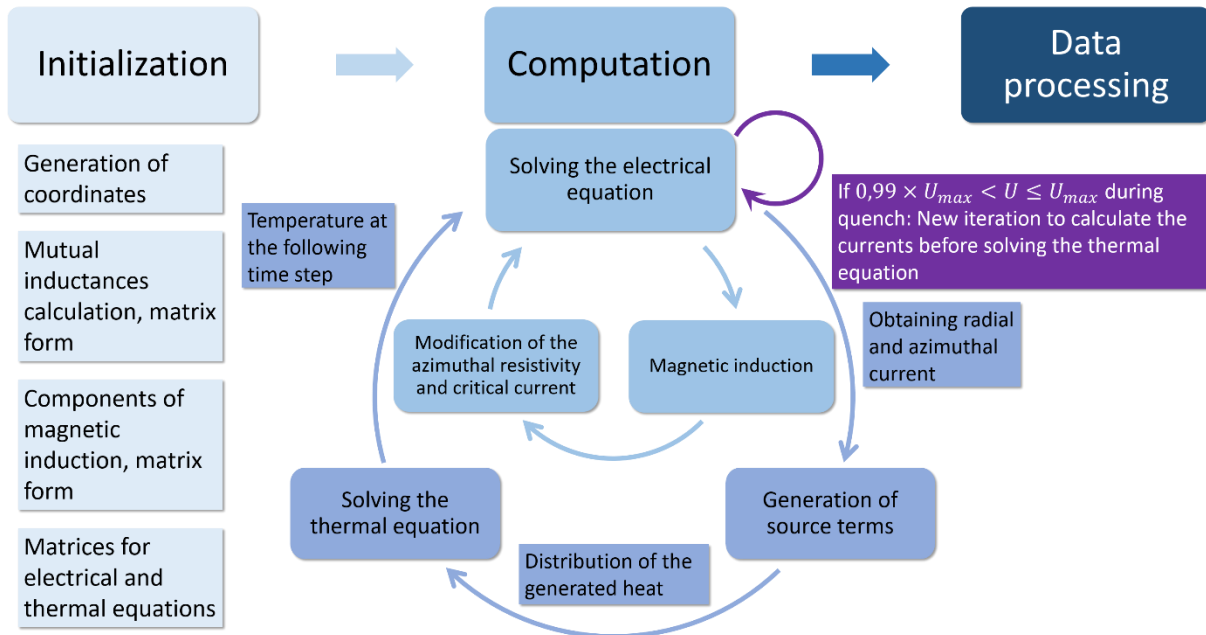


Figure IV-1: Simulation diagram of the PEEC model with voltage limitation during a quench.

IV. 2. 1. 2 Simple pancake with voltage limitation

The aim is to determine the optimum combination of contact resistivity and maximum voltage ($R_{ct} - U_{max}$) to protect the coil as much as possible. Although with a high contact resistivity the self-protected behavior of a pancake can be lost (II. 2. 1), it is possible to use this technology to have a high pancake voltage (compared to a low contact resistivity) at the beginning of a quench. In this section, the maximum value of the temperature will be studied as a function of the maximum value of the imposed voltage U_{max} and the value of the chosen contact resistivity R_{ct} .

IV. 2. 1. 2. 1 Comparison with and without voltage limitation

In this section, the behavior of a simple pancake with the properties presented in Table IV-1 and subjected to voltage limitation will be presented.

The pancake geometry is identical to section II. 2. 1. 2. The pancake is composed of 40 turns and 20 divisions per turn, the current margin on the current margin is 5% and quench is initiated in the 10th sector of the 21st turn with the critical degraded current condition. The main differences are the lower number of divisions per turn n_f . This reduces the calculation time in our case, which is made more importantly here because of the voltage limitation, which requires more iterations. Another modification was made to the thickness of the superconducting layer.

Table IV-1: Parameters of the simple pancake in the case of a quench with degraded sector, with and without voltage limitation.

Parameters	Units	Values
Turns (n_a)	—	40
Divisions per turn (n_f)	—	20
Tape width (h_0)	mm	6
Winding inner diameter (ID)	mm	50
Winding outer diameter (OD)	mm	55.6
Current margin	%	5
Supply current (I_0)	A	657
Initial temperature (T_0)	K	4.2
Coil self-inductance	mH	0.14
Substrate thickness	μm	50
Copper thickness	μm	2×10
Superconductor thickness	μm	1.2
Convective exchange coefficient (h)	$\text{W}/\text{m}^2/\text{K}$	0
Contact resistivity Pancake (R_{ct})	$\mu\Omega.\text{cm}^2$	10 000
Degradation of the sector	%	50
Voltage limitation	V	0.1

In Figure IV-2, the temperature, radial, azimuthal and critical current are shown for different times of the simulation and the behavior of the pancake with voltage limitation is explained below. The average values of the pancake are also shown in Figure IV-3.

- Initially, at $t = 1 \text{ ms}$, the pancake is in its **initial state**: the temperature is 4.2 K. It is in its superconducting state. The current, therefore, flows azimuthally, which generates a magnetic induction on the turns of the pancake, explaining a lower critical current on the inner and external turns of the pancake. There is no radial current initially.
- At $t = 3 \text{ ms}$, **the critical current of the 10th sector of the 21st turn is instantaneous degraded by 50%**. As in the case of paragraph II. 2. 1. 2, this degradation causes a slight redistribution of the current within the pancake. The current redistribution is small as the contact resistivity is relatively high: $R_{ct} = 10\,000 \mu\Omega.\text{cm}^2$. With this partially degraded sector, some of the current flows radially to bypass the local defect, causing a slight heating. The other part of the current flows through the partially degraded sector, generating a local Joule effect, which increases the temperature of the degraded sector. As the pancake is under adiabatic conditions, the cooling of the degraded sector is limited and carried out only by conduction from adjacent sectors with a lower temperature. **Its temperature increases slowly between $t = 3 \text{ ms}$ and $t = 450 \text{ ms}$** (top left of Figure IV-3).
- Beyond $t = 460 \text{ ms}$** , the temperature of several sectors of the pancake becomes so high, strongly decreasing the critical current of these sectors. This causes the appearance of larger radial currents, and therefore a voltage at the ends of the pancake which increases significantly (bottom left of Figure IV-3).
- At $t = 473 \text{ ms}$, the voltage of the pancake reaches the value of the maximum imposed voltage $U_{max} = 0.1 \text{ V}$ (bottom left of Figure IV-3). As the pancake becomes more and more resistive and the voltage is limited to $U_{max} = 0.1 \text{ V}$, the supply current I_0 starts to decrease.
- At $t = 490 \text{ ms}$, the supply current I_0 is lower than the initial value, 467 A compared to 657 A. However, it is still higher than the critical current in some sectors of the pancake due to the temperature, generating Joule effect source terms (bottom right of Figure IV-3). This still generates a temperature increase in the degraded sectors, making the

pancake even more resistive. As the voltage limitation is still active, the supply current I_0 continues to fall.

- The temperature peak $T_{max} \approx 125$ K is reached for $t = 510$ ms (Figure IV-2 and top left of Figure IV-3). Indeed, from then on, the value of the supply current is small, about 100 A. The source terms generated by the contact and azimuthal resistivities are lower. The sector with the highest temperature is cooled by conduction from adjacent sectors with a lower temperature. Thus, the local maximum temperature decreases, while the average temperature of the pancake increases. As the pancake is not cooled, it remains highly resistive.
- The supply current at $t = 570$ ms becomes relatively small: $I_0 \approx 10$ A. With this low value of the supply current, the values of the radial and azimuthal currents are almost zero. The temperature of the pancake becomes more and more homogeneous. The critical current is not zero at any part of the pancake (see the last instant of Figure IV-2).

Thus, thanks to voltage limitation, it is possible to limit the temperature peak within the pancake during a quench. The reduction of the supply current I_0 prevents the temperature from rising too high, even with a moderately high contact resistivity ($R_{ct} = 10\,000 \mu\Omega.cm^2$).

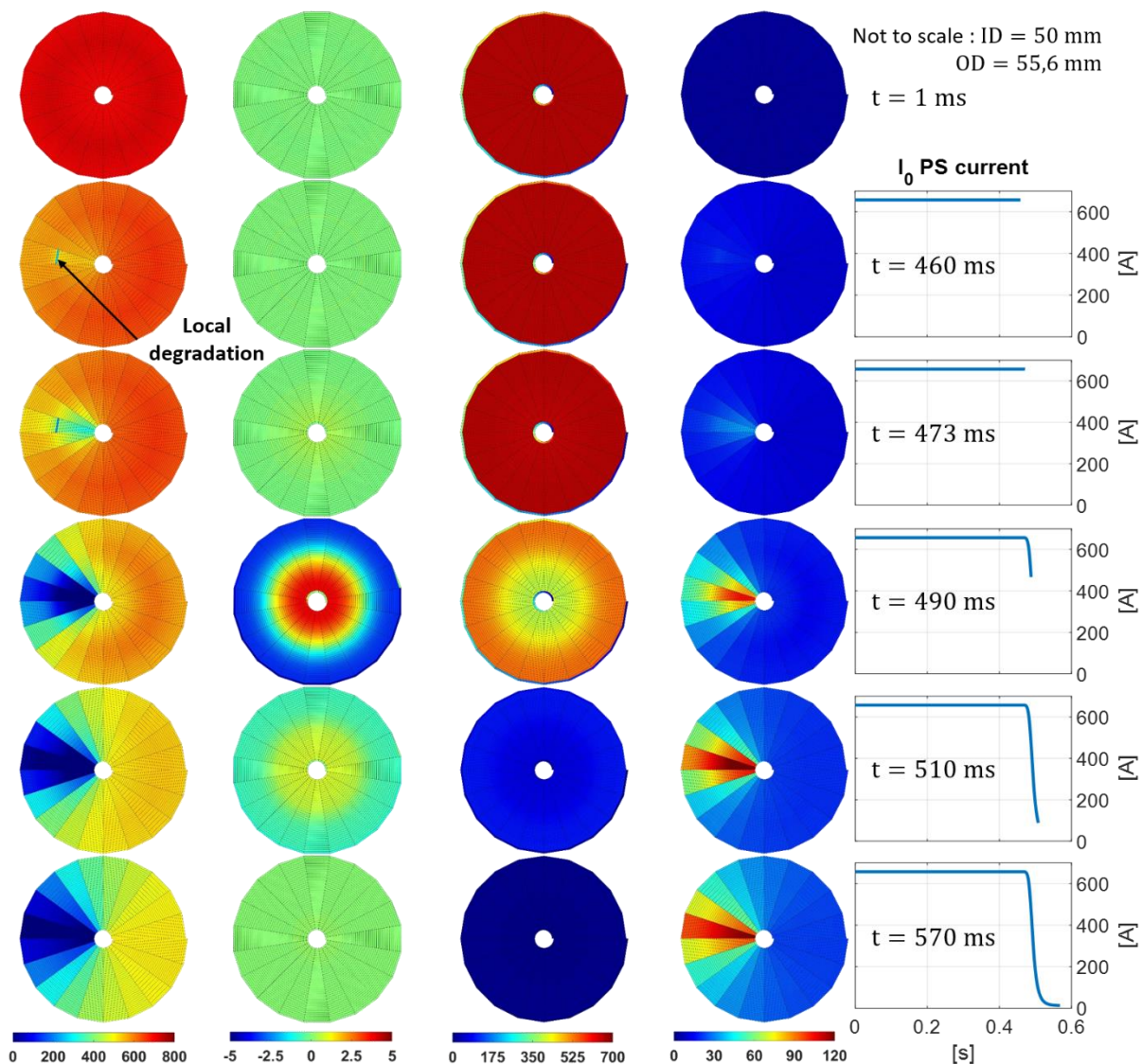


Figure IV-2: Evolution of the temperature, critical, radial and azimuthal current of a simple pancake during a quench with voltage limitation $U_{max} = 0.1$ V ; $R_{ct} = 10\,000 \mu\Omega.cm^2$.

Note: for $t = 490$ ms, we observe that the pancake has a negative radial current for the external turns, and a positive one for the inner turns. These negative radial currents result from the voltage limitation, which imposes a decrease in the supply current I_0 . The presence of negative radial currents is the consequence of the variation of the supply current. They allow the pancake voltage to be equal to the maximum voltage imposed.

In the plots in Figure IV-3, the same pancake was simulated without the voltage limitation, and the results are superimposed on the voltage-limited pancake. As the supply current remains constant during the quench, the voltage of the pancake increases rapidly (bottom left of Figure IV-3), exceeding 20 V within a few milliseconds. The source terms generated by the azimuthal resistances are much larger than the pancake with the voltage limitation, as the supply current remains at $I_0 = 657$ A. This leads to thermal overheating of the pancake. The maximum temperature of the pancake is about 300 K for $t = 0.6$ s, and it increases steadily, reaching 800 K at $t = 1$ s (not shown in the plots in Figure IV-3). The image behavior of the pancake without voltage limitation is comparable to Figure II-19 in section II. 2. 1. 2. 2.

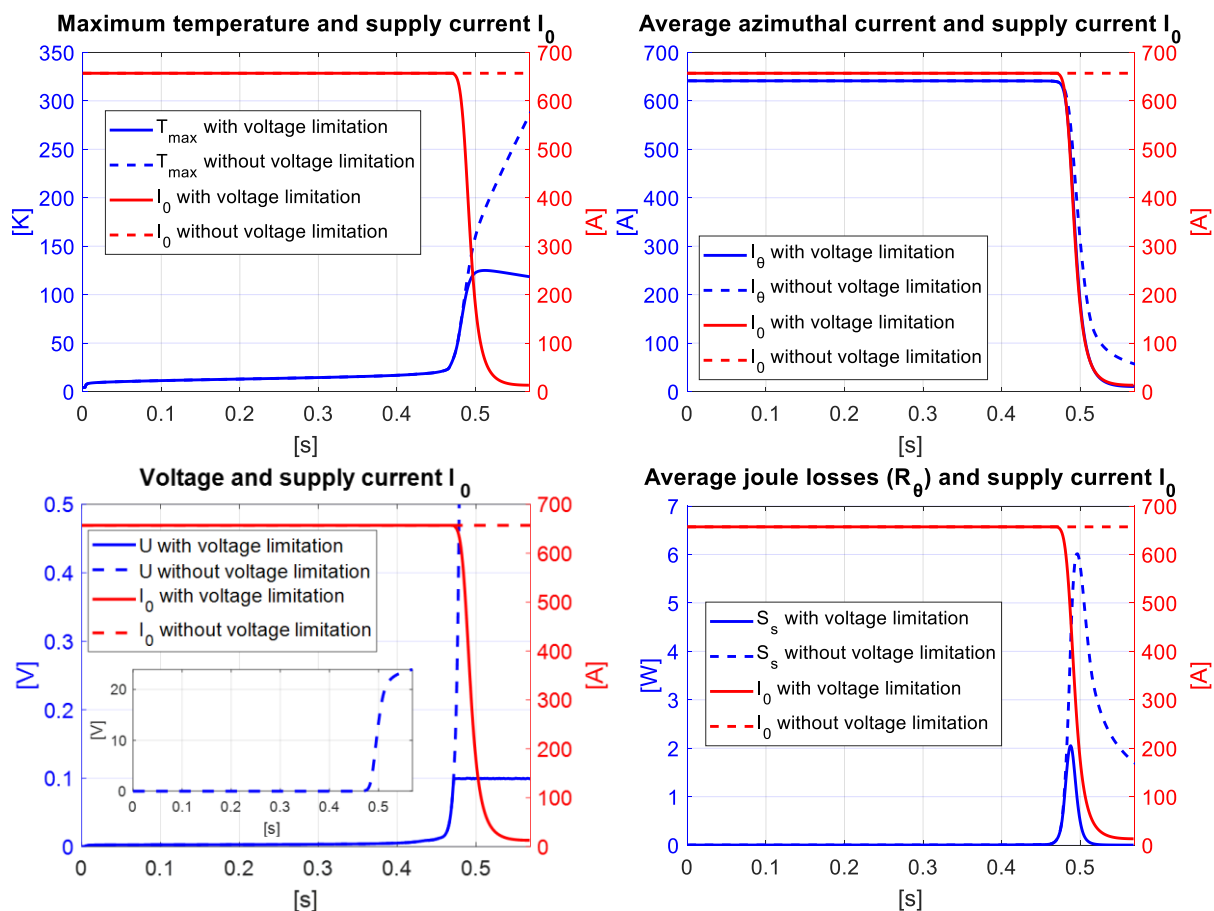


Figure IV-3: Maximum temperature, average azimuthal current, voltage, average losses and supply current of a pancake with and without voltage limitation; $U_{max} = 0.1$ V; $R_{ct} = 10\,000 \mu\Omega.cm^2$.

Without the voltage limitation, the pancake would have burnt locally with $R_{ct} = 10^4 \mu\Omega.cm^2$. Here, with the voltage limitation, the value of the contact resistivity allows a redistribution of the current which makes it possible to measure a voltage at the ends of the pancake and thus to protect it in a passive way by decreasing the supply current I_0 .

An energy balance was carried out on this pancake with and without the voltage limitation (this is an ideal case because a power source is always limited). The method of calculating the different energies is the same as in paragraph II. 3. 2. Without the voltage limitation, the supply current remains constant and since the pancake is resistive, the energy supplied by the power

source is much higher than in the case of the pancake with voltage limitation. **This energy from the power supply is converted into heat in the pancake.** In Table IV-2, the maximum temperature of the pancake without limitation is thus higher than that of the pancake with voltage limitation for the same final time. In the case of the simulation with voltage limitation, a temperature peak of about 120 K is acceptable as it does not damage the conductor.

Table IV-2: Energy balance of the simple pancake with and without voltage limitation.

U_{max} [V]	0.1		Unlimited	
Time [s]	0	0.57	0	0.57
Magnetic energy [J] at $t = 0$ and $t = 0.57$ s	30.7	0.0	30.7	0.4
Energy dissipated [J], Joule effect at $t = 0.57$ s	0	33.0	0	1352.6
Energy of the power supply [J] during 0.57 s	3.1		1322.3	
Total energy [J], initial state at $t = 0$ s	33.8		1352.9	
Total energy [J], final state at $t = 0.57$ s		33.0		1352.9
Maximum local temperature [K] at $t = 0.57$ s	118.8		349.7	

The idea is now to study the influence of the maximum voltage combined with different values of the contact resistivity on the maximum temperature of the pancake. The simulation process introduced above was carried out with different values of U_{max} and R_{ct} .

IV. 2. 1. 2. 2 T_{max} as a function of R_{ct} for different values of U_{max}

The pancake with the properties detailed in Table IV-1 is simulated for different values of maximum voltage U_{max} and different values of contact resistivity R_{ct} :

$$\begin{cases} U_{max} \text{ [V]} \in \{0.005, 0.01, 0.05, 0.1, 0.5, 1, 5, 10\} \\ R_{ct} \text{ [\mu}\Omega \cdot \text{cm}^2] \in \{10^2, 10^3, 10^4, 10^5, 10^6, 10^7\} \end{cases}$$

Figure IV-4 and Table IV-3 list all the values of the maximum temperature as a function of the contact resistivity R_{ct} for different values of maximum voltage U_{max} . The results for 0.1 V, 0.05 V, 0.01 V and 0.005 V are superimposed. Initially, the pancake appears to be self-protected during a quench for all values of R_{ct} and with a voltage limitation up to 1 V.

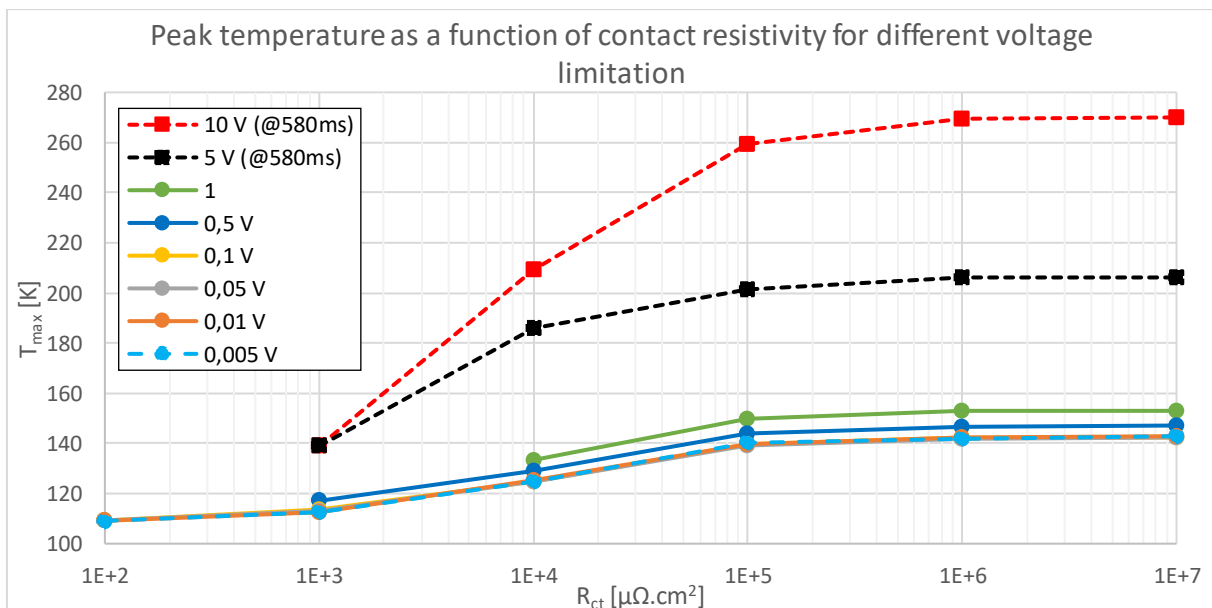


Figure IV-4: Peak temperature as a function of contact resistivity for different voltage limitation for a simple pancake with voltage limitation.

Through all these simulations, different behaviors can be observed with respect to U_{max} .

IV.2.1.2.2.1 $5 \text{ mV} \leq U_{max} \leq 100 \text{ mV}$

The values of T_{max} as a function of R_{ct} are similar for different values of U_{max} . The maximum temperature is higher with an increase of the contact resistivity value (from 109 K to 143 K, Figure IV-4). For these low values of U_{max} , a temperature peak is reached regardless of the value of the contact resistivity:

- If the contact resistivity is low, the current can flow easily from one turn to the other, thus avoiding the local defect and especially without generating Joule effect via the radial resistances. As a reminder, the pancake is under adiabatic conditions, and the critical current of the 10th sector of the 21st turn is constantly degraded by 50% from $t = 3 \text{ ms}$. A constant heating of the pancake is inevitable, causing a quench. Thus, the lower the contact resistivity (more redistribution and therefore less Joule effect generated by the degraded sector), the more the quench is delayed. This can be seen in Figure IV-5 where the higher the contact resistivity, the earlier the temperature peak. Above a certain value of contact resistivity ($R_{ct} \geq 10^5 \mu\Omega \cdot \text{cm}^2$), the behavior is similar.

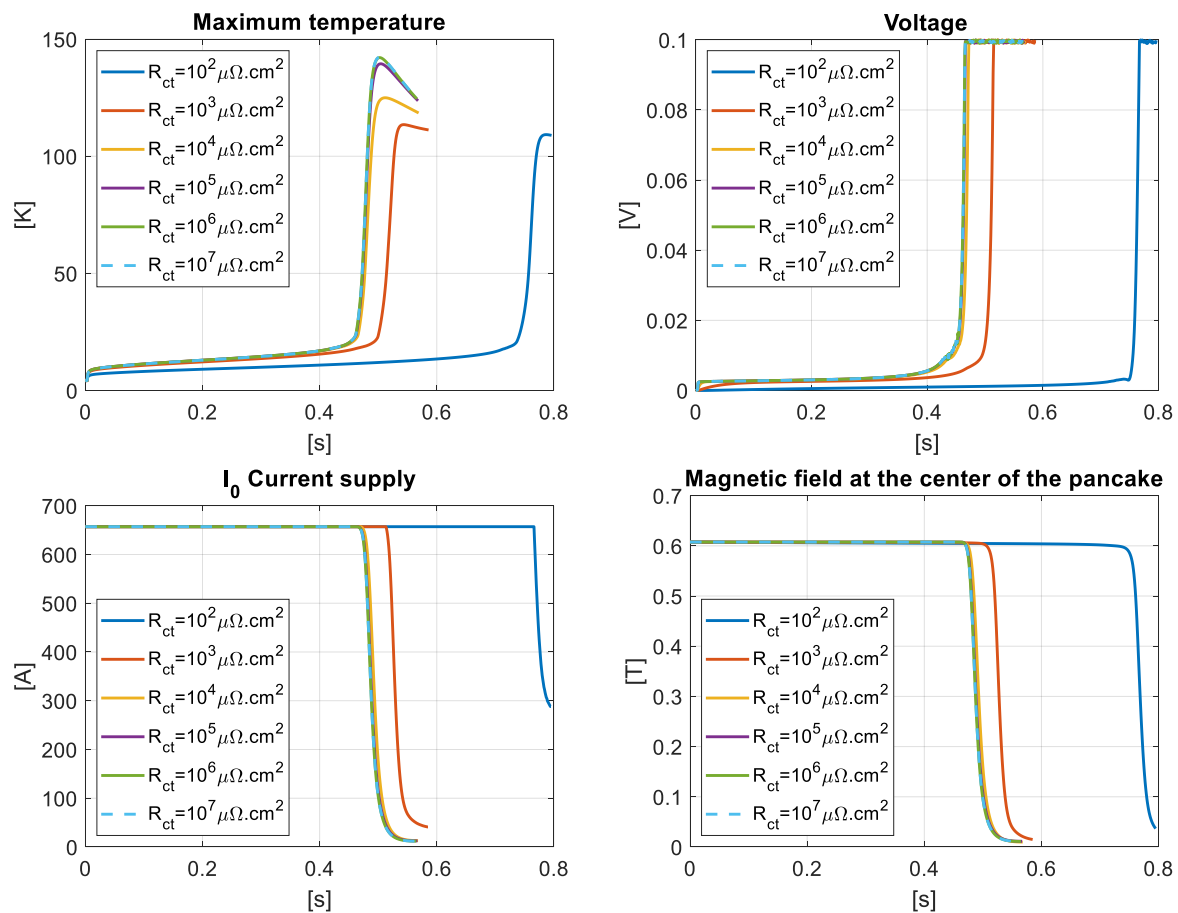


Figure IV-5: Variation of the maximum temperature, voltage, supply current and magnetic induction of the pancake with different contact resistivity values and a voltage limitation set at $U_{max} = 0.1 \text{ V}$.

- In the case where the contact resistivity is high, the low value of U_{max} allows to impose, thanks to the voltage limitation, a low value of the supply current $I_0 < 50 \text{ A}$ when the pancake has quenched (bottom left of Figure IV-5). The currents in the pancake become low, which explains the drop in temperature of the degraded sector after the peak temperature ($t @ T_{max}$), cooled by conduction with the other sectors of the pancake. The more resistive the pancake, the faster the voltage limit will be reached (top right of Figure IV-5), and the higher the decrease in supply current during voltage limitation.

The magnetic field generated by the pancake thus becomes almost zero, and more quickly with a high contact resistivity value (bottom right of Figure IV-5).

In the results of Figure IV-4, the higher the R_{ct} , the higher the maximum temperature. This is explained by the redistribution of the current, which is less important with a high R_{ct} : the current is forced to pass through the degraded area. With a low R_{ct} , the current will be able to flow through the adjacent turns during the quench and therefore the maximum temperature of the pancake T_{max} will increase slightly. Since the current is redistributed more with a lower contact resistivity, the heat generated by Joule effect will be distributed over a larger volume, thus decreasing the maximum temperature. In the case with high R_{ct} , the current will be forced to flow in the degraded area and therefore the maximum temperature of the pancake T_{max} will increase sharply, but over a smaller volume of the pancake. In Figure IV-6, using the value of the critical current for each sector at the time t when the temperature peak is reached, it is well observed that the temperature is more homogeneous in the case where $R_{ct} = 10^4 \mu\Omega.cm^2$ compared to the case where $R_{ct} = 10^7 \mu\Omega.cm^2$. Thus, there are more sectors with zero critical current in the case of lower contact resistivity. The critical current value for all sectors is also lower. This is due to the higher radial currents with lower contact resistivity during the quench and the voltage limitation, which heats up evenly the sectors away from the initially quenched sector.

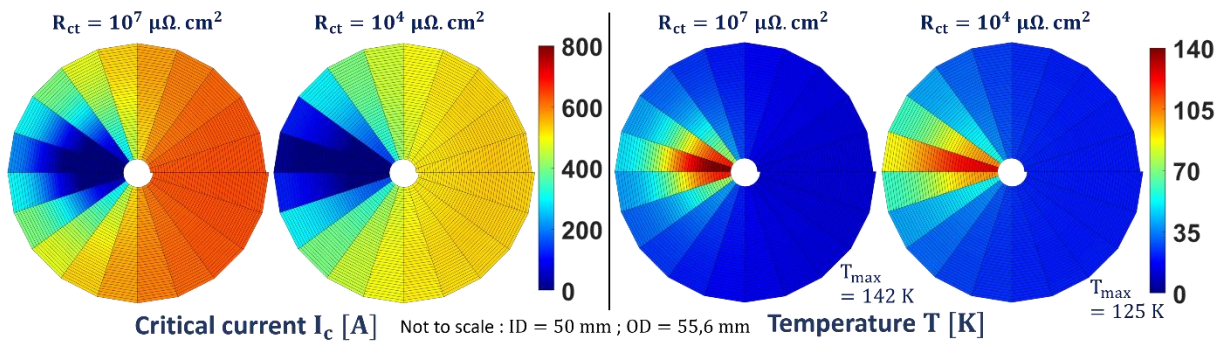


Figure IV-6: Critical current and temperature distribution of a simple pancake during a voltage-limited quench $U_{max} = 0.1 V$, $R_{ct} = 10^4$ and $10^7 \mu\Omega.cm^2$, at time t when the temperature peak is reached.

IV.2.1.2.2.2 $100 \text{ mV} \leq U_{max} \leq 10 \text{ V}$

As in the previous paragraph, the higher the value of the contact resistivity R_{ct} , the higher the value of T_{max} . However, contrary to the previous paragraph, T_{max} increases with a higher value of U_{max} , and this for each value of contact resistivity (Figure IV-4 and Table IV-3). With the voltage limitation set to a higher value, the decrease of current supply I_0 will be smaller and will occur later (continuous line, bottom left and top right of Figure IV-7), and thus the pancake will continue to be supplied with too much current for a few more milliseconds (regardless of the value of $R_{ct} \in [10^3 \mu\Omega.cm^2 ; 10^7 \mu\Omega.cm^2]$). Pancakes with a voltage limitation $U_{max} \in [0.5 V ; 1 V]$ and $R_{ct} = 10^2 \mu\Omega.cm^2$ are not resistive enough during a quench to be voltage limited. The supply current I_0 remains constant. This is why no maximum temperature was found (Figure IV-4 and Table IV-3). Thus, having a high voltage limitation and a low contact resistivity does not provide maximum protection, in the case of our simple pancake. In the other cases, the reduction of the supply current leads to a decrease of the azimuthal current and thus of the magnetic induction (bottom right of Figure IV-7).

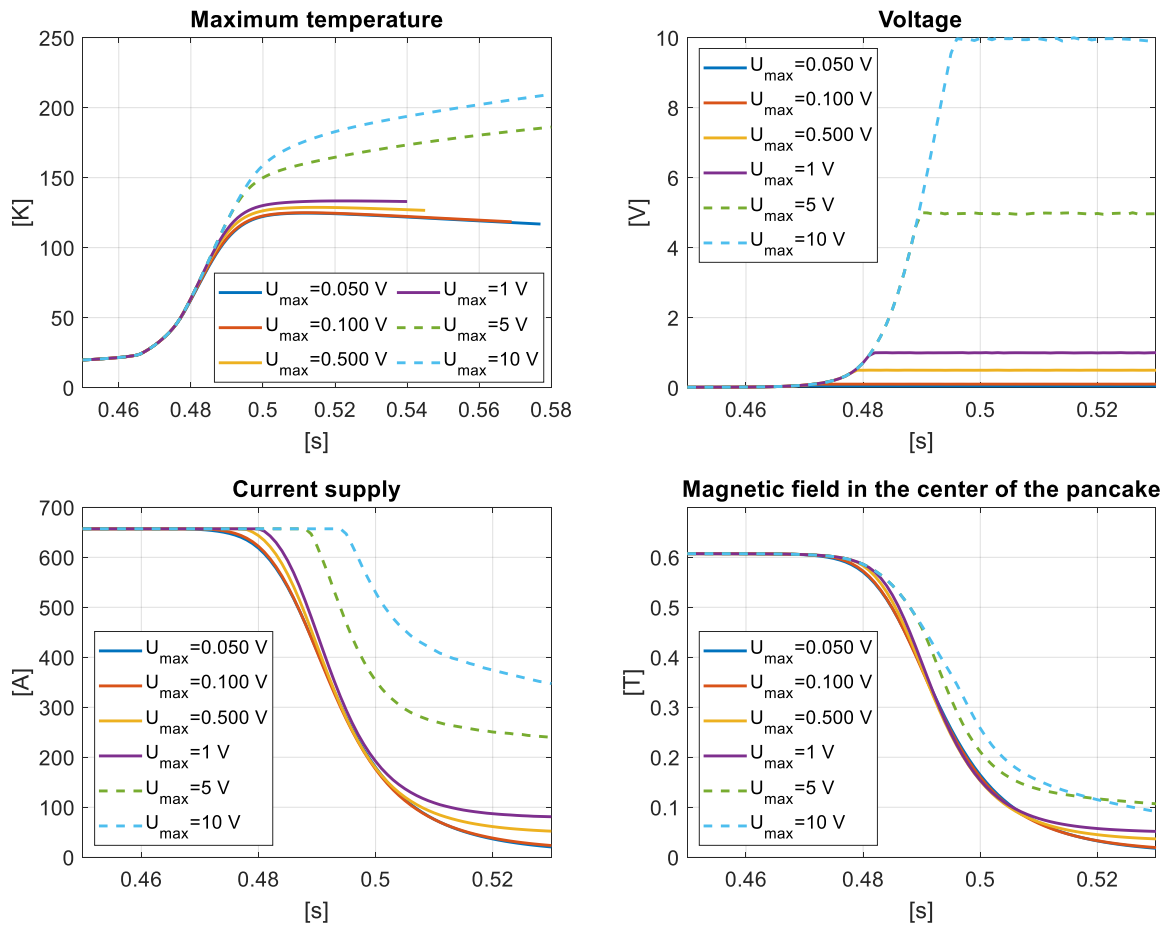


Figure IV-7: Variation of the maximum temperature, voltage, supply current and magnetic induction of the pancake with different voltage limitation values and a contact resistivity set to $R_{ct} = 10^4 \mu\Omega.cm^2$.

In cases where $U_{max} > 1$ V, and regardless of the value of the contact resistivity, the higher voltage limitation leads to a lower I_0 drop. In this situation, a large current continues to flow in the pancake while a highly resistive area is present (that of the degraded sector). Thus, the maximum temperature of the pancake keeps increasing, not showing a temperature peak (example with $R_{ct} = 10^4 \mu\Omega.cm^2$ and $U_{max} = 5$ V and 10 V in dashed in Figure IV-7). In the graph in Figure IV-4, the maximum temperature value for $U_{max} = 5$ V and 10 V has been plotted for $t = 580$ ms. After this time, the maximum temperature for simulations with $U_{max} > 1$ V continues to rise. Thus, imposing only a too high voltage limitation does not allow limiting the temperature increase. In order to avoid damage to the pancake, the supply current must be switched off after the voltage limitation.

Table IV-3: Maximum temperature as a function of contact resistivity for different voltage limitation for a simple pancake with voltage limitation.

T_{max} [K]		U_{max} [V]								
		0,005	0,01	0,05	0,1	0,5	1	5	10	
R_{ct} [$\mu\Omega.cm^2$]	1E+2	109,1	109,1	109,3	109,2	R _{ct} too low for voltage limitation				
	1E+3	112,6	112,5	112,9	113,5	117,1	Too little current reduction imposed by voltage limitation. Constant increase of T_{max}			
	1E+4	124,7	125,1	124,7	125,0	128,8				133,4
	1E+5	140,3	139,8	139,3	139,5	143,8				149,6
	1E+6	141,9	142,3	141,9	142,1	146,9				153,0
	1E+7	143,0	142,9	142,1	142,3	147,1	153,2			

IV. 2. 1. 2. 3 Position of the critical current degradation in the pancake

For all previous simulations, the quench is generated by the 10th sector of the 21st turn, with its critical current instantaneous degraded by 50% from $t = 3$ ms. In the self-field, when the pancake is fully in its superconducting state, the initial critical current of degraded sector is about $I_{c_{n^{\circ}410}} \approx 720$ A. This sector belongs to the sectors of the central turns, where the amplitude of the magnetic induction is less intense, and therefore where the value of the critical current is the most important (left of Figure IV-9 and Table IV-4). In the case of the inner turn, the critical current is about $I_{c_{int}} \approx 694$ A. To generate the quench, the critical current of the sector is instantaneous degraded by 50% and the current margin is 5%: $I_0 = 0.95 I_0$. Thus, degrading a sector on a center or inner/external turn of the pancake by 50% will not cause the same temperature peak when the pancake is quenched (left of Figure IV-8).

Table IV-4: Turn number with a degraded sector and their value of the non-degraded critical current in self-field.

Turn with a degraded sector	2	11	18	21	24	31	39
I_c [A]	694	706	716	720	724	716	704

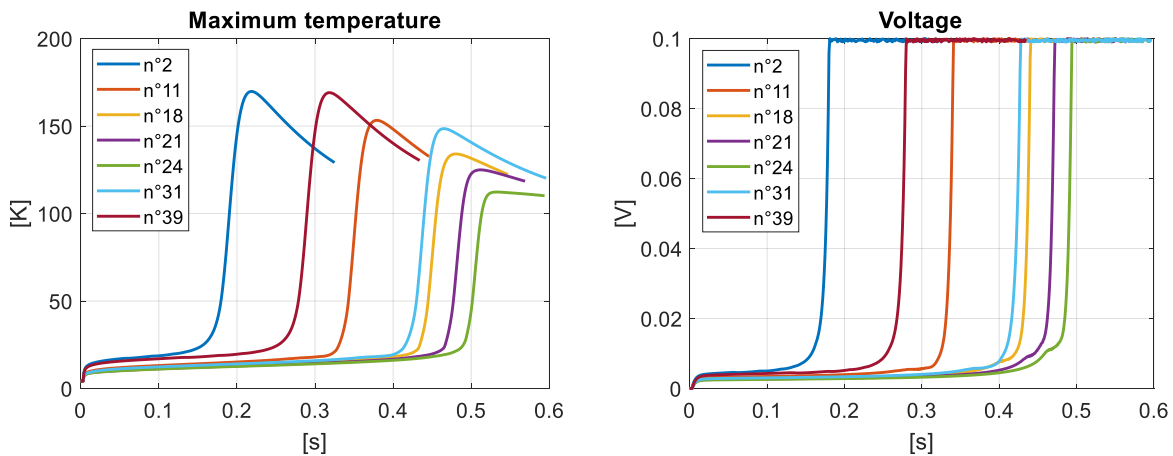


Figure IV-8: Variation of the maximum temperature and voltage of a simple pancake with $R_{ct} = 10^4 \mu\Omega \cdot \text{cm}^2$ and $U_{max} = 0.1$ V, influence of the quench position.

The results in Figure IV-8 group the maximum temperature and voltage of the different simulations of the simple pancake with the properties ($R_{ct} = 10^4 \mu\Omega \cdot \text{cm}^2 / U_{max} = 0.1$ V) presented in Table IV-1 for different positions of the intentionally degraded sector (Table IV-4). The value of the minimum critical current imposed in the pancake is therefore not the same depending on the degraded sector because the value of the critical current depends on the magnetic induction generated by the pancake, which is not uniform over the turns. In these simulations, the degradation of the critical current is more pronounced in the case of the inner turn (turn $n^{\circ}2$) and external turn of the pancake (turn $n^{\circ}39$) compared to the central turns ($n^{\circ}21$ and $n^{\circ}24$). This degradation on turns $n^{\circ}2$ and $n^{\circ}39$ implies a lower critical current value compared to the other cases. This increases the peak temperature of the pancake during the quench. Indeed, the difference between the supply current I_0 and the critical current value of the degraded sector will be higher, which will cause a higher redistribution of the current but especially an increase in the source terms generated by the azimuthal resistivity of the degraded sector.

Furthermore, in the case of a temperature rise on a sector of the inner or external turn of the pancake, the heat generated will have a smaller diffusion volume (radial heat conduction limited by the edges) compared to the case of a quench initially generated on a central turn of the pancake. This behavior can be seen in Figure IV-9 on the right. The position of the degraded sector changes the temperature gradients within the pancake. With a degradation on the second

turn, the heat is mainly concentrated on the inner turns, unlike the degradation of the sector on the 24th turn, where the heat is distributed on all the turns (only on an angular opening). The temperature peak is therefore different.

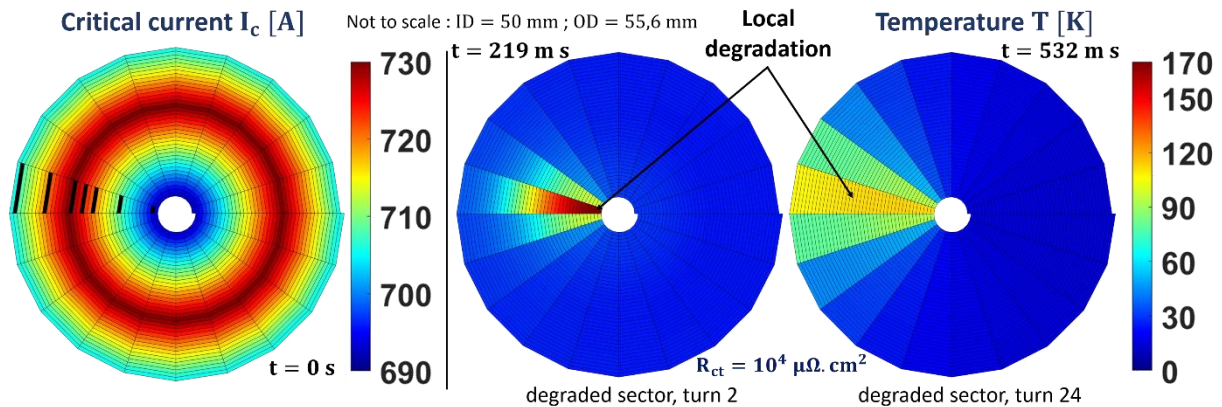


Figure IV-9: On the left, values of the initial critical current of each sector of the pancake in self-field and position of the degraded sectors. On the right, maximum temperature of the pancake $R_{ct} = 10^4 \mu\Omega.cm^2/U_{max} = 0.1 V$ with a degradation on a sector of turn $n^{\circ}2$ and $n^{\circ}24$.

As observed on the left of Figure IV-8, the pancake heats up more and faster in the case where the degraded sector is close to the inner or external turn of the pancake. The resistivity of the pancake is higher, and therefore the voltage limitation is faster (right of Figure IV-8). As the temperature increases more rapidly, the critical current value will be lower and thus a greater current redistribution will occur, generating more radial currents and thus a larger and faster voltage across the pancake.

Thus, generating a quench on a sector belonging to a central turn causes a lower temperature peak compared to the case where the quench is generated on a sector of an inner or external turn of the pancake. The values of the maximum temperatures as a function of the position of the degraded sector for the pancake with the couple $R_{ct} = 10^4 \mu\Omega.cm^2/U_{max} = 0.1 V$ are available in red Figure IV-10.

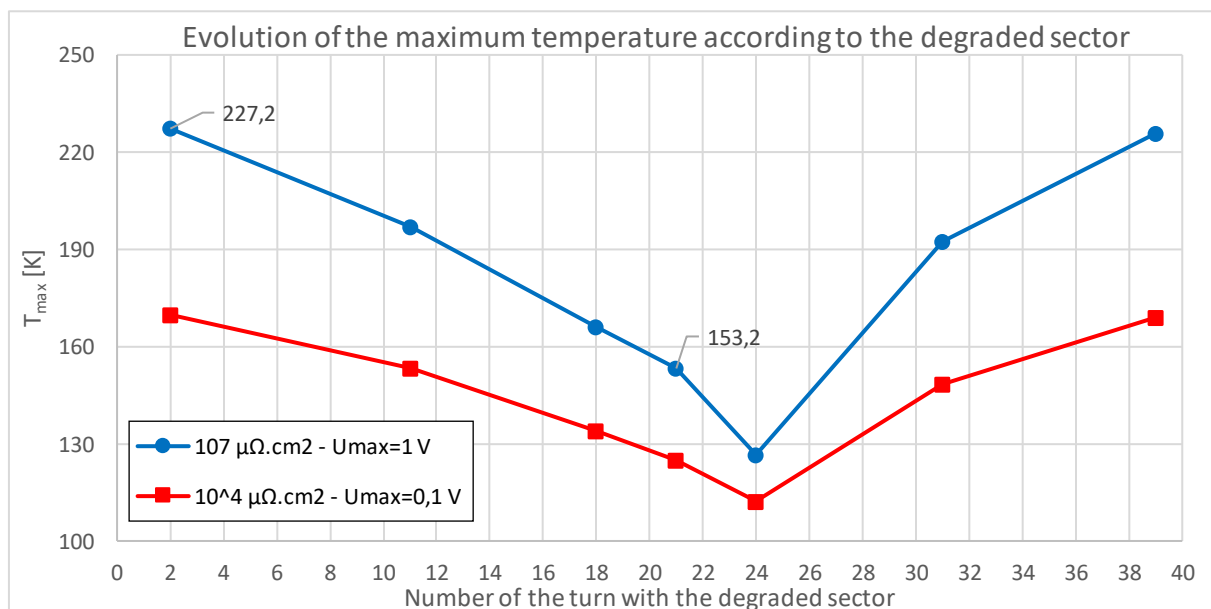


Figure IV-10: Evolution of the maximum temperature according to the degraded sector.

This behavior does not question the protection achieved by the voltage limitation. In our previous simulations (Figure IV-4 and Table IV-3), the maximum temperature recorded over the simulations is $T_{max} = 153.2 K$ for the couple $R_{ct} = 10^7 \mu\Omega.cm^2/U_{max} = 1 V$, with a

degraded sector on the 21st turn. Simulations with $U_{max} = 5$ V and $U_{max} = 10$ V are not taken into account (too little current reduction imposed by voltage limitation, constant increase of T_{max}). This pancake was again simulated with different degradation positions. As for the case of the pancake with the couple $R_{ct} = 10^4 \mu\Omega \cdot \text{cm}^2 / U_{max} = 0.1$ V, the temperature peak is maximum for a degradation on the second turn of the pancake (in blue in Figure IV-10). For the pancake with $R_{ct} = 10^7 \mu\Omega \cdot \text{cm}^2 / U_{max} = 1$ V and a degraded sector on the second turn, the maximum temperature recorded is 227 K, which is still acceptable from the point of view of pancake protection.

The maximum temperature also depends on the number of divisions per turn (n_f) implemented in the PEEC model. This is the subject of the next paragraph.

IV. 2. 1. 2. 4 Study of the number of divisions per turn

In this section, the number of divisions per turn (n_f) is investigated to determine its influence on the calculation of the maximum temperature (T_{max}). For this purpose, the same simple pancake (Table IV-1) with the couple $R_{ct} = 10^4 \mu\Omega \cdot \text{cm}^2 / U_{max} = 0.1$ V is simulated with n_f values ranging from 2 to 30 divisions per turn. The maximum temperature T_{max} as a function of n_f is plotted on the left of Figure IV-11. T_{max} rises with an increase of n_f between 2 and 14. After $n_f = 14$, the maximum temperature decreases and seems to stabilize at a temperature between 110 and 120 K.

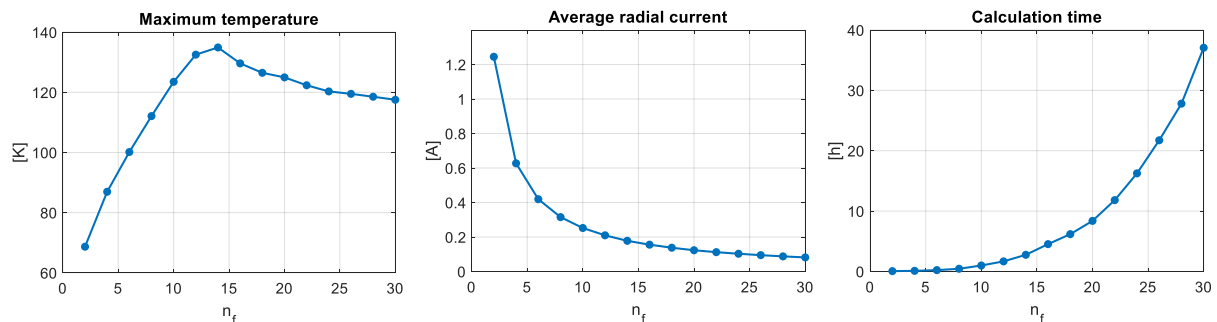


Figure IV-11: Maximum temperature, average radial current when U reaches U_{max} and calculation time as a function of the number of divisions per turn (n_f) for a simple pancake during a quench with $R_{ct} = 10^4 \mu\Omega \cdot \text{cm}^2 / U_{max} = 0.1$ V.

The maximum temperature variations are explained by a change in the value of the radial currents, the volume and the azimuthal and radial resistivity of the sectors.

The value of the average radial current in the pancake when U reaches $U_{max} = 1$ V is proportional to the number of divisions per turn (middle of Figure IV-11). In the case of $n_f = 2$, $I_{r_{aver}} = 1.24$ A when U reaches U_{max} . With $n_f = 20$, the average radial current is 10 times lower ($I_{r_{aver}} = 0.12$ A) because the current initially flowing in 2 radial resistivities is distributed evenly in the 20 resistivities. The radial and azimuthal resistivities are also lower because they are proportional to the length of the sector. Thus, the heat generated by each sector is lower, but the heat is diffused in a smaller volume. Combined with the heat capacity implemented in the PEEC model, T_{max} vary with n_f .

Thus, imposing too many divisions per turn ($n_f > 30$) is not necessary. This does not improve the accuracy of T_{max} and it greatly increases the resolution time. The calculation time as a function of n_f is shown on the right of Figure IV-11. For the cases with $n_f > 26$, the simulation took more than one day. This long simulation time can be explained by the implementation of the voltage limitation, which increases the number of iterations and thus the resolution time.

Conversely, having a lower number of divisions per turn ($n_f \approx 10$) allows the maximum temperature of the pancake to be estimated, but the accuracy of this value is lower. However, reducing n_f does not change the behavior of the pancake with respect to voltage, induction (and thus azimuthal current) and average pancake temperature. It is therefore possible to simulate the behavior of a pancake with values of divisions per turn equal to 10.

IV. 2. 1. 3 Conclusion of a simple pancake with voltage limitation

The maximum temperature for all contact resistivity values and with a maximum voltage of up to 1 V does not exceed 230 K. In the case of voltage limitation, this T_{max} value is reliable for pancake protection, which was not the case with high contact resistivity values without voltage limitation. Imposing a voltage limit of a few millivolts on a pancake is complex to achieve because of the noise present in the signals (current leads and cable voltages). However, a voltage limit of 1 V would protect the pancake well against quenching, without additional protection.

In the case of a higher voltage limitation (with $U_{max} = 5$ V or $U_{max} = 10$ V), the simple voltage limitation does not allow the pancake to be completely protected during the few seconds following the quench. Indeed, too much voltage limitation does not impose a drastic decrease of the supply current I_0 when the limit voltage is reached during the quench. In order to prevent the maximum temperature of the pancake from rising further, the power supply must be switched off. It should be noted, however, that the simulated pancake is not representative of a coil, which generally has 10 to 50 times more turns, and therefore has a much higher resistivity than our simple pancake.

Having an MI winding and a voltage limitation limits the temperature rise, which gives the necessary time to cut the power supply during a quench without burning the magnet. For example, in the case of the pancake with the couple value $R_{ct} = 10^4 \mu\Omega \cdot \text{cm}^2 / U_{max} = 10$ V, 110 ms after the voltage reaches 0.1 V (at $t \approx 470$ ms), the maximum temperature has increased by about 200 K. In the case of the pancake with the same contact resistivity but without voltage limitation, the current redistribution limits the thermal overheating of the pancake but 110 ms after $U = 0.1$ V, the maximum temperature has increased by about 300 K, and keeps rising.

These simulations show that there is no single couple (R_{ct}/U_{max}) to protect a coil, but that a specific protection system must be chosen for each magnet geometry. We will now see this application to a coil consisting of four MI pancakes. In a first phase, the experimental results will be presented, followed by the simulation results in a second phase.

IV. 2. 2 Experimental results: two Theva-SuperPower double pancakes coil

This method of protection has been tested on a coil consisting of two double pancakes powered in series [107]. The two double pancakes consist of a 186 turns pancake with Theva tape, and a 278 turns pancake with SuperPower tape (Figure IV-12). The superconducting tapes are 6 mm wide. The inner diameter of each pancake is 50 mm, the outer diameter is 110 mm. A sapphire plate was inserted between the two simple pancakes, and G10 insulated copper plates were inserted between the two double pancakes (Figure IV-12) to improve the cooling of the coil (more precisely the MI insert). The inductance of a double pancake is 16.9 mH. During the measurements, the magnet is cooled with a liquid helium bath. The acquisition was carried out using a LabVIEW program with NI acquisition cards with different measurement ranges: ± 0.5 V; ± 10 V; ± 60 V and ± 300 V. A Sorensen 8 V - 600 A provided the power supply, allowing the adjustment of the maximum supply voltage. The objective of these tests was to evaluate the stability of this MI winding during a quench with voltage

limitation. The pancakes are metal insulated with 30 μm Durnomag[®] stainless steel tape from Laminerie Matthey SA. The complete parameters of this magnet are available in [107].

For voltage limitation, the maximum value imposed by the power source is set to be 3.9 V or 4.4 V. Taking into account the measurement offsets, the resistivity at the ends of the power source (coil and copper connectors) and the inductive voltage of the coil, with a limitation of 4.4 V on the power source, this amounts to imposing a voltage limitation of about 1 V on the coil.

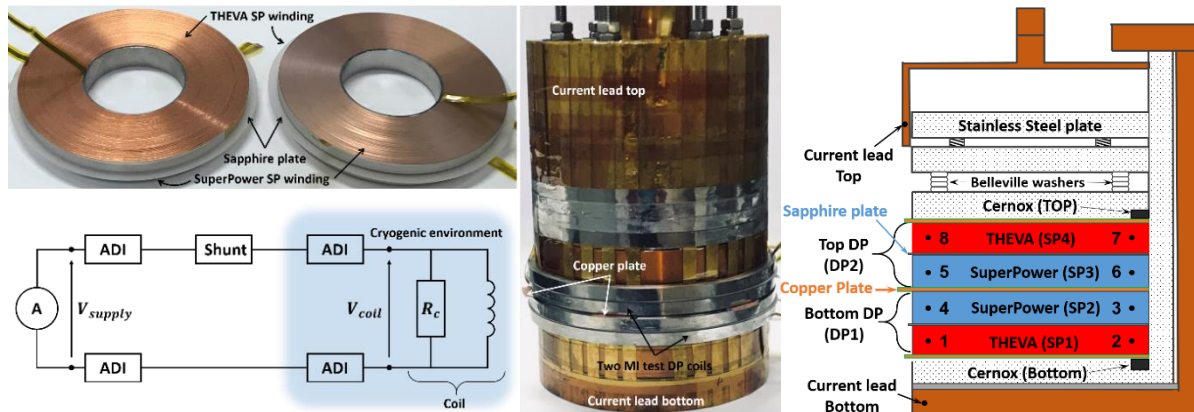


Figure IV-12: On the top left, a photograph of the two MI DP coils used for test. On the middle, picture of the Theva-SuperPower MI HTS insert. At the bottom left, electrical diagram of the installation. On the right, instrumentation diagram. Pictures and schemes from [107].

IV. 2. 2. 1 Voltage limitation during a quench

Several measurements were performed on this insert/magnet. Before and after testing with a voltage limitation, a charge up to 300 A with a ramp at 1 A/s and a discharge at 5 A/s were performed. Through these measurements displayed in Figure IV-13, it is possible to determine the value of the voltage offset ($U_{coil} \approx 0.6$ V at $t = 0$ s), the value of the resistance of the setup (current leads and coil, $R \approx 4$ m Ω), and to check the inductance of the coil ($L_{coil} = 58$ mH) when the supply current is constant.

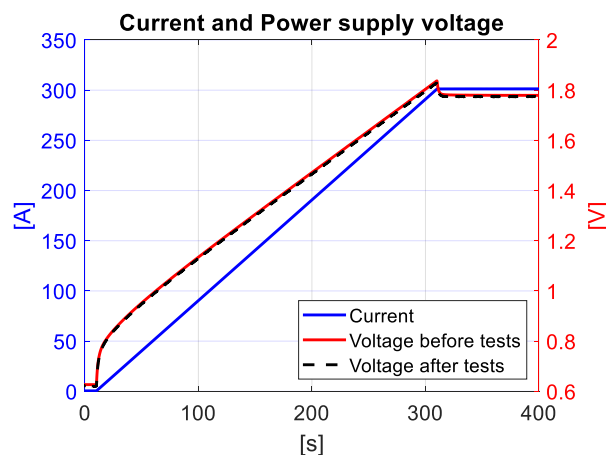


Figure IV-13: Rise to 300 A then constant current, voltage of the Theva-SuperPower MI HTS insert.

Several voltage limitation tests were carried out with different values of the supply current ramp (Table IV-5). For these four tests, the maximum voltage imposed on the supply is set to limit the coil voltage to about 1 V. For the fourth test, the maximum voltage was increased to compensate for the inductive voltage generated during the current ramp. Having a voltage limitation different from 0.5 V during the tests does not affect the protection of the coil. Indeed, when the coil becomes resistive, the voltage increases rapidly. Setting a higher voltage limit of

0.5 V only delays the decrease of the supply current by a few tens of seconds. These few tens of seconds of delay are not a problem in the case of MI windings where the current is redistributed to avoid local defect during a quench.

Table IV-5: Maximum current, maximum induction at center of the coil, plateau current, charging ramp and maximum imposed voltage.

Test	I_{max} [A]	B_{max} [T]	$I_{constant}$ [A]	dI/dt [A/s]	$U_{max, alim}$ [V]
n°1	494	7.01	301	2	3.9
n°2	481	6.855	301	5	3.9
n°3	463	6.541	301	10	3.9
n°4	442	6.122	301	20	4.4

First, a rise to 300 A followed by a plateau at 300 A for two minutes is performed for each test. This step ensures that the coil has not been degraded during the previous tests. After the two-minute plateau, the current increases again with the same value of the steering coefficient until a quench occurs. Figure IV-14 shows the values measured during the last test (n°4). The behavior of the coil is the same as explained in the previous paragraph. By increasing the supply current, the critical current value is exceeded locally in a pancake. This leads to local source terms, which generate a local increase in temperature, further reducing the critical current. A current redistribution takes place in the pancake so that the current bypasses the local defect. This current redistribution generates radial currents and thus a voltage across the coil. The more the critical current value is degraded, the higher the radial currents will be causing a higher coil voltage. When U reaches U_{max} , the voltage limitation causes the supply current to drop, preventing thermal overheating and local burning of the coil. About six seconds after reaching the maximum voltage, the supply current is low but not zero. In order to avoid heating the coil, which is highly resistive, the LabVIEW program sets the supply current to 0 A (Figure IV-14).

The protection was effective for the four tests performed, without damaging the coil. Indeed, the voltage of the power source is the same ($U_{coil} = 1.8$ V) for the four tests when the current is constant at 300 A. Moreover, the verification test after the four tests carried out is identical to the one carried out at the beginning of the experiment (Figure IV-13). As the values are identical, no modification or degradation of the coil can be observed. The temperature sensors at the bottom and top of the coil do not show any temperature above 60 K (Figure IV-14). The first temperature peak for $t \approx 30$ s corresponds to the inductive voltage of the pancake, generating radial currents and thus a uniform temperature rise across the coil. When the supply current I_0 is constant, the coil voltage is zero and it cools down. These values are not representative of the local hot spot temperature of the pancake, but they do show that the pancake has a temperature peak before cooling via the liquid helium bath.

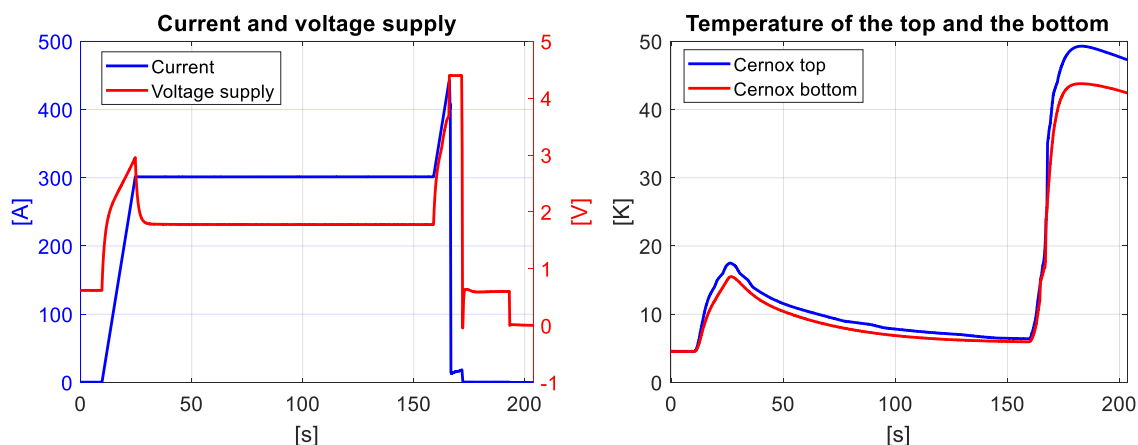


Figure IV-14: Experimental results of two double pancakes with voltage limitation. Current and voltage of the power source and temperature on the top and bottom of the coil of test n°4.

The disadvantage of this method is that the energy is entirely dissipated in the coil and thus in the cryogenic environment (shown in Figure IV-12), causing a rise in temperature which greatly increases the consumption of liquid helium.

For these four simulations, the behavior of the coil during the quench with voltage limitation is relatively identical. The pancake voltages, coil voltage, power supply voltage, magnetic induction in the center of the coil and power supply current from simulation $n^{\circ}4$ during the quench is available in Figure IV-15.

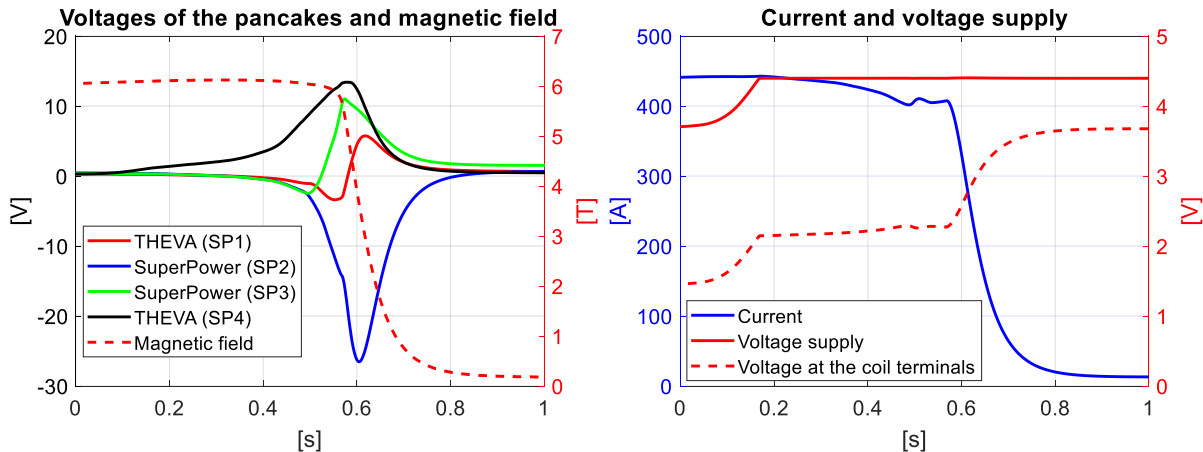


Figure IV-15: Experimental results of the Theva-SuperPower MI HTS insert during a quench with voltage limitation, test $n^{\circ}4$. Pancake voltages, voltage at the coil terminals, power supply voltage, magnetic induction at the center of the coil and power supply current.

The initial instant ($t = 0$ s) in Figure IV-15 corresponds to the time when the voltage of the SP4 pancake is no longer constant, when a rise is observable ($t = 166$ s in Figure IV-14). For $t < 0$ s, the pancake voltages are not zero, the increasing supply current imposes an inductive voltage on the coil (between $t = 158$ s and $t = 166$ s in Figure IV-14). This inductive voltage is measurable on the voltages of the four pancakes but also visible on the voltage at $t = 0$ s of the coil. The inductance of the coil is 57.9 mH and with a ramp of 20 A/s, we obtain a voltage of about 1.2 V (compared to 1.45 V measured on the coil).

Several behaviors during this voltage limitation during a quench can be observed through the data in Figure IV-15:

- **Before the quench**, the power supply voltage is about 3.7 V. This voltage is the sum of the offset of the measured voltage (0.6 V), the inductive voltage ($57.8 \text{ mH} \times 20 \text{ A/s} = 1.2 \text{ V}$) and the voltage generated by the current leads ($\approx 2 \text{ V}$). From $t = 0$ s, a rise in voltage is observable. It is explained by a redistribution of the current to bypass the local defect. Indeed, the value of the supply current is higher than the minimum critical current of the coil. The voltage rise is relatively fast, the limit set at 4.4 V is reached for $t = 170$ ms. By analysing the voltages of the four pancakes, we observe that the voltage of the Theva pancake (SP4) increases, unlike the other three pancakes. It can be deduced from this that the quenching takes place on the Theva pancake (SP4).
- The redistribution of the current in the Theva pancake (SP4) causes a rise in voltage but also a decrease in the magnetic induction generated by the Theva pancake (SP4). This variation in magnetic induction generates electromotive forces on the other three pancakes. A negative voltage is thus measurable at the ends of the three pancakes **between $t = 0$ s and $t = 450$ ms**, and a current loop into the three pancakes takes place. Therefore, they generate more magnetic field, which compensates for the field loss caused by Theva (SP4). The maximum voltage of the power supply is reached at $t = 170$ ms (and limited to 4.4 V), but the decrease of the supply current I_0 is low

because of the negative voltages of the other pancakes which compensate the increase in voltage of the Theva (SP4).

- The appearance of a negative voltage across the other three pancakes generates an azimuthal current higher than the supply current and therefore negative radial currents, which causes the pancakes to heat up. The critical current of the pancakes becomes lower. Moreover, for the SP1 and SP3 pancakes, the new orientation of the field on the tapes also degrades the value of the critical current (II. 3. 1. 1. 1 for further explanations). These two phenomena cause a diffusion of the quench by magnetic coupling. A successive quench on the SuperPower pancake (SP3) from $t = 520$ ms and then on SuperPower (SP4) from $t = 580$ ms is observable via the voltages of the two pancakes. This leads to an even more negative voltage on Theva (SP4), which in turn quenches. This causes a sharp drop in the supply current from $t = 600$ ms.
- For $t > 900$ ms, the voltages of the four pancakes are between 0.5 V and 1.5 V. These voltages are explained by the presence of a non-zero supply current ($I_0 \approx 13$ A for $t > 0.9$ s) and resistivity zones in the coil. The supply current is switched off about 6 s after reaching the value of the maximum supply voltage.

All the detailed behavior of the coil above is achieved mainly with the test data. However, some behaviors, such as the presence of a slope with two director coefficients (**between 0 s $< t < 0.4$ s and 0.4 s $< t < 0.6$ s**) on the Theva (SP4) voltage, are complex to explain only with the experimental data. In order to better understand the behavior of the coil during a voltage-limited quench, the coil was simulated using the PEEC model.

IV. 2. 2. 2 Discharge of the coil for R_{ct} measurement

After performing the voltage limitation tests, several contact resistivity measurements using rapid discharge on the coil were performed. The coil was loaded with several current values (10; 20; 50; 100; 150 and 200 A). The results in Figure IV-16 show that the value of the contact resistivity is higher with increasing charging current.

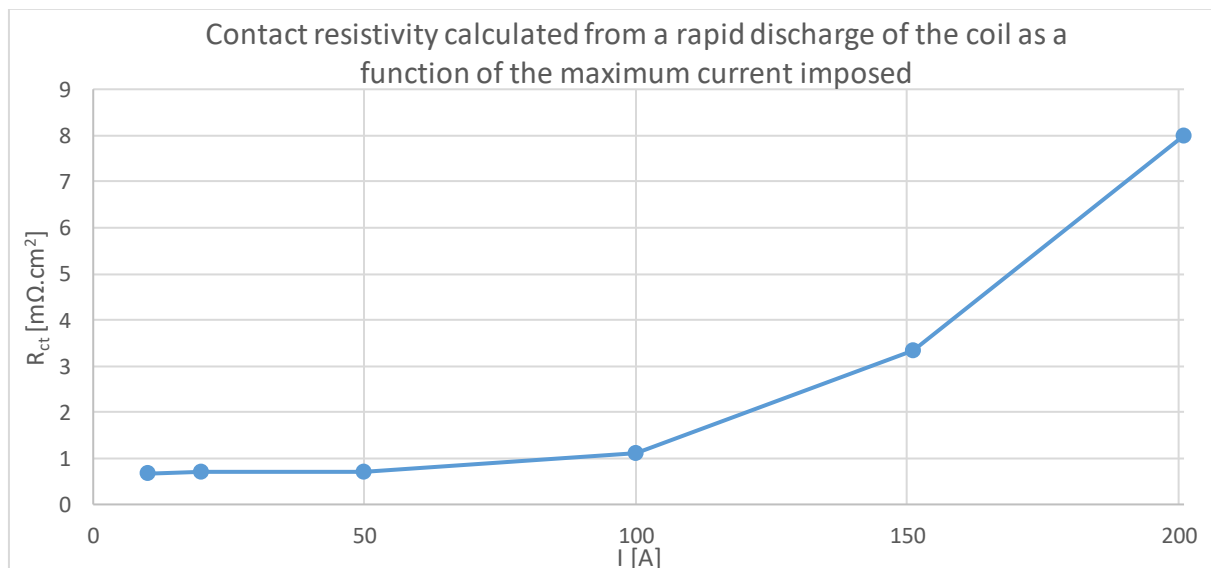


Figure IV-16: Evolution of the contact resistivity calculated from a rapid discharge of the coil as a function of the maximum current imposed.

The different values give a contact resistivity between 0.5 $m\Omega \cdot cm^2$ and 8 $m\Omega \cdot cm^2$. These values are lower compared to the experimental measurements made with superconducting tapes and Durnomag[®] tapes in III. 2. 2. 2. The measured values were about 300 $m\Omega \cdot cm^2$. These two orders of magnitude can be explained by an operating temperature of 4.2 K, whereas the experimental

measurements were carried out at 77 K. They can also be explained by the number of load cycles imposed on the coil during the multiple current rises to carry out the various tests. We will now simulate the case of this coil with the PEEC model.

IV. 2. 3 Simulation: two Theva-SuperPower double pancakes coil

The simulated coil has a relatively high number of turns ($2 \times 186 + 2 \times 278 = 928$). Thus, simulating the entire behavior of the coil (current rise to 300 A, a two-minute plateau and then a further current rise to the quench followed by the post-quench behavior) is not feasible. The most interesting behavior is during the quench. For this purpose, and in order to simulate the coil as well as possible, the chosen parameters are available in Table IV-6.

In order to get as close as possible to the behavior of the coil during a quench with a current limitation caused by a current rise, the simulated coil will initially be loaded with 1% current margin on the load line and in steady state (supply current $I_0 = 439$ A). Then, for $t > 3$ ms, the critical current of a sector on the second inner turn of the Theva pancake (SP4) will be degraded by 100%, its critical current will be zero from $t > 3$ ms. The simulation method is the same as the one presented in paragraph IV. 2. 1.

The co-winding thickness is adjusted to obtain an outer radius relatively close to the experimental measurements. The coil is under adiabatic conditions. Concerning the voltage limitation, the iteration for the same computation time is performed as long as the coil voltage is not between $0.95 \text{ V} \leq U_{coil} \leq 1 \text{ V}$. This reduces the computational time without greatly altering the simulation results with respect to the convergence criterion $0.99 \text{ V} \leq U_{coil} \leq 1 \text{ V}$.

Table IV-6: Parameters of the two double pancakes Theva-SuperPower simulated in the case of a quench with local degradation and with voltage limitation.

Parameters	Units	Values
Turns Theva ($n_{a-Theva}$)	—	186
Turns SuperPower (n_{a-SP})	—	278
Division per turn (n_f)	—	2
Tape width (h_0)	mm	6
Winding inner diameter (ID)	mm	50
Winding outer diameter (OD), Theva and SuperPower	mm	110
Local degradation	%	100
Current margin on the load line	%	1
Supply current (I_0)	A	439
Initial temperature (T_0)	K	4.2
Coil self-inductance	mH	57.9
Substrate thickness Theva	μm	100
Substrate thickness SuperPower	μm	50
Co-winding thickness Theva	μm	38
Co-winding thickness SuperPower	μm	35
Copper thickness, Theva and SuperPower	μm	22
Superconductor thickness	μm	2
Thickness between each pancake	μm	600
Convective exchange coefficient (h)	$\text{W}/\text{m}^2/\text{K}$	0
Contact resistivity Theva and SuperPower (R_{ct})	$\text{m}\Omega.\text{cm}^2$	4
Power supply voltage limitation	V	1
Range for voltage limitation	%	[0.95,1]

Using the mutual inductances calculated for the simulation, it is possible to obtain the value of the self-inductance of the Theva-SuperPower MI HTS insert. With the PEEC model, the inductance value is 16.8 mH compared to 16.9 mH given in [107].

The value of the contact resistivity R_{ct} is, of course, one of the important parameters of this simulation. We will see later that it modifies the behavior of the coil during a quench, as well as the value of the radial thermal conductivity k_r . This second parameter will also be studied here to understand its influence on the behavior of the coil. A value of $R_{ct} = 4 \text{ m}\Omega\cdot\text{cm}^2$ is chosen in view of the contact resistivity measurements carried out using rapid discharge on the coil (IV. 2. 2. 2).

IV. 2. 3. 1 Superposition of experimental measurements and simulation

The results in Figure IV-17 show the superposition of experimental measurements and simulation of the voltage of each pancake, the voltage of the coil, the supply current I_0 and the magnetic induction at the center of the Theva-SuperPower MI HTS insert. The behaviors of the pancakes and the coil between the experimental results and those of the simulation of the coil during a voltage-limited quench are similar, although the results do not coincide.

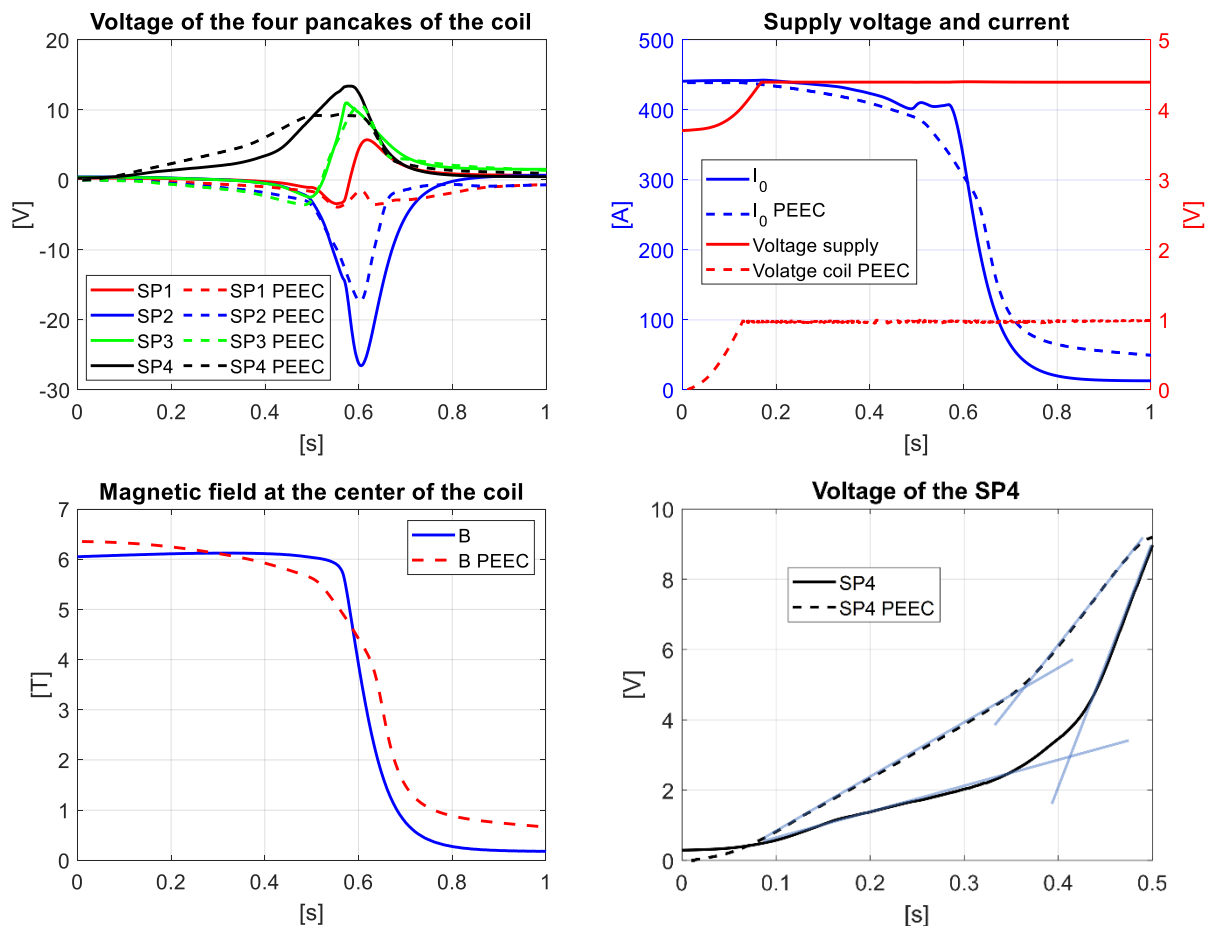


Figure IV-17: Comparison of experimental and simulation results of the Theva-SuperPower MI HTS insert during a voltage-limited quench. Pancake and coil voltages, supply current and magnetic induction at the center of the coil. Double slope on the voltage rise of the SP4 pancake. With $R_{ct} = 4 \text{ m}\Omega\cdot\text{cm}^2$.

Concerning the pancake voltages displayed in Figure IV-17, the values obtained via simulation and experimental measurements have the same evolution.

- Concerning the voltage of the simulated SP4 (the pancake where the quench appears) the voltage increases slightly faster compared to the voltage of the experimental

measurements for $0 \text{ s} < t < 0.5 \text{ s}$. Nevertheless, the peak voltage obtained experimentally is higher compared to the simulation results. The two voltages are still relatively in phase, with a good match for $t > 0.6 \text{ s}$ as the pancake voltage decreases. The double slope behavior of the SP4 voltage is visible through the simulation (bottom right of Figure IV-17). This phenomenon is caused by the value of the radial thermal conductivity k_r and is explained in the following paragraph IV. 2. 3. 3.

- About the voltages of SP3, the two values are relatively close, especially during the transition of the pancake for $t > 0.5 \text{ s}$ when the voltage increases strongly. Before the transition, the inductive voltage on the pancake is well observed, but more pronounced than in the experimental measurements.
- For the voltage of the SP2 pancake, the behavior is close up to 0.55 s , with a strongly negative voltage for $t = 0.6 \text{ s}$, the moment when the SP1 and SP3 pancakes have quenched. However, a difference of almost 10 V can be observed for this minimum.
- The main difference between the simulation and the experimental measurements can be observed in the voltage of the SP1 pancake. Although the measured and simulated voltages are similar up to $t = 0.55 \text{ s}$, the moment of the pancake transition, they differ for $t > 0.55 \text{ s}$. The simulated voltage remains negative but with an increase in voltage for $t = 0.6 \text{ s}$, while the experimental voltage becomes positive. A difference of up to 8 V can be observed.

The voltage evolution of each pancake is nevertheless found with the help of the simulation. This allows a better understanding of the behavior of each pancake and therefore of the coil by means of the simulations.

Concerning the experimental supply voltage and the simulated coil voltage, the values are different because the simulation has no offset ($\approx 0.6 \text{ V}$), does not take into account the inductive voltage ($\approx 1.2 \text{ V}$, caused by the increasing supply current I_0) and the voltage generated by the current leads and cables ($\approx 1.8 \text{ V}$). A difference of about 3.6 V is observable (top right of Figure IV-17). There is a small time lag of 38 ms between the simulation and the experiment regarding the moment when the voltage limitation is reached. The behavior is relatively similar. The same is true for the coil supply current I_0 . The current decreases slightly for $0 \text{ s} < t < 0.5 \text{ s}$ before dropping sharply for $t > 0.5 \text{ s}$ and stabilizing for $t \geq 1 \text{ s}$. However, the current is still higher at the end of the simulation compared to the experimentally current. This difference come from the coil, which is more resistive experimentally, decreasing the supply current more significantly via voltage limiting.

Concerning the evolution of the magnetic induction at the center of the coil (bottom left of Figure IV-17), the behavior is also similar between simulation and experiment. A difference of 0.3 T at $t = 0 \text{ s}$ is observable. This difference can be explained by the screening currents, which are not taken into account in this PEEC model. The magnetic induction decreases sharply from $t > 0.5 \text{ s}$ before remaining relatively low for $t \geq 1 \text{ s}$. Again, a difference of about 0.4 T is measurable between the simulation and experimental results.

In this PEEC model, the contact resistivity is uniform between all turns of each pancake. In reality, the radial tension varies according to the turn number, which changes the value of the turn-to-turn contact resistivity in the coil. This difference between the PEEC model and the experimental one could be corrected by knowing the compression value in the coil between each turn. In addition, during voltage limiting experimentally, the coil voltage will increase and exceed the 1 V voltage because the voltage is actually limited on the supply. Thus, when the supply current decreases, the voltage generated by the current leads is less resistive, the coil voltage increases but still in a limited way. These differences may explain some of the differences between the simulation and experimental results. However, it is perfectly possible

to simulate the general behavior of a coil consisting of four pancakes during a quench with a voltage limitation via the PEEC model. With the help of this simulation, it is for example possible to carry out an energy balance of the coil during the quench, which is presented in the next subsection.

As for all the simulations in this thesis, the value of the contact resistivity affects the behavior of the coil. The same is true for the value of the radial thermal conductivity. These two parameters are studied in the next two sections.

IV. 2. 3. 2 Influence of the contact resistivity

Several parameters were modified and adjusted in order to obtain a similarity between the experimental and simulation results. As explained in paragraph II. 3, the contact resistivity value is the main parameter concerning the behavior of the coil during a quench. The lower its value, the greater the diffusion of the quench by magnetic coupling. Several simulations with the parameters presented in Table IV-6 were executed with the only difference being the value of the contact resistivity ($R_{ct} = 3; 4; 5; 6; 20 \text{ m}\Omega\cdot\text{cm}^2$). The results of the voltages of the four pancakes during the quench for the simulations where $R_{ct} = 3; 5; 20 \text{ m}\Omega\cdot\text{cm}^2$ and $U_{max} = 1 \text{ V}$ are available in Figure IV-18.

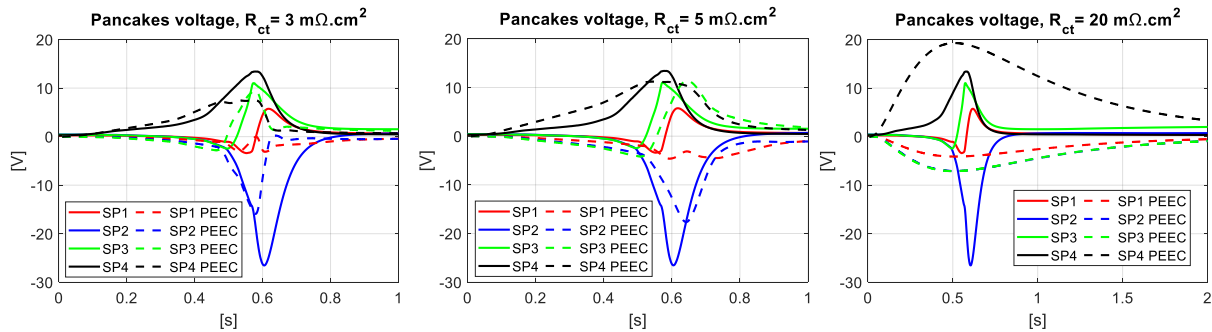


Figure IV-18: Pancake voltages from the simulation of the Theva-SuperPower MI HTS insert during a quench with voltage limitation for different contact resistivity values.

As expected, we can see that the higher the value of the contact resistivity R_{ct} , the less the quench spreads to the adjacent pancakes. This can be seen in the case of $R_{ct} = 20 \text{ m}\Omega\cdot\text{cm}^2$, where the voltage of the SP1 pancake is the only one to become positive. The other three pancakes have negative voltages before returning to zero at $t = 2 \text{ s}$. This behavior indicates that only the SP4 pancake has quenched. Conversely, with $R_{ct} = 3$ and $5 \text{ m}\Omega\cdot\text{cm}^2$, the diffusion of the quench by magnetic coupling occurs on the adjacent pancakes, causing the voltage of the other three pancakes to rise.

The higher the value of the contact resistivity, the higher the pancake voltages, positive or negative, will be. In the simulation of the previous paragraph, we observe a good correspondence between the pancake voltages and the diffusion of the quench by magnetic coupling compared to the experimental measurements for the same value of the contact resistivity ($R_{ct} = 4 \text{ m}\Omega\cdot\text{cm}^2$). With a lower contact resistivity value, the pancake voltages would not be high enough compared to the experimental measurements. In addition, with a higher contact resistivity, the pancake voltages would be too high compared to the experimental measurements, and the diffusion of the quench by magnetic coupling would not take place. In the case of this simulation, $R_{ct} = 4 \text{ m}\Omega\cdot\text{cm}^2$ is a good compromise.

This diffusion of the quench by magnetic coupling can also be observed via an energy balance of the simulations (Table IV-7). In this table, the energy injected into the coil by the power supply is included in the total initial state energy although it is zero for $t = 0 \text{ s}$. The total initial

state energy is therefore the sum of the initial state magnetic energy and the power source energy. The total initial state energy is therefore the sum of the magnetic energy ($t = 0$ s) and the energy injected by the power source. The total final state energy is the sum of the magnetic energy ($t = 1$ s) and the energy dissipated as heat. The method of calculating the different energies is the same as in paragraph II. 3. 2. This energy balance is performed for each simulation at $t_f = 1$ s.

Table IV-7 : Energy balance of the Theva-SuperPower MI HTS insert simulations during a quench with voltage limitation for different contact resistivity values.

R_{ct} [$m\Omega.cm^2$]	3		4		5		6		20	
Time [s]	0	1	0	1	0	1	0	1	0	1
Magnetic energy of the Coil [J]	5563.8	80.7	5563.8	80.6	5563.8	96.8	5563.8	154.1	5563.8	773.4
Energy dissipated, Joule effect SP1 [J]	0	969.8	0	854.6	0	710.7	0	494.9	0	45.9
Energy dissipated, Joule effect SP2 [J]	0	1508.7	0	1374.0	0	1172.1	0	847.7	0	91.7
Energy dissipated, Joule effect SP3 [J]	0	1549.8	0	1522.8	0	1506.3	0	1529.3	0	92.1
Energy dissipated, Joule effect SP4 [J]	0	1636.5	0	1939.1	0	2315.4	0	2826.4	0	4847.5
Energy of the power supply [J]	230.6		245.2		261.8		289.5		286.9	
Total initial state energy [J]	5794.4		5809.0		5825.6		5853.3		5850.7	
Total final state energy [J]	5745.5		5771.1		5801.3		5852.4		5850.6	
Part of energy dissipated in SP1 [%]	17.0	14.9	12.4	8.7	0.9					
Part of energy dissipated in SP2 [%]	26.4	24.0	20.5	14.9	1.8					
Part of energy dissipated in SP3 [%]	27.1	26.6	26.3	26.8	1.8					
Part of energy dissipated in SP4 [%]	28.6	33.9	40.4	49.6	95.5					

From the energy balance of each simulation, it is clear that the lower the contact resistivity, the more energy is dissipated equally across the pancakes. Conversely, if the contact resistivity is high, only the pancake with a local defect will dissipate all the energy of the coil, generating significant temperature rises. When $R_{ct} = 3$ $m\Omega.cm^2$, the SP1, SP2, SP3 and SP4 pancakes dissipate 17%, 26.4%, 27.1% and 28.6% of the energy of the coil respectively. This energy distribution causes a relatively equal average temperature increase between the pancakes. It is different when $R_{ct} = 20$ $m\Omega.cm^2$. The SP1, SP2, SP3 and SP4 pancakes dissipate 0.9%, 1.48%, 1.8% and 95.5% respectively of the energy present in the coil. This uneven distribution causes a significant temperature rise only on the SP4 pancake where the quench occurred. On the other three pancakes, the temperature rise is small as the energy is mainly dissipated on the SP4 pancake.

IV. 2. 3. 3 Influence of radial thermal conductivity

The value of the radial thermal conductivity k_r is an important parameter in the behavior of the pancakes during a quench. In the simulations in Chapter II and those presented earlier, except for the simulations of the Theva-SuperPower double pancakes (IV. 2. 3), the values of the radial thermal conductivity k_r as a function of temperature is shown in Figure IV-19 ($k_{r, PEEC}$). Work has been done by H. Bai [108] on a stack of YBCO superconducting tapes interleaved with insulated StS tapes, also shown in Figure IV-19 ($k_{r, YBCO+StS}$).

The function defining the value of the radial thermal conductivity k_r as a function of temperature in the PEEC model appears to be overestimated. Roughly speaking, a factor of 10 can be observed between the values of the PEEC model and those measured experimentally on the stack of superconducting tapes by H. Bai [108]. Thus, in the simulations of the Theva-SuperPower double pancakes (IV. 2. 3), the radial thermal conductivity value has been divided by 10, also shown in Figure IV-19 ($k_{r, PEEC/10}$).

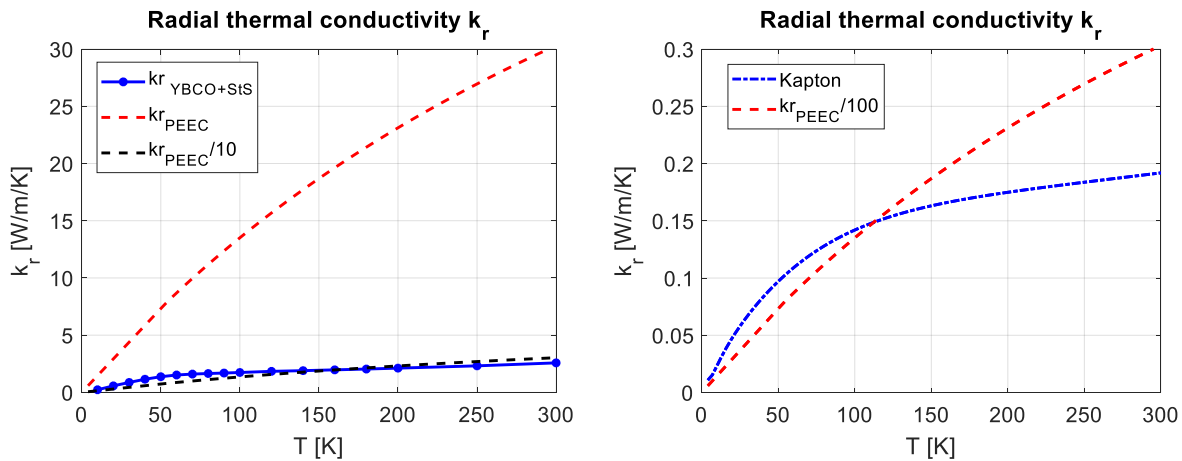


Figure IV-19: Comparison of radial thermal conductivity as a function of temperature between HTS tapes from the PEEC model, from experimental measurements [108] and from Kapton.

Different simulations were thus run with the parameters of Table IV-6 but with different values of radial thermal conductivity (with k_r divided by a factor 1; 5; 10 and 20). The voltages of the four pancakes from these four simulations are shown in Figure IV-20. Thus, with this PEEC model, it is also possible to understand the behavior of a coil during a quench as a function of the radial thermal conductivity, although this was not one of the lines of research during this thesis. However, a minimum value of k_r is imposed. In the case of our function generating $k_r(T)$, it is not possible to divide it by a factor greater than 100. This would mean that the radial thermal conductivity would be lower than that of Kapton, which is a very good thermal insulator (comparison on the right of Figure IV-19).

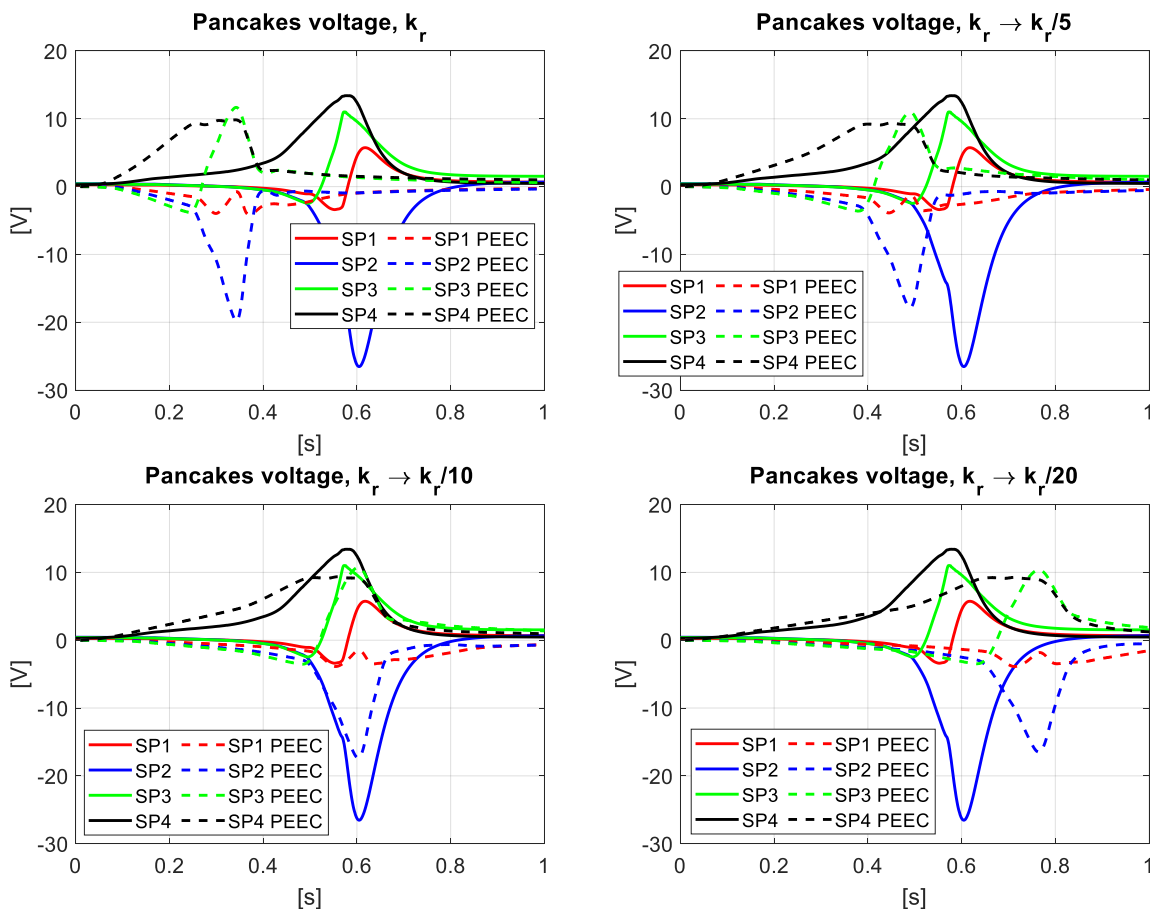


Figure IV-20: Pancake voltages from the simulation of the Theva-SuperPower MI HTS insert during a quench with voltage limitation ($U_{max} = 1$ V) for different values of radial thermal conductivity and $R_{ct} = 4$ m Ω .cm 2 .

The higher the radial thermal conductivity k_r , the faster the voltage rise of the SP4 pancake and the faster the other pancakes will quench. This can be clearly seen by taking the time of the peak voltage of the SP3 pancake as a reference (Figure IV-20 and Table IV-8).

Table IV-8: Time of peak voltage of SP3 as a function of radial thermal conductivity k_r .

Radial thermal conductivity k_r	k_r	$k_r \rightarrow k_r/5$	$k_r \rightarrow k_r/10$	$k_r \rightarrow k_r/20$
Time of peak voltage of SP3	330 ms	480 ms	590 ms	760 ms

The minimum and maximum voltages of the pancakes are identical regardless of the value of the radial thermal conductivity k_r . Indeed, since the contact resistivity is similar between the four simulations ($R_{ct} = 4 \text{ m}\Omega\cdot\text{cm}^2$), the voltages have the same amplitudes.

The value of the radial thermal conductivity also has an influence on the voltage behavior of the SP4 pancake, the one where the quench is generated. Indeed, the lower the radial thermal conductivity, the slower the voltage rise of SP4 and the slower the two distinct ramps.

With a low radial thermal conductivity, heat spreads less quickly to adjacent areas, resulting in a higher local temperature than with a high radial thermal conductivity. The degradation of the critical current is therefore localized. A small number of sectors have an azimuthal current higher than the critical current with low radial thermal conductivity. Conversely, if the radial thermal conductivity is high, heat will diffuse more rapidly, decreasing the critical current of a larger number of sectors (left of Figure IV-21).

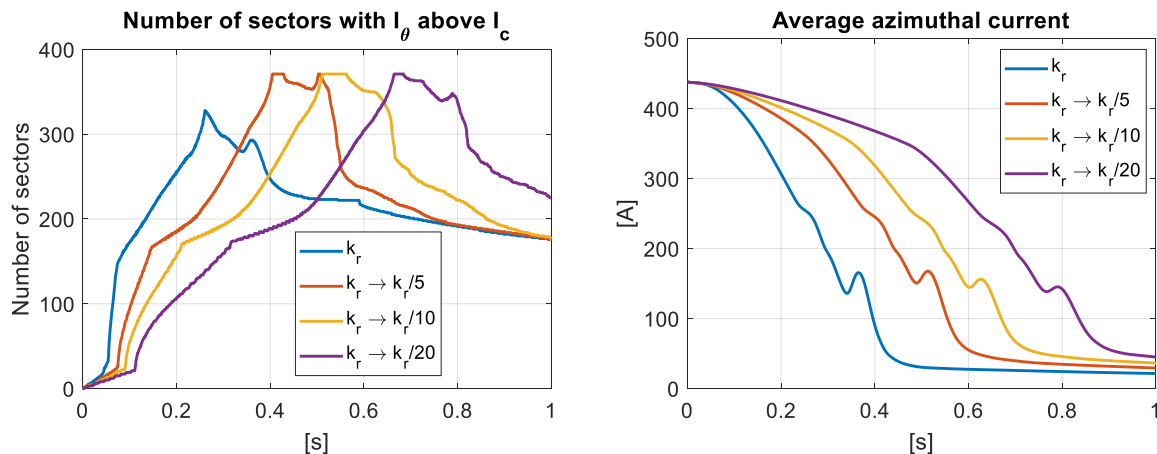


Figure IV-21: On the left, number of sectors with azimuthal current above the critical current. On the right, average azimuthal current for different values of radial thermal conductivity.

In the case where k_r is low, the temperature is thus high but locally. The number of degraded sectors increases more slowly, the current redistribution (the presence of radial currents I_r and thus the appearance of a voltage across the pancake) also occurs more slowly. This behavior can be observed very well with the help of the average azimuthal current (on the right of Figure IV-21). If the current redistribution is small, then the current flows mainly azimuthally. The heat still spreads to adjacent sectors, causing an increase in the number of degraded sectors, which increases the current redistribution. The increase in radial current, combined with an increasing number of degraded sectors, generates more source term, which leads to the quench of the pancake. **In the case of high radial thermal conductivity, heat diffusion is faster, increasing the number of quenched sectors more rapidly, accelerating the pancake quenches.**

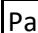
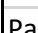
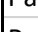
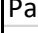
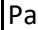


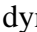
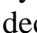
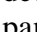
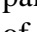
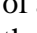
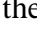
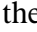

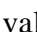
The presence of two voltage rise slopes for a low radial thermal conductivity is explained by two phases of current redistribution. In the first phase, the number of degraded sectors is low, so the current redistribution is low. The heat generated by the quenched sectors diffuses increasing the number of degraded sectors, which generates more source term causing a more

intense redistribution, and thus a faster increase of the SP4 pancake voltage. In the case of high radial thermal conductivity, the number of degraded turns increases rapidly, generating a strong current redistribution from the beginning of the quench. These two phases of current redistribution are possible because the value of the contact resistivity is not very high, which allows a redistribution of the current on the adjacent turns.

A new energy balance was performed to observe the influence of the radial thermal conductivity on the temperature peak (Table IV-9). The method of calculating the different energies is the same as in paragraph II. 3. 2.

Through this energy balance, it can be seen that the lower the radial thermal conductivity, the less heat is diffused to the adjacent sectors causing a higher peak coil temperature. The proportion of energy dissipated in each pancake is relatively equal between these four simulations because the contact resistivity is identical. Fluctuations are however observable. Indeed, the lower the radial thermal conductivity, the lower the proportion of energy dissipated in the SP1, SP2 and SP3 pancakes. The proportion of energy dissipated in SP4 is therefore greater. This change is explained by a less pronounced redistribution of the current in the case of low k_r . The decrease in azimuthal current is less important, which causes a smaller decrease in the flux of the magnetic induction through the SP1, SP2 and SP3 pancakes. This means lower electromotive forces, i.e. lower radial currents and lower temperature rise, without preventing the diffusion of the quench over the three pancakes.

Table IV-9: Energy balance of the Theva-SuperPower MI HTS insert simulations during a quench with voltage limitation for different values of radial thermal conductivity.

k_r [W/m/K]	k_r		$k_r/5$		$k_r/10$		$k_r/20$	
	0	1	0	1	0	1	0	1
Time [s]	0	1	0	1	0	1	0	1
Magnetic energy of the Coil [J]	5563.8	41.8	5563.8	61.5	5563.8	80.6	5563.8	136.0
Energy dissipated, Joule effect SP1 [J]	0	958.7	0	894.4	0	854.6	0	797.6
Energy dissipated, Joule effect SP2 [J]	0	1507.2	0	1422.2	0	1374.0	0	1294.5
Energy dissipated, Joule effect SP3 [J]	0	1612.9	0	1562.4	0	1522.8	0	1460.0
Energy dissipated, Joule effect SP4 [J]	0	1544.2	0	1788.3	0	1939.1	0	2150.3
Energy of the power supply [J]	155.4		207.5		245.2		297.6	
Total initial state energy [J]	5719.2		5771.3		5809.0		5861.4	
Total final state energy [J]	5664.8		5728.8		5771.1		5838.4	
Part of energy dissipated in SP1 [%]	 16.9	 15.7	 14.9	 13.9				
Part of energy dissipated in SP2 [%]	 26.5	 24.9	 24.0	 22.6				
Part of energy dissipated in SP3 [%]	 28.4	 27.4	 26.6	 25.5				
Part of energy dissipated in SP4 [%]	 27.2	 31.3	 33.9	 37.6				

Thus, the radial thermal conductivity k_r is an important parameter concerning the quench dynamics in a coil. In the case of this coil with a contact resistivity of $R_{ct} = 4 \text{ m}\Omega\cdot\text{cm}^2$, decreasing the radial thermal conductivity will delay the diffusion of the quench over the pancakes. A good knowledge of this parameter is therefore essential to simulate the behavior of a coil. In addition, as for the case of the contact resistivity between each turn of the pancakes, the radial thermal conductivity is uniform in the PEEC model, which is not really the case given the variation of the voltage in a pancake as a function of the turn. The value of the radial thermal conductivity is an important parameter in the behavior of the coil. A good knowledge of its value is necessary, especially as it must vary according to the type of co-winding used. Experimental measurements of k_r could not be made. However, as with the electrical contact resistivity, the thermal contact resistivity must depend on the surface condition of the tapes, their hardness, the presence and material of the co-wound tapes and the mechanical stress.

Voltage limitation during a quench can protect a coil consisting of several MI pancakes by limiting the local temperature peak within the coil. The presence of a magnetic shielding also makes it possible to reduce a temperature peak during a transient regime. The purpose of the magnetic shielding is to absorb part of the magnetic energy of the coil. Its behavior is only observed through simulations with the PEEC model in the last part of this Chapter IV.

IV. 3 Magnetic shielding

Magnetic shielding consists of adding turns of NI superconducting tape inside the overbanding, usually made of stainless steel (StS) tape. The presence of additional turns has an effect on the transient behavior of the coil. The magnetic shielding limits the magnetic field fluctuations during a transient phenomenon. Thus, it plays a role in protecting the coil by reducing the induced voltages for all the pancakes. This magnetic shielding also allows the extraction of part of the magnetic energy initially stored in the main pancakes of the coil. Work on such magnetic shielding during rapid magnet transients has been carried out by S. An [59] and T. Mato [109]. They have numerically shown the beneficial effect of such a technique on the temperature peaks (decreased from 80 K to 70 K) and stresses (decreased from 533 MPa to 352 MPa) during a quench of a NI magnet.

We will first quickly see the modifications made to the PEEC model and then study the case of a coil with magnetic shielding in the case of a rapid discharge and a quench.

IV. 3. 1 Magnetic shielding: modification of the PEEC model

IV. 3. 1. 1 Mutual inductances between the pancakes and the magnetic shielding

In the case of magnetic shielding, the additional NI superconducting turns in the overbanding are neither powered nor electrically connected to the central pancake (Figure IV-22). The only connection between the pancake and the magnetic shielding is by magnetic coupling. For this purpose, a calculation of the mutual inductances between the sectors of the pancake and the magnetic shielding has to be made.

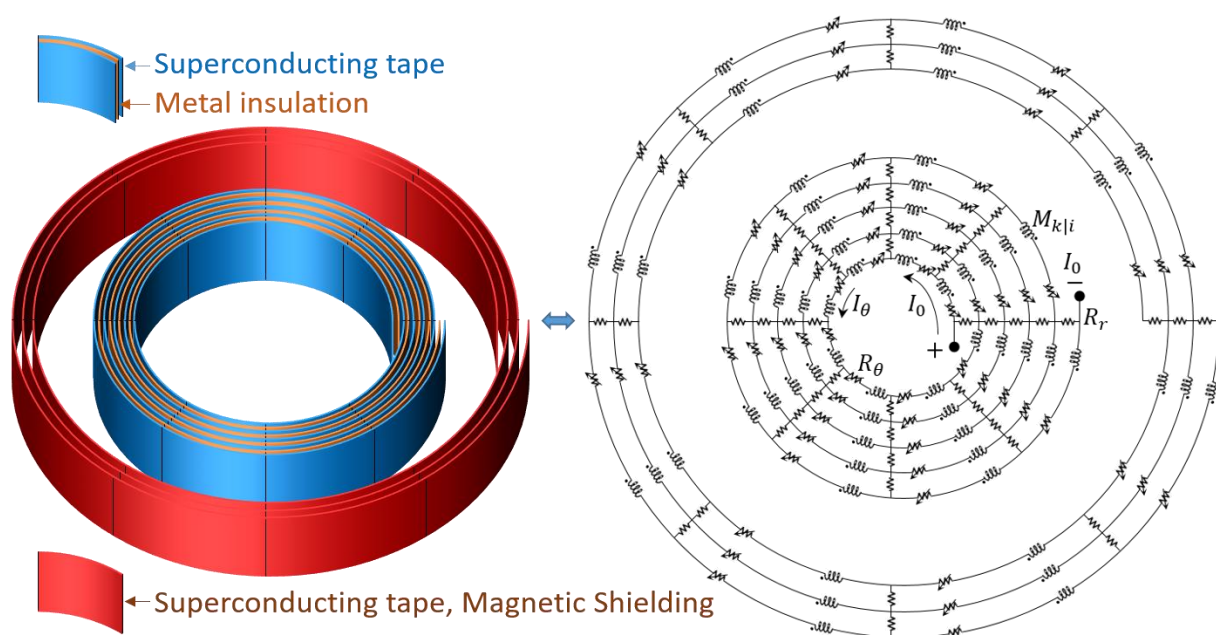


Figure IV-22: Sketch and electrical circuit of a NI-MI simple pancake with Magnetic Shielding.

In the case of magnetic shielding, the radii of the sectors are simply larger than the radii of the sectors of the pancakes. The calculation method is the same as for the case of a mutual inductance between two sectors of a pancake. Equation (7) from paragraph II. 1. 3. 1 is used here to obtain the value of the mutual inductances of the two coaxial fine angular sectors between the pancake and the magnetic shielding. The matrix M of all mutual inductances in the case of a pancake (P) with magnetic shielding (MS) is of the form:

$$M = \begin{pmatrix} M_{P|P} & M_{P|MS} \\ M_{MS|P} & M_{MS|MS} \end{pmatrix}$$

In the case where the pancake and the magnetic shielding are composed of n_a and n_{a-MS} turns respectively; n_f and n_{f-MS} divisions per turn, then $M \in M_{n_a \times n_f + n_{a-MS} \times n_{f-MS}}(\mathbb{R})$. As in the case of a simple pancake, the matrix M grouping all the self and mutual inductances is symmetric: ${}^tM = M$.

In order to simplify the calculation of the mutual matrix M , the number of divisions per turn of the outer pancake is equal to the number of divisions of the inner pancake, i.e. $n_f = n_{f-MS}$. This makes it possible to have a simple to implement code for obtaining mutual inductances and symmetries in the matrix M . The principle of construction of the matrix M is therefore relatively similar to that presented in paragraph II. 1. 3. 1.

The presence of the magnetic shielding increases the number of sectors, which generates a larger matrix system. This increases the computation time compared to the simulation of the same pancake without the presence of the magnetic shielding.

IV. 3. 1. 2 Electrical and thermal equation

For the construction of the electrical equation, the principle is the same as in the case of a coil consisting of two pancakes. The addition of a magnetic shielding increases the size of the matrix system. However, in the case of a magnetic shielding, the additional superconducting turns are not electrically connected to the pancake. Therefore, in order to disregard an electrical connection between the pancake and the magnetic shielding, a change in the vector of the supply current I_0 is made. In the case of a coil consisting of several pancakes with a magnetic shielding around each pancake, the pancakes are powered in series and wound in the same way as in paragraph II. 1. 1. 2. The various magnetic shielding around each pancake are electrically insulated.

No modification is necessary for the thermal part in the case of simple or multi-pancake with the presence of the magnetic shielding. We consider that each pancake are thermally decoupled from each other's. The thermal equations for each pancake are solved in parallel to reduce calculation time.

IV. 3. 2 Simulations with magnetic shielding

IV. 3. 2. 1 Rapid discharge with magnetic shielding

The presence of a magnetic shielding changes the behavior of the coil during a rapid discharge. To observe the phenomenon, a coil consisting of four 200 turns pancakes and 10 turns for magnetic shielding around each pancake is simulated. Convective cooling on the inner and external turns of the pancakes is taken into account. The parameters are available in Table IV-10. The coil is initially charged and then at $t = 3$ ms, the supply current is set to 0 A to simulate a circuit opening. The voltage of the pancakes becomes strongly negative (bottom right of Figure IV-23), the current loops in the pancakes. The simulation is done with and without

the presence of the magnetic shielding (shown in red in the sketch at the top left of Figure IV-23). Either the energy is dissipated only in the four pancakes, or it is distributed unequally between the pancakes and the turns of the magnetic shielding. With the presence of the magnetic shielding, the azimuthal current decrease for the pancakes is faster (bottom left of Figure IV-23). In addition, since part of the magnetic energy of the coil is dissipated in the magnetic shielding, the maximum temperature of each pancake (here comparable to the average temperature since during unloading the radial currents are uniform, and thus the pancake heats up uniformly) is lower compared to the case without magnetic shielding (top right of Figure IV-23). The energy absorbed by the magnetic shielding is dissipated more slowly. Indeed, since the contact resistivity is lower in the case of the magnetic shielding ($R_{ct-MS} < R_{ct}$), the field decay will also be lower, which explains the presence of two time constants on the field decay at the center of the magnet during a fast discharge (top left of Figure IV-23). This weaker field decay for $t > 0.1$ s is explained by the presence of azimuthal current flowing in the magnetic shielding, thus generating a magnetic induction. Finally, the presence of this magnetic shielding avoids a too rapid decay of the magnetic field, which could damage the main winding due to unbalanced forces.

Table IV-10: Parameters of the four pancakes coil in the case of a sudden discharge, with and without magnetic shielding.

Parameters	Units	Values
Turns (n_a)	—	200
Pancakes and pancakes for magnetic shielding	—	4
Turns for magnetic shielding (n_{a-MS})	—	10
Tape width (h_0)	mm	6
Winding inner diameter (ID)	mm	50
Winding outer diameter (OD)	mm	98.6
Winding inner diameter magnetic shielding (ID_{MS})	mm	104.6
Winding outer diameter magnetic shielding (OD_{MS})	mm	105.8
Current margin	%	10
Supply current (I_0)	A	107
Initial temperature (T_0)	K	4.2
Coil self-inductance without magnetic shielding	mH	39.8
Substrate thickness	μm	50
Copper thickness	μm	20
Superconductor thickness	μm	2
Co-winding thickness	μm	50
Co-winding thickness for magnetic shielding	μm	0
Thickness between each pancake	μm	600
Convective exchange coefficient (h)	W/m ² /K	1 000
Contact resistivity Pancake (R_{ct})	$\mu\Omega\cdot\text{cm}^2$	10 000
Contact resistivity of magnetic shielding (R_{ct-MS})	$\mu\Omega\cdot\text{cm}^2$	100

In the results of Figure IV-23, the values of the pancake P_1 are identical with those of the pancake P_4 (likewise with the couples $P_2 - P_3$, $MS_1 - MS_4$ and $MS_2 - MS_3$). Since the coil is symmetrical, it is normal to obtain identical results for the mentioned couples in the case of rapid discharge. The maximum discharge temperature for the P_1 and P_4 pancake without magnetic shielding is 26.9 K, while it drops to 22.8 K with the presence of the magnetic shielding. Similarly, the maximum discharge temperature for the unshielded P_2 and P_3 pancake is 29.1 K, while it drops to 25.3 K with the magnetic shielding. The energy was dissipated as heat in the magnetic shielding, resulting in a rise in temperature, followed by a cooling generated by the convective exchange between the coil and the cryogenic fluid.

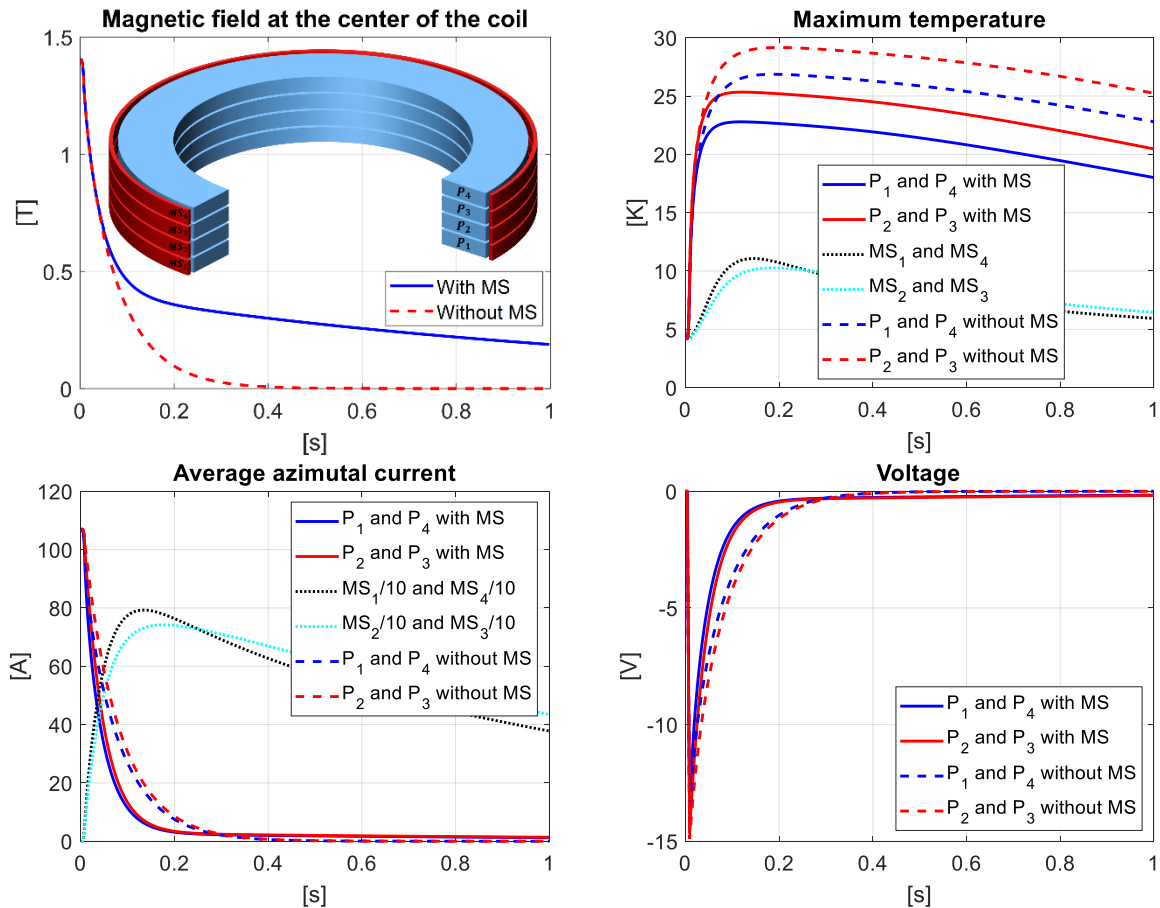


Figure IV-23: Comparison with and without the magnetic shielding; magnetic induction at the center of the magnet, maximum temperature, average azimuthal current and voltage for each pancake and for each the magnetic shielding.

IV. 3. 2. 2 During a quench, without voltage limitation

The presence of a magnetic shielding also plays a role in the behavior of the coil during a quench. It reduces the fluctuations of the magnetic field, which decreases the induced voltages and radial currents, in addition to storing some of the magnetic energy of the coil during a quench. Using the example of the coil consisting of four pancakes with a contact resistivity of $R_{ct} = 9\,000\ \mu\Omega\cdot\text{cm}^2$ (see section II. 3. 1. 2 on coil parameters and quench behavior) and adding a magnetic shielding of 5 turns around each pancake, the quench diffusion no longer occurs on the second pancake P_B of the coil. There is no voltage limitation in this simulation in order to keep the same conditions as in the section II. 3. 1. 2. This behavior is valid only if the value of the contact resistivity of the magnetic shielding is low. For the simulation results shown in Figure IV-24, the contact resistivity value of the magnetic shielding (R_{ct-MS}) is $100\ \mu\Omega\cdot\text{cm}^2$. The inner diameter is 109.8 mm, the outer diameter is 110.6 mm. The properties of the superconducting tape are identical to those of the tape on the central pancakes in the coil.

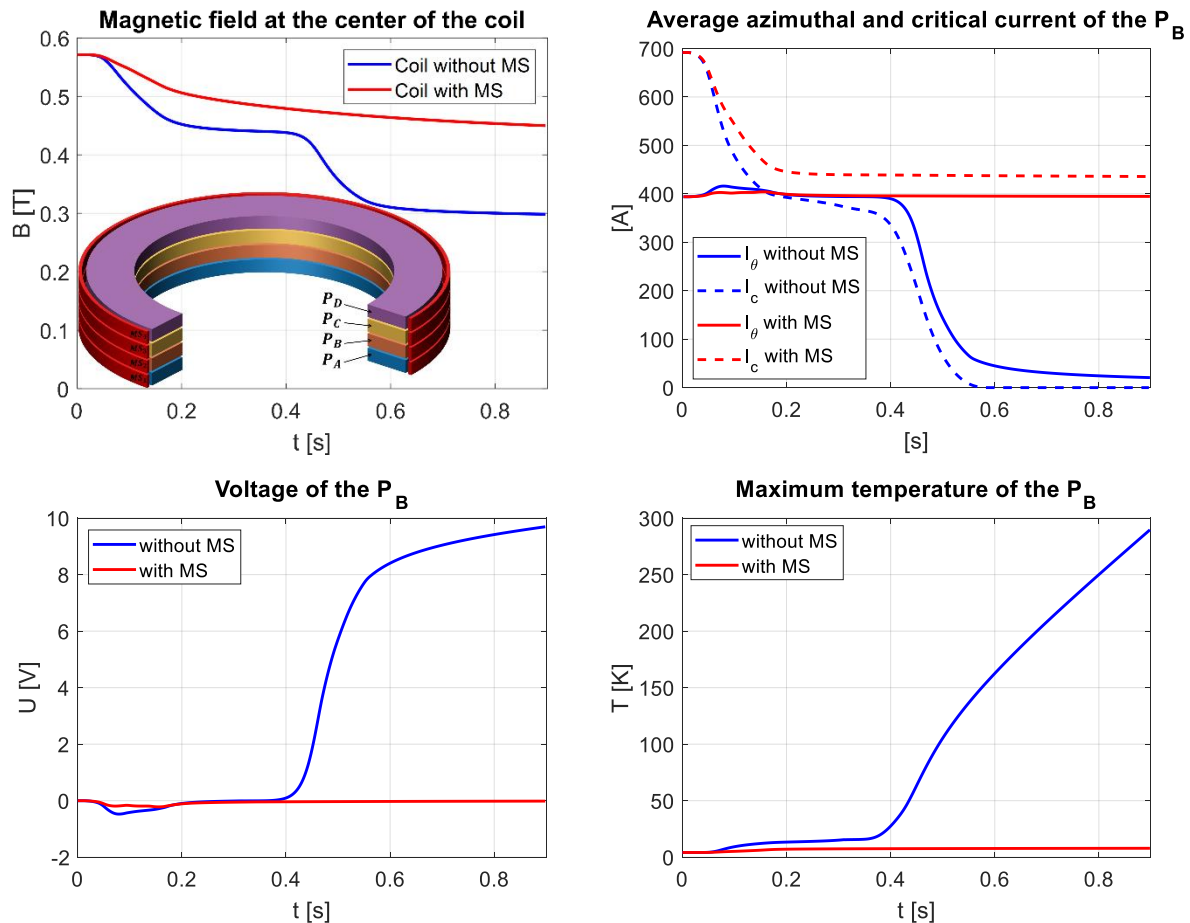


Figure IV-24: Comparison with and without the presence of the magnetic shielding on a coil of four pancakes. Magnetic field in the center of the coil, average azimuthal and critical current of the Pancake B, voltage and maximum temperature of the Pancake B.

Without the magnetic shielding, the quench caused by the introduction of a heat source on the Pancake A (P_A) has caused a drop in the magnetic induction generated by the P_A (top left of Figure IV-24). This fluctuation in the magnetic induction generates inductive voltages on the pancakes B, C and D (P_B , P_C and P_D). The voltage of P_B becomes negative, which results in negative radial currents (and thus an increase in the azimuthal current, top right of Figure IV-24 for $t \approx 0.1$ s). These radial currents cause a rise in temperature, and combined with a change in the orientation of the magnetic induction on the superconducting tapes (see section II. 3. 1. 1), causes a decrease in the critical current. For some turns of P_B , the azimuthal current is higher than the critical current, which leads to a heating of P_B , and then to its quench.

In the case with the magnetic shielding, the appearance of an inductive voltage causes an azimuthal current in the superconducting tapes present in the overbanding. This azimuthal current generates a magnetic induction and thus a less pronounced decrease in magnetic induction compared to the case without magnetic shielding (top left of Figure IV-24). Thus, the electromotive forces generated in P_B are lower. The minimum voltage of P_B is -0.47 V in the case without magnetic shielding, compared to -0.22 V with the presence of the magnetic shielding, at $t \approx 0.1$ s. A lower absolute voltage results in less radial current and therefore a lower heating of the pancake (bottom right of Figure IV-24). A lower temperature implies a higher critical current. The value of the azimuthal current in P_B with the presence of the magnetic shielding is thus lower than the critical current (top right of Figure IV-24). No zone becomes resistive; P_B does not quench, its voltage remains zero.

In the case where the contact resistivity of the magnetic shielding R_{ct-MS} is higher, the radial currents in the superconducting tapes present in the overbanding are lower during the transition of Pancake A. This results in lower azimuthal currents and therefore lower magnetic induction generated by the magnetic shielding (left of Figure IV-25). The variation of the magnetic induction being more important with an increase of the contact resistivity of the magnetic shielding, the inductive voltage of the Pancake B will be, in absolute value, more important (on the right of Figure IV-25). The temperature increase of the Pancake B will be higher, even causing the diffusion of the quench by magnetic coupling for values of contact resistivity of the magnetic shielding that are too high ($R_{ct-MS} > 1\,000\ \mu\Omega\cdot\text{cm}^2$, Figure IV-25).

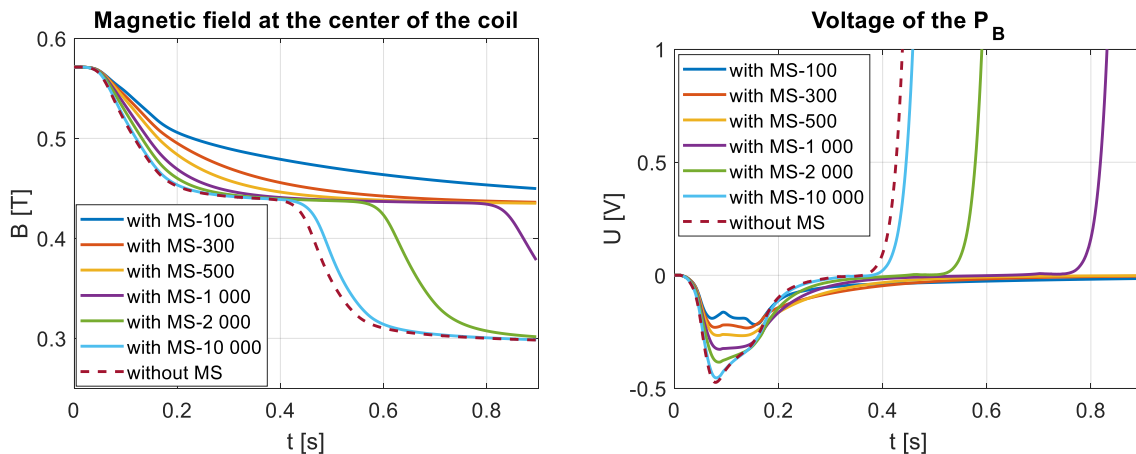


Figure IV-25: Magnetic field at the center of the coil and voltage of the Pancake B for different values of contact resistivity of the magnetic shielding.

The value of the maximum temperature of Pancake B at $t = 0.9$ s, as well as those of pancakes C and D, therefore depends on the value of the contact resistivity of the magnetic shielding.

The maximum temperature of the Pancakes B, C and D at $t = 0.9$ s decreases with a decrease in the value of the contact resistivity of the magnetic shielding (Table IV-11). With a relatively high value of R_{ct-MS} ($R_{ct-MS} > 10\ \text{m}\Omega\cdot\text{cm}^2$), the behavior of the coil is similar to the case without magnetic shielding. It absorbs and dissipates a very small amount of energy, which remains mainly in the coil pancakes. Generating a magnetic shielding with Theva tape is therefore not suitable because its contact resistivity value in the NI case is between $6\,000\ \mu\Omega\cdot\text{cm}^2$ and $8\,000\ \mu\Omega\cdot\text{cm}^2$ at 77 K for mechanical stress between 2 and 70 MPa.

Table IV-11: Maximum temperature of each pancake as a function of the contact resistivity of the magnetic shield.

$R_{ct-MS} [\mu\Omega\cdot\text{cm}^2]$	100	300	500	1 000	2 000	10 000	Without MS
$T_{max} P_A$ [K]	411.1	411.0	411.7	410.7	411.4	411.3	410.5
$T_{max} P_B$ [K]	7.9	9.5	11.2	102.1	219.6	276.1	289.6
$T_{max} P_C$ [K]	5.6	6.6	7.3	11.6	15.1	16.2	16.4
$T_{max} P_D$ [K]	5.1	5.8	6.3	8.7	12.0	13.0	13.1

The maximum temperature of the Pancake A varies very few with the contact resistivity of the magnetic shielding because the temperature increase is mainly influenced by the behavior of the pancake during the quench, i.e. its contact resistivity value.

The principle of the magnetic shielding is to reduce fluctuations in the magnetic field, and thus to reduce induced voltages and radial currents. It also stores some of the magnetic energy of the coil during a quench, reducing the temperature peak in the coil. And this part of the energy is then dissipated inside the SS overbanding and closer to the cooling sources, which reduce the energy dissipated inside the superconducting volume.

IV. 4 Conclusion

The self-protective behavior of a No-Insulation simple or multi-pancake depends on the value of the contact resistivity. If the value is too high, the self-protected behavior is lost and a thermal overheating of the pancake is inevitable. Nevertheless, source voltage limitation reveals as an attractive solution to protect the coil even for high values of contact resistivity. The principle is to see the power source as a voltage source when the coil quenches. With a high contact resistivity, the coil voltage rises sharply at the start of the quench. By limiting the voltage of the power source, the current automatically decreases when the quench propagates inside the coil, thus discharging the coil energy and preventing a thermal overheating.

In order to study this method of protection, modifications were made to the PEEC model to simulate voltage limitation during a quench. By using our PEEC model, it is possible to evaluate the protection behavior / quench behavior and determine the optimum $R_{ct} - U_{max}$ to provide the best protection for the coil, while having a high contact resistivity to charge the coil faster.

This protection with voltage limitation method has been simulated on small simple pancake and then successfully tested on a coil consisting of two double pancakes at 4.2 K in the self-field and on a bigger HTS magnet (NOUGAT). Several quenches were deliberately induced on the coil in self-field without observing any deterioration after the various tests.

A second method of reducing the temperature peak during coil transients is to insert turns of superconducting tape inside the overbanding of each pancake. The presence of a magnetic shielding limits the fluctuation of the magnetic field and therefore the induced voltages. This behavior can also be observed in the PEEC model where magnetic shielding has been implemented consisting of one or more pancakes. With the magnetic shielding, a part of the coil's energy is dissipated in the magnetic shielding, reducing the temperature rise of the main pancakes of the coil. Combining magnetic shielding with voltage limitation on a coil consisting of several MI pancakes is quite possible, offering better protection to the coil.

General conclusion

The various works carried out have improved our knowledge of No- or Metal-Insulation REBCO HTS coils in order to improve their protection during a quench. The aim of this work is to understand the phenomenon of redistribution of radial and azimuthal currents during the transient regime, which provides a self-protecting feature but also can lead to mechanical problems.

A complete magneto-thermo-electric model has been greatly improved and used to observe and understand the phenomenon of current redistribution in coils of several types (pancake, multi-pancakes and racetrack coil) during a quench and transients of the current (ramp-up, ramp-down, abrupt cut in the supply current). This model allows to monitor the values of the radial and azimuthal currents within the pancake as a function of time. This model also permits to understand the influence of the turn-to-turn contact resistivity on the behavior of a NI or MI coil. This is one of the most important parameters. It strongly influences the quench dynamic in a pancake, making it less susceptible to local burnings. This multi-pancake PEEC model allows including this critical parameter in the design phase of a specific magnet and finding the best technological solution for each application. However, the complexity of this model makes the simulation time relatively long. An optimization of the calculation time is necessary to simulate the behavior of a magnet with a much larger geometry. One possible method is to use the fast multipole method (FMM).

The behavior of an NI-MI coil during transient regimes is mainly based on the value of the electrical contact resistivity between each turn. This parameter has to be evaluated to have accurate models. Thus, the turn-to-turn contact resistivity has been measured for several configurations and under different conditions. An experimental setup allowing measuring the contact resistivity between No-Insulation (NI) 6 mm HTS superconducting tapes, cooled down at liquid nitrogen temperature (77 K), as a function of the mechanical stress (up to 70 MPa), has been designed. A large number of samples were tested for different manufacturers, mainly without insulation (NI) or with metallic tape (MI). Changing the nature of the insulation between the tapes changes the value of the contact resistivity and thus the behavior of a coil during transient regimes. All these measurements made it possible to understand and study the parameters that modify the contact resistivity value. It depends on the thickness of the different buffer layers, the surface condition of the superconducting tapes, the presence and number of metallic tapes, the mechanical stress, the hardness and the nature of the metallic tapes. Several ranges of values are achievable depending on the presence of metallic tape between the superconducting tapes.

In order to modify and to tune the contact resistivity between two tapes, an Atomic Layer Deposition (ALD) of Al_2O_3 of 100 nm applied on superconducting or metallic tapes were tested. The idea was to add a thin layer to the surface of the superconducting tapes with a variable resistivity (content of precursors) in order to impose the desired contact resistivity value between the superconducting tapes. However, delamination of this ALD during compression of the tapes makes the method not optimal for this type of application with a thickness of 100 nm. Nevertheless, increasing the thickness to 1 μm is a possibility to solve this delamination problem. Controlling the contact resistivity with ALD 1 μm therefore seems feasible although controlling the R_{ct} value with metallic tapes is therefore currently the most reliable solution.

In the first chapter of this thesis, we have seen that the self-protective character is less pronounced with an increase in contact resistivity. With a low contact resistivity value, the current in the pancake can easily bypass the local defect, making the pancake self-protected but increasing the charging time of the pancake. Conversely, with a higher contact resistivity value, the pancake is less self-protected, but charging time is lower. However, it is quite possible to effectively protect coils with high contact resistivity by adding voltage limitation during a quench. The principle is to use the high increase in the resistivity of an MI pancake during a quench and to adjust the maximum voltage of the current source to obtain a rapid decline of the supply current passively once the voltage is reached, thus discharging the coil energy and preventing a thermal overheating. For this purpose, the PEEC model was completed to study the behavior of a simple or multi-pancake during a quench with different contact resistivity and voltage limitation values of the power supply. Simulations and experimental measurements were carried out on a magnet made of four pancakes to demonstrate the use of MI technology to improve the protection against quenches. This protection with voltage limitation method has been successfully tested on a coil consisting of two double pancakes at 4.2 K in the self-field. Several quenches were deliberately induced on the coil in self-field without observing any deterioration after the various tests.

Appendix

VI. 1 Partial Element Equivalent Circuit (PEEC) model, Chapter II

VI. 1. 1 Electrical equation

VI. 1. 1. 1 Simple pancake

From the electrical diagram of the simple pancake (Figure II-1), it is possible to obtain the electrical equation of the radial current I_r as a function of time using the Kirchhoff's laws:

$\forall i \in [1: (n_a - 1)n_f]$: (for all meshes except the central mesh)

$$\sum_{k=1}^{n_a \times n_f} M_{k|i} \frac{dI_{\theta}^k}{dt} + R_{\theta}^i I_{\theta}^i - R_r^i I_r^i - \sum_{k=1}^{n_a \times n_f} M_{k|i+n_f} \frac{dI_{\theta}^k}{dt} - R_{\theta}^{i+n_f} I_{\theta}^{i+n_f} + R_r^{i+1} I_r^{i+1} = 0 \quad (1. a)$$

For the central / inner mesh:

$$\sum_{j=1}^{n_f} \left(\sum_{k=1}^{n_a \times n_f} M_{k|j} \frac{dI_{\theta}^k}{dt} + R_{\theta}^j I_{\theta}^j \right) - R_r^1 I_r^1 = 0 \quad (1. b)$$

With n_a the number of turns, n_f the number of divisions per turn, i the number of the mesh, k the number of the sector, I_{θ}^k and I_r^k respectively the azimuthal and radial current of a sector, R_{θ}^k and R_r^k respectively the azimuthal and radial resistance of a sector and $M_{k|i}$ the mutual inductance between the sector i and all the other sectors of the pancake (index k). Finally, we have a first-order matrix differential equation (with a constant current supply I_0):

$$M_{SP} \frac{dI_{\theta}}{dt} + R_{\theta} I_{\theta} + R_r I_r = 0 \quad (1. c)$$

M_{SP} the constant matrix taking the set of the mutual inductances values and I_{θ} , I_r , R_{θ} and R_r matrices to write the equations for each mesh. R_r is a constant matrix, while R_{θ} is calculated at each time step. The equality between the radial I_r^k , azimuthal I_{θ}^k and supply I_0 current at each node of the pancake electrical diagram is:

$$K_{\theta} I_{\theta} + K_r I_r = I_0 \rightarrow I_{\theta} = K_{\theta}^{-1} (I_0 - K_r I_r) \rightarrow I_{\theta} = K_{\theta}^{-1} I_0 - H_{pass} I_r \quad (1. d)$$

$H_{pass} = K_{\theta}^{-1} K_r$ is the transfer matrix from I_{θ} to I_r , K_{θ} and K_r are constant matrices consisting only of 0 and 1.

Note: in order to simulate and reproduce the behavior of a coil as well as possible, the supply current I_0 is distributed over the entire first turn of the coil. A simple modification of the I_0 vector is necessary to simulate this behavior.

Finally, for a simple pancake, a first order equation depending only on the radial current I_r :

$$M_{SP} H_{passSP} \frac{dI_{rSP}}{dt} + (R_{\theta SP} H_{passSP} - R_{rSP}) I_{rSP} = R_{\theta SP} K_{\theta SP}^{-1} I_0 \quad (1)$$

The matrix M_{SP} allows us to take into account all the mutual inductances in one sector in relation to another for the solution of equation (1). M_{SP} is constructed from the coefficients of $M_{k|i}$.

$$M_{SP} = \begin{pmatrix} M_{1|1} - M_{1|1+n_f} & M_{2|1} - M_{2|1+n_f} & \cdots & M_{n_a \times n_f|1} - M_{n_a \times n_f|1+n_f} \\ M_{1|2} - M_{1|2+n_f} & M_{2|2} - M_{2|2+n_f} & \cdots & M_{n_a \times n_f|2} - M_{n_a \times n_f|2+n_f} \\ \vdots & \vdots & & \vdots \\ M_{1|(n_a-1)n_f} - M_{1|n_a \times n_f} & M_{2|(n_a-1)n_f} - M_{2|n_a \times n_f} & \cdots & M_{n_a \times n_f|(n_a-1)n_f} - M_{n_a \times n_f|n_a \times n_f} \\ \sum_{j=1}^{n_f} M_{1|j} & \sum_{j=1}^{n_f} M_{2|j} & \cdots & \sum_{j=1}^{n_f} M_{n_a \times n_f|j} \end{pmatrix}$$

With:

- n_a the number of turns
- n_f the number of divisions per turn
- $M_{k|j}$ the mutual inductance between the sector k the sector j of the pancake

The dimension of M_{SP} is $[n_a(n_f - 1) + 1; n_a \times n_f]$.

All rows of the M_{SP} matrix, except the last one, solve equation (1.a) for every mesh in the pancake's electrical circuit, except the central mesh. Equation (1.b), the last row of the M_{SP} matrix, solves the equation for this central mesh.

The constructions of $R_{\theta_{SP}}$ and $R_{r_{SP}}$ are based on the same principle:

$$R_{\theta_{SP}} = \begin{pmatrix} R_{\theta}^1 & 0 & \cdots & \cdots & \cdots & 0 & -R_{\theta}^{1+n_f} & 0 & \cdots & \cdots & \cdots & \cdots & 0 \\ 0 & R_{\theta}^2 & \ddots & & & & & -R_{\theta}^{2+n_f} & \ddots & & & & \vdots \\ \vdots & \ddots & \ddots & \ddots & & & & \ddots & \ddots & \ddots & & & \vdots \\ \vdots & & & & & & & & & & & & \vdots \\ 0 & \cdots & \cdots & \cdots & \cdots & 0 & R_{\theta}^{(n_a-1)n_f} & 0 & \cdots & \cdots & 0 & \cdots & 0 \\ R_{\theta}^1 & R_{\theta}^2 & \cdots & R_{\theta}^{n_f} & 0 & \cdots & \cdots & \cdots & \cdots & \cdots & \cdots & \cdots & 0 \end{pmatrix}$$

The dimension of $R_{\theta_{SP}}$ is $[n_a(n_f - 1) + 1; n_a \times n_f]$.

$$R_{r_{SP}} = \begin{pmatrix} -R_r^1 & R_r^2 & 0 & \cdots & \cdots & \cdots & 0 \\ 0 & -R_r^2 & -R_r^3 & \ddots & & & \vdots \\ \vdots & \ddots & \ddots & \ddots & & & \vdots \\ \vdots & & & & & & 0 \\ 0 & \cdots & \cdots & \cdots & -R_r^{(n_a-1)n_f} & R_r^{(n_a-1)n_f+1} & 0 \\ -R_r^1 & 0 & \cdots & \cdots & 0 & 0 & 0 \end{pmatrix}$$

The dimension of $R_{r_{SP}}$ is $[n_a(n_f - 1) + 1; n_a(n_f - 1) + 1]$.

$$K_{\theta_{SP}} = \begin{pmatrix} 1 & 0 & \cdots & \cdots & 0 \\ -1 & \ddots & \ddots & \ddots & \vdots \\ 0 & \ddots & \ddots & \ddots & 0 \\ \vdots & \ddots & \ddots & \ddots & \vdots \\ 0 & \cdots & 0 & -1 & 1 \end{pmatrix}; K_{r_{SP}} = \begin{pmatrix} 1 & 0 & \cdots & \cdots & \cdots & 0 \\ 0 & \ddots & \ddots & \ddots & \ddots & \vdots \\ \vdots & \ddots & \ddots & \ddots & \ddots & \vdots \\ 0 & \ddots & \ddots & \ddots & \ddots & 0 \\ -1 & \ddots & \ddots & \ddots & \ddots & 0 \\ 0 & \ddots & \ddots & \ddots & 0 & 1 \\ \vdots & \ddots & \ddots & \ddots & \ddots & 0 \\ \vdots & \ddots & \ddots & \ddots & \ddots & \vdots \\ 0 & \cdots & \cdots & 0 & -1 & 0 \end{pmatrix} \text{ with } I_0 = \begin{pmatrix} I_0 \\ 0 \\ \vdots \\ \vdots \\ \vdots \\ \vdots \\ \vdots \\ 0 \end{pmatrix}$$

The dimension of $K_{\theta_{SP}}$ is $[n_a \times n_f; n_a \times n_f]$.

The dimension of $K_{r_{SP}}$ is $[n_a \times n_f; n_a(n_f - 1) + 1]$.

Note: In order to best simulate the behavior of a coil, the supply current I_0 is distributed over the entire first turn of the pancake. A simple modification of the I_0 vector is necessary to simulate this behavior:

$$I_0 = \begin{pmatrix} I_0/n_f \\ \vdots \\ I_0/n_f \\ 0 \\ \vdots \\ 0 \\ -I_0/n_f \\ \vdots \\ -I_0/n_f \end{pmatrix} \begin{matrix} \updownarrow n_f \text{ elements} \\ \updownarrow n_f - 1 \text{ elements} \end{matrix}$$

VI. 1. 1. 2 Multi-pancake

The matrix to take into account the mutual coupling between the two pancakes for equation (2) is as follows:

$$M_{DP} = \begin{pmatrix} M_{1|1} - M_{1|1+n_f} & M_{2|1} - M_{2|1+n_f} & \cdots & M_{2(n_a \times n_f)|1} - M_{2(n_a \times n_f)|1+n_f} \\ M_{1|2} - M_{1|2+n_f} & M_{2|2} - M_{2|2+n_f} & \cdots & M_{2(n_a \times n_f)|2} - M_{2(n_a \times n_f)|2+n_f} \\ \vdots & \vdots & \cdots & \vdots \\ M_{1|(n_a-1)n_f} - M_{1|n_a \times n_f} & M_{2|(n_a-1)n_f} - M_{2|n_a \times n_f} & \cdots & M_{2(n_a \times n_f)|(n_a-1)n_f} - M_{2(n_a \times n_f)|n_a \times n_f} \\ \sum_{j=1}^{n_f} M_{1|j} & \sum_{j=1}^{n_f} M_{2|j} & \cdots & \sum_{j=1}^{n_f} M_{2(n_a \times n_f)|j} \\ M_{1|1+n_a \times n_f} - M_{1|1+n_f+n_a \times n_f} & M_{2|1+n_a \times n_f} - M_{2|1+n_f+n_a \times n_f} & \cdots & M_{2(n_a \times n_f)|1+n_a \times n_f} - M_{2(n_a \times n_f)|1+n_f+n_a \times n_f} \\ M_{1|2+n_a \times n_f} - M_{1|2+n_f+n_a \times n_f} & M_{2|2+n_a \times n_f} - M_{2|2+n_f+n_a \times n_f} & \cdots & M_{2(n_a \times n_f)|2+n_a \times n_f} - M_{2(n_a \times n_f)|2+n_f+n_a \times n_f} \\ \vdots & \vdots & \cdots & \vdots \\ M_{1|2(n_a \times n_f)-n_f} - M_{1|2(n_a \times n_f)} & M_{2|2(n_a \times n_f)-n_f} - M_{2|2(n_a \times n_f)} & \cdots & M_{2(n_a \times n_f)|2(n_a \times n_f)-n_f} - M_{2(n_a \times n_f)|2(n_a \times n_f)} \\ \sum_{j=1}^{n_f} M_{1|j} & \sum_{j=1}^{n_f} M_{2|j} & \cdots & \sum_{j=1}^{n_f} M_{2(n_a \times n_f)|j} \end{pmatrix}$$

For the other matrices in equation (2), the constructions are as follows:

$$R_{\theta_{DP}} = \begin{pmatrix} R_{\theta_{P_1}} & 0 \\ 0 & R_{\theta_{P_2}} \end{pmatrix}; R_{r_{DP}} = \begin{pmatrix} R_{r_{P_1}} & 0 \\ 0 & R_{r_{P_2}} \end{pmatrix}$$

$$K_{\theta_{DP}} = \begin{pmatrix} K_{\theta_{P_1}} & 0 \\ 0 & K_{\theta_{P_2}} \end{pmatrix}; K_{r_{DP}} = \begin{pmatrix} K_{r_{P_1}} & 0 \\ 0 & K_{r_{P_2}} \end{pmatrix}$$

The matrices $R_{\theta_{P_1}}$, $R_{r_{P_1}}$, $K_{\theta_{P_1}}$ and $K_{r_{P_1}}$ are respectively identical to the matrices R_{θ} , R_r , K_{θ} and K_r in the case of the simple pancake. Since our two pancakes are strictly identical, we have: $K_{\theta_{P_1}} = K_{\theta_{P_2}}$ and $K_{r_{P_1}} = K_{r_{P_2}}$.

However, the matrices $R_{\theta_{P_2}}$ and $R_{r_{P_2}}$ are slightly different from $R_{\theta_{P_1}}$ and $R_{r_{P_1}}$ due to the outside-in winding of the second pancake. A modification of the last line of $R_{\theta_{P_2}}$ and $R_{r_{P_2}}$ is performed for the central mesh of the second pancake (related to equation (2)).

$$R_{\theta_{P_2}} = \begin{pmatrix} R_{\theta_{P_2}}^1 & 0 & \dots & \dots & \dots & 0 & -R_{\theta_{P_2}}^{1+n_f} & 0 & \dots & \dots & \dots & \dots & 0 \\ 0 & R_{\theta_{P_2}}^2 & \ddots & & & & \ddots & -R_{\theta_{P_2}}^{2+n_f} & \ddots & & & & \vdots \\ \vdots & \ddots & \ddots & \ddots & & & \ddots & \ddots & \ddots & & & & \vdots \\ \vdots & & & & & & & & & & & & \vdots \\ \vdots & & & & & & & & & & & & \vdots \\ 0 & \dots & \dots & \dots & \dots & 0 & R_{\theta_{P_2}}^{(n_a-1)n_f} & 0 & \dots & \dots & \dots & 0 & -R_{\theta_{P_2}}^{n_a \times n_f} \\ 0 & \dots & \dots & \dots & \dots & \dots & \dots & \dots & 0 & R_{\theta_{P_2}}^1 & R_{\theta_{P_2}}^2 & \dots & R_{\theta_{P_2}}^{n_f} \end{pmatrix}$$

$$R_{r_{P_2}} = \begin{pmatrix} -R_{r_{P_2}}^1 & R_{r_{P_2}}^2 & 0 & \dots & \dots & & & & & & 0 \\ 0 & -R_{r_{P_2}}^2 & R_{r_{P_2}}^3 & \ddots & & & & & & & \vdots \\ \vdots & \ddots & \ddots & \ddots & & & & & & & \vdots \\ \vdots & & & & & & & & & & \vdots \\ \vdots & & & & & & & & & & \vdots \\ 0 & \dots & \dots & \dots & & -R_{r_{P_2}}^{(n_a-1)n_f} & R_{r_{P_2}}^{(n_a-1)n_f+1} & & & & & & -R_{r_{P_2}}^1 \end{pmatrix}$$

The electrical connection between the pancakes is made using the supply current vector I_0 . With two pancakes connected in series and with a current distribution on the first and last turn of each pancake: $K_{\theta_{DP}} I_{\theta} + K_{r_{DP}} I_r = I_0$, so:

$$\begin{pmatrix} K_{\theta_{P_1}} & 0 \\ 0 & K_{\theta_{P_2}} \end{pmatrix} \begin{pmatrix} I_{\theta_1} \\ \vdots \\ I_{\theta_{2(n_a \times n_f)}} \end{pmatrix} + \begin{pmatrix} K_{r_{P_1}} & 0 \\ 0 & K_{r_{P_2}} \end{pmatrix} \begin{pmatrix} I_{r_1} \\ \vdots \\ I_{r_{2(n_a(n_f-1)+1)}} \end{pmatrix} = \begin{pmatrix} I_0/n_f \\ \vdots \\ I_0/n_f \\ 0 \\ \vdots \\ 0 \\ -I_0/n_f \\ \vdots \\ -I_0/n_f \\ I_0/n_f \\ \vdots \\ I_0/n_f \\ 0 \\ \vdots \\ 0 \\ -I_0/n_f \\ \vdots \\ -I_0/n_f \end{pmatrix}$$

$\begin{matrix} \updownarrow n_f \text{ elements} \\ \updownarrow n_f - 1 \text{ elements} \\ \updownarrow n_f \text{ elements} \\ \updownarrow n_f - 1 \text{ elements} \end{matrix}$

VI. 1. 2 Thermal equation

VI. 1. 2. 1 Properties of REBCO tape

The functions generating the material property values are developed by P. Fazilleau [68] and available in Figure VI-1.

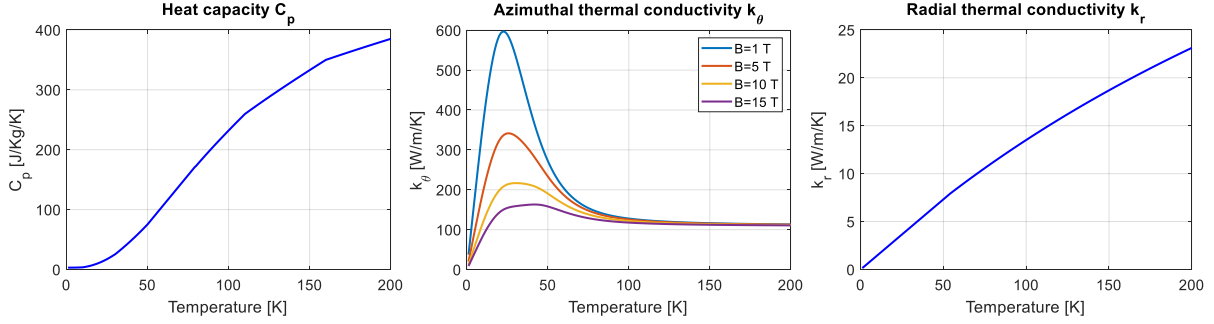


Figure VI-1: Heat capacity, azimuthal and radial thermal conductivity of a REBCO tape.

VI. 1. 2. 2 Simple and multi-pancake

The heat distribution in the pancake using the heat equation in cylindrical coordinates is:

$$\rho C_p \frac{\partial T}{\partial t} = \text{div}(k \nabla T) + S \rightarrow \rho C_p \frac{\partial T}{\partial t} = \frac{k_r}{r} \frac{\partial T}{\partial r} + k_r \frac{\partial^2 T}{\partial r^2} + \frac{k_\theta}{r^2} \frac{\partial^2 T}{\partial \theta^2} + S \quad (3)$$

The value of the radial and azimuthal thermal conductivity (k_r and k_θ) is specific to each sector of the pancake. It is not equal at every point of the pancake as its values depend on the temperature of the sector.

The finite difference expressions are:

$$\left\{ \begin{array}{l} \frac{\partial T}{\partial r} = \frac{T(r + \delta r) - T(r - \delta r)}{2\delta r} + O(\delta r^2) \leftrightarrow \frac{\partial T_i}{\partial r} = \frac{T_{i+n_f} - T_{i-n_f}}{2\delta r} + O(\delta r^2) \\ \frac{\partial^2 T}{\partial r^2} = \frac{T(r + \delta r) + T(r - \delta r) - 2T(r)}{\delta r^2} + O(\delta r^2) \leftrightarrow \frac{\partial^2 T_i}{\partial r^2} = \frac{T_{i+n_f} + T_{i-n_f} - 2T_i}{\delta r^2} + O(\delta r^2) \\ \frac{\partial^2 T}{\partial \theta^2} = \frac{T(\theta + \delta \theta) + T(\theta - \delta \theta) - 2T(\theta)}{\delta \theta^2} + O(\delta r^2) \leftrightarrow \frac{\partial^2 T_i}{\partial \theta^2} = \frac{T_{i+1} + T_{i-1} - 2T_i}{\delta \theta^2} + O(\delta r^2) \end{array} \right. \quad (4)$$

The law for convective exchange is as follows:

$$\vec{\phi} = h(T_{paroi} - T_{fluide})\vec{n} \quad (5)$$

With $\vec{\phi}$ the convective heat flow between the solid and liquid body, h the heat transfer coefficient (in W/m²/K) and $T_{side} - T_{fluid}$ the temperature difference in K between the two bodies.

VI. 1. 2. 2. 1 In the case of the first turn

Using Fourier's law:

$$\vec{\phi} = \phi_r \vec{e}_r + \phi_\theta \vec{e}_\theta = \phi_r \vec{e}_r = -h(T_{side} - T_{fluid})\vec{n}$$

$$\text{And } \phi_r = -k_r \frac{\partial T}{\partial r} = -k_r \frac{T_{1+n_f} - T_{1-n_f}}{2\delta r}$$

$$\text{Hence } k_r \frac{T_{1+n_f} - T_{1-n_f}}{2\delta r} = h(T_i - T_0)$$

Let the expression of T_{1-n_f} be a function of T_{1+n_f} , T_i and T_0 , with $1 \leq i \leq n_f$.

Note: In the case of the first turn, the unit vector normal to the surface of the sectors \vec{n} is in the opposite direction to \vec{e}_r : $\vec{n} = -\vec{e}_r$. Hence, the negative sign in the previous equation.

VI.1.2.2.1.1 For the first element: $i = 1$

$$\rho C_p \frac{\partial T_1}{\partial t} = \frac{k_r T_{1+n_f} - T_{1-n_f}}{r} + k_r \frac{T_{1+n_f} + T_{1-n_f} - 2T_1}{\delta r^2} + \frac{k_\theta T_2 + T_0 - 2T_1}{r^2 \delta \theta^2} + S$$

Using the law for convective exchange, we obtain:

$$k_r (T_{1+n_f} - T_{1-n_f}) = h(T_1 - T_0)2\delta r$$

And with $\phi_\theta = -k_\theta \frac{\partial T}{\partial \theta} = \frac{T_2 - T_0}{2\delta \theta} = 0 \leftrightarrow T_2 = T_0$ only according to \vec{e}_θ .

In the end:

$$\rho C_p \frac{\partial T_1}{\partial t} = T_0 \left[\frac{2h}{\delta r} - \frac{h}{r} \right] + T_1 \left[\frac{h}{r} - \frac{2h}{\delta r} - \frac{2k_r}{\delta r^2} - \frac{2k_\theta}{r^2 \delta \theta^2} \right] + T_2 \left[\frac{2k_\theta}{r^2 \delta \theta^2} \right] + T_{1+n_f} \left[\frac{2k_r}{\delta r^2} \right] + S$$

Without convective exchange, so $h = 0$, hence:

$$\rho C_p \frac{\partial T_1}{\partial t} = T_1 \left[-\frac{2k_r}{\delta r^2} - \frac{2k_\theta}{r^2 \delta \theta^2} \right] + T_2 \left[\frac{2k_\theta}{r^2 \delta \theta^2} \right] + T_{1+n_f} \left[\frac{2k_r}{\delta r^2} \right] + S$$

VI.1.2.2.1.2 For all sectors in the first turn, excluding the first sector: $1 < i \leq n_f$

We always get:

$$k_r (T_{1+n_f} - T_{1-n_f}) = h(T_i - T_0)2\delta r$$

This makes it possible to obtain, with $1 < i \leq n_f$:

$$\rho C_p \frac{\partial T_i}{\partial t} = T_0 \left[\frac{2h}{\delta r} - \frac{h}{r} \right] + T_{i-1} \left[\frac{k_\theta}{r^2 \delta \theta^2} \right] + T_i \left[\frac{h}{r} - \frac{2h}{\delta r} - \frac{2k_r}{\delta r^2} - \frac{2k_\theta}{r^2 \delta \theta^2} \right] + T_{i+1} \left[\frac{k_\theta}{r^2 \delta \theta^2} \right] + T_{i+n_f} \left[\frac{2k_r}{\delta r^2} \right] + S$$

Without convective exchange, so $h = 0$, hence:

$$\rho C_p \frac{\partial T_i}{\partial t} = T_{i-1} \left[\frac{k_\theta}{r^2 \delta \theta^2} \right] + T_i \left[-\frac{2k_r}{\delta r^2} - \frac{2k_\theta}{r^2 \delta \theta^2} \right] + T_{i+1} \left[\frac{k_\theta}{r^2 \delta \theta^2} \right] + T_{i+n_f} \left[\frac{2k_r}{\delta r^2} \right] + S$$

VI. 1. 2. 2. 2 For all sectors of each turn, except the sectors of the first and last turn: $n_f < i < n_a \times n_f - n_f$

$$\rho C_p \frac{\partial T_i}{\partial t} = T_{i-n_f} \left[-\frac{k_r}{r^2 \delta r} + \frac{k_r}{\delta r^2} \right] + T_{i-1} \left[\frac{k_\theta}{r^2 \delta \theta^2} \right] + T_i \left[-\frac{2k_r}{\delta r^2} - \frac{2k_\theta}{r^2 \delta \theta^2} \right] + T_{i+1} \left[\frac{k_\theta}{r^2 \delta \theta^2} \right] + T_{i+n_f} \left[\frac{k_r}{2r \delta r} + \frac{k_r}{\delta r^2} \right] + S$$

VI. 1. 2. 2. 3 In the case of the outside turn

Using Fourier's law:

$$\vec{\phi} = \phi_r \vec{e}_r + \phi_\theta \vec{e}_\theta = \phi_r \vec{e}_r = h(T_{side} - T_{fluid}) \vec{n}$$

$$\text{And } \phi_r = -k_r \frac{\partial T}{\partial r} = -k_r \frac{T_{1+n_f} - T_{1-n_f}}{2\delta r}$$

$$\text{Hence } k_r \frac{T_{1+n_f} - T_{1-n_f}}{2\delta r} = -h(T_i - T_0)$$

Let the expression of T_{1+n_f} be a function of T_{1-n_f} , T_i and T_0 , with $n_a \times n_f - n_f \leq i \leq n_a \times n_f$.

VI.1.2.2.3.1 For the last turn sectors, without the last sector: $n_a \times n_f - n_f \leq i < n_a \times n_f$

It is reminded that with the convective exchange in the case of the external turn, it is possible to obtain the expression of T_{1+n_f} as a function of T_{1-n_f} , T_i and T_0 . In the end, this means:

$$\begin{aligned} \rho C_p \frac{\partial T_i}{\partial t} = T_0 \left[\frac{h}{r} + \frac{2h}{\delta r} \right] + T_{i-n_f} \left[\frac{2k_r}{\delta r^2} \right] + T_{i-1} \left[\frac{k_\theta}{r^2 \delta \theta^2} \right] + T_i \left[-\frac{h}{r} - \frac{2k_r}{\delta r^2} - \frac{2h}{\delta r} - \frac{2k_\theta}{r^2 \delta \theta^2} \right] \\ + T_{i+1} \left[\frac{k_\theta}{r^2 \delta \theta^2} \right] + S \end{aligned}$$

VI.1.2.2.3.2 For the last element: $i = n_a \times n_f$

Finally, for the last sector, we consider the tape thickness too small to generate a convective exchange between the last sector and the outside of the pancake following \vec{e}_θ ($\phi_\theta = 0$).

Therefore, we get $\phi_\theta = -k_\theta \frac{\partial T}{\partial \theta} = \frac{T_{n_a \times n_f + 1} - T_{n_a \times n_f - 1}}{2\delta \theta} = 0 \leftrightarrow T_{n_a \times n_f + 1} = T_{n_a \times n_f - 1}$ only following \vec{e}_θ . In the end, this means:

$$\begin{aligned} \rho C_p \frac{\partial T_{n_a \times n_f}}{\partial t} = T_0 \left[\frac{h}{r} + \frac{2h}{\delta r} \right] + T_{n_f(n_a-1)} \left[\frac{2k_r}{\delta r^2} \right] + T_{n_a \times n_f - 1} \left[\frac{2k_\theta}{r^2 \delta \theta^2} \right] \\ + T_{n_a \times n_f} \left[-\frac{h}{r} - \frac{2k_r}{\delta r^2} - \frac{2h}{\delta r} - \frac{2k_\theta}{r^2 \delta \theta^2} \right] + S \end{aligned}$$

VI. 1. 2. 3 Racetrack

With the heat equation and assuming no heat diffusion along the z-axis, we obtain in Cartesian coordinates:

$$\rho C_p \frac{\partial T}{\partial t} = k_r \frac{\partial^2 T}{\partial x^2} + k_y \frac{\partial^2 T}{\partial y^2} + S, \text{ avec } k_r = k_\theta \text{ et } k_y = k_r \quad (6. a)$$

The finite difference expressions are:

$$\begin{cases} \frac{\partial^2 T}{\partial x^2} = \frac{T(x + \delta x) + T(x - \delta x) - 2T(x)}{\delta x^2} \leftrightarrow \frac{\partial^2 T_i}{\partial x^2} = \frac{T_{i+1} + T_{i-1} - 2T_i}{\delta x^2} \\ \frac{\partial^2 T}{\partial y^2} = \frac{T(y + \delta y) + T(y - \delta y) - 2T(y)}{\delta y^2} \leftrightarrow \frac{\partial^2 T_i}{\partial y^2} = \frac{T_{i+n_{st}} + T_{i-n_{st}} - 2T_i}{\delta y^2} \end{cases} \quad (6. b)$$

VI. 1. 2. 3. 1 In the case of the first turn

The law for convective exchange and Fourier's law allow us to obtain:

$$k_r \frac{T_{i+n_{st}} - T_{i-n_{st}}}{2\delta y} = h(T_i - T_0)$$

In the end, for the straight sectors of the first turn, with $n_{fc} + 1 \leq i \leq n_{fc} + n_{fd}$ and $2n_{fc} + n_{fd} + 1 \leq i \leq n_{st}$:

$$\rho C_p \frac{\partial T_i}{\partial t} = T_0 \left[\frac{2h}{\delta y} \right] + T_{i-1} \left[\frac{k_\theta}{\delta x^2} \right] + T_i \left[-\frac{2k_\theta}{\delta x^2} - \frac{2h}{\delta y} - \frac{2k_r}{\delta y^2} \right] + T_{i+1} \left[\frac{k_\theta}{\delta x^2} \right] + T_{i+n_{st}} \left[\frac{2k_r}{\delta y^2} \right] + S$$

VI. 1. 2. 3. 2 In the case of straight sections for all turns except the first and last turn

There is no convective exchange with the outside. The expression of the temperature as a function of time with $n_{st} + 1 \leq i \leq n_s - n_{st}$ is as follows:

$$\rho C_p \frac{\partial T_i}{\partial t} = T_{i-n_{st}} \left[\frac{k_r}{\delta y^2} \right] + T_{i-1} \left[\frac{k_\theta}{\delta x^2} \right] + T_i \left[-\frac{2k_\theta}{\delta x^2} - \frac{2k_r}{\delta y^2} \right] + T_{i+1} \left[\frac{k_\theta}{\delta x^2} \right] + T_{i+n_{st}} \left[\frac{2k_r}{\delta y^2} \right] + S$$

VI. 1. 2. 3. 3 In the case of straight sections for the last turn without the last sector

The convective exchange with the outside is taken into account. The unit vector normal to the surface of the sectors \vec{n} is in the same direction with respect to \vec{x} : $\vec{n} = \vec{x}$, hence:

$$\phi_y = -k_y \frac{\partial T}{\partial y} = -k_r \frac{T_{i+n_{st}} - T_{i-n_{st}}}{2\delta y}$$

$$\text{Hence } -k_r \frac{T_{i+n_{st}} - T_{i-n_{st}}}{2\delta y} = h(T_i - T_0)$$

This allows obtaining, with $n_s - n_{st} + n_{fc} + 1 \leq i \leq n_s - n_{fd} - n_{fc}$ and $n_s - n_{fd} + 1 \leq i \leq n_s - 1$:

$$\rho C_p \frac{\partial T_i}{\partial t} = T_{i-n_{st}} \left[\frac{k_r}{\delta y^2} \right] + T_{i-1} \left[\frac{k_\theta}{\delta x^2} \right] + T_i \left[-\frac{2k_\theta}{\delta x^2} - \frac{2k_r}{\delta y^2} \right] + T_{i+1} \left[\frac{k_\theta}{\delta x^2} \right] + T_{i+n_{st}} \left[\frac{2k_r}{\delta y^2} \right] + S$$

For the last sector, we keep the same hypothesis as for the pancake: we consider the thickness of the tape too small to have a convective exchange between the last sector and the outside of the pancake following \vec{x} ($\phi_x = 0$). Thus, for $i = n_s$:

$$\phi_x = -k_\theta \frac{\partial T}{\partial x} = \frac{T_{n_s+1} - T_{n_s-1}}{2\delta x} = 0 \leftrightarrow T_{n_s+1} = T_{n_s-1} \text{ only according } \vec{x}.$$

Thus, for $i = n_s$:

$$\rho C_p \frac{\partial T_i}{\partial t} = T_0 \left[\frac{2h}{\delta y} \right] + T_{i-n_{st}} \left[\frac{2k_r}{\delta y^2} \right] + T_{i-1} \left[\frac{2k_\theta}{\delta x^2} \right] + T_i \left[-\frac{2k_\theta}{\delta x^2} - \frac{2h}{\delta y} - \frac{2k_r}{\delta y^2} \right] + S$$

VI. 1. 3 Mutual inductance in racetrack

VI. 1. 3. 1 Mutual between a thin straight sector and a thin angular sector

The generalization of the mutual induction coefficient between two non-wire-shaped circuits is as follows:

$$M_{1 \leftrightarrow 2} = \frac{1}{I_1 I_2} \frac{\mu_0}{4\pi} \int_{V_1} \int_{V_2} \frac{\vec{J}_1 \cdot \vec{J}_2}{r_{12}} d\tau_1 d\tau_2$$

With \vec{J}_1 and \vec{J}_2 the vectors of the volume current densities in A/m² in V_1 and V_2 , r_{12} the distance in m separating a point in V_1 from a point in V_2 and μ_0 in H/m the magnetic permeability of the vacuum. In the case of the mutual between a thin straight sector and a thin angular sector:

$$M_{1\leftrightarrow 2} = M_{S-A} = \frac{1}{I_1 I_2} \frac{\mu_0}{4\pi} \int_{\phi_1}^{\phi_2} \int_{z_{c1}}^{z_{c2}} \int_{z_{r1}}^{z_{r2}} \int_0^{L_r} \frac{\vec{J}_1 \cdot \vec{J}_2}{d} dS_c dS_r$$

With (Figure VI-2):

- $z_c = z_{c2} - z_{c1}$ and $z_r = z_{r2} - z_{r1}$ respectively the height of the angular thin sector and the height of the right thin sector.
- L_r the length of the right thin sector.
- ϕ_1 and ϕ_2 the angles of the thin angular sector.
- dS_c and dS_r respectively the elementary surfaces of the thin angular and straight sector.
- d the distance between a point on the straight thin sector (P_c) and a point on the angled thin sector (P_r).

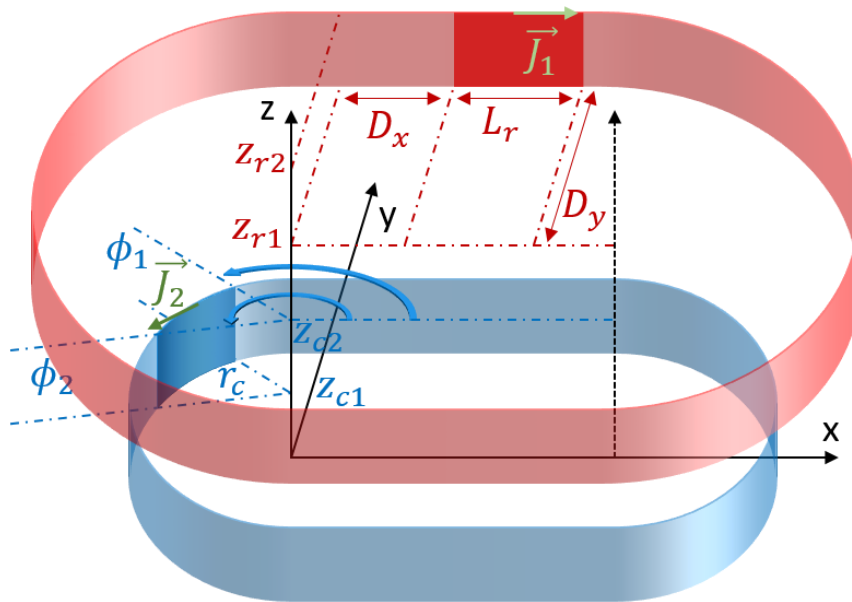


Figure VI-2: Mutual inductance between a thin straight and a thin angular sector.

We have:

$$\vec{J}_1 \cdot \vec{J}_2 = J_1 \vec{e}_x \cdot J_2 \vec{e}_\theta = -J_1 J_2 \sin(\theta_c)$$

With $dS_c = r_c d\theta_c dz_c$; $dS_r = dz_r dX_r$; $J_1 = \frac{I_1}{z_r}$ and $J_2 = \frac{I_2}{z_c}$, we obtain:

$$M_{1\leftrightarrow 2} = \frac{\mu_0}{4\pi} \frac{r_c}{z_r \times z_c} \int_{\phi_1}^{\phi_2} \int_{z_{c1}}^{z_{c2}} \int_{z_{r1}}^{z_{r2}} \int_0^{L_r} \frac{-\sin(\theta_c)}{d} d\theta_c dz_c dz_r dX_r$$

Calculation of d :

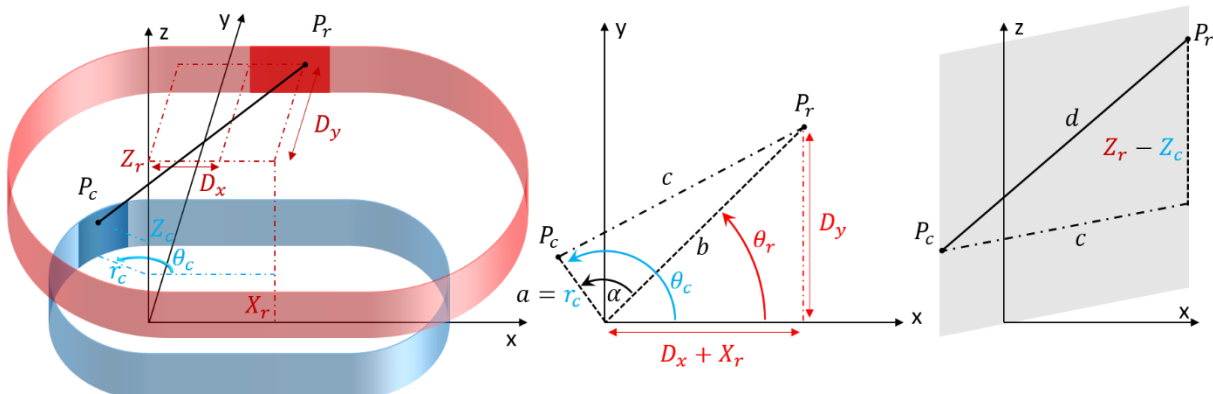


Figure VI-3: Explanatory sketch for obtaining the expression of M_{S-A} .

To obtain the value of $d = \|\overrightarrow{P_c P_r}\|$, we first place in the xy plane. Using Al Kashi's theorem, we obtain:

$$c^2 = a^2 + b^2 - 2ab \cos(\alpha) \leftrightarrow c^2 = r_c^2 + D_y^2 + (D_x + X_r)^2 - 2r_c \sqrt{D_y^2 + (D_x + X_r)^2} \cos(\alpha)$$

$$\text{And } \alpha = \theta_c - \theta_r = \theta_c - \text{atan}\left(\frac{D_y}{D_x + X_r}\right)$$

And in the plane along the z axis and passing through the segment $[P_c, P_r]$, we obtain:

$$d = \sqrt{(Z_r - Z_c)^2 + r_c^2 + D_y^2 + (D_x + X_r)^2 - 2r_c \sqrt{D_y^2 + (D_x + X_r)^2} \cos(\alpha)}$$

VI. 1. 3. 2 Mutual between two thin non-coaxial angular sectors

As in the previous case, we start from the generalization of the mutual induction coefficient between two non-wire-shaped circuits. In the case of the mutual inductance between two non-coaxial thin angular sectors:

$$M_{1 \leftrightarrow 2} = M_{A-A,nc} = \frac{1}{I \times I'} \frac{\mu_0}{4\pi} \int_{z_1'}^{z_2'} \int_{z_1}^{z_2} \int_{\phi_1'}^{\phi_2'} \int_{\phi_2}^{\phi_1} \frac{\vec{J} \cdot \vec{J}'}{d} dS dS'$$

With (Figure VI-4):

- $z = z_2 - z_1$ and $z' = z_2' - z_1'$ respectively the heights of the two angular sectors.
- ϕ and ϕ' the angular openings of the angular sectors.
- dS and dS' the elementary surfaces of the two angular sectors.
- d is the distance between a point in the first angular sector (P) and a point in the second angular sector (P').

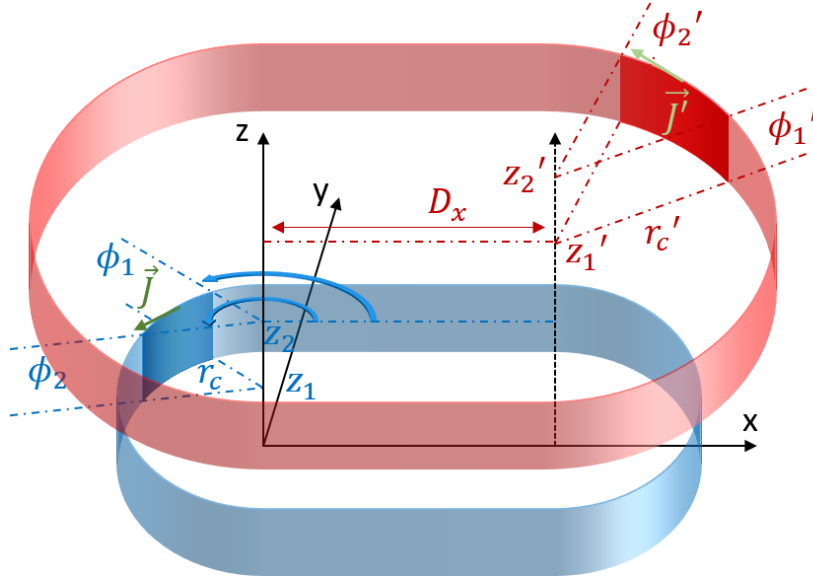


Figure VI-4: Mutual inductance between two non-coaxial angular sectors.

We have:

$$\vec{J} \cdot \vec{J}' = JJ' \cos(\phi - \phi')$$

With $dS = r_c dZ d\phi$; $dS' = r_c' dZ' d\phi'$; $J = \frac{I}{z}$ and $J' = \frac{I'}{z'}$, we obtain:

$$M_{1 \leftrightarrow 2} = \frac{\mu_0}{4\pi} \frac{\mathbf{z} \times \mathbf{z}'}{z \times z'} \int_{z'_1}^{z'_2} \int_{z_1}^{z_2} \int_{\phi'_1}^{\phi'_2} \int_{\phi_1}^{\phi_2} \frac{\cos(\phi - \phi')}{d} dZ d\phi dZ' d\phi'$$

Calculation of d :

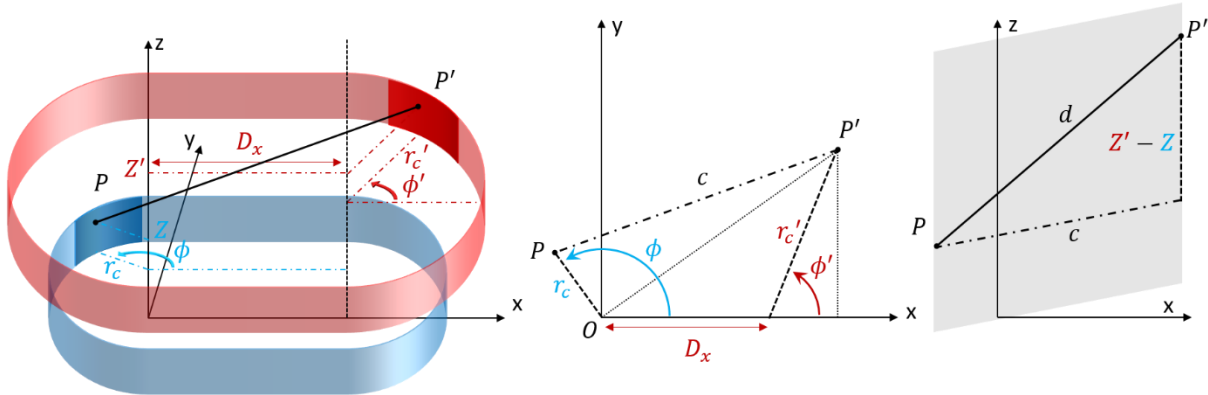


Figure VI-5: Explanatory sketch for obtaining the expression of $M_{A-A,nc}$.

In the xy plan, along \vec{e}_x :

$$\overrightarrow{PP'} \cdot \vec{e}_x = \overrightarrow{PO} \cdot \vec{e}_x + \overrightarrow{OP'} \cdot \vec{e}_x = -r_c \cos(\phi) + D_x + r'_c \cos(\phi')$$

In the xy plan, along \vec{e}_y :

$$\overrightarrow{PP'} \cdot \vec{e}_y = \overrightarrow{PO} \cdot \vec{e}_y + \overrightarrow{OP'} \cdot \vec{e}_y = -r_c \sin(\phi) + r'_c \sin(\phi')$$

We get:

$$c = \sqrt{(-r_c \cos(\phi) + D_x + r'_c \cos(\phi'))^2 + (-r_c \sin(\phi) + r'_c \sin(\phi'))^2}$$

$$\text{So, } c = \sqrt{r_c^2 + r'_c{}^2 + D_x^2 + 2D_x(r'_c \cos(\phi') - r_c \cos(\phi)) - 2r_c r'_c \cos(\phi - \phi')}$$

And in the plane along z and passing through the segment PP' , we obtain:

$$d = \sqrt{r_c^2 + r'_c{}^2 + D_x^2 + 2D_x(r'_c \cos(\phi') - r_c \cos(\phi)) - 2r_c r'_c \cos(\phi - \phi') + (Z' - Z)^2}$$

VI. 2 Contact resistivity measurements between superconducting tapes, Chapter III

Current values for measurements

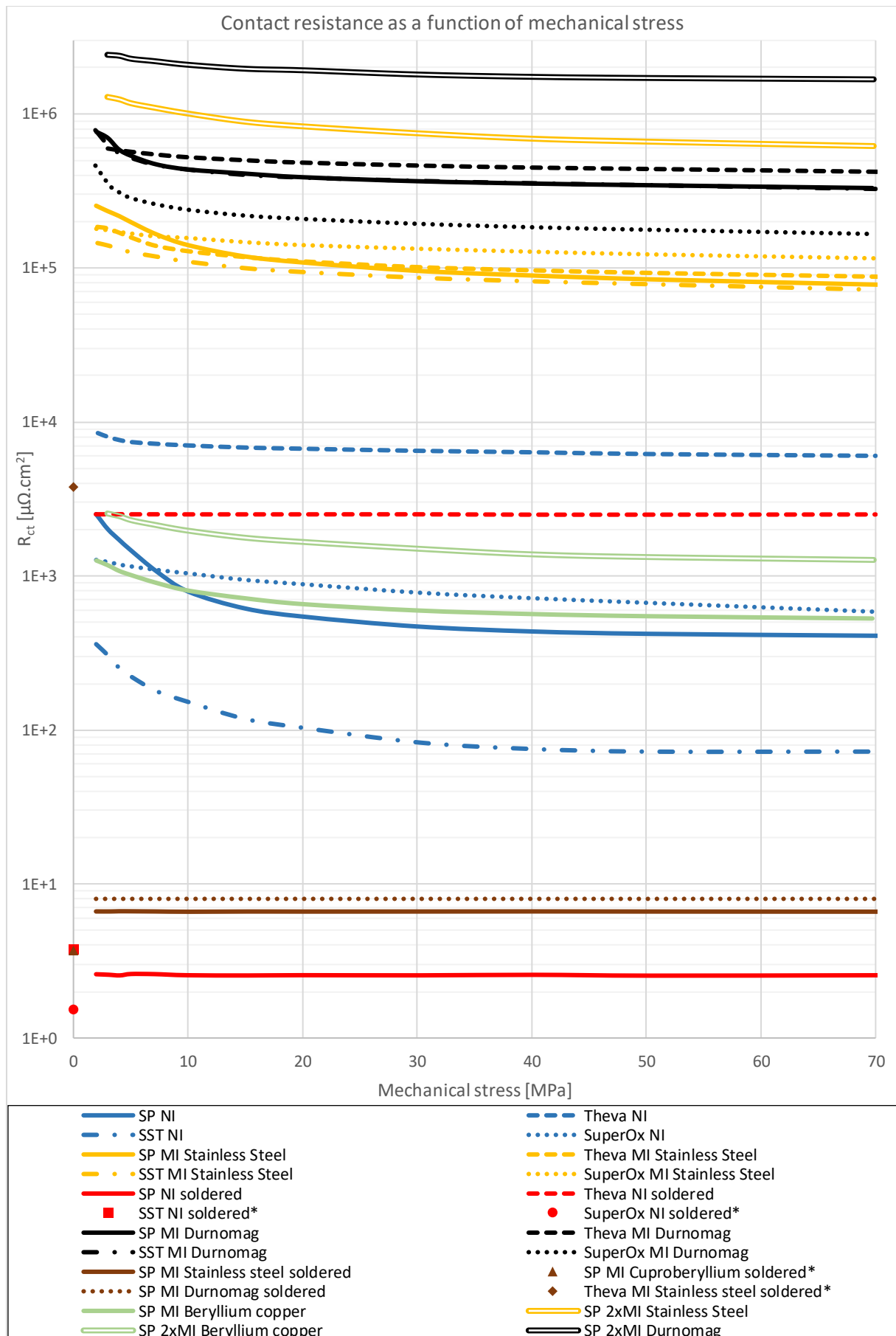
I [A]	SuperPower SP	Theva	Shanghai ST	SuperOx
NI	10	55	50	50
MI Stainless Steel	10	15	10	10
NI soldered	70	70	100	100
MI Stainless Steel soldered	70	10		
MI Beryllium copper soldered	60			
MI Durnomag soldered	60			
MI Durnomag	8	5	10	10
MI Beryllium copper	30			
2×MI Stainless Steel	3			
2×MI Beryllium copper	3			
2×MI Durnomag	3			

Average values taken from the different samples: first phase of cycle 2, from 2 to 70 MPa

R_{ct} [$\mu\Omega.cm^2$]	SuperPower	Theva	Shanghai ST	SuperOx
NI	[100 ; 4 000]	[4 000 ; 15 000]	[60 ; 500]	[300 ; 2 000]
MI Stainless Steel	[70 000 ; 300 000]	[60 000 ; 250 000]	[50 000 ; 200 000]	[75 000 ; 270 000]
NI soldered	2.6	2 511	3.8	1.5
MI Stainless Steel soldered	6.6	2 574		
MI Beryllium copper soldered	3.4			
MI Durnomag soldered	8.1			
MI Durnomag	[260 000 ; 1 000 000]	[250 000 ; 700 000]	[200 000 ; 800 000]	[150 000 ; 500 000]
MI Beryllium copper	[300 ; 2 000]			
2×MI Stainless Steel	[480 000 ; 1 550 000]			
2×MI Beryllium copper	[800 ; 7 000]			
2×MI Durnomag	[1 600 000 ; 2 500 000]			

Average values taken from different samples: first phase of cycle 2, mechanical stress 20 MPa

R_{ct} [$\mu\Omega.cm^2$]	SuperPower	Theva	Shanghai ST	SuperOx
NI	540	6 700	100	890
MI Stainless Steel	108 400	110 700	94 200	135 800
NI soldered	2.7	2 500	3.8	1.5
MI Stainless Steel soldered	6.6	3 700		
MI Beryllium copper soldered	3.7			
MI Durnomag soldered	8.1			
MI Durnomag	387 900	483 800	386 400	208 200
MI Beryllium copper	650			
2×MI Stainless Steel	829 500			
2×MI Beryllium copper	1 660			
2×MI Durnomag	1 919 300			



*: measurement without mechanical stress.

VI. 3 Micro soldering, Chapter III

In order to verify this theory (III. 3. 4. 2. 2), new contact resistivity measurements before and after mechanical shock were carried out on StS samples with the presence of the ALD 100% Al_2O_3 @ 177°C. Different steps constitute the measurements performed (Figure VI-6):

- ①: A globally constant contact resistivity value for a current $I < 3$ A. The current value is too low and the conduction area $S_{①}$ between the tapes too high to generate significant local heat by Joule effect. No solder is generated; the Brany effect is not yet observable.
- ②: a decrease in contact resistivity with a current $I > 3$ A. By increasing the current value, the current density passing through the contact areas becomes increasingly important, although the conduction surface ($S_{①}$) remains constant (constant stress at 70 MPa). The current value is high enough to generate an important temperature rise by Joule effect causing locally a soldering of the micro-contacts. This leads to an increase in the contact area ($S_{②} > S_{①}$) and therefore a decrease in the contact resistivity, and this each time the maximum imposed current value increases. At the end of this phase ②, the maximum imposed current is $I_{max②} = 10,2$ A with the conduction surface $S_{②}$. A hysteresis cycle appears: the phenomenon is non-reversible. By applying again current values I lower than the maximum imposed current value $I_{max②}$, the previous measured R_{ct} values are not recovered. The R_{ct} value for any current $I \leq I_{max②}$ is approximately equal to the R_{ct} value for $I = I_{max②}$. This is because, with the micro soldering still present, the contact area $S_{②}$ generated by $I_{max②}$ is larger than the initial contact area $S_{①}$. Since the conduction area of the ② phase is larger, the contact resistivity will be lower for the same current value compared to the ① phase. The R_{ct} value for $I = 2.2$ A of the ② phase is lower than R_{ct} for $I = 2.2$ A of the ① phase. By increasing the current value once again to $I_{max②}$, the R_{ct} value remains relatively fixed. There is no further decrease in R_{ct} . Nevertheless, a slight decrease in R_{ct} is observable. It is explained by a lower current, generating a lower local temperature rise at the electrical contacts, thus decreasing the contact resistivity value.
- ③: an increase in contact surface. By exceeding the maximum imposed current value ($I_{max②} = 10,2$ A), a local increase in temperature is again generated causing new micro soldering and thus a new decrease in contact resistivity ($S_{③} > S_{②}$). At the end of this phase ③, the maximum current imposed is $I_{max③} = 15,2$ A. Therefore, the contact area with the new solder is larger. The R_{ct} value for $I = 2.2$ A of the ③ phase is again lower than R_{ct} for $I = 2.2$ A of the ② phase. The observed behavior of the contact resistivity following current cycling is the same as with a sample consisting of several rough alumina disks subjected to a constant load [104].
- ④: restoration of the initial contact resistivity value. A mechanical shock is caused to the samples causing the destruction of the micro soldering. The surfaces of the contact areas without micro soldering are restored, and thus the contact resistivity value for $I = 2.2$ A of phase ①.

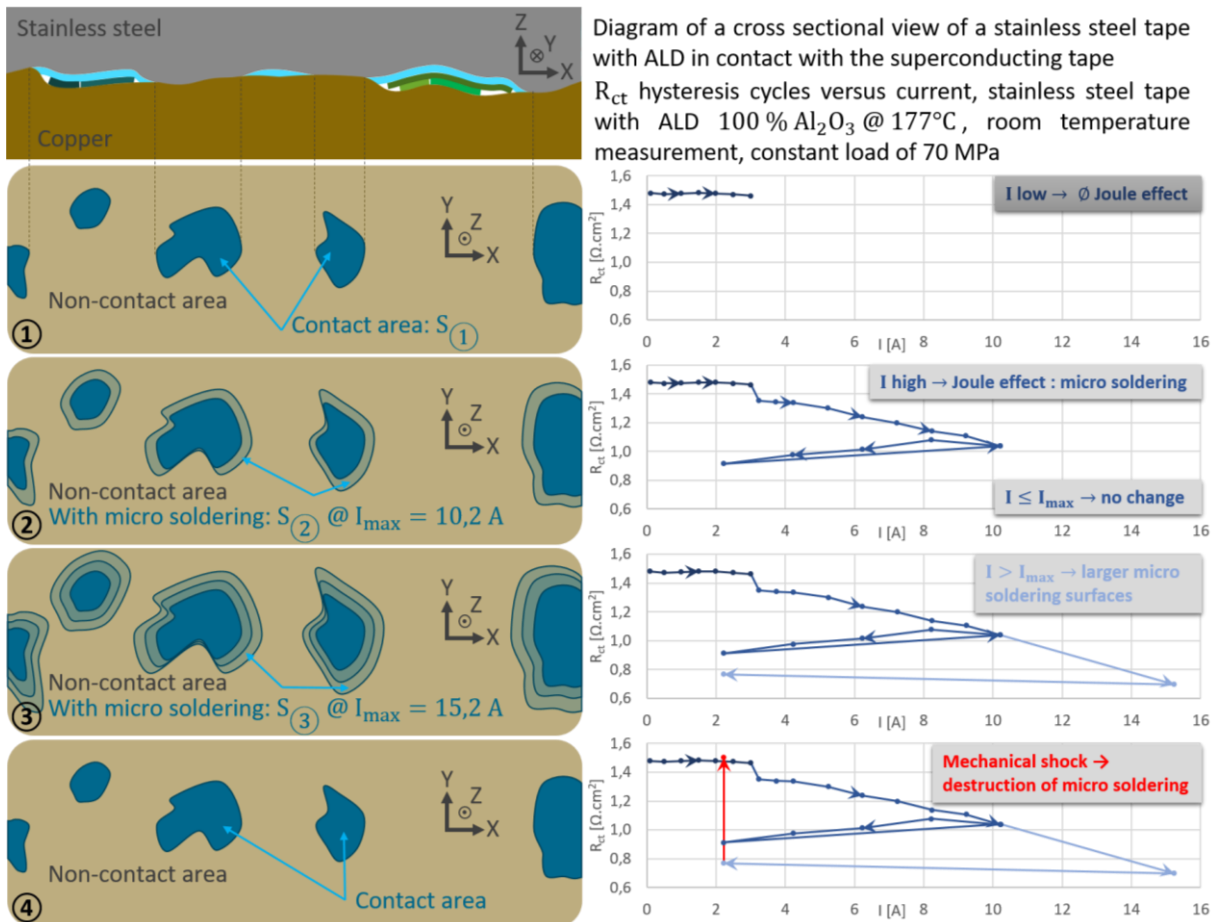


Figure VI-6: R_{ct} versus current, stainless steel tape with ALD 100% Al_2O_3 @ 177°C and constant load of 70 MPa; sketch of generation of micro soldering and restoration of the initial contact resistivity by destruction of the micro soldering via a mechanical shock; room temperature.

The behavior of the contact resistivity as a function of current before or after a mechanical shock is identical. In Figure VI-7, R_{ct} measurements are made with $I = 2.2$; 15.2 and 2.2 A. A decrease in contact resistivity is observable between 2.2 A and 15.2 A (between measurements ① and ②), and a lower R_{ct} value is measurable for $I = 2.2$ A (between measurements ③ and ①) through the creation of micro soldering. A simple mechanical shock restores the initial contact resistivity value. By imposing again currents $I = 2.2$; 15.2 and 2.2 A, we find the same hysteresis cycle (③ \rightarrow ④ \rightarrow ⑤) compare to ① \rightarrow ② \rightarrow ③).

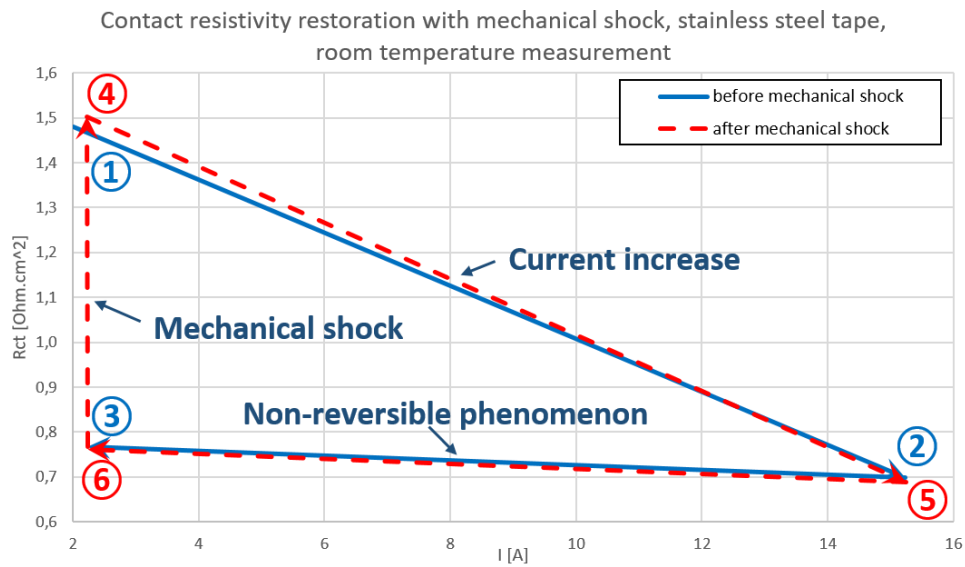


Figure VI-7: Superposition of the two R_{ct} hysteresis cycles versus current before and after mechanical shock, stainless steel tape with ALD 100% Al_2O_3 @ 177°C and constant load of 70 MPa; generation of micro soldering and restoration of the initial contact resistivity by destruction of the micro soldering via a mechanical shock; room temperature measurement.

The current value flowing radially between the superconducting tapes decreases the contact resistivity value in the case of an ALD ZnO/Al_2O_3 , whatever the precursor content and the deposition temperature. The objective of having a controlled contact resistivity with the ALD is clearly not achieved.

Bibliography

- [1] P. J. Ray, “Master’s thesis: Structural investigation of $\text{La}(2-x)\text{Sr}(x)\text{CuO}(4+y)$ - Following staging as a function of temperature,” thesis, figshare, 2016. [doi: 10.6084/m9.figshare.2075680.v2](https://doi.org/10.6084/m9.figshare.2075680.v2).
- [2] G. Grissonnanche *et al.*, “Direct measurement of the upper critical field in cuprate superconductors,” *Nature Communications*, vol. 5, no. 1, Art. no. 1, Feb. 2014, [doi: 10.1038/ncomms4280](https://doi.org/10.1038/ncomms4280).
- [3] A. P. Smith, M. J. Raine, E. Surrey, S. Awaji, T. Okada, and D. P. Hampshire, “3-D Properties in (RE)BCO Tapes Measured in Fields up to 35T,” *IEEE Transactions on Applied Superconductivity*, vol. 29, no. 5, pp. 1–5, Aug. 2019, [doi: 10.1109/TASC.2019.2895218](https://doi.org/10.1109/TASC.2019.2895218).
- [4] L. Bottura, “A practical fit for the critical surface of NbTi,” *IEEE Transactions on Applied Superconductivity*, vol. 10, no. 1, pp. 1054–1057, Mar. 2000, [doi: 10.1109/77.828413](https://doi.org/10.1109/77.828413).
- [5] B. Bordini *et al.*, “Extensive Characterization of the 1 mm PIT Nb3Sn Strand for the 13-T FRESCA2 Magnet,” *IEEE Transactions on Applied Superconductivity*, vol. 22, no. 3, pp. 6000304–6000304, Jun. 2012, [doi: 10.1109/TASC.2011.2178217](https://doi.org/10.1109/TASC.2011.2178217).
- [6] J. Fleiter and A. Ballarino, “Parameterization of the critical surface of REBCO conductors from Fujikura,” pp. 9-Internal Note 2014-24-EDMS Nr: 1426239, Sep. 2014.
- [7] G. Dilasser, “Etude expérimentale et numérique des courants d’écrantage dans les aimants supraconducteurs à haute température critique REBCO,” These de doctorat, Université Grenoble Alpes (ComUE), 2017. [Online]. Available: <https://www.theses.fr/2017GREAT059>
- [8] L. R. Evans, *The Large Hadron Collider: A Marvel of Technology*. EPFL Press, 2009.
- [9] L. Quettier *et al.*, “Commissioning Completion of the Iseult Whole Body 11.7 T MRI System,” *IEEE Transactions on Applied Superconductivity*, vol. 30, no. 4, pp. 1–5, Jun. 2020, [doi: 10.1109/TASC.2020.2983702](https://doi.org/10.1109/TASC.2020.2983702).
- [10] “Plots - MagLab.” <https://nationalmaglab.org/magnet-development/applied-superconductivity-center/plots>
- [11] M. Kikuchi *et al.*, “Development of New Types of DI-BSCCO Wire,” pp. 8-<https://global-sei.com/technology/tr/bn66/pdf/66-09.pdf>.
- [12] M. Okada *et al.*, “Bi-2212/Ag high-field magnets,” *Physica C: Superconductivity*, vol. 335, no. 1, pp. 61–64, Jun. 2000, [doi: 10.1016/S0921-4534\(00\)00143-X](https://doi.org/10.1016/S0921-4534(00)00143-X).
- [13] D. W. Hazelton, “SuperPower 2G HTS Conductor,” pp. 22-<https://indico.cern.ch/event/308828/contributions/1680701/attachments/589805/811805/WAMHTS1.pdf>, 2014.
- [14] F. Ltd, “Introduction of FUJIKURA RE-based HTS Wire,” pp. 25-<https://www.fujikura.co.jp/eng/products/newbusiness/superconductors/01/superconductor.pdf>.

- [15] A. Goyal *et al.*, “Conductors with controlled grain boundaries: An approach to the next generation, high temperature superconducting wire,” *Journal of Materials Research*, vol. 12, no. 11, pp. 2924–2940, Nov. 1997, [doi: 10.1557/JMR.1997.0387](https://doi.org/10.1557/JMR.1997.0387).
- [16] Y. Iijima, N. Tanabe, O. Kohno, and Y. Ikeno, “In-plane aligned YBa₂Cu₃O_{7-x} thin films deposited on polycrystalline metallic substrates,” *Appl. Phys. Lett.*, vol. 60, no. 6, pp. 769–771, Feb. 1992, [doi: 10.1063/1.106514](https://doi.org/10.1063/1.106514).
- [17] linda, “Products - THE VA,” *THEVA english*. <https://www.theva.com/products/>
- [18] W. Prusseit, “HTS-WIRE FOR HIGH FIELD MAGNET APPLICATIONS,” pp. 20-<https://indico.cern.ch/event/1032199/contributions/4359092/attachments/2255357/3826776/THEVA%20%40%20CERN%20roadmap%20workshop%20010621.pdf>, 2021.
- [19] D. C. van der Laan, J. W. Ekin, C. C. Clickner, and T. C. Stauffer, “Delamination strength of YBCO coated conductors under transverse tensile stress,” *Supercond. Sci. Technol.*, vol. 20, no. 8, pp. 765–770, Jun. 2007, [doi: 10.1088/0953-2048/20/8/007](https://doi.org/10.1088/0953-2048/20/8/007).
- [20] “Low-High Temperature Superconductivity | Center of Excellence for Superconductivity Research.” <http://cesur.ankara.edu.tr/>
- [21] F. Borgnolutti *et al.*, “Design Study of a 10-T REBCO Insert Solenoid,” *IEEE Transactions on Applied Superconductivity*, vol. 26, no. 4, pp. 1–5, Jun. 2016, [doi: 10.1109/TASC.2016.2518810](https://doi.org/10.1109/TASC.2016.2518810).
- [22] P. Fazilleau, X. Chaud, F. Debray, T. Lécresse, and J.-B. Song, “38 mm diameter cold bore metal-as-insulation HTS insert reached 32.5 T in a background magnetic field generated by resistive magnet,” *Cryogenics*, vol. 106, p. 103053, Mar. 2020, [doi: 10.1016/j.cryogenics.2020.103053](https://doi.org/10.1016/j.cryogenics.2020.103053).
- [23] P. Pugnati *et al.*, “43+T Grenoble Hybrid Magnet: From Final Assembly to Commissioning of the Superconducting Outsert,” *IEEE Transactions on Applied Superconductivity*, vol. 32, no. 6, pp. 1–7, Sep. 2022, [doi: 10.1109/TASC.2022.3151838](https://doi.org/10.1109/TASC.2022.3151838).
- [24] U. P. Trociewitz *et al.*, “35.4 T field generated using a layer-wound superconducting coil made of (RE)Ba₂Cu₃O_{7-x} (RE = rare earth) coated conductor,” *Appl. Phys. Lett.*, vol. 99, no. 20, p. 202506, Nov. 2011, [doi: 10.1063/1.3662963](https://doi.org/10.1063/1.3662963).
- [25] W. D. Markiewicz *et al.*, “33.8 TESLA WITH A YBa₂Cu₃O_{7-x} SUPERCONDUCTING TEST COIL,” *AIP Conference Proceedings*, vol. 1218, no. 1, Apr. 2010, [doi: 10.1063/1.3422357](https://doi.org/10.1063/1.3422357).
- [26] P. C. Michael *et al.*, “Assembly and Test of a 3-Nested-Coil 800-MHz REBCO Insert (H800) for the MIT 1.3 GHz LTS/HTS NMR Magnet,” *IEEE Transactions on Applied Superconductivity*, vol. 29, no. 5, pp. 1–6, Aug. 2019, [doi: 10.1109/TASC.2019.2901246](https://doi.org/10.1109/TASC.2019.2901246).
- [27] S. Hanai, T. Tsuchihashi, S. Ioka, K. Watanabe, S. Awaji, and H. Oguro, “Development of an 11 T BSCCO Insert Coil for a 25 T Cryogen-free Superconducting Magnet,” *IEEE Transactions on Applied Superconductivity*, vol. 27, no. 4, pp. 1–6, Jun. 2017, [doi: 10.1109/TASC.2017.2657689](https://doi.org/10.1109/TASC.2017.2657689).
- [28] S. Yoon, J. Kim, K. Cheon, H. Lee, S. Hahn, and S.-H. Moon, “26 T 35 mm all-GdBa₂Cu₃O_{7-x} multi-width no-insulation superconducting magnet,” *Supercond. Sci. Technol.*, vol. 29, no. 4, p. 04LT04, Mar. 2016, [doi: 10.1088/0953-2048/29/4/04LT04](https://doi.org/10.1088/0953-2048/29/4/04LT04).

- [29] Q. Wang *et al.*, “High Temperature Superconducting YBCO Insert for 25 T Full Superconducting Magnet,” *IEEE Transactions on Applied Superconductivity*, vol. 25, no. 3, pp. 1–5, Jun. 2015, [doi: 10.1109/TASC.2014.2365630](https://doi.org/10.1109/TASC.2014.2365630).
- [30] L. G. Rubin, B. L. Brandt, R. J. Weggel, S. Foner, and E. J. McNiff, “33.6 T dc magnetic field produced in a hybrid magnet with Ho pole pieces,” *Appl. Phys. Lett.*, vol. 49, no. 1, pp. 49–51, Jul. 1986, [doi: 10.1063/1.97080](https://doi.org/10.1063/1.97080).
- [31] E. J. McNiff, B. L. Brandt, S. Foner, L. G. Rubin, and R. J. Weggel, “Temperature anomalies observed in liquid 4He columns in magnetic fields with field–field-gradient products >21 T²/cm,” *Review of Scientific Instruments*, vol. 59, no. 11, pp. 2474–2476, Nov. 1988, [doi: 10.1063/1.1139931](https://doi.org/10.1063/1.1139931).
- [32] W. D. Markiewicz *et al.*, “Design of a Superconducting 32 T Magnet With REBCO High Field Coils,” *IEEE Transactions on Applied Superconductivity*, vol. 22, no. 3, pp. 4300704–4300704, Jun. 2012, [doi: 10.1109/TASC.2011.2174952](https://doi.org/10.1109/TASC.2011.2174952).
- [33] W. D. Markiewicz, “Protection of HTS Coils in the Limit of Zero Quench Propagation Velocity,” *IEEE Transactions on Applied Superconductivity*, vol. 18, no. 2, pp. 1333–1336, Jun. 2008, [doi: 10.1109/TASC.2008.920527](https://doi.org/10.1109/TASC.2008.920527).
- [34] J. H. Schultz, “Protection of superconducting magnets,” *IEEE Transactions on Applied Superconductivity*, vol. 12, no. 1, pp. 1390–1395, Mar. 2002, [doi: 10.1109/TASC.2002.1018662](https://doi.org/10.1109/TASC.2002.1018662).
- [35] J. Vialle, A. Badel, and P. Tixador, “12 T Insulated REBCO Magnet Used as 1 MJ SMES: Protection Strategies and Preliminary Assembly Tests,” *IEEE Transactions on Applied Superconductivity*, vol. 32, no. 6, pp. 1–7, Sep. 2022, [doi: 10.1109/TASC.2022.3180979](https://doi.org/10.1109/TASC.2022.3180979).
- [36] J. Vialle, A. Badel, B. Rozier, and P. Tixador, “Transient voltages and energy balance in REBCO insulated magnet: experimental and numerical studies,” *Supercond. Sci. Technol.*, vol. 34, no. 11, p. 115012, Sep. 2021, [doi: 10.1088/1361-6668/ac2623](https://doi.org/10.1088/1361-6668/ac2623).
- [37] J. Vialle, A. Badel, P. Tixador, J. Ciceron, F. Forest, and R. Pasquet, “Preliminary Tests of Pancakes From a 12 T REBCO Insulated Solenoid Magnet,” *IEEE Transactions on Applied Superconductivity*, vol. 31, no. 5, pp. 1–5, Aug. 2021, [doi: 10.1109/TASC.2021.3057837](https://doi.org/10.1109/TASC.2021.3057837).
- [38] R. Grabovickic, J. W. Lue, M. J. Gouge, J. A. Demko, and R. C. Duckworth, “Measurements of temperature dependence of the stability and quench propagation of a 20-cm-long RABiTS Y-Ba-Cu-O tape,” *IEEE Transactions on Applied Superconductivity*, vol. 13, no. 2, pp. 1726–1730, Jun. 2003, [doi: 10.1109/TASC.2003.812874](https://doi.org/10.1109/TASC.2003.812874).
- [39] J. W. Lue, M. J. Gouge, R. C. Duckworth, D. F. Lee, D. M. Kroeger, and J. M. Pfothenauer, “Quench tests of a 20-cm-long RABiTS YBCO tape,” *AIP Conference Proceedings*, vol. 613, no. 1, p. 457, May 2002, [doi: 10.1063/1.1472054](https://doi.org/10.1063/1.1472054).
- [40] T. Lécresse *et al.*, “Quench Propagation in YBCO Pancake: Experimental and Computational Results,” *IEEE Transactions on Applied Superconductivity*, vol. 23, no. 3, pp. 4601805–4601805, Jun. 2013, [doi: 10.1109/TASC.2013.2246753](https://doi.org/10.1109/TASC.2013.2246753).
- [41] G. Celentano *et al.*, “Hot Spot Stimulated Transition in YBCO Coated Conductors: Experiments and Simulations,” *IEEE Transactions on Applied Superconductivity*, vol. 19, no. 3, pp. 2486–2489, Jun. 2009, [doi: 10.1109/TASC.2009.2017916](https://doi.org/10.1109/TASC.2009.2017916).

- [42] F.-P. Juster, J. Deregél, B. Hervieu, and J.-M. Rey, “Stability and quench propagation velocities measurements on the ‘racetrack’ mock-up of ATLAS toroid coil,” *IEEE Transactions on Applied Superconductivity*, vol. 10, no. 1, pp. 677–680, Mar. 2000, doi: [10.1109/77.828324](https://doi.org/10.1109/77.828324).
- [43] T. Lécresse, “Contribution à l’étude des aimants supraconducteurs utilisant des matériaux supraconducteurs à haute température de transition,” These de doctorat, Grenoble, 2012. [Online]. Available: <https://www.theses.fr/2012GRENT095>
- [44] C. Lacroix and F. Sirois, “Concept of a current flow diverter for accelerating the normal zone propagation velocity in 2G HTS coated conductors,” *Supercond. Sci. Technol.*, vol. 27, no. 3, p. 035003, Jan. 2014, doi: [10.1088/0953-2048/27/3/035003](https://doi.org/10.1088/0953-2048/27/3/035003).
- [45] R. Gupta *et al.*, “High Field HTS R&D Solenoid for Muon Collider,” *IEEE Transactions on Applied Superconductivity*, vol. 21, no. 3, pp. 1884–1887, Jun. 2011, doi: [10.1109/TASC.2010.2090123](https://doi.org/10.1109/TASC.2010.2090123).
- [46] S. Hahn, D. K. Park, J. Bascunan, and Y. Iwasa, “HTS Pancake Coils Without Turn-to-Turn Insulation,” *IEEE Transactions on Applied Superconductivity*, vol. 21, no. 3, pp. 1592–1595, Jun. 2011, doi: [10.1109/TASC.2010.2093492](https://doi.org/10.1109/TASC.2010.2093492).
- [47] S. B. Kim *et al.*, “The Improved Transient Stabilities of HTS Coils by Removing the Insulation and Inserting the Metal Tapes,” *Physics Procedia*, vol. 45, pp. 249–252, Jan. 2013, doi: [10.1016/j.phpro.2013.05.014](https://doi.org/10.1016/j.phpro.2013.05.014).
- [48] D. G. Yang, Y. H. Choi, Y. G. Kim, J. B. Song, and H. G. Lee, “Analytical and experimental investigation of electrical characteristics of a metallic insulation GdBCO coil,” *Review of Scientific Instruments*, vol. 87, no. 3, p. 034701, Mar. 2016, doi: [10.1063/1.4942911](https://doi.org/10.1063/1.4942911).
- [49] T. Lécresse, A. Badel, T. Benkel, X. Chaud, P. Fazilleau, and P. Tixador, “Metal-as-insulation variant of no-insulation HTS winding technique: pancake tests under high background magnetic field and high current at 4.2 K,” *Supercond. Sci. Technol.*, vol. 31, no. 5, p. 055008, Apr. 2018, doi: [10.1088/1361-6668/aab4ec](https://doi.org/10.1088/1361-6668/aab4ec).
- [50] P. Fazilleau, B. Borgnic, X. Chaud, F. Debray, T. Lécresse, and J.-B. Song, “Metal-as-insulation sub-scale prototype tests under a high background magnetic field,” *Supercond. Sci. Technol.*, vol. 31, no. 9, p. 095003, Jul. 2018, doi: [10.1088/1361-6668/aad225](https://doi.org/10.1088/1361-6668/aad225).
- [51] J. Mun, C. Lee, K. Sim, C. Lee, M. Park, and S. Kim, “Electrical Characteristics of Soldered Metal Insulation REBCO Coil,” *IEEE Transactions on Applied Superconductivity*, vol. 30, no. 4, pp. 1–4, Jun. 2020, doi: [10.1109/TASC.2020.2974842](https://doi.org/10.1109/TASC.2020.2974842).
- [52] J.-B. Song *et al.*, “Dynamic Response of No-Insulation and Partial-Insulation Coils for HTS Wind Power Generator,” *IEEE Transactions on Applied Superconductivity*, vol. 25, no. 3, pp. 1–5, Jun. 2015, doi: [10.1109/TASC.2014.2384739](https://doi.org/10.1109/TASC.2014.2384739).
- [53] Y. H. Choi, S. Hahn, J. B. Song, D. G. Yang, and H. G. Lee, “Partial insulation of GdBCO single pancake coils for protection-free HTS power applications,” *Supercond. Sci. Technol.*, vol. 24, no. 12, p. 125013, Nov. 2011, doi: [10.1088/0953-2048/24/12/125013](https://doi.org/10.1088/0953-2048/24/12/125013).
- [54] B. S. Allimi, S. P. Alpay, C. K. Xie, B. O. Wells, J. I. Budnick, and D. M. Pease, “Resistivity of V₂O₃ thin films deposited on a-plane (110) and c-plane (001) sapphire by pulsed laser deposition,” *Appl. Phys. Lett.*, vol. 92, no. 20, p. 202105, May 2008, doi: [10.1063/1.2921787](https://doi.org/10.1063/1.2921787).

- [55] H.-W. Kim *et al.*, “Enhancement of 2G HTS Coil Stability With V₂O₃ and Perforated HTS Wire,” *IEEE Transactions on Applied Superconductivity*, vol. 28, no. 3, pp. 1–5, Apr. 2018, [doi: 10.1109/TASC.2017.2778086](https://doi.org/10.1109/TASC.2017.2778086).
- [56] T. Lécresse and Y. Iwasa, “A (RE)BCO Pancake Winding With Metal-as-Insulation,” *IEEE Transactions on Applied Superconductivity*, vol. 26, no. 3, pp. 1–5, Apr. 2016, [doi: 10.1109/TASC.2016.2522638](https://doi.org/10.1109/TASC.2016.2522638).
- [57] S. Choi, H. C. Jo, Y. J. Hwang, S. Hahn, and T. K. Ko, “A Study on the No Insulation Winding Method of the HTS Coil,” *IEEE Transactions on Applied Superconductivity*, vol. 22, no. 3, pp. 4904004–4904004, Jun. 2012, [doi: 10.1109/TASC.2011.2175892](https://doi.org/10.1109/TASC.2011.2175892).
- [58] J.-B. Song, S. Hahn, T. Lécresse, J. Voccio, J. Bascuñán, and Y. Iwasa, “Over-current quench test and self-protecting behavior of a 7 T/78 mm multi-width no-insulation REBCO magnet at 4.2 K,” *Supercond. Sci. Technol.*, vol. 28, no. 11, p. 114001, Sep. 2015, [doi: 10.1088/0953-2048/28/11/114001](https://doi.org/10.1088/0953-2048/28/11/114001).
- [59] S. An *et al.*, “A Feasibility Study on ‘Magnetic Dam’ to Absorb Magnetic Energy in NI HTS Magnet During Quench,” *IEEE Transactions on Applied Superconductivity*, vol. 30, no. 4, pp. 1–5, Jun. 2020, [doi: 10.1109/TASC.2020.2972221](https://doi.org/10.1109/TASC.2020.2972221).
- [60] G. Kirby, T. Galvin, D. Coll, R. Stevenson, and P. Livesey, “Varistor Insulation for HTS Magnets,” *IEEE Transactions on Applied Superconductivity*, vol. 32, no. 6, pp. 1–4, Sep. 2022, [doi: 10.1109/TASC.2022.3165732](https://doi.org/10.1109/TASC.2022.3165732).
- [61] K. Katsumata *et al.*, “Influence of the Turn-to-Turn Contact Electrical Resistance on the Thermal Stability in Meter-Class No-Insulation REBCO Pancake Coils During a Local Normal-State Transition,” *IEEE Transactions on Applied Superconductivity*, vol. 27, no. 4, pp. 1–5, Jun. 2017, [doi: 10.1109/TASC.2017.2657679](https://doi.org/10.1109/TASC.2017.2657679).
- [62] A. Ikeda *et al.*, “Transient Behaviors of No-Insulation REBCO Pancake Coil During Local Normal-State Transition,” *IEEE Transactions on Applied Superconductivity*, vol. 26, no. 4, pp. 1–4, Jun. 2016, [doi: 10.1109/TASC.2016.2521412](https://doi.org/10.1109/TASC.2016.2521412).
- [63] Y. Wang, W. K. Chan, and J. Schwartz, “Self-protection mechanisms in no-insulation (RE)Ba₂Cu₃O_x high temperature superconductor pancake coils,” *Supercond. Sci. Technol.*, vol. 29, no. 4, p. 045007, Mar. 2016, [doi: 10.1088/0953-2048/29/4/045007](https://doi.org/10.1088/0953-2048/29/4/045007).
- [64] Y. Liu *et al.*, “Study of contact resistivity of a no-insulation superconducting coil,” *Supercond. Sci. Technol.*, vol. 34, no. 3, p. 035009, Jan. 2021, [doi: 10.1088/1361-6668/abd14d](https://doi.org/10.1088/1361-6668/abd14d).
- [65] T. Wang *et al.*, “Analyses of Transient Behaviors of No-Insulation REBCO Pancake Coils During Sudden Discharging and Overcurrent,” *IEEE Transactions on Applied Superconductivity*, vol. 25, no. 3, pp. 1–9, Jun. 2015, [doi: 10.1109/TASC.2015.2393058](https://doi.org/10.1109/TASC.2015.2393058).
- [66] Y. Wang, H. Song, D. Xu, Z. Y. Li, Z. Jin, and Z. Hong, “An equivalent circuit grid model for no-insulation HTS pancake coils,” *Supercond. Sci. Technol.*, vol. 28, no. 4, p. 045017, Mar. 2015, [doi: 10.1088/0953-2048/28/4/045017](https://doi.org/10.1088/0953-2048/28/4/045017).
- [67] P. Fazilleau, T. Lécresse, and X. Chaud, “Electrical behavior of Metal-as-Insulation prototype coils for the ANR NOUGAT project - Poster ASC Denver - Id: 3LPoH-05.” 2016.
- [68] P. Fazilleau and T. Lécresse, “Calculs électriques et thermiques d’une bobine NI Note LEAS0069,” pp. 18-Internal note, Sep. 2016.

- [69] “Choose an ODE Solver - MATLAB & Simulink - MathWorks France.” <https://fr.mathworks.com/help/matlab/math/choose-an-ode-solver.html>
- [70] G. Aubert, “Inductance mutuelle de deux secteurs angulaires de solénoïdes minces coaxiaux,” pp. 6-Internal note, Sep. 2015.
- [71] Z. Piatek, B. Baron, T. Szczegielniak, D. Kusiak, and A. Pasierbek, “Exact closed form formula for mutual inductance of conductors of rectangular cross section,” *Przegląd Elektrotechniczny*, vol. 89, pp. 61–64, Jan. 2013. [Available online](#).
- [72] E. Rochepault, “Étude de dipôles supraconducteurs en Nb₃Sn à haut champ : isolation électrique à base de céramique et conception magnétique,” Paris Sud - Paris XI, Paris, 2012. [Online]. Available: <http://www.theses.fr/165111410>
- [73] I. S. Gradshteĭn, I. M. Ryzhik, and A. Jeffrey, *Table of integrals, series, and products*, 7th ed. Amsterdam ; Boston: Academic Press, 2007. [Available online](#).
- [74] L. Greengard and V. Rokhlin, “A Fast Algorithm for Particle Simulations,” *Journal of Computational Physics*, vol. 135, no. 2, pp. 280–292, Aug. 1997, [doi: 10.1006/jcph.1997.5706](https://doi.org/10.1006/jcph.1997.5706).
- [75] N. A. Gumerov and R. Duraiswami, *Fast Multipole Methods for the Helmholtz Equation in Three Dimensions*. Elsevier, 2005.
- [76] S. Chaillat, M. Bonnet, and J.-F. Semblat, “A multi-level fast multipole BEM for 3-D elastodynamics in the frequency domain,” *Computer Methods in Applied Mechanics and Engineering*, vol. 197, no. 49, pp. 4233–4249, Sep. 2008, [doi: 10.1016/j.cma.2008.04.024](https://doi.org/10.1016/j.cma.2008.04.024).
- [77] “Multi-Level Fast Multipole BEM for 3-D Elastodynamics | SpringerLink.” https://link.springer.com/chapter/10.1007/978-1-4020-9710-2_2
- [78] J. Van Nugteren, “High Temperature Superconductor Accelerator Magnets,” Ipskamp, 2016. [Online]. Available: <https://cds.cern.ch/record/2228249>
- [79] R. V. Smith, “Review of heat transfer to helium I,” *Cryogenics*, vol. 9, no. 1, pp. 11–19, Feb. 1969, [doi: 10.1016/0011-2275\(69\)90251-3](https://doi.org/10.1016/0011-2275(69)90251-3).
- [80] Université de Paris, “Formation de cryogénie SFV, Documents en Annexe, Recueil de tableaux, graphiques et résumés d’utilité générale.” Oct. 2020.
- [81] T. Lécresse, X. Chaud, P. Fazilleau, C. Genot, and J. Song, “Metal-as-Insulation HTS coils,” *Supercond. Sci. Technol.*, Jan. 2022, [doi: 10.1088/1361-6668/ac49a5](https://doi.org/10.1088/1361-6668/ac49a5).
- [82] X. Wang *et al.*, “Turn-to-turn contact characteristics for an equivalent circuit model of no-insulation ReBCO pancake coil,” *Supercond. Sci. Technol.*, vol. 26, no. 3, p. 035012, Mar. 2013, [doi: 10.1088/0953-2048/26/3/035012](https://doi.org/10.1088/0953-2048/26/3/035012).
- [83] D. H. Kang *et al.*, “Investigation of thermal and electrical stabilities of a GdBCO coil using grease as an insulation material for practical superconducting applications,” *Review of Scientific Instruments*, vol. 85, no. 9, p. 094701, Sep. 2014, [doi: 10.1063/1.4894202](https://doi.org/10.1063/1.4894202).
- [84] J. Kim *et al.*, “Effect of Resistive Metal Cladding of HTS Tape on the Characteristic of No-Insulation Coil,” *IEEE Transactions on Applied Superconductivity*, vol. 26, no. 4, pp. 1–6, Jun. 2016, [doi: 10.1109/TASC.2016.2541687](https://doi.org/10.1109/TASC.2016.2541687).

- [85] J. Lu, R. Goddard, K. Han, and S. Hahn, "Contact resistance between two REBCO tapes under load and load cycles," *Supercond. Sci. Technol.*, vol. 30, no. 4, p. 045005, Feb. 2017, [doi: 10.1088/1361-6668/aa5b05](https://doi.org/10.1088/1361-6668/aa5b05).
- [86] M. Wang *et al.*, "Performance Study on the No-Insulation HTS Coil Wound With Narrow-Stacked Wire," *IEEE Transactions on Applied Superconductivity*, vol. 30, no. 4, pp. 1–5, Jun. 2020, [doi: 10.1109/TASC.2020.2974827](https://doi.org/10.1109/TASC.2020.2974827).
- [87] T. S. Lee *et al.*, "The effects of co-wound Kapton, stainless steel and copper, in comparison with no insulation, on the time constant and stability of GdBCO pancake coils," *Supercond. Sci. Technol.*, vol. 27, no. 6, p. 065018, May 2014, [doi: 10.1088/0953-2048/27/6/065018](https://doi.org/10.1088/0953-2048/27/6/065018).
- [88] J. Y. Jang *et al.*, "Design, construction and 13 K conduction-cooled operation of a 3 T 100 mm stainless steel cladding all-REBCO magnet," *Supercond. Sci. Technol.*, vol. 30, no. 10, p. 105012, Sep. 2017, [doi: 10.1088/1361-6668/aa8354](https://doi.org/10.1088/1361-6668/aa8354).
- [89] J.-B. Song, X. Chaud, B. Borgnic, F. Debray, P. Fazilleau, and T. Lécresse, "Construction and Test of a 7 T Metal-as-Insulation HTS Insert Under a 20 T High Background Magnetic Field at 4.2 K," *IEEE Transactions on Applied Superconductivity*, vol. 29, no. 5, pp. 1–5, Aug. 2019, [doi: 10.1109/TASC.2019.2901212](https://doi.org/10.1109/TASC.2019.2901212).
- [90] S. Noguchi, R. Miyao, H. Okusa, T. Tatsuta, H. Ueda, and S. Kim, "Turn-to-Turn Contact Resistance Measurement of No-Insulation REBCO Pancake Coils," *IEEE Transactions on Applied Superconductivity*, vol. 29, no. 5, pp. 1–5, Aug. 2019, [doi: 10.1109/TASC.2019.2903643](https://doi.org/10.1109/TASC.2019.2903643).
- [91] M. Bonura, C. Barth, A. Joudrier, J. F. Troitino, A. Fête, and C. Senatore, "Systematic Study of the Contact Resistance Between REBCO Tapes: Pressure Dependence in the Case of No-Insulation, Metal Co-Winding and Metal-Insulation," *IEEE Transactions on Applied Superconductivity*, vol. 29, no. 5, pp. 1–5, Aug. 2019, [doi: 10.1109/TASC.2019.2893564](https://doi.org/10.1109/TASC.2019.2893564).
- [92] J. Lu, J. Levitan, D. McRae, and R. Walsh, "Contact resistance between two REBCO tapes: the effects of cyclic loading and surface coating," *Supercond. Sci. Technol.*, vol. 31, no. 8, p. 085006, Jul. 2018, [doi: 10.1088/1361-6668/aacd2d](https://doi.org/10.1088/1361-6668/aacd2d).
- [93] "GetDP: a General Environment for the Treatment of Discrete Problems." <https://getdp.info/>
- [94] "Ansys - Logiciel de simulation d'ingénierie." <https://www.ansys.com/fr-fr>
- [95] "Prescale - film de mesure de pression | Fujifilm [France]." <https://www.fujifilm.com/fr/fr/business/inspection/measurement-film/prescale>
- [96] Y. Zhang, "Progress of 2G HTS wire development and process improvement at SuperPower," pp. 18-MT27: TUE-OR1_602-03, 2021.
- [97] "NI cDAQ-9178 Specifications - National Instruments".
- [98] Y. Zhao *et al.*, "Progress in fabrication of second generation high temperature superconducting tape at Shanghai Superconductor Technology," *Supercond. Sci. Technol.*, vol. 32, no. 4, p. 044004, Feb. 2019, [doi: 10.1088/1361-6668/aafea5](https://doi.org/10.1088/1361-6668/aafea5).
- [99] X. Xiong *et al.*, "Progress in High Throughput Processing of Long-Length, High Quality, and Low Cost IBAD MgO Buffer Tapes at SuperPower," *IEEE Transactions on Applied Superconductivity*, vol. 19, no. 3, pp. 3319–3322, Jun. 2009, [doi: 10.1109/TASC.2009.2018816](https://doi.org/10.1109/TASC.2009.2018816).

- [100] S. Lee *et al.*, “Development and production of second generation high T_c superconducting tapes at SuperOx and first tests of model cables,” *Supercond. Sci. Technol.*, vol. 27, no. 4, p. 044022, Mar. 2014, [doi: 10.1088/0953-2048/27/4/044022](https://doi.org/10.1088/0953-2048/27/4/044022).
- [101] J. Lee, J. Mun, J. Kim, and S. Kim, “Investigation on the Electrical Contact Resistance of Soldered Metal Insulation REBCO Coil,” *IEEE Transactions on Applied Superconductivity*, vol. 31, no. 5, pp. 1–5, Aug. 2021, [doi: 10.1109/TASC.2021.3063653](https://doi.org/10.1109/TASC.2021.3063653).
- [102] S. Noguchi, K. Monma, H. Igarashi, and A. Ishiyama, “Investigation of Current Flow Between Turns of NI REBCO Pancake Coil by 2-D Finite-Element Method,” *IEEE Transactions on Applied Superconductivity*, vol. 26, no. 3, pp. 1–5, Apr. 2016, [doi: 10.1109/TASC.2016.2536945](https://doi.org/10.1109/TASC.2016.2536945).
- [103] J. W. Elam, D. Routkevitch, and S. M. George, “Properties of ZnO / Al₂O₃ Alloy Films Grown Using Atomic Layer Deposition Techniques,” *J. Electrochem. Soc.*, vol. 150, no. 6, p. G339, Apr. 2003, [doi: 10.1149/1.1569481](https://doi.org/10.1149/1.1569481).
- [104] C. Zhai, D. Hanaor, G. Proust, and Y. Gan, “Stress-Dependent Electrical Contact Resistance at Fractal Rough Surfaces,” *Journal of Engineering Mechanics*, vol. 143, no. 3, p. B4015001, Mar. 2017, [doi: 10.1061/\(ASCE\)EM.1943-7889.0000967](https://doi.org/10.1061/(ASCE)EM.1943-7889.0000967).
- [105] F. Elie, “L’effet Branly électrocinétique des milieux granulaires,” Sep. 2013. [Available online](#).
- [106] E. Falcon and B. Castaing, “Electrical conductivity in granular media and Branly’s coherer: A simple experiment,” *American Journal of Physics*, vol. 73, no. 4, pp. 302–307, Apr. 2005, [doi: 10.1119/1.1848114](https://doi.org/10.1119/1.1848114).
- [107] J.-B. Song, X. Chaud, B. Borgnic, F. Debray, P. Fazilleau, and T. Lécresse, “Thermal and Electrical Behaviors of an MI HTS Insert Comprised of THEVA-SuperPower DP Coils Under High Background Magnetic Fields at 4.2 K,” *IEEE Transactions on Applied Superconductivity*, vol. 30, no. 4, pp. 1–6, Jun. 2020, [doi: 10.1109/TASC.2020.2974854](https://doi.org/10.1109/TASC.2020.2974854).
- [108] H. Bai, W. D. Markiewicz, J. Lu, and H. W. Weijers, “Thermal Conductivity Test of YBCO Coated Conductor Tape Stacks Interleaved With Insulated Stainless Steel Tapes,” *IEEE Transactions on Applied Superconductivity*, vol. 23, no. 3, pp. 4600204–4600204, Jun. 2013, [doi: 10.1109/TASC.2012.2229774](https://doi.org/10.1109/TASC.2012.2229774).
- [109] T. Mato, S. Hahn, and S. Noguchi, “Mechanical Damage Protection Method by Reducing Induced Current in NI REBCO Pancake Coils During Quench Propagation,” *IEEE Transactions on Applied Superconductivity*, vol. 31, no. 5, pp. 1–5, Aug. 2021, [doi: 10.1109/TASC.2021.3065879](https://doi.org/10.1109/TASC.2021.3065879).
- [110] C. Genot, T. Lécresse, P. Fazilleau, and P. Tixador, “Transient behavior of a REBCO No-Insulation or Metal-as-Insulation multi-pancake coil using a Partial Element Equivalent Circuit model,” *IEEE Transactions on Applied Superconductivity*, pp. 1–1, 2022, [doi: 10.1109/TASC.2022.3152711](https://doi.org/10.1109/TASC.2022.3152711).

REBCO No- or Metal-Insulation (NI and MI) windings open the way for very high field magnets, but their transient operation must be understood and optimized. The protection of electromagnets made of insulated windings using high-temperature superconductors (HTS) remains difficult to implement because of the low speed of quench propagation. For this reason, the traditional insulation can be removed and replaced with metallic tape. Having a NI or MI coil provides protection and improves the thermal stability of the magnet. The aim of this work is to understand the phenomenon of redistribution of radial and azimuthal currents during transient regimes in NI or MI HTS coils.

For this purpose, a Partial Element Equivalent Circuit (PEEC) code simulating the case of a simple pancake subjected to a quench was used. This model allows to monitor the values of the radial and azimuthal currents within the pancake. The code was modified to simulate the behavior of a coil consisting of several pancakes during a quench, or during other transient regimes. The behavior of an NI-MI coil during transient regimes is mainly based on the value of the electrical contact resistivity between each turn.

Experimental measurements were carried out to measure the contact resistivity between non-insulated 6 mm wide HTS tapes as a function of the mechanical pressure applied to a stack and cooled down at liquid nitrogen temperature. A large number of samples were tested for different manufacturers. Changing the nature of the insulation between the turns changes the value of the contact resistivity and thus the behavior of a coil. In a second part, Atomic Layer Deposition of Al_2O_3 of a few hundred nanometers applied on superconducting or metallic tapes were tested in order to modify the contact resistivity. The aim is to deposit an insulating material on a tape in order to tune the contact resistivity between two tapes.

Finally, the PEEC model was completed to study the behavior of a coil during a quench with voltage limitation of the power supply. The principle is to use the high increase in the resistivity of an MI pancake during a quench and to adjust the maximum voltage of the current source to obtain a rapid decline of the supply current passively once the voltage is reached. Simulations and experimental measurements were carried out on a magnet made of four pancakes to demonstrate the use of MI technology to improve the protection against quenches.